ENVIRONMENTAL CATALYSIS AND THE CORRESPONDING CATALYTIC MECHANISM

EDITED BY: Zhimin Ao, Hongqi Sun and Andres Fullana
PUBLISHED IN: Frontiers in Chemistry

frontiers Research Topics

ISSN 1664-8714
ISBN 978-2-88945-828-8
DOI 10.3389/978-2-88945-828-8

About Frontiers

Frontiers is more than just an open-access publisher of scholarly articles: it is a pioneering approach to the world of academia, radically improving the way scholarly research is managed. The grand vision of Frontiers is a world where all people have an equal opportunity to seek, share and generate knowledge. Frontiers provides immediate and permanent online open access to all its publications, but this alone is not enough to realize our grand goals.

Frontiers Journal Series

The Frontiers Journal Series is a multi-tier and interdisciplinary set of open-access, online journals, promising a paradigm shift from the current review, selection and dissemination processes in academic publishing. All Frontiers journals are driven by researchers for researchers; therefore, they constitute a service to the scholarly community. At the same time, the Frontiers Journal Series operates on a revolutionary invention, the tiered publishing system, initially addressing specific communities of scholars, and gradually climbing up to broader public understanding, thus serving the interests of the lay society, too.

Dedication to Quality

Each Frontiers article is a landmark of the highest quality, thanks to genuinely collaborative interactions between authors and review editors, who include some of the world's best academicians. Research must be certified by peers before entering a stream of knowledge that may eventually reach the public - and shape society; therefore, Frontiers only applies the most rigorous and unbiased reviews.
Frontiers revolutionizes research publishing by freely delivering the most outstanding research, evaluated with no bias from both the academic and social point of view. By applying the most advanced information technologies, Frontiers is catapulting scholarly publishing into a new generation.

What are Frontiers Research Topics?

Frontiers Research Topics are very popular trademarks of the Frontiers Journals Series: they are collections of at least ten articles, all centered on a particular subject. With their unique mix of varied contributions from Original Research to Review Articles, Frontiers Research Topics unify the most influential researchers, the latest key findings and historical advances in a hot research area! Find out more on how to host your own Frontiers Research Topic or contribute to one as an author by contacting the Frontiers Editorial Office: researchtopics@frontiersin.org

ENVIRONMENTAL CATALYSIS AND THE CORRESPONDING CATALYTIC MECHANISM

Topic Editors:
Zhimin Ao, Guangdong University of Technology, China
Hongqi Sun, Edith Cowan University, Australia
Andres Fullana, University of Alicante, Spain

Citation: Ao, Z., Sun, H., Fullana, A., eds. (2019). Environmental Catalysis and the Corresponding Catalytic Mechanism. Lausanne: Frontiers Media.
doi: 10.3389/978-2-88945-828-8

Table of Contents

05 ***Editorial: Environmental Catalysis and the Corresponding Catalytic Mechanism***
Zhimin Ao, Hongqi Sun and Andres Fullana

SECTION 1
PHOTOCATALYSIS

07 ***The Promoting Role of Different Carbon Allotropes Cocatalysts for Semiconductors in Photocatalytic Energy Generation and Pollutants Degradation***
Weiwei Han, Zhen Li, Yang Li, Xiaobin Fan, Fengbao Zhang, Guoliang Zhang and Wenchao Peng

23 ***Facile Fabrication of BiOI/BiOCl Immobilized Films With Improved Visible Light Photocatalytic Performance***
Yingxian Zhong, Yuehua Liu, Shuang Wu, Yi Zhu, Hongbin Chen, Xiang Yu and Yuanming Zhang

34 ***Photocatalytic Degradation of 4-Nitrophenol by C, N-TiO_2: Degradation Efficiency vs. Embryonic Toxicity of the Resulting Compounds***
Oluwatomiwa A. Osin, Tianyu Yu, Xiaoming Cai, Yue Jiang, Guotao Peng, Xiaomei Cheng, Ruibin Li, Yao Qin and Sijie Lin

43 ***Graphene Oxide/BiOCl Nanocomposite Films as Efficient Visible Light Photocatalysts***
Weitian Lin, Xiang Yu, Yi Zhu and Yuanming Zhang

56 ***Adsorption and Photocatalytic Processes of Mesoporous SiO_2-Coated Monoclinic $BiVO_4$***
Duangdao Channei, Auppatham Nakaruk, Wilawan Khanitchaidecha, Panatda Jannoey and Sukon Phanichphant

63 ***Catalytic and Photocatalytic Nitrate Reduction Over Pd-Cu Loaded Over Hybrid Materials of Multi-Walled Carbon Nanotubes and TiO_2***
Cláudia G. Silva, Manuel F. R. Pereira, José J. M. Órfão, Joaquim L. Faria and Olívia S. G. P. Soares

SECTION 2
CATALYTIC CONVERSION OF BIOMASS AND PPCPs

73 ***Hydrodeoxygenation of Bio-Derived Phenol to Cyclohexane Fuel Catalyzed by Bifunctional Mesoporous Organic–Inorganic Hybrids***
Liuye Mo, Wanjin Yu, Huangju Cai, Hui Lou and Xiaoming Zheng

82 ***The Correlation of Adsorption Behavior Between Ciprofloxacin Hydrochloride and the Active Sites of Fe-doped MCM-41***
Ying Wu, Yiming Tang, Laisheng Li, Peihong Liu, Xukai Li, Weirui Chen and Ying Xue

SECTION 3

COMPUTATIONAL CATALYSIS

93 ***First Principles Study on the CO Oxidation on Mn-Embedded Divacancy Graphene***

Quanguo Jiang, Jianfeng Zhang, Zhimin Ao, Huajie Huang, Haiyan He and Yuping Wu

104 ***The Activity Improvement of the TM_3(hexaiminotriphenylene)$_2$ Monolayer for Oxygen Reduction Electrocatalysis: A Density Functional Theory Study***

Beibei Xiao, Hui Zhu, HouYi Liu, XiaoBao Jiang and Qing Jiang

frontiers in Chemistry

EDITORIAL
published: 13 February 2019
doi: 10.3389/fchem.2019.00075

Editorial: Environmental Catalysis and the Corresponding Catalytic Mechanism

Zhimin Ao[1]*, *Hongqi Sun*[2] and *Andres Fullana*[3]

[1] Guangzhou Key Laboratory of Environmental Catalysis and Pollution Control, Guangdong Key Laboratory of Environmental Catalysis and Health Risk Control, School of Environmental Science and Engineering, Institute of Environmental Health and Pollution Control, Guangdong University of Technology, Guangzhou, China, [2] School of Engineering, Edith Cowan University, Joondalup, WA, Australia, [3] Department of Chemical Engineering, University of Alicante, Alicante, Spain

Keywords: environment remediation, catalysts, clean energy, photocatalysis, biomass conversion, density functional theory, catalytic mechanism

Editorial on the Research Topic

Environmental Catalysis and the Corresponding Catalytic Mechanism

The ever growing environmental pollution has stimulated the rapid development of environmental catalysis in recent years. Environmental catalysis is a multidisciplinary research field for which more and more chemists, materials scientists, as well as environmentalists have devoted their efforts working in this field because of the bright potentials in improving human health and life quality. With the progresses in controllable materials synthesis, advanced characterizations (electron microscopy, spectroscopy, etc.), high-level analytical chemistry, together with the computational studies, catalysis continues to be the driving force for generation of clean energy, abatement of major pollutants in air and water, and meantime the theories behind the catalytic reactions are illustrated. In the current Research Topic, an elegant collection of original research and review articles reporting the synthesis of high-performance catalysts, their applications in various catalytic technologies for environment remediation, and relevant theoretical calculations for understanding the catalytic mechanisms is presented.

Photocatalysis remains to be a research focus for the environmental catalysis community due to the wide applications in carbon dioxide reduction, oxidation of volatile organic compounds (VOCs), elimination of aqueous organic pollutants and disinfection, water splitting (Chen et al., 2011; Zheng et al., 2016; Wang et al., 2017). Particularly, the synthesis of visible light and near-infrared (NIR) light responsive semiconductor photocatalysts is of immense interests to scientists because visible light and NIR light occupy around 90% of the solar light energy, in comparison to the no more than 5% for ultraviolet light (UV). To enhance the visible light absorption of the most popularly used TiO_2, several routes including creating defects and element doping are developed Qin and Lin et al., introduced carbon and nitrogen elementals into TiO_2 simultaneously and demonstrated the improved catalytic property of such C, N-TiO_2 catalyst compared to anatase TiO_2 under simulated sunlight irradiation for degradation of 4-nitrophenol. Moreover, they also evaluated the embryonic toxicity of intermediate degradation compounds (Osin et al.). Silva et al., synthesized Pd-Cu loaded over hybrid materials of carbon nanotubes and TiO_2 for nitrate reduction. It reported that the Pd-Cu loaded on the hybrid materials have high photocatalytic performance for NO_3^- conversion (Silva et al.). Other than TiO_2, the bismuth compounds as a new class of photocatalytic materials have been paid much attention in recently. Among them, bismuth oxychloxide (BiOCl) exhibits excellent photocatalysis behaviors driven by UV light. To expand its light absorption to visible light spectrum, efforts to fabricate graphene oxide/BiOCl nanocomposite

OPEN ACCESS

Edited and reviewed by:
Pascal Granger,
Lille University of Science and Technology, France

Correspondence:
Zhimin Ao
zhimin.ao@gdut.edu.cn

Specialty section:
This article was submitted to Green and Sustainable Chemistry, a section of the journal Frontiers in Chemistry

Received: *17 November 2018*
Accepted: *28 January 2019*
Published: *13 February 2019*

Citation:
Ao Z, Sun H and Fullana A (2019) Editorial: Environmental Catalysis and the Corresponding Catalytic Mechanism. Front. Chem. 7:75. doi: 10.3389/fchem.2019.00075

film and BiOI/BiOCl film are reported by Zhu and Zhang et al., respectively (Lin et al.; Zhong et al.). $BiVO_4$ is found to be a visible light-activated photocatalyst due to the narrower band gap than TiO_2, the involvement of graphene oxide or BiOI can further improve the photocatalytic performance for RhB degradation. However, the poor specific surface area limits its catalytic performance. To this end, Channei et al. utilized a co-precipitation method to coat SiO_2 onto $BiVO_4$ and obtained SiO_2/$BiVO_4$ composites with larger surface area and higher photocatalytic activity and degradation efficiency towards methylene blue dye with respect to monoclinic $BiVO_4$ (Channei et al.). Furthermore, a comprehensive overview on semiconductors loaded with carbon cocatalysts as photocatalysts for water splitting and pollutant degradation was provided by Peng et al., aiming to give a clue to the rational design of low-cost photocatalysts with more efficient solar light utilization. The synthesis methods of various types of carbon-semiconductor composite photocatalysts were summarized, the contribution of different carbon allotropes like C_{60}, carbon nanotubes, graphene to the enhanced photocatalytic activity were compared and the cocatalytic effect mechanisms were discussed (Han et al.).

Catalytic conversion of biomass to biofuels is another emerging topic in the environmental catalysis field out of the urge to transform the agricultural wastes into resources and to reduce the carbon dioxide emission from fossil fuels combustion (Wang and Xiao, 2015; Xiong et al., 2015). Heterogeneous acidic catalysts and enzyme biocatalysts are among the leading candidates for the conversion of lignocellulosic biomass to fuels and value-added chemicals. One relevant paper presented the good catalytic performance of bifunctional catalysts which were synthesized by decorating propyl/phenyl-sulfonic acid group functionalized mesoporous silica materials SBA-15 with Pt particles in the reaction of hydrodeoxygenation of bio-derived phenol to produce cyclohexane fuel (Mo et al.).

Pharmaceutical and personal care products (PPCPs) are emerging contaminants, which are widely present in pharmaceutical and hospital wastewater, even natural water. In this Research Topic, Fe-MCM-41s were fabricated at different conditions to adsorb widely used antibiotics ciprofloxacin hydrochloride (CPX) for its removal from waste water (Wu et al.). Owing to the rise of supercomputers, computational studies become important complementary tools for elucidation of the inherent mechanisms of catalytic reactions. Currently *Ab initio* techniques like Density Functional Theory (DFT) are popularly adopted for theoretical calculations. Here in this Research Topic, two examples of DFT studies on the mechanisms of CO oxidation catalyzed by Mn-embedded divacancy graphene and boosted oxygen reduction reaction performance catalyzed by two-dimensional metal–organic frameworks TM_3(hexaiminotriphenylene)$_2$ monolayer (where TM = Ni, Co, Fe, Pd, Rh, Ru, Pt, Ir, and Os) were shown (Jiang et al.; Xiao et al.).

We believe that this collection, Environmental Catalysis and the Corresponding Catalytic Mechanism, illustrates the advancements of catalysis for environment remediation and innovations in clean energy with diminished production of undesired by-products. At the same time, challenges and perspectives for this field are also addressed with the hope that future interests will be focused to help establish a world with clean air and water, as well as sustainable and green energy for human to live in.

AUTHOR CONTRIBUTIONS

ZA drafted the manuscript. HS and AF made substantial improvements, and all authors approved for publication.

ACKNOWLEDGMENTS

ZA was supported by National Natural Science Foundation of China (21777033 and 21607029), Science and Technology Program of Guangdong Province (2017B020216003), and Science and Technology Program of Guangzhou City (201707010359).

REFERENCES

Chen, X., Liu, L., Yu, P. Y., and Mao, S. S., (2011). Increasing solar absorption for photocatalysis with black hydrogenated titanium dioxide nanocrystals. *Science* 331, 746–750. doi: 10.1126/science.1200448

Wang, L., and Xiao, F.-S. (2015). Nanoporous catalysts for biomass conversion. *Green Chem.* 17, 24–39. doi: 10.1039/C4GC01622J

Wang, X., Wang, F., Sang, Y., and Liu, H. (2017). Full-Spectrum Solar-Light-Activated Photocatalysts for light–chemical energy conversion. *Adv. Energy Mat.* 7:1700473. doi: 10.1002/aenm.201700473

Xiong, H., Schwartz, T. J., Andersen, N. I., Dumesic, J. A., and Datye, A. K. (2015). Graphitic-carbon layers on oxides: toward stable heterogeneous catalysts for biomass conversion reactions. *Angew. Chem. Int. Edition* 54, 7939–7943. doi: 10.1002/anie.201502206

Zheng, Q., Durkin, D. P., Elenewski, J. E., Sun, Y., Banek, N. A., Hua, L., et al. (2016). Visible-light-responsive graphitic carbon nitride: rational design and photocatalytic applications for water treatment. *Environ. Sci. Technol.* 50, 12938–12948. doi: 10.1021/acs.est.6b02579

Conflict of Interest Statement: The authors declare that the research was conducted in the absence of any commercial or financial relationships that could be construed as a potential conflict of interest.

frontiers in Chemistry

REVIEW
published: 31 October 2017
doi: 10.3389/fchem.2017.00084

The Promoting Role of Different Carbon Allotropes Cocatalysts for Semiconductors in Photocatalytic Energy Generation and Pollutants Degradation

Weiwei Han, Zhen Li, Yang Li, Xiaobin Fan, Fengbao Zhang, Guoliang Zhang and Wenchao Peng**

School of Chemical Engineering and Technology, Tianjin University, Tianjin, China

Semiconductor based photocatalytic process is of great potential for solving the fossil fuels depletion and environmental pollution. Loading cocatalysts for the modification of semiconductors could increase the separation efficiency of the photogenerated hole-electron pairs, enhance the light absorption ability of semiconductors, and thus obtain new composite photocatalysts with high activities. Kinds of carbon allotropes, such as activated carbon, carbon nanotubes, graphene, and carbon quantum dots have been used as effective cocatalysts to enhance the photocatalytic activities of semiconductors, making them widely used for photocatalytic energy generation, and pollutants degradation. This review focuses on the loading of different carbon allotropes as cocatalysts in photocatalysis, and summarizes the recent progress of carbon materials based photocatalysts, including their synthesis methods, the typical applications, and the activity enhancement mechanism. Moreover, the cocatalytic effect among these carbon cocatalysts is also compared for different applications. We believe that our work can provide enriched information to harvest the excellent special properties of carbon materials as a platform to develop more efficient photocatalysts for solar energy utilization.

Keywords: carbon allotropes, semiconductor, photocatalysis, cocatalysts, energy generation, pollutants degradation

OPEN ACCESS

Edited by:
Andres Fullana,
University of Alicante, Spain

Reviewed by:
Xiaoguang Duan,
Curtin University, Australia
Jiguang Deng,
Beijing University of Technology, China

****Correspondence:***
Fengbao Zhang
fbzhang@tju.edu.cn
Wenchao Peng
wenchao.peng@tju.edu.cn

Specialty section:
This article was submitted to Green and Environmental Chemistry, a section of the journal Frontiers in Chemistry

Received: *06 September 2017*
Accepted: *06 October 2017*
Published: *31 October 2017*

Citation:
Han W, Li Z, Li Y, Fan X, Zhang F, Zhang G and Peng W (2017) The Promoting Role of Different Carbon Allotropes Cocatalysts for Semiconductors in Photocatalytic Energy Generation and Pollutants Degradation. Front. Chem. 5:84. doi: 10.3389/fchem.2017.00084

INTRODUCTION

Environmental pollution and fossil fuels depletion are the most serious social problems nowadays. Since the discovery of the photocatalytic splitting of water on TiO_2 electrodes by Fujishima and Honda in 1972, photocatalysis technology has become one of the most promising technologies for energy generation and environment remediation (Fujishima and Honda, 1972). Moreover, solar energy is clean, sustainable, and inexhaustible, which is therefore the most hopeful resource to solve the energy and environment problems (Chen et al., 2010a). Mostly, photocatalysis is a semiconductor-mediated process (Chen et al., 2010b; Wang et al., 2014; Zhang et al., 2016b). So far, kinds of semiconductor materials, including metal oxides, metal sulfides and metal containing salts have been used as photocatalysts. Some metal free materials, such as silicon, sulfur, graphic

carbon nitride (g–C_3N_4), have also been developed as photocatalysts for the utilization of sunlight (Peng et al., 2013; Cao and Yu, 2014; Devi and ArunaKumari, 2014; He et al., 2015). However, some fundamental problems must be resolved before their real application, which are (1) low utilization efficiency of solar energy; (2) poor quantum efficiency; (3) severe photo corrosion (Zhang and Guo, 2013; Chowdhury and Balasubramanian, 2014; Han et al., 2015; Xie et al., 2015; Liu Y. et al., 2017b). To address these obstacles, modification of semiconductors with suitable cocatalysts is a frequent and effective solution (Yang J. H. et al., 2013). Metal nanoparticles and their compounds, especially noble metal based materials, are always used as cocatalysts (Bai et al., 2014; Zhang et al., 2015a; Zhong et al., 2016). Although they are effective to enhance the photocatalytic activity, the high cost and rare storage on earth limit their practical application (Ran et al., 2014). To develop cheap, highly efficient alternatives to replace noble metal based cocatalysts is still a great challenge in the photocatalysis filed.

Recently, carbon materials, including activated carbon (AC), fullerenes (C_{60}), carbon nanotubes (CNTs), graphene (GR), and other carbon allotropes, have been widely investigated as cocatalysts for semiconductors in photocatalysis (Xiang et al., 2012; Ouzzine et al., 2014; Cao and Yu, 2016; Paulo et al., 2016; Yu et al., 2016). Specially, CNTs and GR have large specific surface areas (SSAs), excellent electric conductivity, high mechanical strength, and good thermal, and chemical stability, making them ideal substitute for noble metal cocatalysts (Zhang et al., 2012; Wang et al., 2013, 2017; Di et al., 2015; Han et al., 2016). **Figure 1** shows the structure models of the carbon materials and their photocatalytic applications as cocatalysts simply. Many kinds of carbon cocatalysts based composites have been reported for photocatalytic reactions, and the cocatalytic mechanisms have also been discussed (Woan et al., 2009; Chen et al., 2011; Lee W. J. et al., 2012; Xie et al., 2013; Shearer et al., 2014; Li et al., 2015). For example, a graphene–TiO_2 NPs hybrid was successfully synthesized by wrapping amorphous TiO_2 NPs with GO using a one-step hydrothermal method by Lee and coworkers (Lee J. S. et al., 2012). The hybrid exhibited superior photocatalytic activity for the photodegradation of MB under the visible light irradiation. Fan et al. prepared a novel 3D AgX/graphene aerogels (X = Br, Cl) structured composite, which exhibited excellent photocatalytic and cycling performance for the degradation of MO and reduction of Cr^{VI} (Fan Y. et al., 2015). They also investigated photocatalytic enhancement mechanism of the graphene aerogels in the composite, which could effectively suppress the recombination of photogenerated holes, and electrons as a capable substrate for the photocatalyst. Tian et al. reported a new CQDs/hydrogenated TiO_2 (H-TiO_2) photocatalyst by assembling CQDs on the surface of H-TiO_2 (Tian et al., 2015). The photocatalytic activity of CQDs/H-TiO_2 was superior to P25, TiO_2 nanobelts, and H-TiO_2 nanobelts for the degradation of MO under UV-visible-NIR irradiation. The CQDs have excellent photo-induced electron transfer and reservoir properties, which could convert NIR light to visible light to be in full used by H-TiO_2 and effectively suppress the recombination of electron-hole pairs. Generally, loading carbon materials as cocatalysts for semiconductors, the synergistic effect between them can increase the active sites, widen the absorption range of the solar light, facilitate the separation of the electron-hole pairs, and thus enhancing the photocatalytic activity.

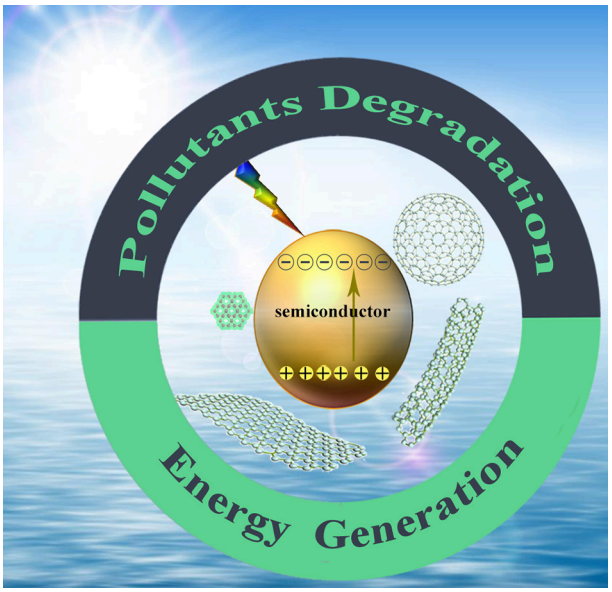

FIGURE 1 | Schematic illustration of the photocatalytic applications of carbon materials based semiconductor composites.

To develop carbon materials based composite has attracted great attention for low cost and highly active photocatalysts. Lots of researches have been done on this subject, but a systematic summary about the key roles of different carbon allotropes as cocatalysts is still lacking. Herein, we aim to provide an overview on recent advances in the synthesis, multiple applications and mechanism of different carbon allotropes based composite photocatalysts. On behalf of this review, we wish more carbon based photocatalysts could be synthesized for environment remediation and energy generation.

PHOTOCATALYSTS SYNTHESIS

The synthesis process will affect the morphologies, properties and activities of the composite photocatalyts greatly. As shown in **Table 1**, we summarized the typical synthesis methods of the recently reported carbon based photocatalysts. The semiconductors could be loaded on carbon materials by one-step grinding, stirring, ultrasonic assisted dispersing or by some complicated multi-step synthesis methods. It can be concluded that mechanical mixing, hydrothermal/solvothemal, and sol-gel process are more frequently used. In addition, photocatalytic reduction and microwave-assisted method are also reported, and they may have a great potential due to the green and sustainable synthetic processes.

TABLE 1 | Preparation methods and applications of carbon materials based semiconductor composites.

Photocatalyst	Synthetic method	Photocatalytic applications	Light source	Reaction system (catalyst amount/solution)	Photocatalytic activity	References
CdS−1D ZnO−2D GR	Two-step refluxing	Anaerobic reduction of 4-nitroaniline	300 W Xe lamp ($\lambda \geq 420$ nm)	10 mg/40 ml (10 mg·L^{-1}) with 40 mg $HCOONH_4$	Conversion of 95% with high selectivity for PPD (> 98%) in 16 min	Han et al., 2015
TiO_2/AC	Sol-gel	Oxidation of propene	UV lamp (radiation peaks at 257.7 nm or 365 nm)	–/100 ppmv [flow rates of 30 and 60 ml min^{-1} (STP)]	Conversion of nearly 60% for flow rate of 30 ml min^{-1}	Ouzzine et al., 2014
Graphene–CNTs–CdS	Hydrothermal	Degradation of MB	Visible light irradiation	20 mg/50 ml (10 mg·L^{-1}) MB solution	DP of ca. 40% in 30 min	Wang et al., 2013
CNT@TiO_2	Solvothermal	Degradation of MO	300 W Xe lamp	50 mg/100 ml (15 mg·L^{-1}) MO solution	8 times increment of the reaction rate compared to bare TiO_2	Di et al., 2015
CNT–confined TiO_2	Restrained hydrolysis	Degradation of MB	Xe lamp ($\lambda \geq 420$ nm)	20 mg/50 ml (20 mg·L^{-1}) organic pollutant solution	DP of 97.8% in 90 min	Chen et al., 2011
NCNT/TiO_2 core/shell nanowires	Biomineralization followed by calcination	Degradation of MB or p-nitrophenol (PNP)	450 W Xe lamp ($\lambda \geq 420$ nm)	Volume of 0.64 cm^2/3.5 ml (10 ppm) MB or PNP solution	DP of ca. 100% in 4 h for MB	Lee W. J. et al., 2012
Graphene–wrapped TiO_2 NPs	One-step hydrothermal treatment followed by calcination	Degradation of MB	450 W Xe lamp ($\lambda \geq 420$ nm)	8 mg/8 ml (2.7×10^{-2} mM) MB solution	DP of ca. 90% in 1 h; rate constant $k = 3.41 \times 10^{-2}$ min^{-1}	Lee J. S. et al., 2012
CQDs/hydrogenated TiO_2 nanobelts	Oil bath reflux	Degradation of MO; hydrogen evolution	UV source: 350 W mercury lamp (254 nm); visible light source: 300 W Xe lamp; NIR light source: 250 W infrared lamp ($\lambda < 760$ nm)	20 mg/20 ml (20 mg·L^{-1}) MO solution; 50 mg (with 1wt% Pt) /100 ml aqueous solution containing methanol (20% v/v)	DP of > 86%, 50% in 25 min under UV light, visible light irradiation, respectively; DP of 32% in 120 min under NIR light irradiation; 7.42 mmol $h^{-1}g^{-1}$	Tian et al., 2015
Graphene/ZnO	Hydrothermal	Degradation of deoxynivalenol	UV light (254 nm, 365 nm)	25 mg/50 ml (15 ppm) DON	DP of 99% in 30 min	Bai et al., 2017
Carbon nanotube–SiC	*In situ* growth	H_2 evolution	300 W Xe lamp ($\lambda \geq 420$ nm)	50 mg/100 ml of 0.1 M Na_2S solution	R_{H2}: 108 μmol h^{-1} g^{-1}; 3.1 times higher than SiC	Zhou et al., 2015
$BiVO_4$/CDs/CdS	Precipitation	Water splitting into H_2 and O_2	300 W Xe lamp ($\lambda > 420$ nm)	80 mg/100 ml ultrapure water	1.24 mol h^{-1}	Wu et al., 2017
Graphite-like carbon spheres@TiO_{2-x}	Two-step hydrothermal	H_2 evolution; degradation of RhB, MB, CIP and 4-CP	UV-LEDs; 350 W Xe lamp ($\lambda > 420$ nm)	50 mg/80 ml (0.5 M) Na_2S/Na_2SO_3 solution; 80 mg/80 ml (10 mg·L^{-1}) pollutants solution	255.2 μmol h^{-1} g^{-1}, 5.4 times higher than TiO_{2-x}; 3.6/6.3 (RhB/MB) times higher than TiO_2	Jiang et al., 2017
CdS NWs–CNT	Electrostatic self-assembly	Reduction of aromatic nitro organics	300 W Xe lamp ($\lambda > 420$ nm)	10 mg/40 ml (20 mg·L^{-1})	Nearly complete reduction of 4-NA in 5min	Weng et al., 2014
RGO–CdS	Microwave-assisted hydrothermal	Reduction of CO_2	300 W Xe lamp ($\lambda \geq 420$ nm)	100 mg/0.25 ml (4 M HCl And 0.12 g $NaHCO_3$)	2.51 μmol h^{-1} g^{-1} QE: 0.8% at 420 nm	Yu J. et al., 2014
GR–CdS	Solvothermal	Selective reduction of aromatic nitro compounds	300 W Xe lamp ($\lambda \geq 420$ nm)	10 mg/30 ml (20 mg·L^{-1}) with 20mg ammonium oxalate	Conversion of almost 80% for 4-NA	Liu et al., 2014
A-Fe_2O_3/graphene	Hydrothermal	Degradation of RhB	350 W Xe lamp	30 mg/30 ml (10 mg·L^{-1}) RhB solution with 0.7 ml H_2O_2 (≥ 30 wt%)	DP of 98% in 20 min	Han et al., 2014

(Continued)

TABLE 1 | Continued

Photocatalyst	Synthetic method	Photocatalytic applications	Light source	Reaction system (catalyst amount/solution)	Photocatalytic activity	ReferenceS
MWCNT–TiO_2 sphere	Hydrothermal	Degradation of gaseous styrene	365 nm UV-LED spot lamp	100 mg/25 ± 1.5 ppmv gaseous styrene	DP of 55.4% in 180 min	An et al., 2012
AC/Bi_2WO_6	Hydrothermal	Degradation of RhB	300 W Ultra-Vitalux lamp	250 mg/250 ml (10ppm) RhB	Totally degraded in 30 min	Murcia-Lopez et al., 2013
Carbon dots/g-C_3N_4/ZnO	Impregnation-thermal	Degradation of tetracycline (TC)	Xe lamp ($\lambda \geq 420$ nm)	50 mg/100 ml (10 mg·L^{-1}) RhB solution	DP of almost 100% in 30 min	Guo et al., 2017
CNT/Ag_3PO_4	Ultrasound followed by stir	Degradation of RhB	300 W Xe lamp ($\lambda > 400$ nm)	75 mg/75 ml (10 mg·L^{-1}) TC solution	DP of ca. 10% in 12 min	Xu et al., 2014
TiO_2/C_{60}	Sonication followed by light irradiation	Degradation of MB and 4-CP	84W light sources ($\lambda >$ 420 nm)	17 mg/25 ml (144 μM) MB; 15 mg/15 ml (10 mg·L^{-1}) 4-CP	DP of 47% for MB and 82% for 4-CP in 40 min; 2 and 5 times of rate constant values of the bare TiO_2	Mukthar Ali and Sandhya, 2014
GO–CdS	Two-phase mixing	degradation of various water pollutants and disinfection	Solar light simulator ($\lambda \geq$ 420 nm)	20 mg/50 ml (20 mg·L^{-1}) water pollutants solution	DP of over 80% for AO7; nearly 100% of both *E. coli* and *B. subtilis* were killed in 25 min	Gao et al., 2013
CdS/GO	Solvothermal	H_2 evolution	300 W Xe lamp ($\lambda > 420$ nm)	50 mg/100 ml of 1.25 M $(NH4)_2SO_3$ solution	1470 μmol h^{-1}	Hong et al., 2015
TiO_2/MWCNTs and TiO_2/AC	Sol-gel	Degradation of Acid Blue 92	125 W high-pressure mercury lamp	60 ppm/20 ppm AB92	2 times of TiO_2/MWCNTs faster than TiO_2/AC in 120 min	Zarezade et al., 2011
CNTs/TiO_2	Sol-gel	Degradation of MB	three UV-A lamps	20 mg/200 ml (10 mg·L^{-1})	DP of ca. 45% in 180 min	Li Z. et al., 2011
GO–TiO_2 NFs	Sol-gel	Photocatalytic H_2 evolution; dye-sensitized H_2 evolution	300 W Xe lamp ($\lambda >$ 320 nm); (420 nm)	0.5 g·L^{-1}/ 10 vol% methanol aqueous solution; $[RuL_3] =$ 10μM, $[EDTA]_0 = 10$ mM	The photocatalytic hydrogen production and photocurrent generation increased by 1.7 and 8.5 times	Kim et al., 2014
$LaFeO_3$-rGO	High temperature sol-gel	Oxidation of MB or RhB	300 W Xe lamp ($\lambda >$ 400 nm)	10 mg/100 ml (0.5 mg·L^{-1}) MB solution or (1.25 mg·L^{-1}) RhB solution	DP of ca. 98% in 70 min for MB	Ren et al., 2016
ZnS–rGO	Microwave irradiation	Degradation of MB and RhB	250 W tungsten halogen lamp	50 mg·L^{-1}/ 0.1 mM dye solution	DP of 55.23% for MB and 90.37% for RhB in 120 min	Thangavel et al., 2016
Graphene/Cu_2O	CVD method	Degradation of MO	300 W Xe lamp	20 mg/80 ml (30 mg·L^{-1}) MO solution	DP of ca. 80% in 30 min	Zhang et al., 2016a
CdS–GR (RGO, SEG)	Solvothermal	Selective oxidation of benzyl alcohol in water	300 W Xe lamp (760 > λ > 420 nm)	8 mg/1.5 ml alcohol oxygen-saturated ultrapure water with 0.1 mmol alcohol	Conversion of ca. 35% for benzyl alcohol; the selectivity of ca. 72% for benzaldehyde	Zhang et al., 2013a
Ag@AgBr/CNT	Deposition-precipitation	CO_2 reduction	150 W Xe lamp ($\lambda >$ 420 nm)	500 mg/100 ml (0.2 M) $KHCO_3$ solution	30 μmol h^{-1} g^{-1} for methane	Abou Asi et al., 2013
PSGM/rGO/CdS	Hydrothermal	H_2 evolution	300 W Xe lamp ($\lambda >$ 400 nm)	100 mg/100 ml (0.5 M) Na_2S/Na_2SO_3 solution	175 μmol h^{-1}; QE: 3.99% at 420 nm	Xu et al., 2016
RGO/InGaZn	Hydrothermal	H_2 evolution	125 W Hg visible lamp ($\lambda >$ 400 nm)	50 mg/50 ml (10 vol% CH_3OH)	435.4 μmol h^{-1}	Martha et al., 2014
$(CNT–TiO_2)_{ox}$	One-pot oxidation	H_2 evolution	150 W mercury vapor lamp	170 mg/170 ml (10 vol% methanol or 0.02 M saccharide)	292.5 μmol h^{-1}	Silva et al., 2015

(Continued)

TABLE 1 | Continued

Photocatalyst	Synthetic method	Photocatalytic applications	Light source	Reaction system (catalyst amount/solution)	Photocatalytic activity	ReferenceS
CQDs/P25	Hydrothermal	H_2 evolution	500 W halogen lamp ($\lambda > 450$ nm)	50 mg/25 ml (6.25 ml methanol)	9.1 μmol h^{-1} under UV-Vis light irradiation; 0.5 μmol h^{-1} under visible light irradiation	Yu H. et al., 2014
SWCNTs/TiO_2	Hydrolysis	Degradation of organic pollutants	17 W mercury arc lamp ($\lambda = 254$ nm); 1500 W Xe lamp ($700 > \lambda > 320$ nm)	50 mg/500 ml of organic pollutants solution	Comparable degradation rates regarding Degussa P25 under UV irradiation	Murgolo et al., 2015
Ag_3PO_4-MoS_2/graphene	Two-step hydrothermal	Degradation of phenols	500 W Xe lamp ($\lambda > 420$ nm)	20 mg/50 ml (20 mg·L^{-1}) DCP solution	Nearly completed in 20 min, 60 min under simulated solar light, visible light irradiation	Peng et al., 2014
CQDs/ZnS	Hydrothermal and bath reflux	Degradation of MB, RhB, CIP	300 W Xe lamp ($\lambda > 380$ nm)	30 mg/50 ml (20 mg·L^{-1}) for MB, RhB; 50 ml (10 mg·L^{-1}) for CIP	Degradation rate is 1.67 and 2.11 times higher than ZnS for MB and RhB; DP is more than ZnS for CIP	Ming et al., 2016
C_{60}@a–TiO_2	Solution phase method	degradation of MB	8 W medium-pressure mercury lamp	100 mg/250 ml (5 mg·L^{-1}) MB solution	Nearly completed in 60 min	Qi et al., 2016
GO–TiO_2 CNT–TiO_2	Liquid phase deposition	Degradation of Microcystin-LA	300 W Xe lamp; two 15 W fluorescent lamps ($\lambda >$ 420 nm)	5 mg/10 ml (0.2 μM) MC-LA solution	DP of 100% in 5 min under solar light irradiation; DP of 88% in 2 h under visible light irradiation	Sampaio et al., 2015
CdS–cluster-decorated graphene	Solvothermal	H_2 evolution	350 W Xe lamp ($\lambda \geq 420$ nm)	20 mg/80 ml (8 ml lactic acid) mixed solution	1.12 mmol h^{-1} QE: 22.5% at 420 nm	Ye et al., 2012
GO–Ta_2O_5 CNT–Ta_2O_5	Hydrothermally assisted sol-gel	H_2 evolution	High pressure Hg lamp	50 mg/no mentioned	1,600 μmol h^{-1} for CNT–Ta_2O_5; 140 μmol h^{-1} for GO–Ta_2O_5	Cherevan et al., 2014
TiO_2-GR	Hydrothermal	Gas-phase degradation of benzene	Four 4W UV Lamps (254 nm)	300 mg/20 ml min^{-1} (250 ppm) benzene	Conversion of 6.4%; average mineralization ratio of 76.2%	Zhang et al., 2010
AgSiOx@CNT AgSiOx@RGO	In suit one-step	Degradation of MB	300 W Xe lamp ($780 > \lambda >$ 400 nm)	50 mg/50 ml (50 ppm) of MB solution	Completed in 10 min by AgSiOx@CNT; completed in 7 min by AgSiOx@RGO	Jing et al., 2017
CDs/$ZnIn_2S_4$	Hydrothermal	Degradation of MO	300 W Xe lamp ($\lambda \geq 420$ nm)	50 mg/100 ml (10 mg·L^{-1}) dye solutions	DP of 100% in 40 min, 2.34 times higher than $ZnIn_2S_4$	Shi et al., 2017
CdS–carbon (C_{60}, CNT, and GR)	Solvothermal	Selective oxidation of alcohols	300 W Xe lamp ($\lambda \geq 420$ nm)	8 mg/1.5 ml oxygen-saturated BTF (0.1 mmol alcohol)	Conversion of 40%, 61% and 42% along with 100% selectivity over CdS–RGO, CdS–C_{60} and CdS–CNT in 3 h	Zhang et al., 2013b
CNT/Cd0.1Zn0.9S	Hydrothermal	H_2 evolution	300 W Xe lamp ($\lambda \geq 420$ nm)	50 mg/80 ml (0.35 M Na_2S and 0.25 M Na_2SO_3) aqueous solution	1,563.2 μmol h^{-1} g^{-1}; QE: 7.9%	Yu et al., 2012
TiO_2/graphene aerogels (GAs)	Hydrothermal	Degradation of MO	300 W Xe lamp	no mentioned/70 ml (10 mg·L^{-1}) MO solutions	DP of 90% in 5 h	Qiu et al., 2014

Hydrothermal/Solvothemal Methods

Hydrothermal or solvothermal methods are the most frequently used ways due to their mild reaction conditions, high product purity, controllable morphology, good crystallinity, and uniform distribution of obtained products (Li Q. et al., 2011). For example, Liu et al. synthesized GR–CdS nanocomposites by an one-step solvothermal method using DMSO as reductant and sulfure source (Liu et al., 2014). In the preparation procedure, GO was dispersed in DMSO to obtain the GO–DMSO dispersion, $Cd(CH_3COO)_2{\cdot}2H_2O$ was then added. The mixture was then treated at 453 K for 12 h to obtain the final composites. The photocatalytic activity of GR–CdS nanocomposites for selective reduction of aromatic nitro compounds was dramatically enhanced compared to the pure CdS. This can be ascribed to the synergistic effect with graphene addition, the increased visible light absorption range and intensity, the improved lifetime and charge transfer ability, and the enhanced adsorption capacity of this nanocomposite toward the nitro compounds.

Han et al. synthesized 2D hexagonal α-Fe_2O_3/graphene nanoplate composites by a simple one-step hydrothermal method with no template (Han et al., 2014). Using hydrothermal method, not only the effective reduction of the GO to graphene was achieved, but intimate contact was also formed between the α-Fe_2O_3 nanoplates and graphene. A significant enhancement for photocatalytic degradation of RhB could be observed after the combination with graphene cocatalyst. An et al. fabricated MWCNT–TiO_2 sphere composites by a facile one-step hydrothermal method using TiF_4 as titanium source and CNTs as structure regulator (An et al., 2012). The effects of hydrothermal temperature and hydrothermal time on the structural characteristics of MWCNT–TiO_2 photocatalysts were investigated. Decreasing hydrothermal temperature or prolonging the hydrothermal time could lead to the enhancement of the photocatalytic degradation efficiency of both gaseous (i.e., styrene) and aqueous (i.e., MO) phase. Decreasing the hydrothermal temperature could lead to the crystallite size decrease of TiO_2 (**Table 2**), while prolonging the hydrothermal time will increase the synergistic effects between TiO_2 and MWCNTs, thus promoting the photocatalytic performance.

As reported by Murcia-López et al. the calcination could be applied after hydrothermal process to prepare the AC/Bi_2WO_6 and AC/TiO_2/Bi_2WO_6 photocatalysts (Murcia-Lopez et al., 2013). The introduction of optimized percentage of AC (2 wt%) could form 3D-hierarchical structures of both AC/Bi_2WO_6 and AC/TiO_2/Bi_2WO_6, which exhibited improved photocatalytic activities for the RhB degradation under both UV-vis and visible illumination compared to pure Bi_2WO_6. Here, the presence of AC could stimulate the 3D-hierarchical structure formation, and will increase the surface area and absorption ability of the catalyst at the same time.

TABLE 2 | Crystallite size of TiO_2 in Pure TiO_2 and MWCNT–TiO_2 photocatalysts.

Samples prepared under different conditions	Crystallite size (nm)
Pure TiO_2	44.7
7.2 wt % MWCNTs	33.1
18.9 wt % MWCNTs	30.1
31.7 wt % MWCNTs	29.9
48.2wt % MWCNTs	30.6
51.6 wt % TiO_2	23.2
68.4 wt % TiO_2	26.7
81.1 wt % TiO_2	30.1
89.6 wt % TiO_2	35.2
120°C	24.2
150°C	26.7
180°C	27.3
210°C	28.4
24 h	25.5
48 h	26.5
72 h	26.7

Reprinted from An et al. (2012), Copyright 2012, with permission from American Chemical Society.

Mechanical Mixing Method

The loading of carbon cocatalysts can also be performed by simple mechanical mixing processes, such as magnetic stirring, ball milling, and ultrasonication (Xu et al., 2014; Guo et al., 2017). Ali et al. used C_{60} as cocatalysts for the modification of TiO_2 using a simple sonication assisted mixing method (Mukthar Ali and Sandhya, 2014). The C_{60} molecules were first dispersed in β-cyclodextrin (CD), and then mixed with the suspension of TiO_2 with the assistance of sonication under sunlight. According to the HRTEM images of the composites, C_{60} cocatalysts are dispersed in the composite without aggregation. They believed that the non-aggregated C_{60} cocatylysts played a key role in increasing the amount of reactive oxygen species (ROS) and suppressing photogenerated charge recombination, thus leading to the enhanced photocatalytic activity. The photocatalytic activity of the composite shows 2 and 5 times higher than the bare TiO_2 for the degradation of MB and 4-CP, respectively. Gao and his coworkers successfully synthesized GO–CdS composites by a novel two-phase mixing method (Gao et al., 2013). By simply stirring for 24 h, the two phases are mixed into a homogeneous solution, and CdS nanoparticles are then uniformly deposited on GO sheets (see Scheme 1 in the original paper, Gao et al., 2013). The obtained composites show higher photocatalytic degradation and disinfection activities than CdS under visible light irradiation.

However, using the mechanical mixing method, the interaction force between semiconductors and carbon materials is a little weak without the formation of chemical bonds, resulting in a relatively lower activity enhancement compared to that from hydrothermal/solvothemal methods. For example, Hong and his coworkers reported that CdS/GO photocatalysts synthesized by *in situ* solvothermal method showed much higher H_2 evolution activity than that synthesized by mechanical loading (Hong et al., 2015).

Sol-Gel Method

The sol-gel method is another widely applied method to get a close chemical interaction between semiconductors and carbon cocatalysts (Zarezade et al., 2011; Morales-Torres et al., 2012; Ng et al., 2012). Generally, this method need to prepare the sol

first, which is then mixed with the carbon materials uniformly. Subsequently, the gel is formed by aging followed with high temperature calcination to obtain the final composites. This method can control the crystal structure and uniformity of the supported nanoparticles, thus can fabricate photocatalysts with high activities. Li et al. used surfactant wrapping sol-gel method for the synthesis of CNT/TiO_2 core-shell nanocomposites (Li Z. et al., 2011). Using this method, they prepared uniform and distinct nanoscale anatase TiO_2 layer on the CNTs with tailored TiO_2 layer thickness with different Ti precursors (TEOTi, TTIP, and TBT). The CNT/TiO_2 composite prepared from TBT has thinner TiO_2 layer that provides shorter traveling distance for electron transferring to the CNT core, the activity for the degradation of MB was therefore higher than those prepared from TEOTi and TTIP. Kim et al. prepared GO–TiO_2 nanofibers (NFs) by using a sol-gel method and an electrospinning technique (Kim et al., 2014). They also compared the activity of GO–TiO_2 NF with GO(s)–TiO_2 NF (prepared by covering GO sheets on external surface of TiO_2 NF). Due to the stronger electronic coupling between GO and TiO_2 matrix and the reduced light shielding effect by hiding GO inside of TiO_2 NF, the photocatalytic H_2 production of GO–TiO_2 NF was higher than GO(s)–TiO_2 NF.

Although the materials prepared by sol-gel method have high purity and uniform particle size, some problems still exist, such as relatively long reaction time, large shrinkage during drying, and easy sintering with high temperature calcination. For example, Ren et al. prepared nanostructured $LaFeO_3$ nanoparticles (NPs) with rGO as a 2D template using a high temperature sol-gel method (Ren et al., 2016). Although the addition of C-support or rGO reduces the sintering degree of $LaFeO_3$, it remains difficult to avoid sintering during the high temperature calcination for a long time.

Other Methods

Microwave-assisted method is a green synthesis method based on the characteristics of microwave heating with tremendous advantages (Tian et al., 2016). Preparation of catalysts with special structure and high yield would be finished in a very short time using microwave heating. Thangavel et al. prepared the ZnS–rGO nanohybrids via microwave irradiation for 20 s over two cycles (Thangavel et al., 2016). Interestingly, Raman spectrum of the hybrids indicates the complete reduction of GO into rGO via the microwave treatment. After 2 h of irradiation, the ZnS–rGO showed higher degradation efficiency for MB (about 55.23%) and RhB (about 90.37%) than that of bare ZnS (about 40.79% for MB and 56.56% for RhB), respectively. They attributed the high activity to tight intermolecular binding, good interfacial contact between ZnS and rGO in the hybrid, and enhanced charge-transfer properties of rGO in nanohybrid. Zhang et al. successfully synthesized the graphene/Cu_2O composites by a CVD (chemical vapor deposition) method. They also investigated the effects of the CVD growth parameters on the graphene flakes. The obtained composites were effective for the photocatalytic methyl orange degradation (Zhang et al., 2016a).

PHOTOCATALYTIC APPLICATIONS

The photocatalytic activity of pure semiconductors can be enhanced by the addition of carbon materials as cocatalysts. The obtained composites are mainly used for the photocatalytic pollutants degradation, water splitting, CO_2 reduction, organic synthesis and so on (Abou Asi et al., 2013; Zhang et al., 2013a; Colmenares et al., 2016; Li K. et al., 2016; Zeng et al., 2017). In the following sections, we will focus their applications for photocatalytic hydrogen evolution and pollutants degradation.

Photocatalytic Hydrogen Evolution

Hydrogen is considered as one of the most potential alternative energy in the twenty-first century (Zhang et al., 2015b; Zou and Zhang, 2015). Among the present hydrogen production methods, photocatalytic water splitting driven by sustainable solar energy is an ideal way to achieve clean hydrogen production (Matsuoka et al., 2007; Wang et al., 2009; Hisatomi et al., 2014). **Figure 2** describes the photocatalytic water splitting process with the presence of cocatalysts. Under the light irradiation, the electrons are photoexcited from the valence band (VB) to the conduction band (CB), while the holes are left in the VB, resulting in the separation of electrons and holes. Generally, for photocatalytic water splitting, the CB potential of semiconductor has to be more negative than hydrogen electrode potential EH^+/H_2, while the VB potential should be more positive than oxygen electrode potential EO_2/H_2O (Xu et al., 2016). Moreover, due to the impact of semiconductor band bending and presence of surface overpotential, the band gap of semiconductor should be larger than 1.23 eV to split water into H_2 and O_2 (Matsuoka et al., 2007; Moniz et al., 2015).

Carbon materials are effective H_2 evolution cocatalysts for the semiconductors mainly due to their large surface area and good charge mobility on their surface. Martha et al. synthesized RGO/InGaZn nanocomposites using a one-pot hydrothermal method (Martha et al., 2014). They also evaluated the effects of

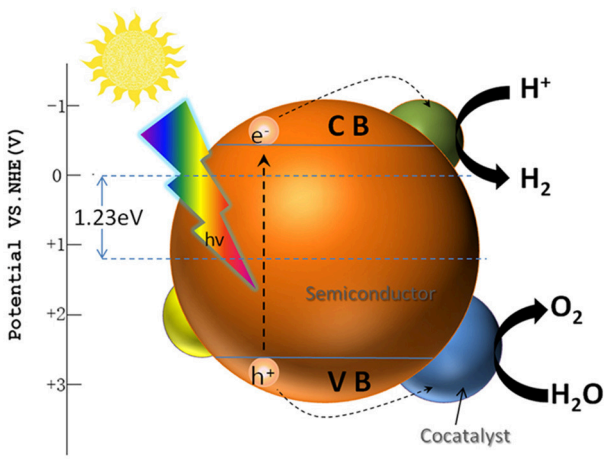

FIGURE 2 | Fundamentals of semiconductor photocatalytic water splitting for hydrogen evolution.

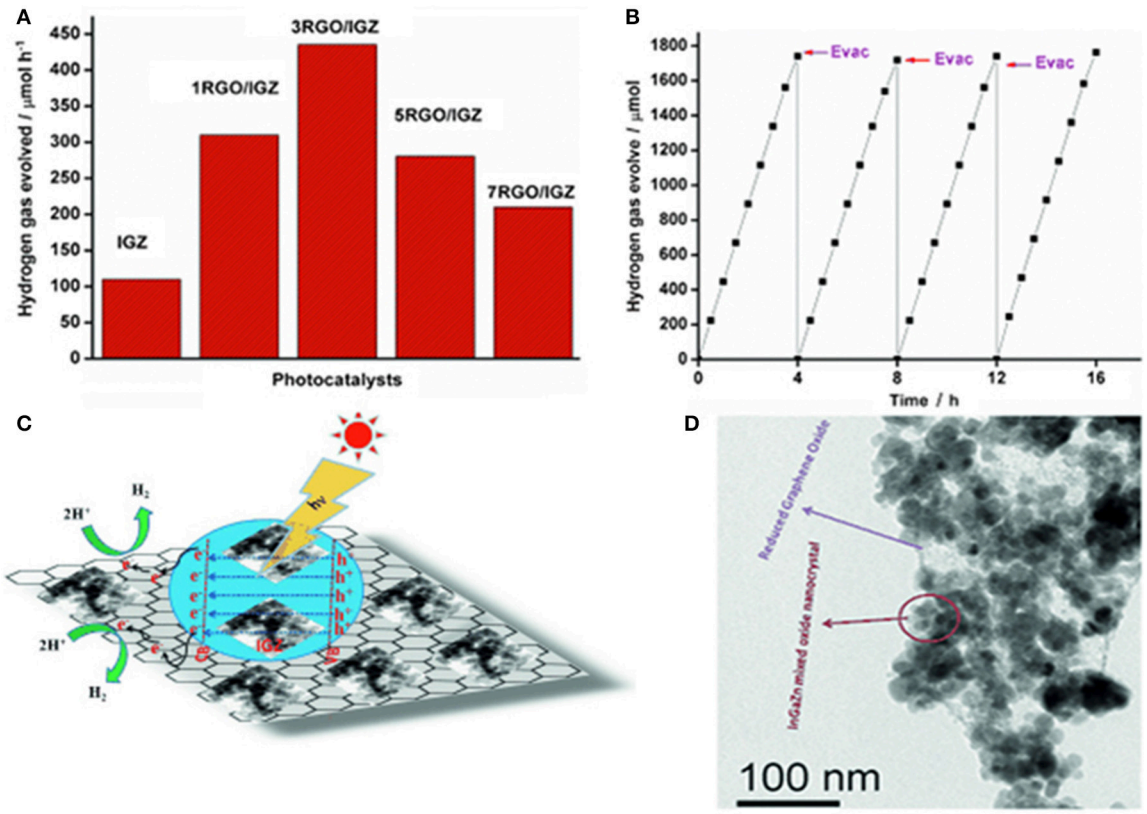

FIGURE 3 | (A) Photocatalytic H_2 evolution over IGZ, 1RGO/IGZ, 3RGO/IGZ, 5RGO/IGZ, and 7RGO/IGZ under visible-light irradiation; **(B)** Time course of H_2 evolution over 3RGO/IGZ; **(C)** Mechanism of photocatalytic H_2 composites; **(D)** TEM image of 3RGO/IGZ (Reprinted from Martha et al., 2014, Copyright 2014, with permission from Wiley-VCH).

RGO percentage on the H_2 evolution activity under visible-light irradiation ($\lambda > 400$ nm) (**Figure 3**). Three wt% rGO was proved to be the best loading percentage, and the H_2 generation rate can be as high as 435 μmol/h (**Figure 3A**). As shown in **Figure 3D**, InGaZn was uniformly dispersed on the surface of RGO, which was beneficial for the electrons moving from InGaZn to RGO. Moreover, the RGO could also provide more active adsorption sites and photocatalytic reaction centers. The stability test of RGO/InGaZn composite was also tested, and no deactivation could be found after four recycles (**Figure 3B**).

Silva et al. combined TiO_2 and CNTs using two different methods: hydration-dehydration labeled as (CNT_{ox}-TiO_2) and one-pot oxidation (labeled as $(CNT–TiO_2)_{ox}$) (Silva et al., 2015). One wt% Pt was then loaded followed by calcination at 473 K and 673 K, respectively. The optimized catalyst Pt/$(CNT–TiO_2)_{ox}$-473 could obtain a H_2 evolution rate of 485 μmol/h, 2.4 times compared to the Pt/TiO_2-473. According to the infrared attenuated total reflectance (ATR) spectra (see Figure 1 in the original paper, Silva et al., 2015), the bands from C = C and C–H are weaker in $(CNT–TiO_2)_{ox}$ than in CNT_{ox}-TiO_2, indicating a better dispersion of the TiO_2 particles at the surface of CNT in $(CNT–TiO_2)_{ox}$. This conclusion can be further confirmed by SEM and TEM images in. The better photocatalysis performance of $(CNT–TiO_2)_{ox}$ might be related to the stronger interface interaction between TiO_2 and CNT, which is promoted by the oxidative treatment according to the ATR analysis.

Loading carbon materials as cocatayst, the bandgap of semiconductors could be narrowed to utilize the visible light with longer wavelength. Yu et al. prepared the CQDs/P25 composites with a "dyade"-like structure and applied them for photocatalytic hydrogen evolution under both UV-vis and visible light irradiation (**Figure 4**) (Yu H. et al., 2014). With methanol as the sacrificial agent, CQDs/P25–1.5 wt% showed the best photocatalytic performance under UV-vis light irradiation, and the evolution rate could reach 9.1 μmol/h, 4 times higher than that of pure P25 (2.3 μmol/h). While CQDs/P25–2.0 wt% was the optimized one under visible light with a H_2 evolution rate of 0.5 μmol/h. The photocurrent response of these composites are shown in **Figures 4A,B**, which are consistent with the photocatalytic results. They believed that CQDs played dual roles to improve the photocatalytic activity of P25. CQDs could act as electron acceptors to improve the charge separation under UV-vis light irradiation. Meanwhile, they also served as a photosensitizer to sensitize P25 into a visible light response "dyade" structure for H_2 evolution under visible light irradiation.

Heteroatom doped carbon materials, such as nitrogen doped graphene, are proved to be better cocatalysts for semiconductor photocatalysts in recent years (Putri et al.,

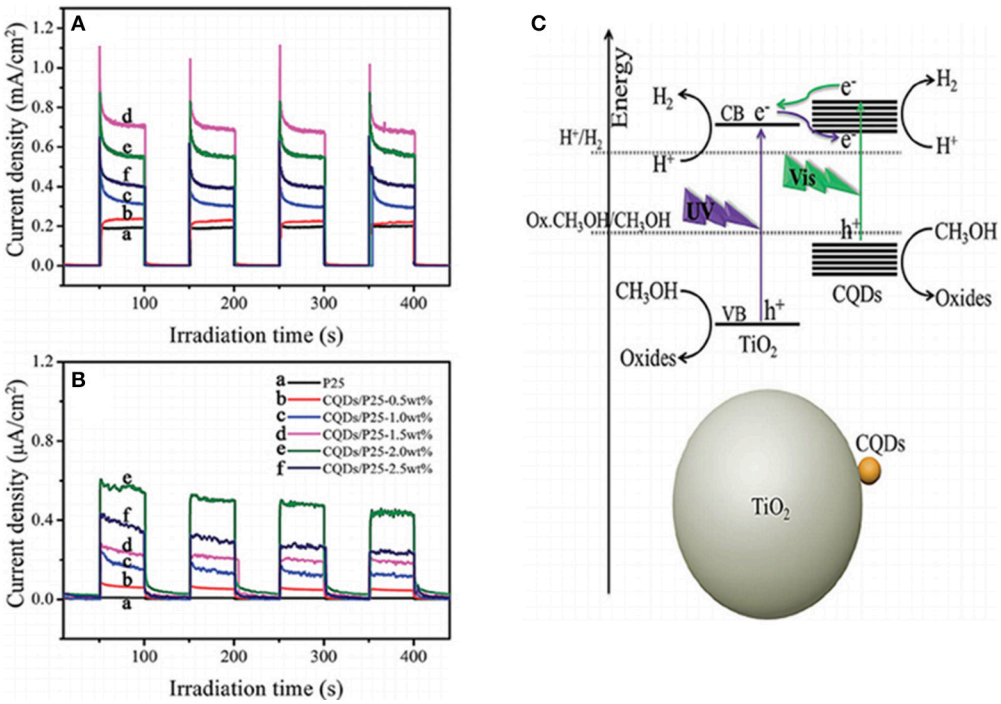

FIGURE 4 | (A) Schematic illustration for the photocatalytic H_2 production mechanism over the CQDs/P25 under UV-Vis and visible light ($\lambda > 450$ nm) irradiation; **(B,C)** The transient photocurrent response of P25 and the CQDs/P25 composites with different amount of CQDs in 1 M Na_2SO_4 aqueous solution under UV-Vis light and visible light ($\lambda > 450$ nm) irradiation (Reprinted from Yu H. et al., 2014, Copyright 2014, with permission from Royal Society of Chemistry).

2015). Yue et al. synthesized a ternary visible-light-driven photocatalyst for hydrogen evolution reaction. After decorating the CdS/Nb_2O_5 heterojunction structure with N-doped graphene (NGR) nanosheets (Yue et al., 2017), the hybrid photocatalyst (2 wt% NGR) exhibited a high H_2 evolution rate of 100 μmol h^{-1} g^{-1}, which was about 7.7 times than the pure CdS. Doping with nitrogen atom could change the electron density of the GR surface, thus can separation the photogenerated charges more efficiently. Jia et al. synthesized a series of nanocomposites by coupling CdS nanoparticles with NGR through calculation (Jia et al., 2011). The N-graphene/CdS was proved to be more efficient photocatalysts for hydrogen evolution compared to the CdS supported on undoped graphene. Significantly, the photocatalytic H_2 evolution rate of the N-graphene (2 wt %)/CdS reached 210 μmol h^{-1} without the addition of metal cocatalyst, which was much higher than graphene/CdS (99 μmol h^{-1}) and GO/CdS (95 μmol h^{-1}) with the same percentage of cocatalysts.

Photocatalytic Degradation of Pollutants

Photocatalytic degradation of pollutants is another important application of photocatalysts. Photocatalysts can adsorb and degrade pollutants in water and toxic gas in air under illustration, which thus has great potential for environmental remediation. Previous studies have shown that photocatalysis technology can not only degrade organic pollutants into CO_2, H_2O, and inorganic salt, but also eliminate the heavy metal ions (Akpan and Hameed, 2009; Peng et al., 2014; Murgolo et al., 2015; Jing et al., 2017).

Ming et al. synthesized dandelion-like ZnS/CQDs hybrid materials using hydrothermal method with CTAB as surfactant (Ming et al., 2016). As shown in **Figures 5A–D**, some dark dots are distributed on the ZnS nanowires uniformly. Coating the optimal content of 2 wt% CQDs, the photocatalyst showed the highest degradation rate, which was about 1.67 and 2.11 times higher than bare ZnS for MB and RhB, respectively. As illustrated in **Figure 5E**, the intensity of the PL emission band decreased obviously after the loading of CQDs on ZnS. The 2 wt% CQDs/ZnS possessed the lowest intensity, suggesting the lowest recombination possibility of photoexcited holes and electrons. They also proposed the photocatalytic mechanisms on the CQDs/ZnS hybrid:

$$ZnS + hv \rightarrow e_{ZnS}^{-} + h_{ZnS}^{+} \quad (1)$$

$$e_{ZnS}^{-} \rightarrow e_{CQDs}^{-} \quad (2)$$

$$e_{CQDs}^{-} + O_2 \rightarrow {}^{*}O_2^{-} \quad (3)$$

$$h_{ZnS}^{+} + H_2O \rightarrow {}^{*}OH^{-} \quad (4)$$

$$2\,{}^{*}OH \rightarrow H_2O_2 \quad (5)$$

$$H_2O_2 + {}^{*}O_2^{-} \rightarrow OH^{-} + {}^{*}OH + O_2 \quad (6)$$

$${}^{*}OH + \text{dye} \rightarrow H_2O + CO_2 + \text{intermediates} \quad (7)$$

Qi and his co-workers prepared a series of fullerene-modified anatase TiO_2 (C_{60}@a-TiO_2) nanocomposites by a simple solution phase method (Qi et al., 2016). By the introduction of C_{60}, the activity of C_{60}@a-TiO_2 for photocatalytic degradation of MB

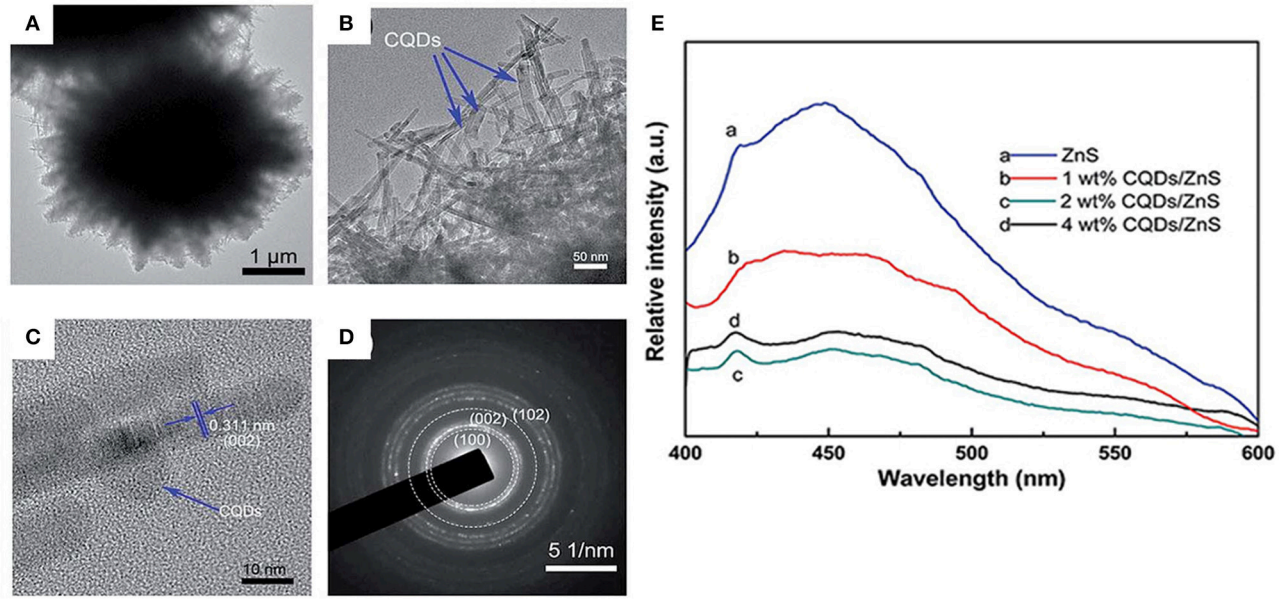

FIGURE 5 | (A,B) TEM images of CQDs/ZnS hybrid materials; **(C)** HRTEM image of the CQDs/ZnS hybrid materials; **(D)** SAED of the dandelion-like ZnS; **(E)** PL spectra of pure ZnS and CQDs/ZnS hybrid materials (Reprinted from Ming et al., 2016, Copyright 2016, with permission from Royal Society of Chemistry).

could be enhanced greatly under UV-A light irradiation. In order to confirm the electronic structures of C_{60}@a-TiO_2, the density functional theory (DFT) was used for a theoretical calculation toward the C_{60}-COOH@a-TiO_2 (101) surface. The adsorption energy and the projected density of states (PDOS) for the C_{60}-COOH@a-TiO_2 (101) surface were calculated. Strong covalent interaction between C_{60} and the a-TiO_2 (101) surface was present with the calculated adsorption energy of 3.61 eV. Moreover, the introduction of C_{60} narrows the band gap to 0.8 eV, resulting in the red shift of light absorption edge of the C_{60}-COOH@a-TiO_2 heterojunctions. According to the DFT results, there is an additional doping state present between the valance band and conduction band by the incorporation of C_{60} on the a-TiO_2 (101) surface. The activity of C_{60}@a-TiO_2 is therefore enhanced with more efficient charge separation efficiency and increased light absorption range.

Sampaio et al. used both GO–TiO_2 and CNT–TiO_2 materials for the photocatalytic degradation of the cyanobacterial toxin, microcystin-LA (MC-LA) under simulated solar light and visible light irradiation (Sampaio et al., 2015). The GO–TiO_2 composite containing 4 wt% of GO exhibited the highest photocatalytic activity under both simulated solar light and visible light irradiation. The enhanced activity of GO–TiO_2 was attributed to the optimal assembly and interfacial coupling between TiO_2 nanoparticles and GO sheets, which can effectively inhibit electron-hole recombination. While the activity of CNT–TiO_2 for the MC-LA removal under visible light irradiation was mostly due to adsorption instead of photocatalytic degradation.

Murgolo et al. fabricated a composite photocatalyst by combining SWCNTs with nano-sized TiO_2 NRs (Murgolo et al., 2015). The composite showed tailored photocatalytic properties for the photocatalytic degradation of a mixture of 22 organic pollutants under both UV and simulated solar light. The experiment results showed that this composite displayed comparable degradation rates over Degussa P25 under UV irradiation. While the SWCNTs/TiO_2 showed slightly lower efficiency than Degussa P25 under simulated solar irradiation. The SWCNTs/TiO_2 can be reused easily by a mild centrifugation or a filtration. This photocatalyst has proved to be a promising candidate in photocatalytic pollutants degradation, which can also be integrated with a biological step for the enhanced removal of emerging organic pollutants.

Heteroatoms doped carbon materials are also effective cocatalysts for photocatalytic degradation reaction. Liu et al. synthesized N-CNT/mpg-C_3N_4 composites via thermal polycondensation (Liu J. et al., 2017). N-CNT has better electronic conductivity and more defective structure than undoped CNT, which could therefore accept electrons more easily. Benefiting from the synergistic effect between N-CNT and mpg-C_3N_4, the composites show enhanced photo-degradation activity for rhodamine B, methyl orange and tetracycline hydrochloride under visible light irradiation. Due to the special 2D structure of graphene, which can also be combined with other layered materials to fabricate hybrid cocatalysts (Chen et al., 2017; Peng et al., 2017). Our group have used the MoS_2/graphene hybrids for the modification of CdS and Ag_3PO_4, and the obtained composites showed improved photocatalytic activity for phenols degradation and nitroaromatic compounds detoxification (Peng et al., 2014, 2016). The photo-activity of the final composite could also be adjusted by changing the ratio of MoS_2 and graphene.

COMPARISON OF CARBON ALLOTROPES AS COCATALYSTS

There have been some other relevant reviews on this subject, but as far as we are concerned, a horizontal comparison of these carbon cocatalysts in photocatalysis field is still lack. In this section, we summarized some examples which compared different carbon cocatalysts for the modification of semiconductors. Zarezade et al. used sol-gel method to synthesize TiO_2/AC and TiO_2/MWCNT hybrid materials (Zarezade et al., 2011). Although the surface area of TiO_2/MWCNTs was smaller than that of TiO_2/ACs, the activity of TiO_2/MWCNTs was even higher for photocatalytic degradation of AB92. The defects of MWCNTs could be used as anchor sites for the growth of TiO_2 crystallites, which can lead to the uniform distribution of TiO_2 on the MWCNT surface. After calcination of the composite at 500°C (**Figure 6A**), a remarkable photocatalytic performance could be achieved with a maximum degradation percentage of 86% in 2 h (**Figure 6B**).

Ye's group compared the photocatalytic behaviors of CdS–graphene (CdS–GR) and CdS–carbon nanotube (CdS–CNT) nanocomposites as photocatalysts for the hydrogen evolution and the degradation of methyl orange (MO) under visible-light irradiation (Ye et al., 2012). **Figure 7A** reveals that both the CdS–GR and the CdS–CNT composites display enhanced photocatalytic H_2 evolution activities. Furthermore, the CdS–GR composite is more efficient than the CdS–CNT composite under their optimized mass ratios. The H_2 evolution rate over the CdS–GR composite could reach 70 μmol h^{-1}, which is 1.3 times higher than that of the CdS–CNT (52 μmol h^{-1}). Similarly, **Figure 7B** shows that GR is more efficient to enhance the photocatalytic performance of CdS for the degradation of MO. The degradation percentage of MO over the optimized CdS–GR (1: 0.01) is as large as 95%, 1.8 times higher than that of the optimized CdS–CNT (1: 0.03) after 60 min irradiation (**Figure 7C**). The stronger interaction and larger contact interface between CdS and GR facilitate the transfer of photogenerated electrons from CdS to GR, leading to a higher efficiency in the separation of photogenerated electron-hole pairs and a higher photocatalytic performance of the CdS–GR composite than the CdS–CNT composite.

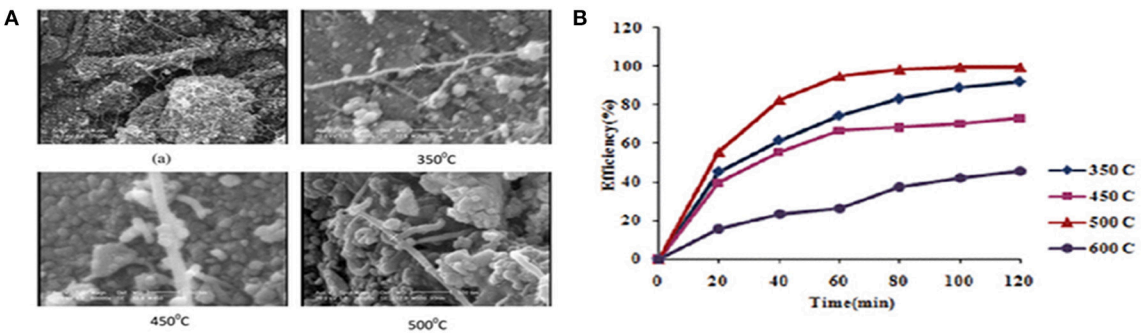

FIGURE 6 | (A) SEM images of the **(A)** acid treated MWCNTs (1 mm), and TiO_2/MWCNTs calcined at various temperatures; **(B)** Effect of calcination temperatures on photocatalytic activity of TiO_2/MWCNTs (Reprinted from Zarezade et al., 2011, Copyright 2011, with permission from Royal Society of Chemistry).

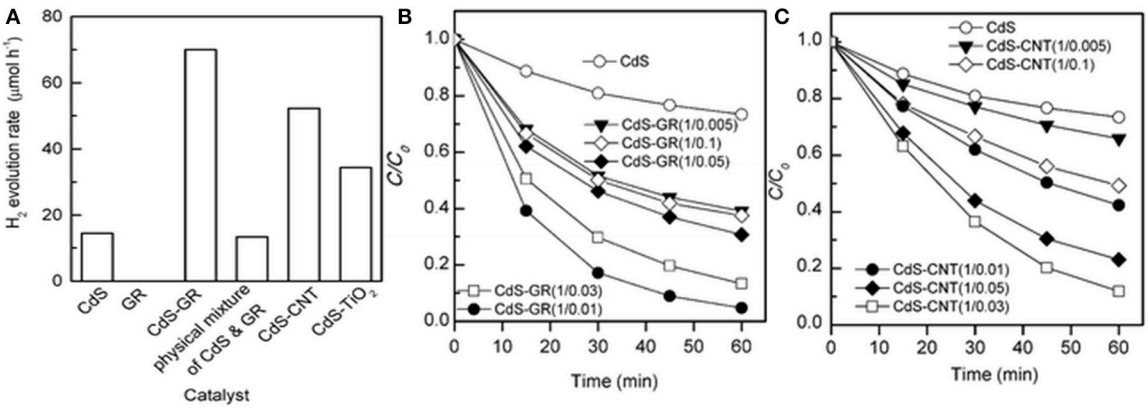

FIGURE 7 | (A) Comparison of photocatalytic H_2 evolution rate of different photocatalysts; **(B)** Photocatalytic degradation of MO over the CdS–GR and **(C)** CdS–CNT composites with different mass ratios of CdS: carbon material under visible-light irradiation (Reprinted from Ye et al., 2012, Copyright 2012, with permission from Royal Society of Chemistry).

Cherevan and coworkers hybridized both multi-walled CNTs and graphene oxide (GO) with Ta_2O_5 semiconductor via a *in situ* hydrothermally assisted sol-gel method (Cherevan et al., 2014). Surprisingly, CNT–Ta_2O_5 hybrid exhibited superior performance over GO–Ta_2O_5 hybrid, and a maximum H_2 evolution rate of 1,600 μmol h^{-1} could be obtained for CNT–Ta_2O_5. This result is opposite to many other studies, which could be attributed to two reasons: (1) the amount of Ta_2O_5 in the GO hybrid is much lower than in the CNT hybrid; (2) annealed CNTs are expected to possess better charge transfer properties than highly defective GO.

Jing et al. compared the degradation efficiencies of methylene blue (MB) over AgSiOx@CNT and AgSiOx@RGO nanocomposites under visible light (Jing et al., 2017). Interestingly, AgSiOx@CNT has a better photodegradation performance than AgSiOx@RGO at a small amount of CNTs, while the removal rate with AgSiOx@RGO is faster than AgSiOx@CNT at high carbon contents. This is probably because the different functional mechanism of these two carbon materials. The low content of CNT could boost the synergistic effect of the nanocomposite by reducing the electron transfer resistances and prolonging the lifetime of electron-hole pairs. However, as for AgSiOx@RGO, adsorption effect is dominant rather than photodegradation as RGO contains residual oxygen-containing groups.

Yang et al. presented a comparative study of photocatalytic selective oxidation on several carbon based photocatalysts (Yang M. Q. et al., 2013). They synthesized a series of TiO_2-GR, –CNT, and –C_{60} photocatalysts by combining sol-gel with hydrothermal methods. These three different carbon allotropes affected slightly in the morphology, crystal phase, particle size, pore volume and surface area the of the supported TiO_2 nanocrystals. The TiO_2-carbon (GR, CNT, and C_{60}) have similar photocatalytic activities and analogous reaction mechanisms toward selective oxidation of benzyl alcohol. Different preparation methods could obtain different structural composition and synergetic interaction between TiO_2 and carbon, which therefore have a greater impact on the photocatalytic performance of TiO_2-carbon composites. The comparison shows that GR fails to prove its unique advantage compared to the other two carbon allotropes. Similarly, Zhang et al. investigated TiO_2-Graphene as high-performance photocatalyst for the gas-phase degradation of benzene (Zhang et al., 2010). They concluded that GR was in essence the same as other carbon materials (carbon nanotube, activated carbon, and fullerene) as cocatalysts on enhancement of photocatalytic activity of TiO_2, although GR has unique structural and electronic properties in comparison with other carbon allotropes.

Due to the special 2D structure and excellent physical/chemical properties, we expected the graphene will show better performance compared to other carbon allotropes (An and Yu, 2011; Zhang et al., 2011). However, it didn't show superior cocatalytic properties compared to the CNT or carbon quantum for the modification of some semiconductors (Ma et al., 2016). Researchers has tried to modify the graphene further by heteroatoms doping or activation method, which could increase its electric conductivity or surface area. The performance of the modified graphene could be then enhanced further as photocatalytic cocatalysts, thus increasing its real application potential.

MECHANISM OF CARBON COCATALYSTS FOR PHOTOCATALYTIC ACTIVITY IMPROVEMENT

It has been proposed that the photocatalytic activity enhancement is due to the synergistic effect between semiconductor and carbon materials. Generally, carbon materials play four primary roles as cocatalysts for the activity enhancement of the semiconductors (Tan et al., 2012; Bai et al., 2016). (1) They provide a structure with larger specific surface area over which the active component can be well-dispersed, thus increasing the active sites. Activated carbon is amorphous carbon with a specific surface up to 3,000 m^2 g^{-1} (Strobel et al., 2006). Graphene, the 2-dimensional nanosheets composed of sp^2-hybridized carbon atoms, possesses an extremely high specific surface area (theory value of 2,630 m^2 g^{-1}) (Fan X. et al., 2015). While the CQDs can distribute uniformly on the surface of semiconductor materials because of its small size. (2) During the photocatalytic degradation of organic pollutants, carbon materials can be used as adsorbent to improve the adsorption capacity of semiconductors (Matos et al., 2001; Ai et al., 2015). (3) Carbon materials can be doped as a photosensitizer for bandgap narrowing, which is favorable for expanding the visible light absorption region of semiconductors. (4) By the formation of carbon materials–semiconductor heterojunction, the excellent electron transfer could be achieved, leading to the enhanced charge separation efficiency and photocatalytic activity (Guldi et al., 2006; Li X. et al., 2016; Shi et al., 2017).

CONCLUSIONS AND FUTURE PROSPECTS

Carbon materials are important photocatalytic cocatalysts due to their low cost and high efficient. In this review, we summarized the recent development of the carbon materials based semiconductor photocatalysts, including their synthesis methods and the applications for H_2 evolution and pollutants degradation. Zero-dimensional C_{60}, CQDs, one-dimensional CNTs, two-dimensional GR, and activated carbon are all involved to provide valuable information for metal free cocatalysts selection. Although much progress has been achieved, some essential issues are still unaddressed, especially for the activity and stability enhancement mechanisms. Studies about the interface between the semiconductors and the cocatalysts should be helpful for new carbon materials based photocatalysts development. Computational chemistry using DFT could also provide valuable information for the photocatalysts design. Although more in-depth studies are still needed, carbon materials based photocatalysts have great

potential to address various environmental and energy-related problems.

AUTHOR CONTRIBUTIONS

WH chose the references and edit the draft. ZL provided assistance for literature search and some revision. YL, XF, FZ, and GZ provided professional advice. WP designed the main content and revised the manuscript. All authors read and approved the final manuscript version to be submitted.

ACKNOWLEDGMENTS

This research was supported by the project No. 21506158 from the National Natural Science Foundation of China (NSFC).

REFERENCES

Abou Asi, M., Zhu, L., He, C., Sharma, V. K., Shu, D., Li, S., et al. (2013). Visible-light-harvesting reduction of CO_2 to chemical fuels with plasmonic Ag@AgBr/CNT nanocomposites. *Catal. Today* 216, 268–275. doi: 10.1016/j.cattod.2013.05.021

Ai, B., Duan, X., Sun, H., Qiu, X., and Wang, S. (2015). Metal-free graphene-carbon nitride hybrids for photodegradation of organic pollutants in water. *Catal. Today* 258, 668–675. doi: 10.1016/j.cattod.2015.01.024

Akpan, U. G., and Hameed, B. H. (2009). Parameters affecting the photocatalytic degradation of dyes using TiO_2-based photocatalysts: a review. *J. Hazard. Mater.* 170, 520–529. doi: 10.1016/j.jhazmat.2009.05.039

An, T., Chen, J., Nie, X., Li, G., Zhang, H., Liu, X., et al. (2012). Synthesis of carbon nanotube-anatase TiO_2 sub-micrometer-sized sphere composite photocatalyst for synergistic degradation of gaseous styrene. *ACS Appl. Mater. Interfaces* 4, 5988–5996. doi: 10.1021/am3016476

An, X. Q., and Yu, J. C. (2011). Graphene-based photocatalytic composites. *RSC Adv.* 1, 1426–1434. doi: 10.1039/c1ra00382h

Bai, S., Wang, L., Chen, X., Du, J., and Xiong, Y. (2014). Chemically exfoliated metallic MoS_2 nanosheets: a promising supporting co-catalyst for enhancing the photocatalytic performance of TiO_2 nanocrystals. *Nano Res.* 8, 175–183. doi: 10.1007/s12274-014-0606-9

Bai, S., Yin, W., Wang, L., Li, Z., and Xiong, Y. (2016). Surface and interface design in cocatalysts for photocatalytic water splitting and CO_2 reduction. *RSC Adv.* 6, 57446–57463. doi: 10.1039/C6RA10539D

Bai, X., Sun, C., Liu, D., Luo, X., Li, D., Wang, J., et al. (2017). Photocatalytic degradation of deoxynivalenol using graphene/ZnO hybrids in aqueous suspension. *Appl. Catal. B* 204, 11–20. doi: 10.1016/j.apcatb.2016.11.010

Cao, S. W., and Yu, J. G. (2016). Carbon-based H_2-production photocatalytic materials. *J. Photochem. Photobiol. C Photochem. Rev.* 27, 72–99. doi: 10.1016/j.jphotochemrev.2016.04.002

Cao, S., and Yu, J. (2014). g-C_3N_4-based photocatalysts for hydrogen generation. *J. Phys. Chem. Lett.* 5, 2101–2107. doi: 10.1021/jz500546b

Chen, C., Ma, W., and Zhao, J. (2010a). Semiconductor-mediated photodegradation of pollutants under visible-light irradiation. *Chem. Soc. Rev.* 39, 4206–4219. doi: 10.1039/b921692h

Chen, W., Fan, Z., Zhang, B., Ma, G., Takanabe, K., Zhang, X., et al. (2011). Enhanced visible-light activity of Titania via confinement inside carbon nanotubes. *J. Am. Chem. Soc.* 133, 14896–14899. doi: 10.1021/ja205997x

Chen, X. B., Shen, S. H., Guo, L. J., and Mao, S. S. (2010b). Semiconductor-based photocatalytic hydrogen generation. *Chem. Rev.* 110, 6503–6570. doi: 10.1021/cr1001645

Chen, Y., Sun, H., and Peng, W. (2017). 2D Transition Metal dichalcogenides and graphene-based ternary composites for photocatalytic hydrogen evolution and pollutants degradation. *Nanomaterials* 7:e62. doi: 10.3390/nano7030062

Cherevan, A. S., Gebhardt, P., Shearer, C. J., Matsukawa, M., Domen, K., and Eder, D. (2014). Interface engineering in nanocarbon-Ta_2O_5 hybrid photocatalysts. *Energy Environ. Sci.* 7, 791–796. doi: 10.1039/C3EE42558D

Chowdhury, S., and Balasubramanian, R. (2014). Graphene/semiconductor nanocomposites (GSNs) for heterogeneous photocatalytic decolorization of wastewaters contaminated with synthetic dyes: a review. *Appl. Catal. B Environ.* 160, 307–324. doi: 10.1016/j.apcatb.2014.05.035

Colmenares, J. C., Varma, R. S., and Lisowski, P. (2016). Sustainable hybrid photocatalysts: titania immobilized on carbon materials derived from renewable and biodegradable resources. *Green Chem.* 18, 5736–5750. doi: 10.1039/C6GC02477G

Devi, L. G., and ArunaKumari, M. L. (2014). Synergistic effect between orthorhombic α -sulfur and TiO_2 as co-photocatalysts for efficient degradation of methylene blue: a mechanistic approach. *J. Mol. Catal. Chem.* 391, 99–104. doi: 10.1016/j.molcata.2014.04.012

Di, J., Li, S. X., Zhao, Z. F., Huang, Y. C., Jia, Y., and Zheng, H. J. (2015). Biomimetic CNT@TiO_2 composite with enhanced photocatalytic properties. *Chem. Eng. J.* 281, 60–68. doi: 10.1016/j.cej.2015.06.067

Fan, X., Zhang, G., and Zhang, F. (2015). Multiple roles of graphene in heterogeneous catalysis. *Chem. Soc. Rev.* 44, 3023–3035. doi: 10.1039/C5CS00094G

Fan, Y., Ma, W., Han, D., Gan, S., Dong, X., and Niu, L. (2015). Convenient recycling of 3D AgX/Graphene aerogels (X = Br, Cl) for efficient photocatalytic degradation of water pollutants. *Adv. Mater.* 27, 3767–3773. doi: 10.1002/adma.201500391

Fujishima, A., and Honda, K. (1972). Electrochemical photolysis of water at a semiconductor electrode. *Nature* 238, 37–38. doi: 10.1038/238037a0

Gao, P., Liu, J., Sun, D. D., and Ng, W. (2013). Graphene oxide-CdS composite with high photocatalytic degradation and disinfection activities under visible light irradiation. *J. Hazard. Mater.* 250–251, 412–420. doi: 10.1016/j.jhazmat.2013.02.003

Guldi, D. M., Rahman, A., Sgobba, V., and Ehli, C. (2006). Multifunctional molecular carbon materials-from fullerenes to carbon nanotubes. *Chem. Soc. Rev.* 35, 471–487. doi: 10.1039/b511541h

Guo, F., Shi, W., Guan, W., Huang, H., and Liu, Y. (2017). Carbon dots/g-C_3N_4/ZnO nanocomposite as efficient visible-light driven photocatalyst for tetracycline total degradation. *Sep. Purification Technol.* 173, 295–303. doi: 10.1016/j.seppur.2016.09.040

Han, C., Chen, Z., Zhang, N., Colmenares, J. C., and Xu, Y. J. (2015). Hierarchically CdS decorated 1D ZnO nanorods-2D graphene hybrids: low temperature synthesis and enhanced photocatalytic performance. *Adv. Funct. Mater.* 25, 221–229. doi: 10.1002/adfm.201402443

Han, C., Zhang, N., and Xu, Y. J. (2016). Structural diversity of graphene materials and their multifarious roles in heterogeneous photocatalysis. *Nano Today* 11, 351–372. doi: 10.1016/j.nantod.2016.05.008

Han, S., Hu, L., Liang, Z., Wageh, S., Al-Ghamdi, A. A., Chen, Y., et al. (2014). One-step hydrothermal synthesis of 2D hexagonal nanoplates of alpha-Fe_2O_3/graphene composites with enhanced photocatalytic activity. *Adv. Funct. Mater.* 24, 5719–5727. doi: 10.1002/adfm.201401279

He, J., Sun, H., Indrawirawan, S., Duan, X., Tade, M. O., and Wang, S. (2015). Novel polyoxometalate@g-C(3)N(4) hybrid photocatalysts for degradation of dyes and phenolics. *J. Colloid Interface Sci.* 456, 15–21. doi: 10.1016/j.jcis.2015.06.003

Hisatomi, T., Kubota, J., and Domen, K. (2014). Recent advances in semiconductors for photocatalytic and photoelectrochemical water splitting. *Chem. Soc. Rev.* 43, 7520–7535. doi: 10.1039/C3CS60378D

Hong, Y., Shi, P., Wang, P., and Yao, W. (2015). Improved photocatalytic activity of CdS/reduced graphene oxide (RGO) for H_2 evolution by strengthening the connection between CdS and RGO sheets. *Int. J. Hydrogen Energy* 40, 7045–7051. doi: 10.1016/j.ijhydene.2015.04.005

Jia, L., Wang, D.-H., Huang, Y.-X., Xu, A.-W., and Yu, H.-Q. (2011). Highly durable N-Doped Graphene/CdS nanocomposites with enhanced

photocatalytic hydrogen evolution from water under visible light irradiation. *J. Phys. Chem. C* 115, 11466–11473. doi: 10.1021/jp2023617

Jiang, Z., Wan, W., Wei, W., Chen, K., Li, H., Wong, P. K., et al. (2017). Gentle way to build reduced titanium dioxide nanodots integrated with graphite-like carbon spheres: from DFT calculation to experimental measurement. *Appl. Catal. B* 204, 283–295. doi: 10.1016/j.apcatb.2016.11.044

Jing, Y. Q., Gui, C. X., Qu, J., Hao, S. M., Wang, Q. Q., and Yu, Z. Z. (2017). Silver silicate@carbon nanotube nanocomposites for enhanced visible light photodegradation performance. *Acs Sust. Chem. Eng.* 5, 3641–3649. doi: 10.1021/acssuschemeng.6b02650

Kim, H. I., Kim, S., Kang, J. K., and Choi, W. (2014). Graphene oxide embedded into TiO_2 nanofiber: effective hybrid photocatalyst for solar conversion. *J. Catal.* 309, 49–57. doi: 10.1016/j.jcat.2013.08.028

Lee, J. S., You, K. H., and Park, C. B. (2012). Highly photoactive, low bandgap TiO_2 nanoparticles wrapped by graphene. *Adv. Mater.* 24, 1084–1088. doi: 10.1002/adma.201104110

Lee, W. J., Lee, J. M., Kochuveedu, S. T., Han, T. H., Jeong, H. Y., Park, M., et al. (2012). Biomineralized N-doped CNT/TiO_2 core/shell nanowires for visible light photocatalysis. *ACS Nano* 6, 935–943. doi: 10.1021/nn204504h

Li, K., Peng, B., and Peng, T. (2016). Recent advances in heterogeneous photocatalytic CO_2 conversion to solar fuels. *ACS Catal.* 6, 7485–7527. doi: 10.1021/acscatal.6b02089

Li, Q., Guo, B., Yu, J., Ran, J., Zhang, B., Yan, H., et al. (2011). Highly efficient visible-light-driven photocatalytic hydrogen production of CdS-cluster-decorated graphene nanosheets. *J. Am. Chem. Soc.* 133, 10878–10884. doi: 10.1021/ja2025454

Li, Q., Li, X., Wageh, S., Al-Ghamdi, A. A., and Yu, J. (2015). CdS/Graphene nanocomposite photocatalysts. *Adv. Energy Mater.* 5:1500010. doi: 10.1002/aenm.201500010

Li, X., Yu, J., Wageh, S., Al-Ghamdi, A. A., and Xie, J. (2016). Graphene in photocatalysis: a review. *Small* 12, 6640–6696. doi: 10.1002/smll.201600382

Li, Z., Gao, B., Chen, G. Z., Mokaya, R., Sotiropoulos, S., and Puma, G. L. (2011). Carbon nanotube/titanium dioxide (CNT/TiO_2) core-shell nanocomposites with tailored shell thickness, CNT content and photocatalytic/photoelectrocatalytic properties. *Appl. Catal. B Environ.* 110, 50–57. doi: 10.1016/j.apcatb.2011.08.023

Liu, J., Song, Y., Xu, H., Zhu, X., Lian, J., Xu, Y., et al. (2017). Non-metal photocatalyst nitrogen-doped carbon nanotubes modified mpg-C(3)N(4):facile synthesis and the enhanced visible-light photocatalytic activity. *J. Colloid Interface Sci.* 494, 38–46. doi: 10.1016/j.jcis.2017.01.010

Liu, S. Q., Yang, M. Q., Zhang, N., and Xu, Y. J. (2014). Nanocomposites of graphene-CdS as photoactive and reusable catalysts for visible-light-induced selective reduction process. *J. Energy Chem.* 23, 145–155. doi: 10.1016/S2095-4956(14)60129-7

Liu, Y., Ding, S., Xu, J., Zhang, H., Yang, S., Duan, X., et al. (2017b). Preparation of a p-n heterojunction $BiFeO_3$ @TiO_2 photocatalyst with a core–shell structure for visible-light photocatalytic degradation. *Chin. J. Catal.* 38, 1052–1062. doi: 10.1016/S1872-2067(17)62845-6

Ma, Y., Lu, N., Lu, Y., Guan, J. N., Qu, J., Liu, H. Y., et al. (2016). Comparative study of carbon materials synthesized "greenly" for 2-CP removal. *Sci. Rep.* 6:29167. doi: 10.1038/srep29167

Martha, S., Padhi, D. K., and Parida, K. (2014). Reduced graphene oxide/InGaZn mixed oxide nanocomposite photocatalysts for hydrogen production. *ChemSusChem* 7, 585–597. doi: 10.1002/cssc.201300685

Matos, J., Laine, J., and Herrmann, J. M. (2001). Effect of the type of activated carbons on the photocatalytic degradation of aqueous organic pollutants by UV-irradiated titania. *J. Catal.* 200, 10–20. doi: 10.1006/jcat.2001.3191

Matsuoka, M., Kitano, M., Takeuchi, M., Tsujimaru, K., Anpo, M., and Thomas, J. M. (2007). Photocatalysis for new energy production. *Catal. Today* 122, 51–61. doi: 10.1016/j.cattod.2007.01.042

Ming, F. W., Hong, J. Q., Xu, X., and Wang, Z. C. (2016). Dandelion-like ZnS/carbon quantum dots hybrid materials with enhanced photocatalytic activity toward organic pollutants. *RSC Adv.* 6, 31551–31558. doi: 10.1039/C6RA02840C

Moniz, S. J. A., Shevlin, S. A., Martin, D. J., Guo, Z.-X., and Tang, J. (2015). Visible-light driven heterojunction photocatalysts for water splitting–a critical review. *Energy Environ. Sci.* 8, 731–759. doi: 10.1039/C4EE03271C

Morales-Torres, S., Pastrana-Martinez, L. M., Figueiredo, J. L., Faria, J. L., and Silva, A. M. T. (2012). Design of graphene-based TiO_2 photocatalysts-a review. *Environ. Sci. Pollut. Res.* 19, 3676–3687. doi: 10.1007/s11356-012-0939-4

Mukthar Ali, M., and Sandhya, K. Y. (2014). Visible light responsive titanium dioxide–cyclodextrin–fullerene composite with reduced charge recombination and enhanced photocatalytic activity. *Carbon N.Y.* 70, 249–257. doi: 10.1016/j.carbon.2014.01.003

Murcia-Lopez, S., Navio, J. A., and Hidalgo, M. C. (2013). Role of activated carbon on the increased photocatalytic activity of AC/Bi_2WO_6 coupled materials. *Appl. Catal. Gen.* 466, 51–59. doi: 10.1016/j.apcata.2013.06.022

Murgolo, S., Petronella, F., Ciannarella, R., Comparelli, R., Agostiano, A., Curri, M. L., et al. (2015). UV and solar-based photocatalytic degradation of organic pollutants by nano-sized TiO_2 grown on carbon nanotubes. *Catal. Today* 240, 114–124. doi: 10.1016/j.cattod.2014.04.021

Ng, Y. H., Ikeda, S., Matsumura, M., and Amal, R. (2012). A perspective on fabricating carbon-based nanomaterials by photocatalysis and their applications. *Energy Environ. Sci.* 5:9307. doi: 10.1039/c2ee22128d

Ouzzine, M., Romero-Anaya, A. J., Lillo-Ródenas, M. A., and Linares-Solano, A. (2014). Spherical activated carbon as an enhanced support for TiO_2/AC photocatalysts. *Carbon N. Y.* 67, 104–118. doi: 10.1016/j.carbon.2013.09.069

Paulo, S., Palomares, E., and Martinez-Ferrero, E. (2016). Graphene and carbon quantum dot-based materials in photovoltaic devices: from synthesis to applications. *Nanomaterials* 6:157. doi: 10.3390/nano6090157

Peng, K. Q., Wang, X., Li, L., Hu, Y., and Lee, S. T. (2013). Silicon nanowires for advanced energy conversion and storage. *Nano Today* 8, 75–97. doi: 10.1016/j.nantod.2012.12.009

Peng, W. C., Chen, Y., and Li, X. Y. (2016). MoS_2/reduced graphene oxide hybrid with CdS nanoparticles as a visible light-driven photocatalyst for the reduction of 4-nitrophenol. *J. Hazard. Mater.* 309, 173–179. doi: 10.1016/j.jhazmat.2016.02.021

Peng, W. C., Wang, X., and Li, X. Y. (2014). The synergetic effect of $MoS_{(2)}$ and graphene on $Ag_{(3)}PO_{(4)}$ for its ultra-enhanced photocatalytic activity in phenol degradation under visible light. *Nanoscale* 6, 8311–8317. doi: 10.1039/c4nr01654h

Peng, W., Li, Y., Zhang, F., Zhang, G., and Fan, X. (2017). Roles of two-dimensional transition metal dichalcogenides as cocatalysts in photocatalytic hydrogen evolution and environmental remediation. *Ind. Eng. Chem. Res.* 56, 4611–4626. doi: 10.1021/acs.iecr.7b00371

Putri, L. K., Ong, W.-J., Chang, W. S., and Chai, S.-P. (2015). Heteroatom doped graphene in photocatalysis: a review. *Appl. Surf. Sci.* 358, 2–14. doi: 10.1016/j.apsusc.2015.08.177

Qi, K., Selvaraj, R., Al Fahdi, T., Al-Kindy, S., Kim, Y., Wang, G. C., et al. (2016). Enhanced photocatalytic activity of anatase-TiO_2 nanoparticles by fullerene modification: a theoretical and experimental study. *Appl. Surf. Sci.* 387, 750–758. doi: 10.1016/j.apsusc.2016.06.134

Qiu, B., Xing, M., and Zhang, J. (2014). Mesoporous TiO_2 nanocrystals grown *in situ* on graphene aerogels for high photocatalysis and lithium-Ion batteries. *J. Am. Chem. Soc.* 136, 5852–5855. doi: 10.1021/ja500873u

Ran, J., Zhang, J., Yu, J., Jaroniec, M., and Qiao, S. Z. (2014). Earth-abundant cocatalysts for semiconductor-based photocatalytic water splitting. *Chem. Soc. Rev.* 43, 7787–7812. doi: 10.1039/C3CS60425J

Ren, X., Yang, H., Gen, S., Zhou, J., Yang, T., Zhang, X., et al. (2016). Controlled growth of $LaFeO_3$ nanoparticles on reduced graphene oxide for highly efficient photocatalysis. *Nanoscale* 8, 752–756. doi: 10.1039/C5NR06338H

Sampaio, M. J., Silva, C. G., Silva, A. M. T., Pastrana-Martinez, L. M., Han, C., Morales-Torres, S., et al. (2015). Carbon-based TiO_2 materials for the degradation of Microcystin-LA. *Appl. Catal. B-Environ.* 170, 74–82. doi: 10.1016/j.apcatb.2015.01.013

Shearer, C. J., Cherevan, A., and Eder, D. (2014). Application and future challenges of functional nanocarbon hybrids. *Adv. Mater. Weinheim.* 26, 2295–2318. doi: 10.1002/adma.201305254

Shi, W., Lv, H., Yuan, S., Huang, H., Liu, Y., and Kang, Z. (2017). Synergetic effect of carbon dots as co-catalyst for enhanced photocatalytic performance of methyl orange on $ZnIn_2S_4$ microspheres. *Sep. Purif. Technol.* 174, 282–289. doi: 10.1016/j.seppur.2016.11.013

Silva, C. G., Sampaio, M. J., Marques, R. R. N., Ferreira, L. A., Tavares, P. B., Silva, A. M. T., et al. (2015). Photocatalytic production of hydrogen from methanol

and saccharides using carbon nanotube-TiO_2 catalysts. *Appl. Catal. B Environ.* 178, 82–90. doi: 10.1016/j.apcatb.2014.10.032

Strobel, R., Garche, J., Moseley, P. T., Jorissen, L., and Wolf, G. (2006). Hydrogen storage by carbon materials. *J. Power Sources* 159, 781–801. doi: 10.1016/j.jpowsour.2006.03.047

Tan, L. L., Chai, S. P., and Mohamed, A. R. (2012). Synthesis and applications of graphene-based TiO_2 photocatalysts. *ChemSusChem* 5, 1868–1882. doi: 10.1002/cssc.201200480

Thangavel, S., Krishnamoorthy, K., Kim, S. J., and Venugopal, G. (2016). Designing ZnS decorated reduced graphene-oxide nanohybrid via microwave route and their application in photocatalysis. *J. Alloys Compd.* 683, 456–462. doi: 10.1016/j.jallcom.2016.05.089

Tian, F., Wu, Z., Yan, Y., Ye, B. C., and Liu, D. (2016). Synthesis of visible-light-responsive Cu and N-Codoped AC/TiO_2 photocatalyst through microwave irradiation. *Nanoscale Res. Lett.* 11:292. doi: 10.1186/s11671-016-1503-9

Tian, J., Leng, Y., Zhao, Z., Xia, Y., Sang, Y., Hao, P., et al. (2015). Carbon quantum dots/hydrogenated TiO_2 nanobelt heterostructures and their broad spectrum photocatalytic properties under UV, visible, and near-infrared irradiation. *Nano Energy* 11, 419–427. doi: 10.1016/j.nanoen.2014.10.025

Wang, C., Cao, M., Wang, P., and Ao, Y. (2013). Preparation, characterization of CdS-deposited graphene–carbon nanotubes hybrid photocatalysts with enhanced photocatalytic activity. *Mater. Lett.* 108, 336–339. doi: 10.1016/j.matlet.2013.06.102

Wang, H., Zhang, L., Chen, Z., Hu, J., Li, S., Wang, Z., et al. (2014). Semiconductor heterojunction photocatalysts: design, construction, and photocatalytic performances. *Chem. Soc. Rev.* 43, 5234–5244. doi: 10.1039/C4CS00126E

Wang, J., Wang, Z., and Zhu, Z. (2017). Synergetic effect of $Ni(OH)_2$ cocatalyst and CNT for high hydrogen generation on CdS quantum dot sensitized TiO_2 photocatalyst. *Appl. Catal. B* 204, 577–583. doi: 10.1016/j.apcatb.2016.12.008

Wang, X., Maeda, K., Thomas, A., Takanabe, K., Xin, G., Carlsson, J. M., et al. (2009). A metal-free polymeric photocatalyst for hydrogen production from water under visible light. *Nat. Mater.* 8, 76–80. doi: 10.1038/nmat2317

Weng, B., Liu, S. Q., Zhang, N., Tang, Z. R., and Xu, Y. J. (2014). A simple yet efficient visible-light-driven CdS nanowires-carbon nanotube 1D−1D nanocomposite photocatalyst. *J. Catal.* 309, 146–155. doi: 10.1016/j.jcat.2013.09.013

Woan, K., Pyrgiotakis, G., and Sigmund, W. (2009). Photocatalytic carbon-nanotube-TiO_2 composites. *Adv. Mater.* 21, 2233–2239. doi: 10.1002/adma.200802738

Wu, X., Zhao, J., Wang, L., Han, M., Zhang, M., Wang, H., et al. (2017). Carbon dots as solid-state electron mediator for $BiVO_4$/CDs/CdS Z-scheme photocatalyst working under visible light. *Appl. Catal. B* 206, 501–509. doi: 10.1016/j.apcatb.2017.01.049

Xiang, Q. J., Yu, J. G., and Jaroniec, M. (2012). Graphene-based semiconductor photocatalysts. *Chem. Soc. Rev.* 41, 782–796. doi: 10.1039/C1CS15172J

Xie, G., Zhang, K., Guo, B., Liu, Q., Fang, L., and Gong, J. R. (2013). Graphene-based materials for hydrogen generation from light-driven water splitting. *Adv. Mater. Weinheim.* 25, 3820–3839. doi: 10.1002/adma.201301207

Xie, X. Q., Kretschmer, K., and Wang, G. X. (2015). Advances in graphene-based semiconductor photocatalysts for solar energy conversion: fundamentals and materials engineering. *Nanoscale* 7, 13278–13292. doi: 10.1039/C5NR 03338A

Xu, H., Wang, C., Song, Y. H., Zhu, J. X., Xu, Y. G., Yan, J., et al. (2014). CNT/Ag_3PO_4 composites with highly enhanced visible light photocatalytic activity and stability. *Chem. Eng. J.* 241, 35–42. doi: 10.1016/j.cej.2013. 11.065

Xu, J., Wang, L., and Cao, X. (2016). Polymer supported graphene–CdS composite catalyst with enhanced photocatalytic hydrogen production from water splitting under visible light. *Chem. Eng. J.* 283, 816–825. doi: 10.1016/j.cej.2015.08.018

Yang, J. H., Wang, D. E., Han, H. X., and Li, C. (2013). Roles of cocatalysts in photocatalysis and photoelectrocatalysis. *Accouts Chem. Res.* 46, 1900–1909. doi: 10.1021/ar300227e

Yang, M. Q., Zhang, N., and Xu, Y. J. (2013). Synthesis of fullerene-, carbon nanotube-, and graphene-TiO(2) nanocomposite photocatalysts for selective oxidation: a comparative study. *ACS Appl. Mater. Interfaces* 5, 1156–1164. doi: 10.1021/am3029798

Ye, A., Fan, W., Zhang, Q., Deng, W., and Wang, Y. (2012). CdS–graphene and CdS–CNT nanocomposites as visible-light photocatalysts for hydrogen evolution and organic dye degradation. *Catal. Sci. Technol.* 2:969. doi: 10.1039/c2cy20027a

Yu, H., Shi, R., Zhao, Y., Waterhouse, G. I. N., Wu, L. Z., Tung, C. H., et al. (2016). Smart utilization of carbon dots in semiconductor photocatalysis. *Adv. Mater.* 28, 9454–9477. doi: 10.1002/adma.201602581

Yu, H., Zhao, Y., Zhou, C., Shang, L., Peng, Y., Cao, Y., et al. (2014). Carbon quantum dots/TiO_2 composites for efficient photocatalytic hydrogen evolution. *J. Mater. Chem. A* 2:3344. doi: 10.1039/c3ta14108j

Yu, J., Jin, J., Cheng, B., and Jaroniec, M. (2014). A noble metal-free reduced graphene oxide–CdS nanorod composite for the enhanced visible-light photocatalytic reduction of CO_2 to solar fuel. *J. Mater. Chem. A* 2:3407. doi: 10.1039/c3ta14493c

Yu, J., Yang, B., and Cheng, B. (2012). Noble-metal-free carbon nanotube-$Cd_{0.1}Zn_{0.9}S$ composites for high visible-light photocatalytic H_2-production performance. *Nanoscale* 4, 2670–2677. doi: 10.1039/c2nr30129f

Yue, Z. K., Liu, A. J., Zhang, C. Y., Huang, J., Zhu, M. S., Du, Y. K., et al. (2017). Noble-metal-free hetero-structural CdS/Nb_2O_5/N-doped-graphene ternary photocatalytic system as visible-light-driven photocatalyst for hydrogen evolution. *Appl. Catal. B-Environ.* 201, 202–210. doi: 10.1016/j.apcatb.2016.08.028

Zarezade, M., Ghasemi, S., and Gholami, M. R. (2011). The effect of multiwalled carbon nanotubes and activated carbon on the morphology and photocatalytic activity of TiO_2/C hybrid materials. *Catal. Sci. Technol.* 1, 279–284. doi: 10.1039/c0cy00042f

Zeng, X., Wang, Z., Meng, N., McCarthy, D. T., Deletic, A., and Pan, J. H., et al. (2017). Highly dispersed TiO_2 nanocrystals and carbon dots on reduced graphene oxide: Ternary nanocomposites for accelerated photocatalytic water disinfection. *Appl. Catal. B* 202, 33–41. doi: 10.1016/j.apcatb.2016. 09.014

Zhang, D., Hu, B., Guan, D., and Luo, Z. (2016a). Essential roles of defects in pure graphene/Cu_2O photocatalyst. *Catal. Commun.* 76, 7–12. doi: 10.1016/j.catcom.2015.12.013

Zhang, K., and Guo, L. (2013). Metal sulphide semiconductors for photocatalytic hydrogen production. *Catal. Sci. Technol.* 3:1672. doi: 10.1039/c3cy00018d

Zhang, L., Fu, X., Meng, S., Jiang, X., Wang, J., and Chen, S. (2015a). Ultra-low content of Pt modified CdS nanorods: one-pot synthesis and high photocatalytic activity for H_2 production under visible light. *J. Mater. Chem. A* 3, 23732–23742. doi: 10.1039/C5TA07459B

Zhang, N., Yang, M. Q., Tang, Z. R., and Xu, Y. J. (2013a). CdS–graphene nanocomposites as visible light photocatalyst for redox reactions in water: a green route for selective transformation and environmental remediation. *J. Catal.* 303, 60–69. doi: 10.1016/j.jcat.2013.02.026

Zhang, N., Zhang, Y. H., and Xu, Y. J. (2012). Recent progress on graphene-based photocatalysts: current status and future perspectives. *Nanoscale* 4, 5792–5813. doi: 10.1039/c2nr31480k

Zhang, N., Zhang, Y., Yang, M. Q., Tang, Z. R., and Xu, Y. J. (2013b). A critical and benchmark comparison on graphene-, carbon nanotube-, and fullerene-semiconductor nanocomposites as visible light photocatalysts for selective oxidation. *J. Catal.* 299, 210–221. doi: 10.1016/j.jcat.2012.11.021

Zhang, P., Wang, T., and Gong, J. (2015b). Mechanistic understanding of the plasmonic enhancement for solar water splitting. *Adv. Mater. Weinheim.* 27, 5328–5342. doi: 10.1002/adma.201500888

Zhang, X. H., Peng, T. Y., and Song, S. S. (2016b). Recent advances in dye-sensitized semiconductor systems for photocatalytic hydrogen production. *J. Mater. Chem. A* 4, 2365–2402. doi: 10.1039/C5TA08939E

Zhang, Y., Tang, Z.-R., Fu, X., and Xu, Y.-J. (2011). Engineering the Unique 2D Mat of Graphene to Achieve Graphene-TiO_2 Nanocomposite for Photocatalytic selective transformation: what advantage does graphene have over its forebear carbon nanotube? *ACS Nano* 5, 7426–7435. doi: 10.1021/nn202519j

Zhang, Y. H., Tang, Z. R., Fu, X. Z., and Xu, Y. J. (2010). TiO_2-graphene nanocomposites for gas-phase photocatalytic degradation of volatile aromatic pollutant: is TiO_2-graphene truly different from other TiO_2-carbon composite materials? *ACS Nano* 4, 7303–7314. doi: 10.1021/nn1024219

Zhong, Y., Zhao, G., Ma, F., Wu, Y., and Hao, X. (2016). Utilizing photocorrosion-recrystallization to prepare a highly stable and efficient CdS/WS_2 nanocomposite photocatalyst for hydrogen evolution. *Appl. Catal. B* 199, 466–472. doi: 10.1016/j.apcatb.2016.06.065

Zhou, X. F., Li, X., Gao, Q. Z., Yuan, J. L., Wen, J. Q., Fang, Y. P., et al. (2015). Metal-free carbon nanotube-SiC nanowire heterostructures with enhanced photocatalytic H_2 evolution under visible light irradiation. *Catal. Sci. Technol.* 5, 2798–2806. doi: 10.1039/C4CY01757A

Zou, X., and Zhang, Y. (2015). Noble metal-free hydrogen evolution catalysts for water splitting. *Chem. Soc. Rev.* 44, 5148–5180. doi: 10.1039/C4CS00448E

Conflict of Interest Statement: The authors declare that the research was conducted in the absence of any commercial or financial relationships that could be construed as a potential conflict of interest.

frontiers in Chemistry

ORIGINAL RESEARCH
published: 12 March 2018
doi: 10.3389/fchem.2018.00058

Facile Fabrication of BiOI/BiOCl Immobilized Films With Improved Visible Light Photocatalytic Performance

Yingxian Zhong[1†], Yuehua Liu[1†], Shuang Wu[1], Yi Zhu[1], Hongbin Chen[1], Xiang Yu[2] and Yuanming Zhang[1*]*

[1] Department of Chemistry, Jinan University, Guangzhou, China, [2] Analytical and Testing Center, Jinan University, Guangzhou, China

HIGHLIGHTS

- A facial method was used to fabricate BiOI/BiOCl film at room temperature.
- 30% BiOI/BiOCl showed an excellent photocatalytic activity and stability.
- Improvement of photocatalytic activity was owed to expanded visible light absorption and high separation efficiency of charge.

Photocatalysis has been considered to be one of the most promising ways to photodegrade organic pollutants. Herein, a series of BiOI/BiOCl films coating on FTO were fabricated through a simple method at room temperature. The photocatalytic efficiency of 30%BiOI/BiOCl could reach more than 99% aiming to degrading RhB and MB after 90 and 120 min, respectively. Compared with BiOCl, 30%BiOI/BiOCl showed 12 times higher efficiency when degrading RhB. In comparison with BiOI, 30%BiOI/BiOCl showed 5 and 6 times higher efficiency when degrading RhB and MB, respectively. These obvious enhancements were attributed to expanded visible light absorption and high separation performance of photoinduced charge. Moreover, the photocatalytic activity of 30%BiOI/BiOCl had no obvious decrease after five recycles, suggesting that it was a promising photocatalyst for the removal of MB and RhB pollutants. Finally, the possible growth process for the BiOI/BiOCl thin films and photocatalysis mechanism were investigated in details. This work would provide insight to the reasonable construction of BiOX heterojunction and the photocatalytic mechanism in degrading organic pollutants.

Keywords: BiOI/BiOCl film, visible light, heterojunction, photodegradation, recycle

OPEN ACCESS

Edited by:
Zhimin Ao,
Guangdong University of Technology, China

Reviewed by:
Fa-tang Li,
Hebei University of Science and Technology, China
Kaixuan Bu,
Rutgers University, The State University of New Jersey, United States

***Correspondence:**
Yi Zhu
tzhury@jnu.edu.cn
Yuanming Zhang
tzhangym@jnu.edu.cn

[†]These authors have contributed equally to this work.

Specialty section:
This article was submitted to Green and Sustainable Chemistry, a section of the journal Frontiers in Chemistry

Received: *13 December 2017*
Accepted: *23 February 2018*
Published: *12 March 2018*

Citation:
Zhong Y, Liu Y, Wu S, Zhu Y, Chen H, Yu X and Zhang Y (2018) Facile Fabrication of BiOI/BiOCl Immobilized Films With Improved Visible Light Photocatalytic Performance. Front. Chem. 6:58. doi: 10.3389/fchem.2018.00058

INTRODUCTION

Recently, semiconductor photocatalysts have been potential materials in energy storage, organic pollutants degradation and so on Kisch (2013). Since TiO_2 had been reported to produce H_2 under UV light (Fujishima and Honda, 1972), transitional mental oxides have been applied as photocatalysts, such as ZnO (Soci et al., 2007), SnO_2 (Law et al., 2002), and WO_3 (Baeck et al., 2003). However, many of them have wide bandgap and are activated by UV-light (4% of solar light). To utilize more solar light, searchers pay a lot of efforts to find new photocatalysts which could maximize the utilization of solar light. Among those photocatalysts, BiOCl is considered as a new kind of promising layered material for photocatalysis due to its unique layered

structure, high chemical and optical stability, corrosion resistance and nontoxicity (Li J. et al., 2014; Ding et al., 2015; Li et al., 2017). BiOCl has layered structure consisting of $[Bi_2O_2]^{2+}$ sandwiched between two slabs of Cl^-, which produces internal static electric fields to separate photogenerated electrons and holes (Cheng et al., 2014; Mi et al., 2016). However, the practical application of BiOCl has been hindered owing to its wide bandgap and relatively high recombination rate of photoinduced carriers (Dong et al., 2012; Xiao et al., 2012).

Aiming at solving these shortcomings, many strategies have been reported to enhance the photocatalytic efficiency of BiOCl, including: (i) impurity element doping, such as $BiOCl_xBr_yI_z$ (Sun X. et al., 2015) and $BiOCl_xI_{1-x}$ (Kim et al., 2014), (ii) surface functionalization, like inducing oxygen vacancies in BiOCl (Jiang et al., 2013), (iii) construction of the plasmonic photocatalysis system, such as Ag/BiOCl (Liu H. et al., 2012) and Ag-AgX-BiOX (X = Cl, Br, I) (Cheng et al., 2011; Xiong et al., 2011; Cao et al., 2013), (iv) construction of semiconductor heterojunctions (Jiang et al., 2011; Wang et al., 2015). Construction of semiconductor heterojunctions has been widely explored in recent years because of two advantages. First, materials with wide bandgap could match with lots of semiconductors at the energy level. In that way, it is propitious to electron and hole separation by building an interfacial electric field between different semiconductors. Cui's work showed that photodegradation efficiency of Ag_3PO_4/BiOI was nearly 10 times that of BiOI (Cui et al., 2013). And Cui's group found that photodegradation efficiency of BiOI/Bi_2WO_6 was about 6.1 times higher than that of pure Bi_2WO_6 under visible light irradiation (Li et al., 2013). Ao's work showed that Ag_2MoO_4/g-C_3N_4 highly improved photocatalytic degradation performance for different organic pollutants under sunlight irradiation (Wu et al., in press). Secondly, coupled with narrow band semiconductors, BiOCl could expand visible light absorption and utilize more solar energy. Narrow bandgap materials act as the light absorber and generate photoinduced carriers with proper energy, indicating that it is a very efficient visible-light-activated photocatalyst (Wang et al., 2017). Therefore, many BiOCl/narrow bandgap materials, such as BiOCl-C_3N_4 (Wang et al., 2013), BiOCl/$Bi_{24}O_{31}Cl_{10}$ (Li F. et al., 2014), BiOCl/Bi_2S_3 (Cheng et al., 2012), BiOCl/BiOI (Sun L. et al., 2015), BiOCl/BiOBr (Zhang et al., 2013), and $NaBiO_3$/BiOCl (Chang et al., 2010), have been successfully prepared.

Based on the advantages mentioned above, BiOI is a great candidate to couple with BiOCl, which is a narrow bandgap semiconductor (1.72 eV) and has a similar layered structure (Jiang et al., 2011; Huang et al., 2015; Ning et al., 2016). Once coupled with BiOI, BiOI/BiOCl is expected to achieve the aims as followed: (i) to enhance visible light absorption, (ii) to accelerate separation efficiency of photoinduced electrons and holes (Cao et al., 2011; Xiao et al., 2012; Wang et al., 2016). Although there are a few reports about BiOI/BiOCl, most of them are powder synthesized through hydrothermal and solvothermal methods, which needs high temperature and pressure. Additionally, powder catalysts are hard to be separated and recovered because they are easily dispersed into solution when used in pollutants degradation (Zhao et al., 2015). Unlike powder catalysts, immobilized photocatalysts become more promising in practical application for easy separation and high reusability (Liu X. et al., 2012). Therefore, BiOI/BiOCl film is of great advantage in practical organic pollutants degradation.

In this work, a facial method was used to fabricate a series of BiOI/BiOCl immobilized films at room temperature. The possible growth process of BiOI/BiOCl film was investigated in detail. All BiOI/BiOCl films showed better photocatalytic performance than pristine BiOCl film. UV-vis diffusion reflectance spectra, photocurrent, fluorescence spectra (PL) and trapping experiment were used to gain insights into the reasons for remarkable enhancement of photocatalytic activity and the possible photocatalysis mechanism of BiOI/BiOCl film. Besides, recycle experiments were used to measure the stability and duration of BiOI/BiOCl film.

EXPERIMENTAL

Synthesis of *x*BiOI/BiOCl Film

In a typical procedure, 3.0 g $BiCl_3$ was mixed with 100 mL ethanol and 1 mL HCl, and stirred for 1 h to form $BiCl_3$ solution. Similarly, BiI_3 solution was prepared using BiI_3, HI and ethanol in the same way. After that, $BiCl_3$ solution and BiI_3 solution were mixed with different molar ratio.1 mL of mixture solution was dropped onto FTO glass. After being dried at 100°C for 1 h, the films were dipped into distilled water for 30 min to form BiOI/BiOCl (as shown in **Scheme 1**). Finally, the samples dried at 60°C for 2 h. The *x*BiOI/BiOCl composites with molar ratios of

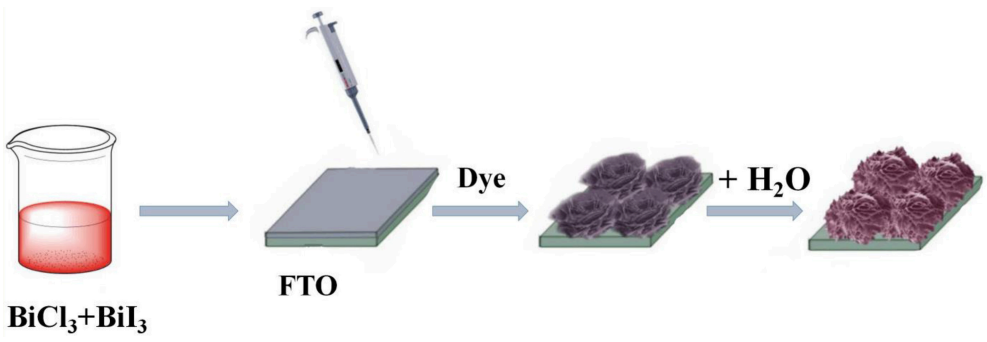

SCHEME 1 | Illustration of the preparation of BiOI/BiOCl composites on FTO.

BiOI to BiOCl at 10, 30, and 60% were named as 10%BiOI/BiOCl, 30%BiOI/BiOCl, 60%BiOI/BiOCl, respectively.

Characterization of Photocatalysts

The morphologies and phase structures of *x*BiOI/BiOCl films were observed by Field emission scanning electron microscopy (FE-SEM, Zeiss ULTRA 55), transmission electron microscopy (JEOL 2010F) and high-resolution transmission electron microscopy (JEOL 2100 F) and X-ray diffractometry (XRD, equipped with a Cu Ka X-ray source). The optical properties of as-synthesized catalysts were tested by UV–vis spectrophotometer (DRS, Hitachi- UV-3010, using $BaSO_4$ for the baseline measurement) and photoluminescence spectroscopy (PL, RF-5301PC). FT-IR spectra were recorded on an Aipha-Centuart FT-IR spectrometer.

The visible-light-driven photocatalytic efficiencies of *x*BiOI/BiOCl films were evaluated the degradation of Rhodamine B (RhB, 2.5 mg L^{-1}) and methylene blue (MB, 2.5 mg L^{-1}) in a reactor equipped with a 350 W Xe lamp with >420 nm filter as the light source. The as-obtained BiOI/BiOCl film was putting into a reactor, in which 100 mL dye solution were poured. Before irradiation, the solution was continuously stirring in the dark for 30 min to ensure establish adsorption-desorption equilibrium. At certain time interval, 4 mL of the suspension were sampled; the concentration of dye solution was measured by recording the absorption band maximum in the absorption spectra. For comparison, the photocatalytic activities of BiOCl and BiOI were characterized under same condition. In addition, 30%BiOI/BiOCl photocatalyst was examined by 5-cycle to characterize its stability. Before entering next cycle, samples were washed by deionized water and alcohol three times. Dried at 100°C for 1 h and reuse in fresh dye solution.

Electrochemical Measurements

Photocurrent of samples was studied by there-electrode system in a quartz cell, which was using Pt plate as counter electrode, Ag/AgCl as reference electrode, and the as-prepared samples as working electrode on electrochmical workstation (CHI660C.Shang-hai.). 0.1 M Na_2SO_4 solution was used as the electrolyte. The surface area of the working electrode was 4 × 5 cm^2. A 350 W Xe lamp with an filter ($\lambda > 420$ nm) was used as the visible-light source.

RESULTS AND DISCUSSION

XRD Patterns

Figure 1 showed XRD patterns of the as-prepared *x*BiOI/BiOCl films. It could be seen that all the diffraction peaks of BiOI and BiOCl were in good agreement with the standard cards (JCPDS No. 73-2062) and (JCPDS No. 06-0249) without any impurity peaks, which indicated that they exhibited tetragonal structure and corresponded to the FT-IR results (**Figure S2**). The characteristic peaks of BiOI and BiOCl coexisted in the XRD patterns, demonstrating the formation of BiOI/BiOCl composite without the present of $BiOCl_xI_{1-x}$ solid solutions (Huang et al., 2015). With the increase of percentage of BiOI in the composites, the strength of diffraction peaks of BiOI gradually increased, on the contrary, the intensity of BiOCl simultaneously decreased. Additional, it could see that FTO peaks in **Figure 1**, it might be due to the uneven film on glass of the sample.

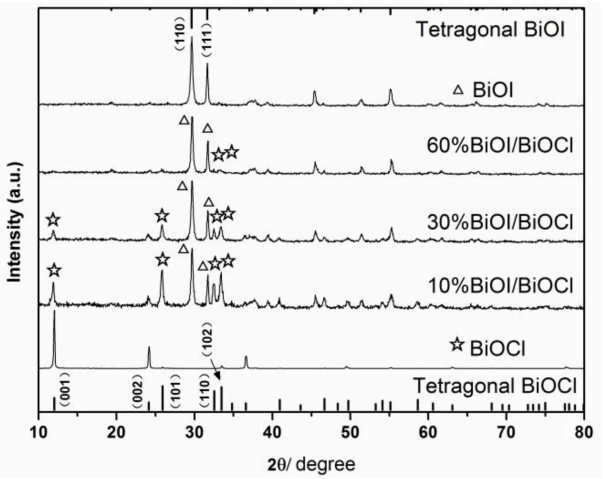

FIGURE 1 | XRD patterns of the as-prepared films.

SEM, TEM, HRTEM, and EDS Images

All the samples were systematically analyzed by SEM. From **Figure 2A**, it could be observed that pristine BiOCl was composed of numerous nanosheets and its surface was very smooth. Differently, under similar preparation conditions, pristine BiOI presented hierarchical microspheres consisting of a series nanosheet in **Figure 2B**. As for *x*BiOI/BiOCl (**Figures 2C–E**), it could be observed that *x*BiOI/BiOCl showed hierarchical structure with BiOCl nanosheets adhering tightly on BiOI and the particle sizes of *x*BiOI/BiOCl obviously increased in comparison with pristine BiOCl. Additionally, color of sample gradually deepened compared with pristine BiOCl when percentage of BiOI increased in **Figure 2F**.

The morphology and structure of as-obtained samples were further characterized by TEM and HRTEM images. The microstructures of pristine BiOCl, pristine BiOI and 30%BiOI/BiOCl were shown in **Figure 3**. The interactions between BiOCl and BiOI were so strong that ultrasonication did not separate them during the sample preparation procedure for TEM characterization (Xiao and Zhang, 2010). **Figures 3B,D,F** indicated that the samples were highly crystallized. In **Figure 3B**, the lattice fringe with a *d*-spacing of 0.735 nm matched well with (001) lattice plane of BiOCl, while in **Figure 3F**, the interlayer distance of 0.280 nm responsed to the (280) plane of BiOI. **Figure 3D** showed the HRTEM of 30%BiOI/BiOCl, clear fringes with the lattice spacing of 0.264 and 0.280 nm could be indexed to (102) lattice plane of BiOCl and (110) lattice plane of BiOI, respectively. TEM results were in good consistent with XRD patterns in **Figure 1**. The results clearly confirmed the formation of heterostructure between BiOCl and BiOI. In addition, the elemental distributions of 30%BiOI/BiOCl were studied through EDS elemental mapping. The corresponding

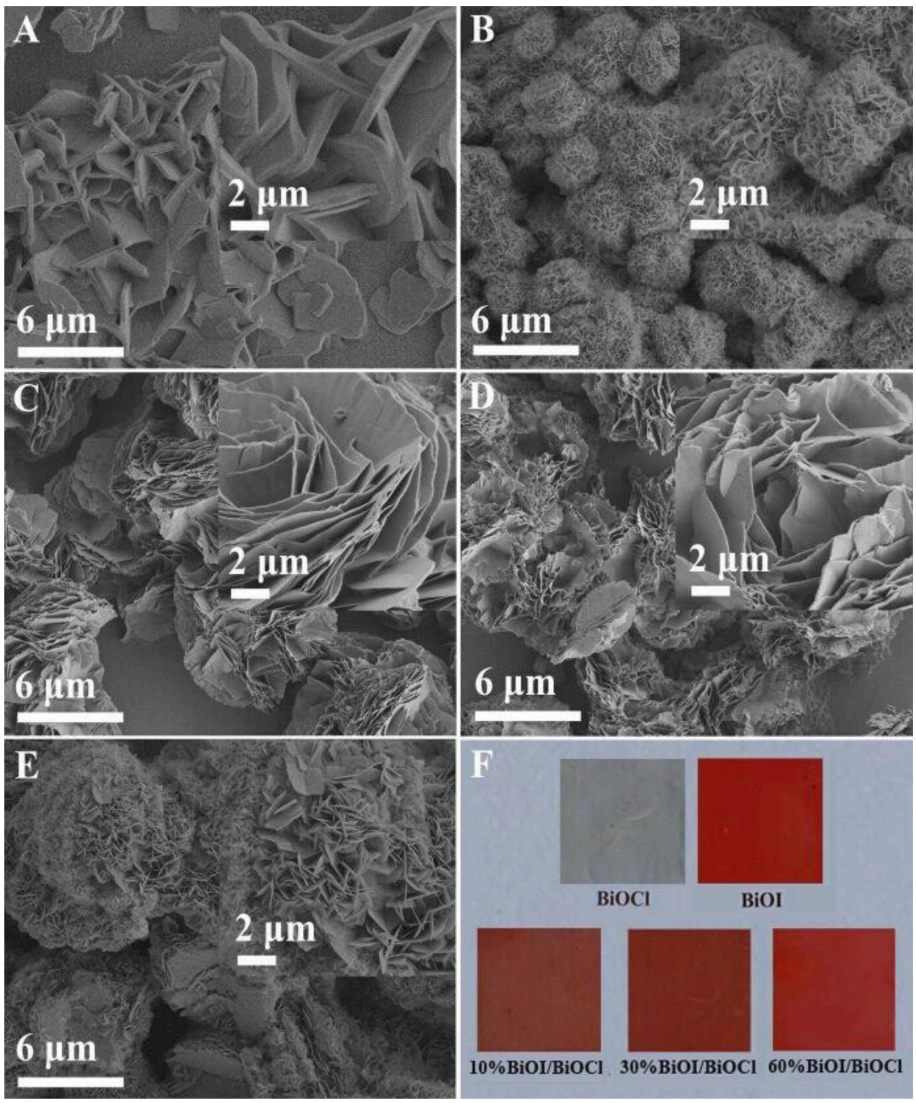

FIGURE 2 | SEM images of BiOCl, BiOI and BiOI/BiOCl film: **(A)** BiOCl;**(B)** BiOI; **(C)** 10%BiOI/BiOCl; **(D)** 30%BiOI/BiOCl; **(E)** 60%BiOI/BiOCl; **(F)** Picture of as-synthesized samples.

results for 30%BiOI/BiOCl were shown in **Figures 4A–E**. It could be obviously seen that the sample consist of only I, Bi, Cl, O, elements. The results of EDS mapping confirmed the composition, structure and the high purity of 30% BiOI/BiOCl composite.

Growth Process of *x*BiOI/BiOCl Film

In order to understand the growth process of BiOI/BiOCl film in this work, SEM images and XRD patterns of 30%BiOI/BiOCl film at different time stage were shown in **Figure 5**. The whole process was divided into three stages. In the first stage (0 min), as shown in **Figure 5I**, the peaks collected from 0 min sample could be indexed as a composition of BiOCl and BiI_3. After the mix solution consisting of BiI_3 and $BiCl_3$ was dropped on FTO, there was a hydrolyzation competition between them. $BiCl_3$ was hydrolyzed to form BiOCl prior to the hydrolyzation of BiI_3 when ethanol volatilized, because the K_{sp} (BiOCl) was smaller than K_{sp} (BiOI). As shown in **Figure 5B**, BiI_3 broke down on the nanosheets structure of BiOCl to form into hierarchical structure. Besides, the diffraction peak at around 11.9° corresponding to the (001) plane shifted to smaller 2θ in **Figure 5I**. That might be because the ionic radius of I^- (220 pm) was larger than that of Cl^- (181 pm). In the second stage (1–15 min), BiI_3 was hydrolyzed to BiOI. In **Figure 5I**, with the increase of reaction time, diffraction peak of BiI_3 disappeared and the intensity of BiOI became stronger. In the meantime, the extent of hydrolyzation caused the shifting of the diffraction peak of (001) to bigger 2θ. **Figures 5C–E** showed that hierarchical BiOI and nanosheets-structure BiOCl formed a tidily hierarchical structure in the second stage. In the third stage (30 min), BiI_3 was hydrolyzed totally, and BiOI/BiOCl was formed.

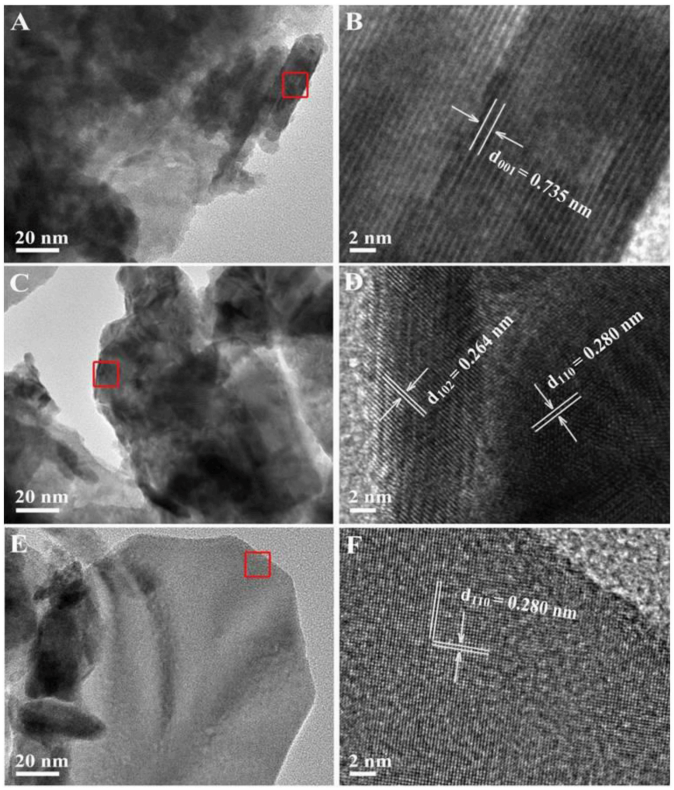

FIGURE 3 | (A) TEM and **(B)** HRTEM images of BiOCl, **(C)** TEM and **(D)** HRTEM of 30%BiOI/BiOCl, **(E)** TEM and **(F)** HRTEM of BiOI.

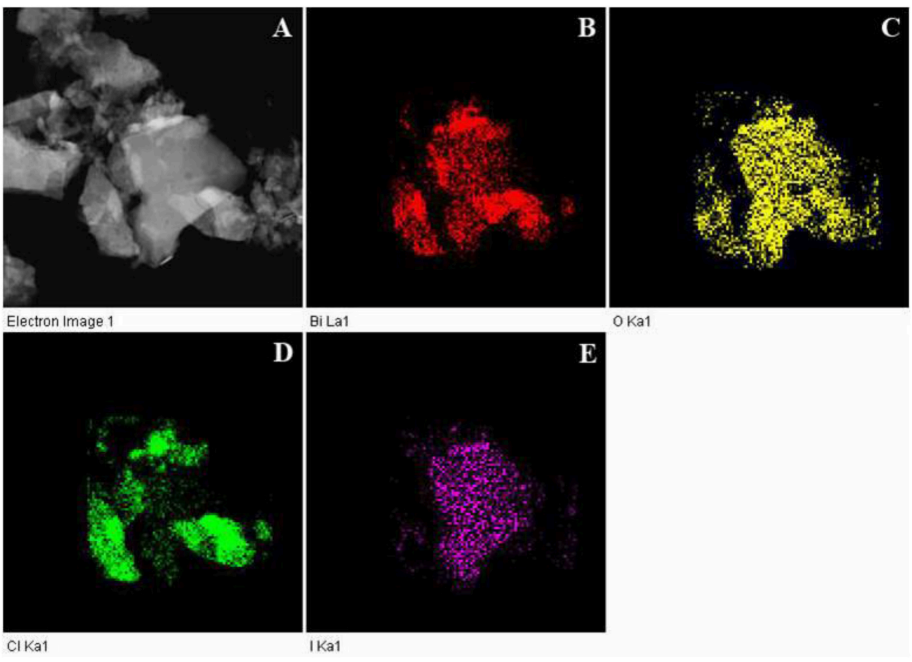

FIGURE 4 | EDS images of 30%BiOI/BiOCl **(A)** and Bi **(B)**, O **(C)**, Cl **(D)**, I **(E)** elemental maps.

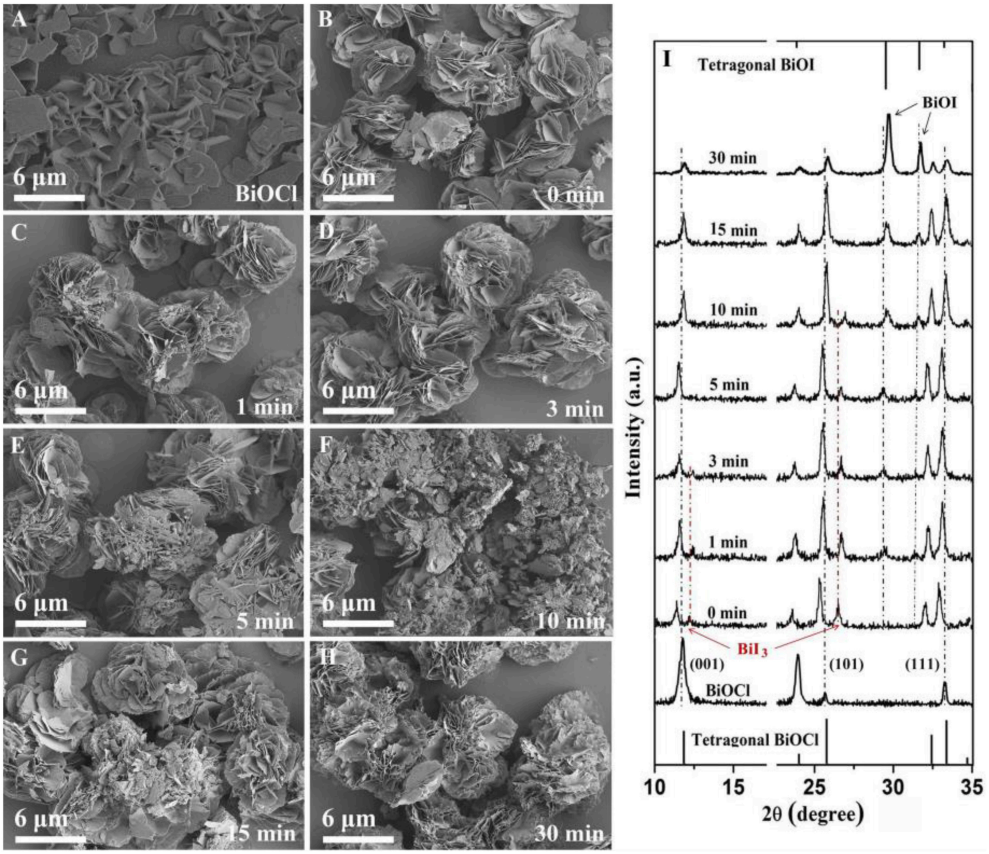

FIGURE 5 | SEM images of **(A)** BiOCl and 30%BiOI/BiOCl after different hydrolysis times **(B)** 0 min, **(C)** 1 min, **(D)** 3 min, **(E)** 5 min, **(F)** 10 min, **(G)** 15 min, **(H)** 30 min, **(I)** XRD patterns of 30%BiOI/BiOCl after different hydrolysis time.

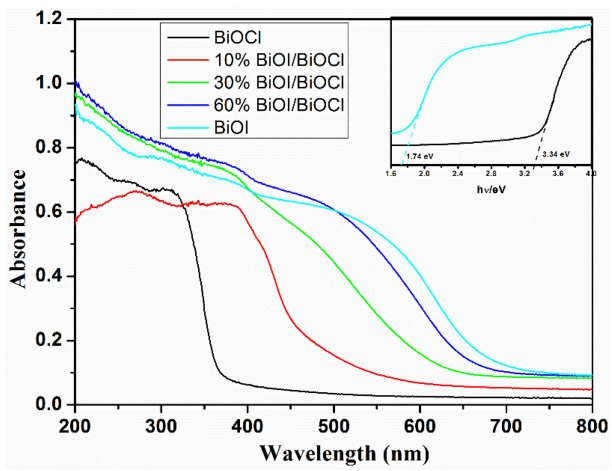

FIGURE 6 | UV-vis diffuse reflectance spectrum (DRS) of *x*BiOI/BiOCl films.

Optical Properties

The UV-vis diffuse reflectance spectra (DRS) of xBiOI/BiOCl films were shown in **Figure 6**. BiOCl had a strong absorption edge around 360 nm, meanwhile, BiOI had a strong absorption edge around 700 nm. Compared to BiOCl, *x*BiOI/BiOCl showed an absorption edge shifting to larger wavelength with the increase of BiOI percentage. This shifting was in accordance with the color change of as-prepared samples (**Figure 2F**) caused by the addition of BiOI. The band gap energy of a semiconductor could be calculated from the following equation:

$$\alpha h\nu = A(h\nu - Eg)^{n/2} \quad (1)$$

where α, ν, Eg, and A were the absorption coefficient, light frequency, band gap energy, and a constant, respectively (Ning et al., 2016). Among them, n depended on the characteristics of the transition in a semiconductor. For example, $n = 1$ (direct transition) or $n = 4$ (indirect transition). BiOX belonged to indirection transition, thus n was estimated to be 4. The band gap of BiOI and BiOCl were 1.74 and 3.34 eV, respectively. With narrowing of band gap, *x*BiOI/BiOCl could exhibit enhanced visible light absorption, subsequently resulting in improved photocatalytic activity.

Besides optical absorption property, separation efficiency of photogenerated carriers played an important role in photodegradation. Photocurrent could directly indicate the capability of charge separation. The higher photocurrent density

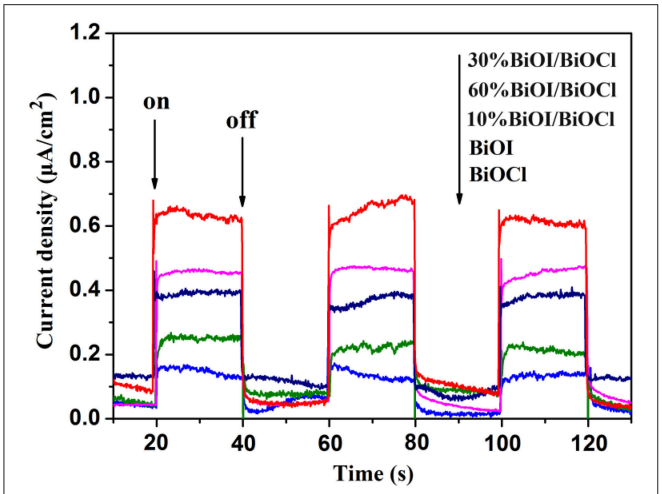

FIGURE 7 | Visible light photocurrent of *x*BiOI/BiOCl films.

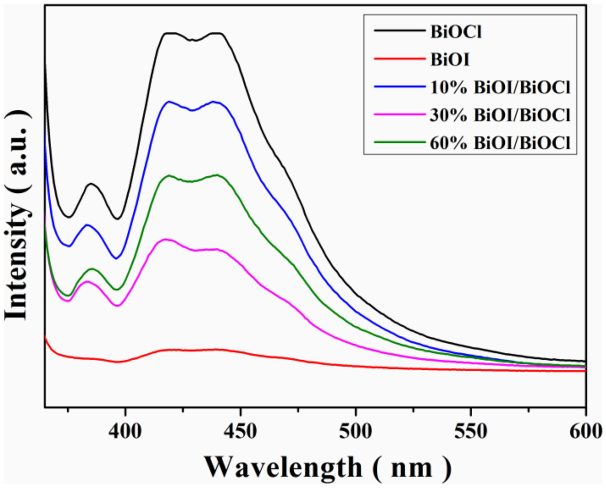

FIGURE 8 | Fluorescence spectra of *x*BiOI/BiOCl films.

corresponded to the greater capability of charge separation. **Figure 7** showed the photocurrent responses of the as-prepared photocatalysts under several on/off visible light irradiation cycles. BiOCl and BiOI showed a poor photocurrent response while the response of *x*BiOI/BiOCl increased. The photocurrent density of 30%BiOI/BiOCl was almost 6 times as high as that of pristine BiOCl and 3 times as high as that of pristine BiOI, revealing that 30%BiOI/BiOCl had superior separation efficiency of photogenerated carriers.

Photoluminescence spectra were used to characterize the photogenerated carriers' recombination rate of as-prepared samples, since the PL emission originated from free carrier's recombination. The higher PL intensity meaned the higher recombination rate in the photocatalytic procedure (Cao et al., 2011). As shown in **Figure 8**, BiOCl showed a strong emission peak with high intensity at approximate 420 and 440 nm, meanwhile, BiOI exhibited a low intensity. Decline of the PL intensity implied that adding BiOI could successful suppress recombination process during photocatalysis. In addition, 30%BiOI/BiOCl shown the lower intensity indicated the lower recombination rate, thus could promote photocatalytic activity.

Photocatalytic Properties

The photodegradation efficiency of the *x*BiOI/BiOCl films were evaluated by degradating RhB and MB under visible-light irradiation. As shown in **Figure 9A**, the degradation percentage of RhB by pristine BiOCl was 48% in 90 min. It was about 70% by pristine BiOI in 90 min. Compared with pristine BiOCl and BiOI, *x*BiOI/BiOCl film showed a great degradation: 30% BiOI/BiOCl could degrade more than 99% of RhB in 90 min. To further illustrate the photocatalytic reaction, pseudo-first-order kinetics were fitted from the degradation process (Ning et al., 2016),

$$\ln(C_0/C) = kt \quad (2)$$

where the value of rate constant k was equal to the corresponding slope of the fitting line as shown in **Figure 9C**. The rate constant value for 30%BiOI/BiOCl was 0.07315 min^{-1}, which was 12 times higher than BiOCl (0.00575 min^{-1}) and 5 times higher than BiOI (0.01303 min^{-1}), respectively. **Figure 9B** showed the photocatalytic performance of the *x*BiOI/BiOCl evaluated by degradating MB under visible-light irradiation. 48% of MB was self-degraded under visible light irradiation. Compared with self-degradation of MB, the photocatalytic performance of BiOCl was negligible and BiOI could only degrade 60% MB. The photocatalytic performance of *x*BiOI/BiOCl film was much better than pristine BiOCl and BiOI. More than 99% of MB was degraded using 30%BiOI/BiOCl film in 120 min. According to **Figure 9D**, the rate constant value of 30%BiOI/BiOCl was 0.05218 min^{-1}, which was 6 times higher than BiOI (0.00772 min^{-1}). This better photocatalytic performance might be due to the enhanced visible light absorption and improved separation efficiency of photoinduced carriers.

Reusability of 30%BiOI/BiOCl Film

Efforts were made in this work to identify the stability and practicality of as prepared catalysts for dye degradation, which was a significant factor to be considered in real application. 30%BiOI/BiOCl film was reused for RhB and MB degradation in five cycles under the same condition and the result was shown in **Figures 9E,F**. It was remarkable that the efficiencies had no obvious decrease after 5 cycles, revealing its great reusability. In term of XRD patterns in **Figure S1**, there was no obvious change in phase and structure of 30%BiOI/BiOCl film after 5 cycles, demonstrating its excellent stability. The excellent reusability and stability indicated its great potential in practical application.

Photocatalytic Mechanism

The energy band structures of BiOX were evaluated using the following equation (Xiao et al., 2016):

$$E_{VB} = X - E^e + 0.5E_g \quad (3)$$

$$E_{CB} = E_{VB} - E_g \quad (4)$$

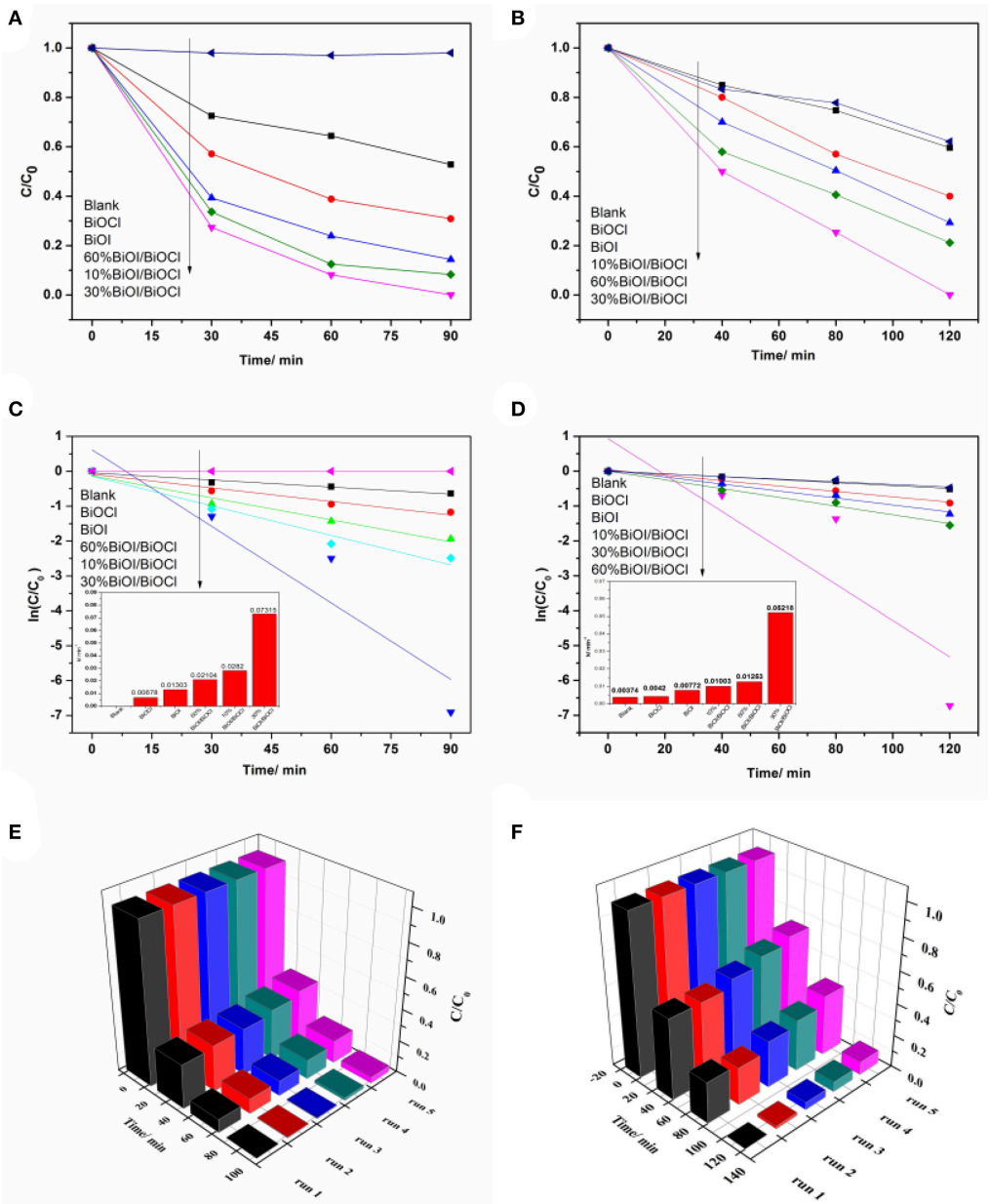

FIGURE 9 | Photodegradation of dyes using *x*BiOI/BiOCl films: **(A)** RhB; **(B)** MB; pseudo-first-order reaction kinetics of 30%BiOI/BiOCl film: **(C)** RhB; **(D)** MB; and repeated degradation of dyes with 30%BiOI/BiOCl film under visible light irradiation: **(E)** RhB; **(F)** MB.

Where E_{VB} was the valence band edge potentials, X was the electronegativity of BiOX, which was the geometric mean of the electronegativity of constituent atoms, E^e was the energy of free electrons on the hydrogen scale (about 4.5 eV), E_g was the band gap energy, E_{CB} was the conductance band edge potentials (Xiao et al., 2016). The E_{VB} of BiOCl and BiOI were 3.60 eV and 2.11 eV, respectively. And the E_{CB} of BiOCl and BiOI were 0.26 and 0.37 eV, respectively.

Active species of 30%BiOI/BiOCl film was detected by typical trapping experiments. Benzoquinone (BQ) was used as superoxide radical species ($\bullet O_2^-$) scavenger, while dimethylcarbinol (IPA) was used as quencher of •OH and EDTA-2Na was used as hole scavenger (h^+). In **Figures 10A,B**, IPA could significantly decrease the photocatalytic efficiency; otherwise, BQ and EDTA-2Na had less effect on it. **Figure 10** indicated that •OH, $\bullet O_2^-$ and h^+ were active species during the degradation of RhB and MB. A possible mechanism of BiOI/BiOCl film was proposed based on the above discussion. In **Figure 11**, BiOI could utilize visible-light with energy <2.95 eV (λ > 420 nm). Photoinduced electrons could be excited to a higher potential edge of BiOI (−0.84 eV) which was negative than that of BiOCl (0.26 eV). Then, photogenerated electrons could transfer to the CB of BiOCl, leaving the holes on the VB of BiOI. Thus, photogenerated carriers could be effectively

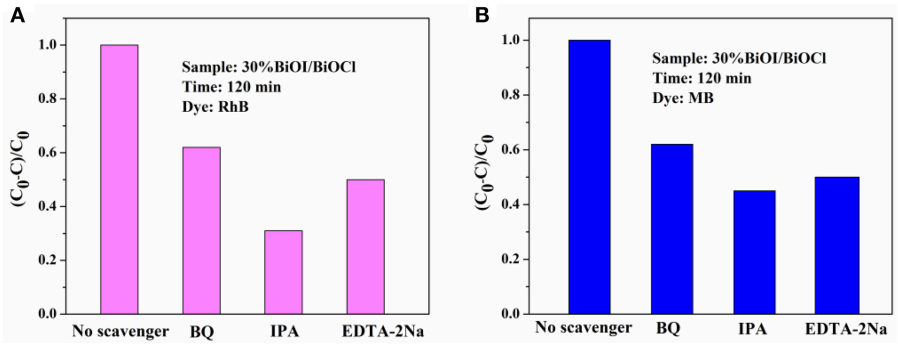

FIGURE 10 | Trapping experiments of active species during visible light photodegradation: **(A)** RhB and **(B)** MB.

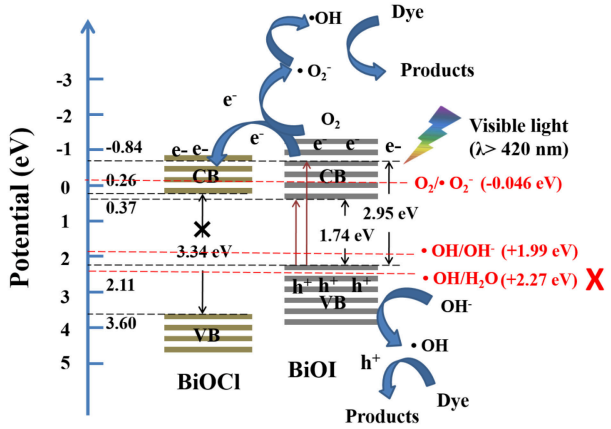

FIGURE 11 | The proposed photodegradation mechanism of RhB and MB by BiOI/BiOCl films.

separated. The E_{VB} of BiOI (2.11 eV) was negative than the potential of ·OH/H_2O (2.27 eV), so •OH was generated by OH^- ($E_{•OH/OH^-}$ = 1.99 eV) rather than H_2O (Zeng et al., 2016). Compared to the potentials of $O_2/•O_2^-$ (−0.046 eV), electrons in the BiOI/BiOCl could reduce O_2 to $•O_2^-$, followed by the generation of •OH (Wang et al., 2013; Zeng et al., 2016). In this way, h^+, $•O_2^-$ and •OH oxidized the organic compounds. which played an important role in the degradation process.

CONCLUSIONS

In conclusion, BiOI/BiOCl films were successfully prepared using a facile method at room temperature. The growth process studies indicated that there was a hydrolyzation competition between BiOCl and BiOI in synthesis protocol. 30%BiOI/BiOCl could eliminate more than 99% of RhB within 90 min, which was 12 times higher than that of BiOCl. Besides RhB, 30% BiOI/BiOCl also showed a great photocatalytic performance toward MB. When degrading RhB, the efficiency of 30% BiOI/BiOCl was 5 and 12 times higher than that of pristine BiOI and BiOCl respectively. While degrading MB, 30%BiOI/BiOCl showed 6 times higher efficiency than that of pristine BiOI. These excellent enhancements were attributed to extended visible light region and high separation efficiency of charge. Five recycles indicated the as-prepared film exhibited a great reusability. In general, this work provided not only an easy and facial method to gain BiOI/BiOCl film but also insights for preparing photocatalysts which effectively utilized visible light with excellent reusability.

AUTHOR CONTRIBUTIONS

YmZ, YZ, and HC participated in the design of this study; XY provided assistance for SEM, TEM, and data analysis; YxZ and YL carried out the experiments and drafted the manuscript. All the authors read and prove the final manuscript.

ACKNOWLEDGMENTS

This work was supported by National Natural Science Foundation of China (21706091 and 21276104) and GuangDong Provincial Department of Science and Technology Application Research and Development Supporting Special Fund Project (2015B020235007).

SUPPLEMENTARY MATERIAL

The Supplementary Material for this article can be found online at: https://www.frontiersin.org/articles/10.3389/fchem.2018.00058/full#supplementary-material

Figure S1 | XRD patterns of 30% BiOI/BiOCl films: fresh and after 5 cycles.

Figure S2 | FT-IR spectra of samples: BiOCl, 30% BiOI/BiOCl, BiOCl.

REFERENCES

Baeck, S. H., Choi, K. S., Jaramillo, T. F., Stucky, G. D., and McFarland, E. W. (2003). Enhancement of photocatalytic and electrochromic properties of electrochemically fabricated mesoporous WO_3 thin films. *Adv. Mater.* 15, 1269-1273. doi: 10.1002/adma.200304669

Cao, J., Xu, B., Luo, B., Lin, H., and Chen, S. (2011). Novel BiOI/BiOBr heterojunction photocatalysts with enhanced visible light photocatalytic properties. *Catal. Commun.* 13, 63–68. doi: 10.1016/j.catcom.2011.06.019

Cao, J., Zhao, Y., Lin, H., Xu, B., and Chen, S. (2013). Facile synthesis of novel Ag/AgI/BiOI composites with highly enhanced visible light photocatalytic performances. *J. Solid State Chem.* 206, 38–44. doi: 10.1016/j.jssc.2013.07.028

Chang, X., Yu, G., Huang, J., Li, Z., Zhu, S., Yu, P., et al. (2010). Enhancement of photocatalytic activity over $NaBiO_3$/BiOCl composite prepared by an in situ formation strategy. *Catal. Today* 153, 193–199. doi: 10.1016/j.cattod.2010.02.069

Cheng, H., Huang, B., and Dai, Y. (2014). Engineering BiOX (X = Cl, Br, I) nanostructures for highly efficient photocatalytic applications. *Nanoscale* 6, 2009–2026. doi: 10.1039/c3nr05529a

Cheng, H., Huang, B., Qin, X., Zhang, X., and Dai, Y. (2012). A controlled anion exchange strategy to synthesize Bi_2S_3 nanocrystals/BiOCl hybrid architectures with efficient visible light photoactivity. *Chem. Commun. (Camb).* 48, 97–99. doi: 10.1039/c1cc15487g

Cheng, H., Huang, B., Wang, P., Wang, Z., Lou, Z., Wang, J., et al. (2011). *In situ* ion exchange synthesis of the novel Ag/AgBr/BiOBr hybrid with highly efficient decontamination of pollutants. *Chem. Commun. (Camb).* 47, 7054–7056. doi: 10.1039/c1cc11525a

Cui, Z., Si, M., Zheng, Z., Mi, L., Fa, W., and Jia, H. (2013). Preparation and characterization of Ag_3PO_4/BiOI composites with enhanced visible light driven photocatalytic performance. *Catal. Commun.* 42, 121–124. doi: 10.1016/j.catcom.2013.08.011

Ding, L., Wei, R., Chen, H., Hu, J., and Li, J. (2015). Controllable synthesis of highly active BiOCl hierarchical microsphere self-assembled by nanosheets with tunable thickness. *Appl. Catal. B Environ.* 172-173, 91–99. doi: 10.1016/j.apcatb.2015.02.019

Dong, F., Sun, Y., Fu, M., Wu, Z., and Lee, S. C. (2012). Room temperature synthesis and highly enhanced visible light photocatalytic activity of porous BiOI/BiOCl composites nanoplates microflowers. *J. Hazard. Mater.* 219-220, 26–34. doi: 10.1016/j.jhazmat.2012.03.015

Fujishima, A., and Honda, K. (1972). Electrochemical photolysis of water at a semiconductor electrode. *Nature* 238, 37–38.

Huang, H., Han, X., Li, X., Wang, S., Chu, P. K., and Zhang, Y. (2015). Fabrication of multiple heterojunctions with tunable visible-light-active photocatalytic reactivity in BiOBr-BiOI full-range composites based on microstructure modulation and band structures. *ACS Appl. Mater. Interfaces* 7, 482–492. doi: 10.1021/am5065409

Jiang, J., Zhang, L., Li, H., He, W., and Yin, J. J. (2013). Self-doping and surface plasmon modification induced visible light photocatalysis of BiOCl. *Nanoscale* 5, 10573–10581. doi: 10.1039/c3nr03597b

Jiang, J., Zhang, X., Sun, P., and Zhang, L. (2011). ZnO/BiOI Heterostructures: photoinduced charge-transfer property and enhanced visible-light photocatalytic activity. *J. Phys. Chem. C* 115, 20555–20564. doi: 10.1021/jp205925z

Kim, W. J., Pradhan, D., Min, B.-K., and Sohn, Y. (2014). Adsorption/photocatalytic activity and fundamental natures of BiOCl and $BiOCl_xI_{1-x}$ prepared in water and ethylene glycol environments, and Ag and Au-doping effects. *Appl. Catal. B Environ.* 147, 711–725. doi: 10.1016/j.apcatb.2013.10.008

Kisch, H. (2013). Semiconductor photocatalysis–mechanistic and synthetic aspects. *Angew. Chem. Int. Edn. Engl.* 52, 812–847. doi: 10.1002/anie.201201200

Law, M., Kind, H., Messer, B., Kim, F., and Yang, P. (2002). Photochemical sensing of NO_2 with SnO_2 nanoribbon nanosensors at room temperature. *Angew. Chem. Int. Edn.* 41, 2405–2408. doi: 10.1002/1521-3773(20020703)41:13<2405::aid-anie2405>3.0.co;2-3

Li, F., Wang, Q., Wang, X., Li, B., Hao, Y., Liu, R., et al. (2014). *In-situ* one-step synthesis of novel $BiOCl/Bi_{24}O_{31}Cl_{10}$ heterojunctions via self-combustion of ionic liquid with enhanced visible-light photocatalytic activities. *Appl. Catal. B Environ.* 150-151, 574–584. doi: 10.1016/j.apcatb.2014.01.009

Li, H., Cui, Y., and Hong, W. (2013). High photocatalytic performance of $BiOI/Bi_2WO_6$ toward toluene and reactive brilliant red. *Appl. Surf. Sci.* 264, 581–588. doi: 10.1016/j.apsusc.2012.10.068

Li, J., Yu, Y., and Zhang, L. (2014). Bismuth oxyhalide nanomaterials: layered structures meet photocatalysis. *Nanoscale* 6, 8473–8488. doi: 10.1039/c4nr02553a

Li, Z., Qu, Y., Hu, K., Humayun, M., Chen, S., and Jing, L. (2017). Improved photoelectrocatalytic activities of BiOCl with high stability for water oxidation and MO degradation by coupling RGO and modifying phosphate groups to prolong carrier lifetime. *Appl. Catal. B Environ.* 203, 355–362. doi: 10.1016/j.apcatb.2016.10.045

Liu, H., Cao, W., Su, Y., Wang, Y., and Wang, X. (2012). Synthesis, characterization and photocatalytic performance of novel visible-light-induced Ag/BiOI. *Appl. Catal. B Environ.* 111-112, 271–279. doi: 10.1016/j.apcatb.2011.10.008

Liu, X., Fan, C., Wang, Y., Wang, Y., Zhang, X., and Liang, Z. (2012). Low temperature preparation of flower-like BiOCl film and its photocatalytic activity. *Sci. Chin. Chem.* 55, 2438–2444. doi: 10.1007/s11426-012-4549-2

Mi, Y., Wen, L., Wang, Z., Cao, D., Xu, R., Fang, Y., et al. (2016). Fe(III) modified BiOCl ultrathin nanosheet towards high-efficient visible-light photocatalyst. *Nano Energy* 30, 109–117. doi: 10.1016/j.nanoen.2016.10.001

Ning, S., Ding, L., Lin, Z., Lin, Q., Zhang, H., Lin, H., et al. (2016). One-pot fabrication of Bi_3O_4Cl/BiOCl plate-on-plate heterojunction with enhanced visible-light photocatalytic activity. *Appl. Catal. B Environ.* 185, 203–212. doi: 10.1016/j.apcatb.2015.12.021

Soci, C., Zhang, A., Xiang, B., Dayeh, S. A., Aplin, D. P., Park, J., et al. (2007). ZnO nanowire UV photodetectors with high internal gain. *Nano Lett.* 7, 1003–1009. doi: 10.1021/nl070111x

Sun, L., Xiang, L., Zhao, X., Jia, C.-J., Yang, J., Jin, Z., et al. (2015). Enhanced visible-light photocatalytic activity of BiOI/BiOCl heterojunctions: key role of crystal facet combination. *ACS Catal.* 5, 3540–3551. doi: 10.1021/cs501631n

Sun, X., Zhang, Y., Li, C., Zhang, Z., Peng, Z., Si, H., et al. (2015). $BiOCl_xBr_yI_z$ (x+y+z=1) solid solutions with controllable band gap and highly enhanced visible light photocatalytic performances. *J. Alloys Compd.* 638, 254–260. doi: 10.1016/j.jallcom.2015.03.150

Wang, Q., Shi, X., Liu, E., Crittenden, J. C., Ma, X., Zhang, Y., et al. (2016). Facile synthesis of AgI/BiOI-Bi_2O_3 multi-heterojunctions with high visible light activity for Cr(VI) reduction. *J. Hazard. Mater.* 317, 8–16. doi: 10.1016/j.jhazmat.2016.05.044

Wang, X. J., Yang, W. Y., Li, F. T., Zhao, J., Liu, R. H., Liu, S. J., et al. (2015). Construction of amorphous TiO_2/BiOBr heterojunctions via facets coupling for enhanced photocatalytic activity. *J. Hazard. Mater.* 292, 126–136. doi: 10.1016/j.jhazmat.2015.03.030

Wang, X., Wang, F., Sang, Y., and Liu, H. (2017). Full-spectrum solar-light-activated photocamtalysts for light-chemical energy conversion. *Adv. Energy Mater.* 7:1700473. doi: 10.1002/aenm.201700473

Wang, X., Wang, Q., Li, F., Yang, W., Zhao, Y., Hao, Y., et al. (2013). Novel BiOCl–C_3N_4 heterojunction photocatalysts: *in situ* preparation via an ionic-liquid-assisted solvent-thermal route and their visible-light photocatalytic activities. *Chem. Engineer. J.* 234, 361–371. doi: 10.1016/j.cej.2013.08.112

Wu, M., Lv, H. Y., Wang, T., Ao, Z. M., Sun, H. Q., Wang, C. Y., et al. (in press). Ag_2MoO_4 nanoparticles encapsulated in g-C_3N_4 for sunlight photodegradation of pollutants. *Catal. Today*. doi: 10.1016/j.cattod.2018.01.019

Xiao, X., Hao, R., Liang, M., Zuo, X., Nan, J., Li, L., et al. (2012). One-pot solvothermal synthesis of three-dimensional (3D) BiOI/BiOCl composites with enhanced visible-light photocatalytic activities for the degradation of bisphenol-A. *J. Hazard. Mater.* 233-234, 122–130. doi: 10.1016/j.jhazmat.2012.06.062

Xiao, X., Tu, S., Lu, M., Zhong, H., Zheng, C., Zuo, X., et al. (2016). Discussion on the reaction mechanism of the photocatalytic degradation of organic contaminants from a viewpoint of semiconductor photo-induced electrocatalysis. *Appl. Catal. B Environ.* 198, 124–132. doi: 10.1016/j.apcatb.2016.05.042

Xiao, X., and Zhang, W.-D. (2010). Facile synthesis of nanostructured BiOI microspheres with high visible light-induced photocatalytic activity. *J. Mater. Chem.* 20, 5866-5870. doi: 10.1039/c0jm00333f

Xiong, W., Zhao, Q., Li, X., and Zhang, D. (2011). One-step synthesis of flower-like Ag/AgCl/BiOCl composite with enhanced visible-light photocatalytic activity. *Catal. Commun.* 16, 229–233. doi: 10.1016/j.catcom.2011.09.027

Zeng, C., Hu, Y., Guo, Y., Zhang, T., Dong, F., Du, X., et al. (2016). Achieving tunable photocatalytic activity enhancement by elaborately engineering composition-adjustable polynary heterojunctions photocatalysts. *Appl. Catal. B Environ.* 194, 62–73. doi: 10.1016/j.apcatb.2016.04.036

Zhang, J., Xia, J., Yin, S., Li, H., Xu, H., He, M., et al. (2013). Improvement of visible light photocatalytic activity over flower-like BiOCl/BiOBr microspheres synthesized by reactable ionic liquids. *Colloids Surf. A Physicochem. Eng. Aspects* 420, 89–95. doi: 10.1016/j.colsurfa.2012.11.054

Zhao, J., Lv, X., Wang, X., Yang, J., Yang, X., and Lu, X. (2015). Fabrication of BiOX (X=Cl, Br, and I) nanosheeted films by anodization and their photocatalytic properties. *Mater. Lett.* 158, 40–44. doi: 10.1016/j.matlet.2015.05.037

Conflict of Interest Statement: The authors declare that the research was conducted in the absence of any commercial or financial relationships that could be construed as a potential conflict of interest.

frontiers in Chemistry

ORIGINAL RESEARCH
published: 04 June 2018
doi: 10.3389/fchem.2018.00192

Photocatalytic Degradation of 4-Nitrophenol by C, N-TiO_2: Degradation Efficiency vs. Embryonic Toxicity of the Resulting Compounds

Oluwatomiwa A. Osin[1,2], Tianyu Yu[1,2], Xiaoming Cai[3], Yue Jiang[1], Guotao Peng[1], Xiaomei Cheng[4], Ruibin Li[5], Yao Qin[4] and Sijie Lin[1,2]**

[1] College of Environmental Science and Engineering, State Key Laboratory of Pollution Control and Resource Reuse, Shanghai Institute of Pollution Control and Ecological Security, Biomedical Multidisciplinary Innovation Research Institute, Shanghai East Hospital, Tongji University, Shanghai, China, [2] UN Environment-Tongji Institute of Environment for Sustainable Development, Tongji University, Shanghai, China, [3] Center for Genetic Epidemiology and Genomics, School of Public Health, Jiangsu Key Laboratory of Preventive and Translational Medicine for Geriatric Diseases, Medical College of Soochow University, Suzhou, China, [4] Institute for Translational Nanomedicine, Shanghai East Hospital, Institute for Biomedical Engineering & Nano Science, Tongji University School of Medicine, Shanghai, China, [5] School for Radiological and Interdisciplinary Sciences (RAD-X), Jiangsu Provincial Key Laboratory of Radiation Medicine and Protection, Medical College of Soochow University, Suzhou, China

OPEN ACCESS

Edited by:
Zhimin Ao, Guangdong University of Technology, China

Reviewed by:
Yuanming Zhang, Jinan University, China
Haiyuan Zhang, Changchun Institute of Applied Chemistry (CAS), China

***Correspondence:**
Yao Qin
lilyqin@tongji.edu.cn
Sijie Lin
lin.sijie@tongji.edu.cn

Specialty section:
This article was submitted to Green and Sustainable Chemistry, a section of the journal Frontiers in Chemistry

Received: *31 March 2018*
Accepted: *14 May 2018*
Published: *04 June 2018*

Citation:
Osin OA, Yu T, Cai X, Jiang Y, Peng G, Cheng X, Li R, Qin Y and Lin S (2018) Photocatalytic Degradation of 4-Nitrophenol by C, N-TiO_2: Degradation Efficiency vs. Embryonic Toxicity of the Resulting Compounds. Front. Chem. 6:192. doi: 10.3389/fchem.2018.00192

The photocatalytic activity of TiO_2 based photocatalysts can be improved by structural modification and elemental doping. In this study, through rational design, one type of carbon and nitrogen co-doped TiO_2 (C, N-TiO_2) photocatalyst with mesoporous structure was synthesized with improved photocatalytic activity in degrading 4-nitrophenol under simulated sunlight irradiation. The photocatalytic degradation efficiency of the C, N-TiO_2 was much higher than the anatase TiO_2 (A-TiO_2) based on absorbance and HPLC analyses. Moreover, using zebrafish embryos, we showed that the intermediate degradation compounds generated by photocatalytic degradation of 4-nitrophenol had higher toxicity than the parent compound. A repeated degradation process was necessary to render complete degradation and non-toxicity to the zebrafish embryos. Our results demonstrated the importance of evaluating the photocatalytic degradation efficiency in conjunction with the toxicity assessment of the degradation compounds.

Keywords: 4-nitrophenol, mesoporous C, N-TiO_2, photocatalytic degradation, intermediate compounds, embryonic toxicity

INTRODUCTION

Photocatalytic degradation of organic pollutants is considered as an efficient, clean, and cost-effective alternative for contaminated water treatment (Wang et al., 1999; Kiros et al., 2013; Osin et al., 2017). Among various types of nano-photocatalysts, titanium dioxide (TiO_2) based photocatalysts are the most popular ones owing to their low cost, simple but reliable synthesis methods, resistance to photo-corrosion, and chemical stability (Carp et al., 2004; Herrmann et al., 2007; Rajeshwar et al., 2008; Akpan and Hameed, 2009). TiO_2 has been used to perform photocatalytic oxidation of contaminants in both aqueous and air media (Fox and Dulay, 1993; Hoffmann et al., 1995; Linsebigler et al., 1995). However, due to their large bandgap (3.2 eV), TiO_2 requires UV light activation (<387 nm), which means only a small portion of the solar spectrum could be used for photocatalytic applications (Wen et al., 2011).

To increase the utility of the visible light spectrum, one common strategy to improve the efficiency of TiO_2 based photocatalysts is to dope or co-dope metal or non-metal elements into the crystalline structure (Asahi et al., 2001). Doping with non-metals, such as nitrogen (Asahi et al., 2001; Burda et al., 2003; Diwald et al., 2004; Cheng et al., 2012), carbon (Lettmann et al., 2001; Sakthivel and Kisch, 2003; Dong et al., 2011), fluorine (Li et al., 2005a,b), and sulfur (Ohno et al., 2004; Yu et al., 2005) has proven to be effective to narrow the bandgap. Among them, nitrogen-doped TiO_2 (N-TiO_2) resulted a considerable increase of the photocatalytic activity in the visible light spectrum. Carbon doping can make TiO_2 sensitive to visible light with improved adsorption capacity for organic pollutant molecules (Park et al., 2006; Dong et al., 2011). Moreover, the simultaneous doping of two types of atoms into TiO_2, such as N–F (Li et al., 2005a,b; Giannakas et al., 2013; Wang et al., 2014), N–S (Yu et al., 2006), and C–N (Wang and Lim, 2010, 2011; Hassan et al., 2014; Trevisan et al., 2014), has recently attracted considerable interests, for the possible integrated or synergistic effects by the co-doped elements.

Meanwhile, it is important to note that a complete degradation of organic pollutants by photocatalysts was difficult to achieve (Dong et al., 2015). And the intermediate compounds generated during photocatalytic degradation might render higher toxicity than their parent compound (Dong et al., 2015; Li et al., 2016). Li et al. previously reported that transformation products (TPs) of acesulfame generated by the photocatalytic processes using TiO_2 photocatalyst were even more toxic than the parent compound (Li et al., 2016). These results were similar to a study carried out by Sang et al. reporting the successful and substantial photocatalytic degradation of acesulfame and sucralose under simulated natural UV conditions. However, real-time observation revealed that the transformation of acesulfame led to a collection of more persistent by-products that were 500 times more toxic than the parent compound inducing significantly elevated toxicity in both marine bacteria and zebrafish embryos (Sang et al., 2014). Therefore, while evaluating the effectiveness of photocatalytic degradation, it is also important to consider the potential hazardous effects exerted by the intermediate degradation compounds (Li et al., 2017; Osin et al., 2017).

Against this background, we set out to explore the use of C and N co-doping to create a TiO_2 based photocatalyst with higher catalytic and degradation efficiency toward 4-nitrophenol, a representative organic pollutant. Under simulated sunlight irradiation, the as-synthesized C, N-TiO_2 showed much higher catalytic activity in comparison with the anatase TiO_2 (A-TiO_2) Using model organism zebrafish embryos, we showed the intermediate compounds of 4-nitrophenol were more toxic than the parent compound. And repeated photocatalytic degradation process could render non-toxicity as a result of a complete degradation of 4-nitrophenol.

MATERIALS AND METHODS

Materials and Reagents

In this study, different concentrations of reagents (**Table 1**) were used to obtain the best doping element ratios and concentrations, which determined the catalytic activity of the as-synthesized particles. 4-nitrophenol of 98% purity was used as a representing pollutant in this study. In the preparation of the modified TiO_2, titanium tetrachloride ($TiCl_4$, 99.9%), ammonia ($NH3.H_2O$, 28–30%) and citric acid ($C_6H_8O_7$, 95.5%) were used as titanium (Ti), nitrogen (N) and carbon (C) source. Perchloric acid ($HClO_4$, 70–72%) was added to serve as a pore-making agent during the synthesis process based on Equation 1:

TABLE 1 | Concentration variations of reagents.

Parameters	Concentration				
Ammonia (ml)	60	90*	120		
Citric Acid (g)	1.15	2.30*	3.45	4.61	9.22
Perchloric Acid (ml)	0.7*	0.9	1.2		

**Optimum concentrations which produced the best activity and selectivity of the catalyst.*

$$4HClO_4 \rightarrow 2H_2O + 7O_2 \overset{\sim 300^\circ C}{\uparrow} + 2Cl_2 \overset{\sim 300^\circ C}{\uparrow} \quad (1)$$

All reagents were purchased from Aladdin Reagent Co., Shanghai, China and were of analytical (AR) grade, used without further purification.

Synthesis and Physicochemical Characterizations of C, N-TiO_2

The C, N-TiO_2 was synthesized by adding $TiCl_4$ carefully into citric acid solution and stirred for 30 min. A white suspension was obtained after ammonia (NH_3) solution was added into the solution dropwise. The mixed solution was stirred for another 30 min in an ice bath. After $HClO_4$ was added, the reaction temperature was increased to 100°C while stirring. The slurry obtained was dried in a vacuum oven for 5 h. Thereafter, the light yellow powder was collected and then annealed at 450°C for 2 h with a ramp of 5°C /min in air. The powder obtained was grinded and used for the further analyses.

The size and crystallinity of the as-synthesized C, N-TiO_2 were determined by transmission electron microscope (JEM-2100, JEOL Ltd., Japan) and X-ray diffractometer (Bruker D8 Advanced XRD, Bruker Co., Germany), respectively. Chemical compositions and oxidation states of the sample were analyzed using X-ray photoelectron spectroscopy (XPS) with monochromated Al Kα radiation ($h\nu = 1486.6$ eV). Binding energies were calibrated using C 1s peak of C-C bond set at 284.8 eV. The fitting and analysis of the spectra was performed in XPS PEAK version 4.1. N_2 adsorption-desorption isotherms were measured on Micromeritics ASAP 2,460 device at 77K. Before detection, the sample was degassed at 373K.

Photocatalytic Degradation

The photocatalytic activities of the C, N-TiO_2 and commercial anatase-TiO_2 (A-TiO_2) were carried out in a photoreactor coupled with a simulated sunlight source (Shanghai Deyangyibang Instruments CO., LTD, DY-D type, also shown in Figure S1). Amount of 20 mL of 4-nitrophenol at 7.0×10^{-2} mM was transferred into glass tubes and placed orderly in the photo-reactor. Amount of 10 mg of the C, N-TiO_2 and A-TiO_2

were added, and the adsorption process of all experiments was done in the dark for 2 h. A magnetic stirrer was used to achieve a satisfactory suspension of the photocatalyst and the homogeneity of the reacting mixture. Samples at 30 min intervals were withdrawn, centrifuged at 8,000 rpm for 10 min, and used for further analysis. The percent of 4-nitrophenol removal was analyzed using a UV-vis spectroscopy, measuring the absorbance at 317nm, while observed first-order rate constants (k, min^{-1}) were measured from Equations (2) and (3), respectively.

$$4-nitrophenol\ removal\ (\%) = \frac{co - ct}{co} \times 100 \quad (2)$$

$$ln\left(\frac{co}{ct}\right) = kt \quad (3)$$

Where, Co and Ct are the initial and remaining 4-nitrophenol concentrations at a given time of the reaction; k is the observed first-order rate constants.

The degradation efficiency of 4-nitrophenol were also measured by high performance liquid chromatography (HPLC). HPLC analysis was performed on an Agilent 1,100 Series LC system (Agilent technologies, Santa Clara, CA) equipped with a binary pump and an ultraviolet-visible diode array detector to quantify the degradation. Samples were separated on an Eclipse Plus C18 reversed phase HPLC column (2.1 × 150 mm, 100Å, 3.5 μm, Agilent technologies, Santa Clara, CA) with an isocratic gradient of methanol and 5 mM phosphoric acid solution (35:65, v/v) over 15 min at a flow rate of 200 μL/min. Injection volumes were 5 μL and the detection wavelength was 254 nm. The mineralization efficiency was measured by a total organic carbon analyzer (TOC-L-CPH Shimadzu, Japan).

Zebrafish Embryo Toxicity Testing

The AB wild-type adult zebrafish (*Danio rerio*) were maintained at 28 ± 0.5°C on a 14 h:10 h light/dark cycle in a fish breeding circulatory system (Haisheng, Shanghai, China) and were fed twice daily with live brine shrimps (*Artemia salina*). Two pairs of male/female fish were placed in a single mating box separated by a divider 1 day prior to spawning. Spawning was triggered by removing the divider in the morning and the embryos were collected 2 h afterwards. Using a stereomicroscope (Olympus-SZ61, Olympus Ltd., Japan), healthy and fertilized embryos at 4 h post fertilization (hpf) were selected and placed in U-bottom 96-well plates (Costar-3599, Corning, US), with one embryo per well. Each well was then filled with 200 μL of each concentration series of the test-sample suspension (4-nitrophenol, C, N-TiO_2, A-TiO_2 and the degradation products) as well as H-buffer as negative controls. Three replicates were carried out for each treatment, each using 12 embryos. The developmental status of the zebrafish embryos was observed at 24, 48, and 72 hpf. The toxicological endpoints included hatching interference, phenotypic abnormalities and mortality (necrosis of the embryos). All experiments were carried out in accordance with the Animal Ethics Committee at Tongji University, with protocol approved by the Animal Center of Tongji University (Protocol #TJLAC-018-020).

Statistical Analysis

All treatments were performed with at least three replicates. Data were reported as average ± standard deviations. Statistical analysis was carried out by Student's t-test to evaluate the statistical significant differences of the hatching success rate and mortality rate between the treatment groups and the negative control group. $P < 0.01$ was considered statistically significant between experimental and control groups.

RESULTS AND DISCUSSION

Composition and Chemical State Analysis of C, N-TiO_2

Figure 1A shows the XPS survey spectrum of C, N-TiO_2. It was clear that only It, O, N and C elements were detected and the corresponding atomic proportions were 29.8, 53.88, 1.25, and

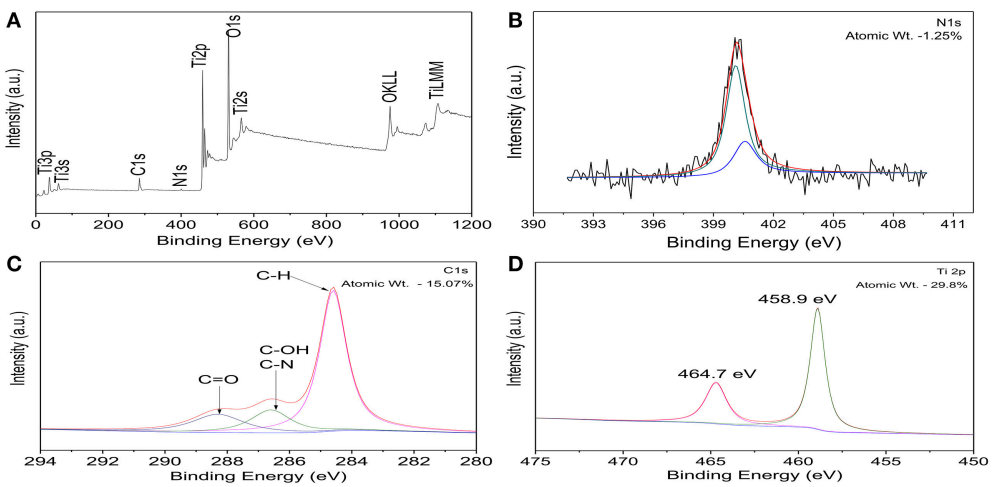

FIGURE 1 | (A) XPS survey spectrum of C, N-TiO_2. High resolution XPS spectra of C, N-TiO_2: **(B)** N1s **(C)** C1s **(D)** Ti2p.

15.07%, respectively. N and C were assigned to the doping species and adventitious carbon of the apparatus, respectively. The high-resolution XPS spectra of Ti2p, C1s, N1s, and O1s region were shown in **Figures 1B–D** and Figure S2.

Figure 1B shows the nitrogen region of the XPS measured spectrum for the C, N-doped TiO_2. The N1s binding energy peaks were broad and asymmetric in the range of 396–403 eV and centered around 400eV (further divided into two peaks centered at 400.1 and 400.5 eV) which can be attributed to the 1 s electron binding energy of the N atom in the environment of O-Ti-N and N-O-Ti (Chen and Burda, 2004; Cong et al., 2007; Xu et al., 2008; Bellardita et al., 2009). Therefore, the nitrogen doped into TiO_2 mainly existed in the form of substitutional N which resulted in the formation of new energy levels in the forbidden band of TiO_2 and led to the enhancement of photocatalytic activity in the visible range (Cheng et al., 2012).

Deconvolution of C1s region showed a main peak at 284.6 eV corresponding to C-H and can be assigned to the adventitious carbon contamination adsorbed from the ambient (Wu and Wang, 2013) (**Figure 1C**). In addition, the peak observed at 284.6 eV refer to the formation of C–OH and C–N bonds. Consequently, the overlap of the peaks corresponding to both C–OH and C–N bonds allows no distinction between the two ones. However, the peak at 288.6 eV indicates the formation of C = O bond that corresponds to a carbonate species present in C-doped titanium systems and that carbon may substitute some of the lattice titanium atoms forming a Ti–O–C structure (Ren et al., 2007). It has been reported that high amount of carbon led to an increased absorption in the visible region, however, it also enhanced the recombination of the charge carriers. This problem was solved by the synergistic effect from the presence of two (or more) complementary dopants (Ren et al., 2007; Li et al., 2010), leading to an improved photoactivity of TiO_2 in the visible light region, compared to either pure or single-doped TiO_2.

In the high resolution spectra of Ti_{2p} spectra shown in **Figure 1D**, peaks at 459.2 and 465 eV corresponds to the spin orbit coupling of $Ti2P_{3/2}$ and $Ti2P_{1/2}$, respectively. It also shows that only the signals corresponding to Ti^{4+} were detected and can be attributed to the binding energy separation between the $2p_{1/2}$ and $2p_{3/2}$ peaks of ∼5.8 eV (Abdullah et al., 2016). Furthermore, the Ti_{2p} XPS peak of un-doped TiO_2 has been reported to appear normally at 459.5 eV (Saha and Tomkins, 1992). Therefore, the nitrogen incorporation shifted the XPS spectrum to a lower binding energy (459.2 instead of 459.5 eV). In correspondence with that of N 1s, the O 1s XPS spectra (shown in Figure S2) also shows a broadening at 531.5 eV which confirms the presence of another type of oxygen due to the more covalent nature of N-TiO_2 (Chi et al., 2007). This might be related to the presence of oxygen and nitrogen from the same lattice units in TiO_2, which confirmed the interstitial doped form (Cong et al., 2007; Pelaez et al., 2010).

Phase Structure, Crystal Structure and Morphologies of C, N-TiO_2

The representative TEM images in **Figure 2** illustrate the crystal phase as well as the size distribution of C, N-TiO_2. The product showed an obvious mesoporous structure caused by the aggregation of C, N-TiO_2 nanograins of 10–20 nm in size, which were also shown in the SEM image of Figure S3. $HClO_4$ was a novel pore-making agent in our recipe of preparing C, N-TiO_2. As shown in Figure S4, without the addition of $HClO_4$, the product looks amorphous with very few pores.

As expected, the porous structure showed a large surface area of 159.903 m^2/g and an average pore diameter of 3.64 nm (**Figure 3B**). As previously mentioned, since the specific surface area (SSA) is one of the key factors determining the catalytic efficiency of catalysts, it is reasonable to expect that the as-synthesized porous C, N-TiO_2 would achieve enhanced catalytic performance in the following degradation of 4-nitrophenol compared to A-TiO_2, with the grain size of 20 nm and surface area of 50 m^2/g.

The crystal structures and particle size of the C, N-TiO_2 were shown in **Figure 3A**. Only the anatase phase was detected

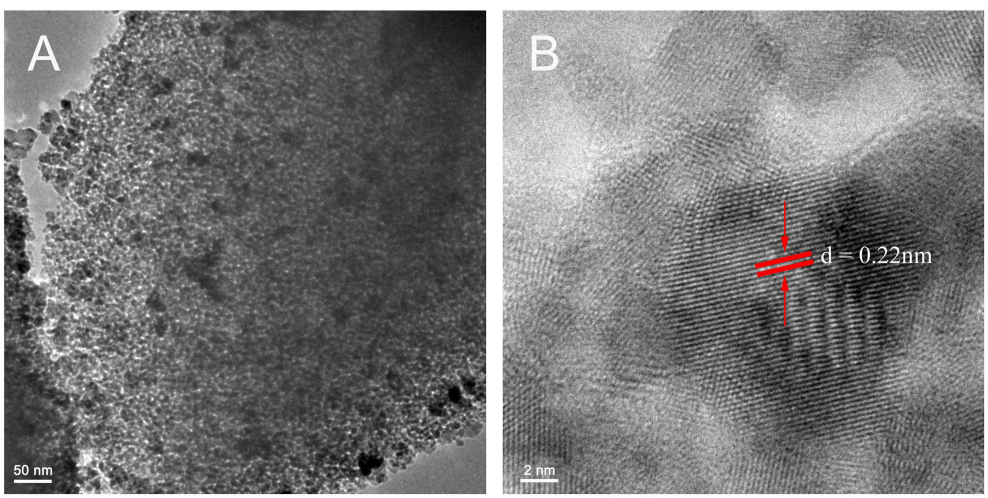

FIGURE 2 | (A) Representative TEM image (low magnification) for as-prepared C, N-TiO_2. **(B)** Representative TEM image (high magnification) for as-prepared C, N-TiO_2. The distance between the lattice fringes (red parallel lines) pointed by the red arrows is 0.22 nm.

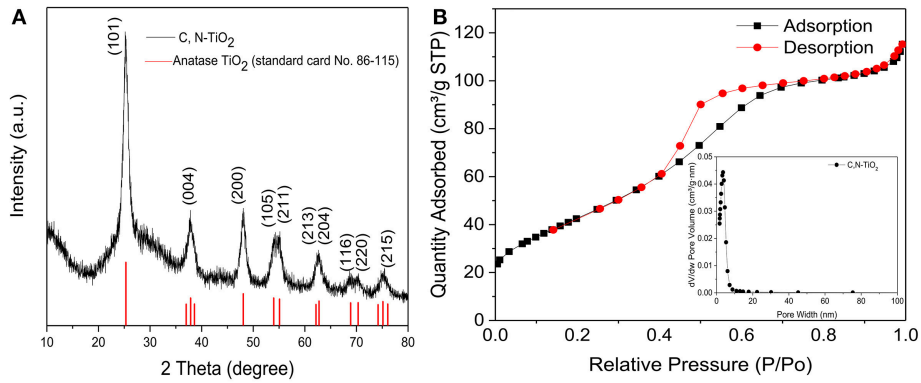

FIGURE 3 | (A) X-ray diffraction (XRD) patterns of C, N-TiO_2. **(B)** Nitrogen adsorption-desorption isotherms and the corresponding pore-size distributions (the inset) of C, N-TiO_2.

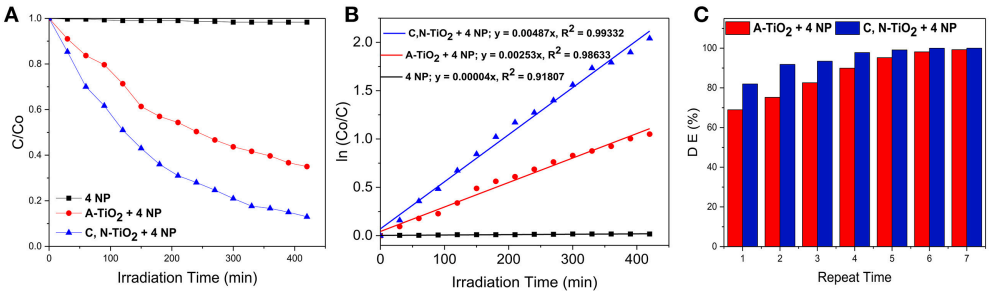

FIGURE 4 | (A) Photocatalytic degradation of 4-nitrophenol. **(B)** First order kinetic analysis for the 4-nitrophenol degradation over C, N-TiO_2 and A-TiO_2. **(C)** Degradation of 4-nitrophenol over A-TiO_2 and C, N- TiO_2 after multiple runs.

from the diffraction peaks of the as-synthesized C, N-TiO_2. This could be attributed to the alkaline reaction conditions during the synthesis process and the N-doping as well. It has been reported that carbon introduction does not modify the crystal of the TiO_2 (Trevisan et al., 2014).

Photocatalytic Activity of C, N-TiO_2

The photocatalytic activity of C, N-TiO_2 and A-TiO_2 in the degradation of 4-nitrophenol from an initial concentration of 7.0 $\times$ 10^{-2} mM under simulated sunlight is shown in **Figure 4A**. The reactivity of the photocatalysts was represented by the ratio of residual concentration to initial concentration of 4-nitrophenol, C/Co, as a function of irradiation time. C, N-TiO_2 and A-TiO_2 degraded 87 and 65% of 4-nitrophenol in 420 min under simulated sunlight irradiation, respectively. The semi-logarithmic plots of concentration data gave a straight line (**Figure 4B**), indicating that the photocatalytic degradation of 4-nitrophenol can be described by the first-order kinetic model, ln $C = -kt + \ln Co$, with a k constant of 4.87 $\times$ 10^{-3} min^{-1} and 2.53 $\times$ 10^{-3} for C, N-TiO_2 and A-TiO_2, respectively.

However, a complete degradation was not achieved under 420 min irradiation: a challenge reported in several other studies (San et al., 2002; Hassan et al., 2014; Dong et al., 2015; Rezaei-Vahidian et al., 2017). To achieve a complete degradation, we repeated the photocatalytic degradation for multiple runs, under the same condition with freshly prepared catalysts at each repetition. A-TiO_2 was able to achieve almost 100% degradation after 7 times of multiple treatments, while the C, N-TiO_2 demonstrated a higher efficiency and achieved almost complete degradation on the 5th treatment (as shown in **Figure 4C**). Furthermore, according to the total organic carbon quantification, the photocatalytic degradation using C, N-TiO_2 was able to mineralize the 4-nitrophenol to about 40% after 7 h (**Figure 5A**). And after 7 repeated treatments, 4-nitrophenol was mineralized to about 60% (**Figure 5B**).

Zebrafish Embryo Toxicity Test

To assess the toxic effects of 4-nitrophenol on zebrafish, embryos were treated with different concentrations (1, 5, 10, 15, and 20 mg/L) for 72 h. The hatching and mortality rates were assessed during the exposure period, at 24, 48, 72 hpf. Figure S5 shows that 4-nitrophenol exhibited a concentration-dependent toxicity, exerting a decreased hatching rates and increased mortality. To assess and compare the possible effects of C, N-TiO_2 and A-TiO_2, embryos were treated with different concentrations (1, 5, 10, 50, 100, 250, and 500 mg/L) of these samples for 72 h. **Figure 6** shows that no obvious toxicity were found for both C, N-TiO_2, and A-TiO_2 at all concentrations tested. These results coincided well with Zhu et al. who found both nano and bulk forms of TiO_2 were non-toxic to zebrafish (Zhu et al., 2008).

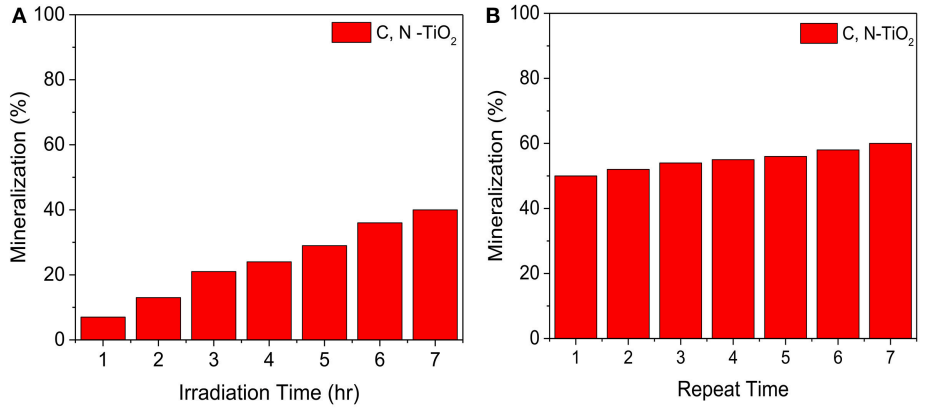

FIGURE 5 | (A) TOC after 7 h degradation **(B)** TOC after multiple degradation.

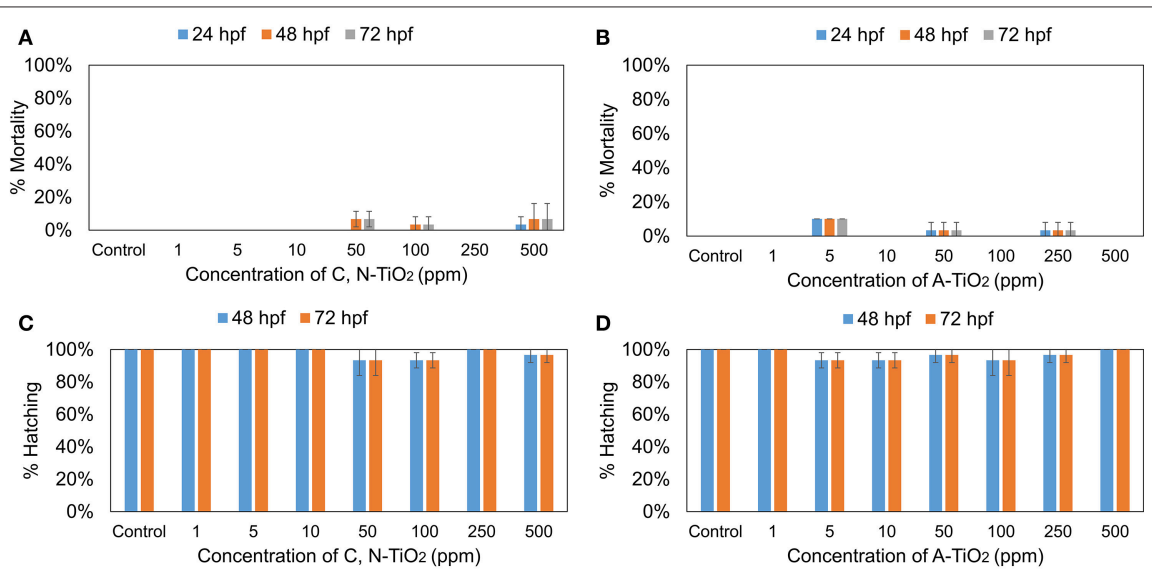

FIGURE 6 | (A,B) Mortality rate and **(C,D)** Hatching rate of zebrafish treated with C, N-TiO_2 and A-TiO_2. (Values are expressed as means ± S.D).

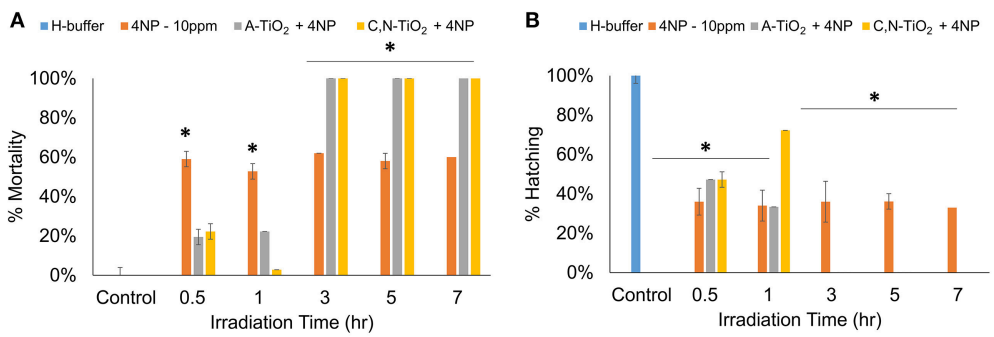

FIGURE 7 | Degradation time-dependent toxicity of zebrafish treated after 72hpf. **(A)** Mortality rate, **(B)** Hatching rate. (Values are expressed as means ± S.D, *$P < 0.01$).

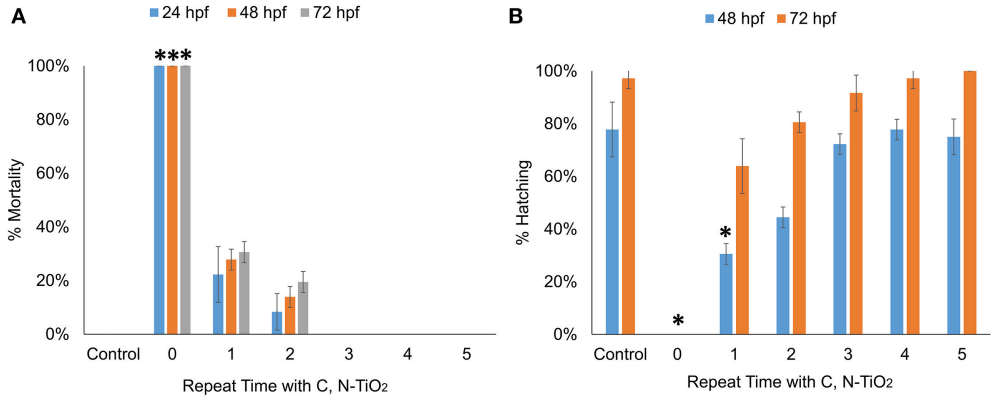

FIGURE 8 | Multiple degradation time-dependent toxicity of zebrafish embryos after 24, 48, and 72 hpf. **(A)** Mortality rate **(B)** Hatching rate. (Values are expressed as means ± S.D, $^*P < 0.01$).

Interestingly, the analysis on the intermediate compounds produced by photocatalytic degradation showed much higher toxicity than the parent compound. Embryos treated with intermediate compounds obtained within 1 h of degradation showed a decrease in toxicity as compared to 4-nitrophenol, exhibiting a decrease in mortality rates and an increase in hatching rates of zebrafish embryos. This effect could be attributed to a decrease in concentration of 4-nitrophenol during the photocatalytic process. However, highly significant effects were observed when embryos were exposed to products obtained after 3 h of degradation, possibly due to the formation of more toxic intermediate compounds. Results showed an increase in mortality rate and decrease in hatching rate in embryos treated with degradation products obtained after 3 h irradiation time at all developmental stages (**Figure 7** and Figure S6). In particular, exposure to all intermediate products obtained after 3 h degradation led to 0% hatching rate and 100% mortality rate, respectively (as shown in **Figure 7**).

Comparative experiments showed that the hatching rate and mortality rate of embryos exposed to degradation products by A-TiO_2 was significantly lower than that C, N-TiO_2, suggesting that higher degradation efficiency led to the formation of more toxic intermediate compounds, thus causing more severe inhibition of hatch and a higher mortality rate. Figure S7 shows embryos treated with the degradation by-products obtained at 1, 3, and 7 h irradiation time after 72 hpf. We observed five types of malformations: pericardial edema (PE), tail malfunction (TM), bent spine (BS), unhatched dead embryo (UDE) and disintegrated embryo (DE). All samples induced high percentages of these abnormalities and malformations. However, malfunctions including unhatched dead embryo and disintegrated embryo were induced by byproducts obtained at 3 and 7 h irradiation time respectively.

The mortality rates and hatching rates of zebrafish embryos exposed to intermediate products obtained after multiple degradation at 24, 48, and 72 hpf are shown in **Figures 8A,B**. There was a significant decrease in toxicity after the first run of degradation. Exposure to products obtained after multiple degradation had no significant effect on the mortality rate and hatching rate of embryos, suggesting that all toxic intermediate compounds had been successfully degraded. HPLC analyses were consistent with this statement. As **Figure 9** showed, before degradation, 4-nitrophenol showed a distinct peak at the mark of 12-min elution time. After 3 h irradiation, a decreased of the peak at 12-min mark indicated a decrease in the concentration of 4-nitrophenol while the appearance of two small peaks at the marks of 3 and 5-min indicated the formation of intermediate compounds. With 5 repeated treatment, all peaks disappeared indicated a complete degradation of 4-nitrophenol therefore no toxicity was observed.

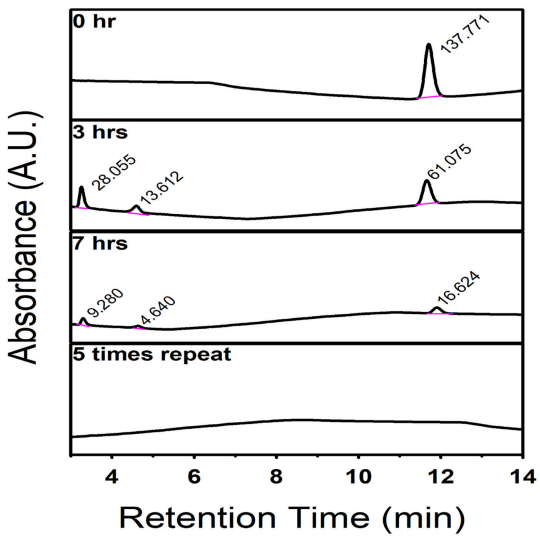

FIGURE 9 | HPLC spectrum showing the degradation of 4-nitrophenol by C, N-TiO_2, the intermediate compounds formation after 3 h irradiation and the complete degradation after 5 repeated process.

According to our HPLC study shown in Figure S8 as well as the analysis result reported by Luo et al. (2013), the intermediate compounds (represented by the peaks appear in the 3-min and 5-min elution time) are likely 4-nitrobenzene-1,2-diol and

4-nitrobenzene-1,3-diol. The compounds were likely the same composition but different concentrations when using A-TiO_2 and C, N-TiO_2 as the catalyst respectively.

CONCLUSION

In summary, through C and N co-doping, we have synthesized a type of mesoporous C, N-TiO_2 photocatalyst by a simple sol-gel method combined with calcination process. The modified photocatalyst exhibited a large surface area, pore volume and simple crystal structure of anatase. C, N-TiO_2 showed higher photocatalytic efficiency during the degradation of 4-nitrophenol than pure A-TiO_2 under simulated light irradiation due to the synergistic effect of carbon and nitrogen co-doping. However, a complete degradation was not achieved under 420 min and intermediate degradation products of 4-nitrophenol displayed a much higher toxicity in zebrafish embryos. A repeated degradation process was necessary to achieve complete degradation and render the compound non-toxic to the zebrafish embryos. Our results further emphasized the necessity of paying close attention to the toxicity potentials of degradation compounds while performing photocatalytic degradation to ensure comprehensive assessment of the threats and significance of these chemicals to the natural environment.

AUTHOR CONTRIBUTIONS

OO contributed to the design and planning of the work, performed experiments, data analysis and drafted the manuscript. TY contributed in the zebrafish embryonic toxicity assessment and graphical design. XCa contributed to the HPLC analysis. YJ contributed to the photodegradation experiments. XCh contributed to the materials synthesis and data analysis. GP contributed to the toxicity assessment and data analysis. RL, YQ, and SL designed, planned and supervised the research and contributed to the manuscript writing. All authors read and approved the final manuscript.

ACKNOWLEDGMENTS

This work was supported by the Recruitment Program of 1000plan Youth and NSFC Grant #21607115 and #21777116 awarded to SL. Additional acknowledgement to the MOFCOM Scholarship awarded to OO.

SUPPLEMENTARY MATERIAL

The Supplementary Material for this article can be found online at: https://www.frontiersin.org/articles/10.3389/fchem.2018.00192/full#supplementary-material

REFERENCES

Abdullah, A. M., Al-Thani, N. J., Tawbi, K., and Al-Kandari, H. (2016). Carbon/nitrogen-doped TiO_2: new synthesis route, characterization and application for phenol degradation. *Arab. J. Chem.* 9, 229–237. doi: 10.1016/j.arabjc.2015.04.027

Akpan, U. G., and Hameed, B. H. (2009). Parameters affecting the photocatalytic degradation of dyes using TiO_2-based photocatalysts: a review. *J. Hazard. Mater*. 170, 520–529. doi: 10.1016/j.jhazmat.2009.05.039

Asahi, R., Morikawa, T., Ohwaki, T., Aoki, K., and Taga, Y. (2001). Visible-light photocatalysis in nitrogen-doped titanium dioxides. *Science* 293, 269–271. doi: 10.1126/science.1061051

Bellardita, M., Addamo, M., Di Paola, A., Palmisano, L., and Veneziab, A. M. (2009). Preparation of N-doped TiO_2: characterization and photocatalytic performance under UV and visible light. *Phys. Chem. Chem. Phys*. 11, 4084–4093. doi: 10.1039/b816708g

Burda, C., Lou, Y., Chen, X., Samia, A.C., Stout, J., and Gole, J. L. (2003). Enhanced nitrogen doping in TiO_2 nanoparticles. *Nano Lett*. 3, 1049–1051. doi: 10.1021/nl034332o

Carp, O., Huisman, C. L., and Reller, A. (2004). Photoinduced reactivity of titanium dioxide. *Prog. Solid State Chem*. 32, 33–177. doi: 10.1016/j.progsolidstchem.2004.08.001

Chen, X., and Burda, C. (2004). Photoelectron spectroscopy investigation of nitrogen-doped titania nanoparticles. *J. Phys. Chem. B*. 108, 15446–15449. doi: 10.1021/jp0469160

Cheng, X., Yua, X., Xinga, Z., and Wana, J. (2012). Enhanced photocatalytic activity of nitrogen doped TiO_2 anatase nano-particle under simulated sunlight irradiation. *Energy Procedia*. 16, 598–605. doi: 10.1016/j.egypro.2012.01.096

Chi, B., Zhao, L., and Jin, T. (2007). Electrochemical photolysis of water at a semiconductor electrode. *J. Phys. Chem. C*. 111, 6189–6193. doi: 10.1021/jp067490n

Cong, Y., Zhang, J. L., Chen, F., and Anpo, M. (2007). Synthesis and characterization of nitrogen-doped TiO_2 nano photocatalyst with high visible light activity. *J. Phys. Chem. C*. 111, 6976–6982. doi: 10.1021/jp0685030

Diwald, O., Thompson, T. L., Zubkov, T., Goralski, E. G., Walck, S. D., and Yates, J. T. (2004). Photochemical activity of nitrogen-doped rutile TiO_2 (110) in visible light. *J. Phys. Chem. B* 108, 6004–6008. doi: 10.1021/jp031267y

Dong, F., Guo, S., Wang, H. Q., Li, X. F., and Wu, Z. B. (2011). Enhancement of the visible light photocatalytic activity of Cdoped TiO_2 nanomaterials prepared by a green synthetic approach. *J. Phys. Chem. C*. 115, 13285–13292. doi: 10.1021/jp111916q

Dong, H., Zeng, G., Tang, L., Fan, C., Zhang, C., He, X., et al. (2015). An overview on limitations of TiO_2-based particles for Photocatalytic degradation of organic pollutants and the corresponding countermeasure. *Water Res*. 79, 128–146. doi: 10.1016/j.watres.2015.04.038

Fox, M. A., and Dulay, M. T. (1993). Heterogeneous photocatalysis. *Chem. Rev*. 83, 341–357. doi: 10.1021/cr00017a016

Giannakas, A. E., Seristatidou, E., Deligiannakis, Y., and Konstantinou, I. (2013). Photocatalytic activity of N-doped and N–F co-doped TiO_2 and reduction of chromium (VI) in aqueous solution: an EPR study. *Appl. Catal. B Environ*. 132, 460–468. doi: 10.1016/j.apcatb.2012.12.017

Hassan, M. E., Chen, J., Liu, G., Zhu, D., and Cai, J. (2014). Enhanced photocatalytic degradation of methyl orange dye under the daylight irradiation over CN-TiO_2 modified with OMS-2. *Materials* 7, 8024–8036. doi: 10.3390/ma7128024

Herrmann, J. M., Duchamp, C., Karkmaz, M., Hoai, B. T., Lachheb, H., and Puzenat, E. G. (2007). Environmental green chemistry as defined by photocatalysis. *J. Hazard. Mater*. 146, 624–629. doi: 10.1016/j.jhazmat.2007.04.095

Hoffmann, M. R., Martin, S. T., Choi, W., and Bahnemann, D. W. (1995). Environmental applications of semiconductor photocatalysis. *Chem. Rev*. 95, 69–96. doi: 10.1021/cr00033a004

Kiros, G., Yadav, O. P., and Tadesse, A. (2013). Effect of Ag-N co-doping in nanosize TiO_2 on photo-catalytic degradation of methyl orange Dye. *J. Surf. Sci. Technol*. 29, 1–14. doi: 10.18311/jsst/2013/1861

Lettmann, C., Hildenbrand, K., Kisch, H., Macyk, W., and Maier, W. F. (2001). Visible light photodegradation of 4-chlorophenol with a coke containing titania photocatalyst. *Appl. Catal. B Environ*. 32, 215–227. doi: 10.1016/S0926-3373(01)00141-2

Li, A. J., Schmitz, O. J., Stephan, S., Lenzen, C., Yue, P. Y., Li, K., et al. (2016). Photocatalytic transformation of acesulfame: transformation products identification and embryotoxicity study. *Water Res.* 89, 68–75. doi: 10.1016/j.watres.2015.11.035

Li, A. J., Wu, P., Law, J. C., Chow, C. H., Postigo, C., Guo, Y., et al. (2017). Transformation of acesulfame in chlorination: kinetics study, identification of byproducts, and toxicity assessment. *Water Res.* 117, 157–166. doi: 10.1016/j.watres.2017.03.053

Li, S., Yu, J., and Wang, W. (2010). Effects of annealing on microstructures and photoactivity of fluorinated N-doped TiO_2. *Phys. Chem. Chem. Phys.* 12, 12308–12315. doi: 10.1039/C0CP00036A

Li, D., Haneda, H., Hishita, S., and Ohashi, N. (2005a). Visible-light-driven N–F–Codoped TiO_2 photocatalysts. 1. Synthesis by spray pyrolysis and surface characterization. *Chem. Mater.* 17, 2588–2595. doi: 10.1021/cm049100k

Li, D., Haneda, H., Hishita, S., and Ohashi, N. (2005b). Visible-light-driven N–F–Codoped TiO_2 photocatalysts. 2. optical characterization, photocatalysis, and potential application to air purification. *Chem. Mater.* 17, 2596–2602. doi: 10.1021/cm049099p

Linsebigler, A. L., Lu, G., and Yates, J. T. (1995). Photocatalysis on TiO_2 surfaces: principles, mechanisms, and selected results. *Chem. Rev.* 95, 735–758. doi: 10.1021/cr00035a013

Luo, X., Deng, F., Min, L., Luo, S., Guo, B., Zeng, G., et al. (2013). Facile one-step synthesis of inorganic-framework molecularly imprinted TiO_2/WO_3 nanocomposite and its molecular recognitive photocatalytic degradation of target contaminant. *Environ. Sci. Technol.* 47, 7404–7412. doi: 10.1021/es4013596

Ohno, T., Akiyoshi, M., Umebayashi, T., Asai, K., Mitsui, T., and Matsumura, M. (2004). Preparation of S-doped TiO_2 photocatalysts and their photocatalytic activities under visible light. *Appl. Catal. A* 265, 115–121. doi: 10.1016/j.apcata.2004.01.007

Osin, O. A., Yu, T., and Lin, S. (2017). Oil refinery wastewater treatment in the Niger Delta, Nigeria: current practices, challenges, and recommendations. *Environ. Sci. Pollut. Res.* 24, 22730–22740. doi: 10.1007/s11356-017-0009-z

Park, J. H., Kim, S., and Bard, A. J. (2006). Novel carbon-doped TiO_2 nanotube arrays with high aspect ratios for efficient solar water splitting. *Nano Lett.* 6, 24–28 doi: 10.1021/nl051807y

Pelaez, M., Falaras, P., Likodimos, V., Kontos, A. G., de la Cruz, A. A., O'Shea, K., et al. (2010). Synthesis, structural characterization and evaluation of sol-gel-based NF-TiO2 films with visible light-photoactivation for the removal of microcystin-LR. *Appl. Catal. B.* 99, 378–387. doi: 10.1016/j.apcatb.2010.06.017

Rajeshwar, K., Osugi, M. E., Chanmanee, W., Chenthamarakshan, C. R., Zanoni, M. V. B., Kajitvichyanukul, P., et al. (2008). Heterogeneous photocatalytic treatment of organic dyes in air and aqueous media. *J. Photochem. Photobiol. C Photochem. Rev.* 9, 171–192. doi: 10.1016/j.jphotochemrev.2008.09.001

Ren, W., Ai, Z., Jia, F., Zhang, L., Fan, X., and Zou, Z. (2007). Low temperature preparation and visible light photocatalytic activity of mesoporous carbon-doped crystalline TiO_2. *Appl. Catal. B Environ.* 69, 138–144. doi: 10.1016/j.apcatb.2006.06.015

Rezaei-Vahidian, H., Zarei, A. R., and Soleymani, A. R. (2017). Degradation of nitro-aromatic explosives using recyclable magnetic photocatalyst: catalyst synthesis and process optimization. *J. Hazard. Mater.* 325, 310–318. doi: 10.1016/j.jhazmat.2016.12.001

Saha, N. C., and Tomkins, H. C. (1992). Titanium nitride oxidation chemistry, an X-Ray photoelectron spectroscopy study. *J. Appl. Phys.* 72, 3072–3079. doi: 10.1063/1.351465

Sakthivel, S., and Kisch, H. (2003). Photocatalytic and photoelectrochemical properties of nitrogen-doped titanium dioxide. *Chem. Phys.* 4, 487–490. doi: 10.1002/cphc.200200554

San, N., Hatipoglu, A., Koçtürk, G., and Çinar, Z. (2002). Photocatalytic degradation of 4-nitrophenol in aqueous TiO_2 suspensions: theoretical prediction of the intermediates. *J. Photochem. Photobiol. A Chem.* 146, 189–197. doi: 10.1016/S1010-6030(01)00620-7

Sang, Z., Jiang, Y., Tsoi, Y. K., and Leung, K. S. (2014). Evaluating the environmental impact of artificial sweeteners: a study of their distributions, photodegradation and toxicities. *Water Res.* 52, 260–274. doi: 10.1016/j.watres.2013.11.002

Trevisan, V., Olivo, A., Pinna, F., Signoretto, M., Vindigni, F., Cerrato, G., et al. (2014). C-N/TiO_2 photocatalysts: effect of co-doping on the catalytic performance under visible light. *Appl. Catal. B Environ.* 160–161, 152–160. doi: 10.1016/j.apcatb.2014.05.015

Wang, K., Hsieh, H., Ko, Y. H., and Chang, R. C. (1999). Photocatalytic degradation of wastewater from manufactured fiber by titanium dioxide suspensions in aqueous solution. *Environ. Int.* 25, 671–676. doi: 10.1016/S0160-4120(99)00035-5

Wang, W., Ni, Y., Lu, C., and Xu, Z. (2014). Hydrogenation Temperature related inner structures and visible-light-driven photocatalysis of N–F co-doped TiO_2 nanosheets. *Appl. Surf. Sci.* 290, 125–130. doi: 10.1016/j.apsusc.2013.11.013

Wang, X., and Lim, T. (2010). Solvothermal synthesis of C–N codoped TiO_2 and photocatalytic evaluation for bisphenol A degradation using a visible-light irradiated LED photoreactor. *Appl. Catal. B Environ.* 100, 355–364. doi: 10.1016/j.apcatb.2010.08.012

Wang, X., and Lim, T. (2011). Effect of hexamethylenetetramine on the visible-light photocatalytic activity of C–N codoped TiO_2 for bisphenol A degradation: evaluation of photocatalytic mechanism and solution toxicity. *Appl. Catal. A Gen.* 399, 233–241. doi: 10.1016/j.apcata.2011.04.002

Wen, C. Z., Jiang, H. B., Qiao, S. Z., Yang, H. G., and Lu, G. Q. (2011). Synthesis of high-reactive facets dominated anatase TiO_2. *J. Mater. Chem.* 21, 7052–7061. doi: 10.1039/c1jm00068c

Wu, D., and Wang, L. (2013). Low-temperature synthesis of anatase C-N-TiO_2 photocatalyst with enhanced visible-light-induced photocatalytic activity. *Appl. Surf. Sci.* 271, 357–361. doi: 10.1016/j.apsusc.2013.01.202

Xu, J. H., Li, J. X., Dai, W. L., Cao, Y., Li, H. X., and Fan, K. N. (2008). Simple fabrication of twist-like helix N, S-codoped titania photocatalyst with visible-light response. *Appl. Catal. B Environ.* 79, 72–80. doi: 10.1016/j.apcatb.2007.10.008

Yu, J. C., Ho, W., Yu, J., Yip, H., Wong, P. K., and Zhao, J. (2005). Efficient visible-light-induced photocatalytic disinfection on sulfur-doped nanocrystalline titania. *Environ. Sci. Technol.* 39, 1175–1179. doi: 10.1021/es035374h

Yu, J., Zhou, M., Cheng, B., Zhao, X., and Mol, J. (2006). Preparation, characterization and photocatalytic activity of *in situ* N, S-codoped TiO_2 powders. *Catal. A Chem.* 246, 176–184. doi: 10.1016/j.molcata.2005.10.034

Zhu, X., Zhu, L., Duan, Z., Qi, R., Li, Y., and Lang, Y. (2008). Comparative toxicity of several metal oxide nanoparticle aqueous suspensions to zebrafish (*Danio rerio*) early developmental stage. *J. Environ. Sci. Health A.* 43, 278–284. doi: 10.1080/10934520701792779

Conflict of Interest Statement: The authors declare that the research was conducted in the absence of any commercial or financial relationships that could be construed as a potential conflict of interest.

frontiers in Chemistry

ORIGINAL RESEARCH
published: 24 July 2018
doi: 10.3389/fchem.2018.00274

Graphene Oxide/BiOCl Nanocomposite Films as Efficient Visible Light Photocatalysts

Weitian Lin[1], *Xiang Yu*[2], *Yi Zhu*[1]* *and Yuanming Zhang*[1]

[1] Department of Chemistry, Jinan University, Guangzhou, China, [2] Analytical & Testing Center, Jinan University, Guangzhou, China

A novel graphene oxide/BiOCl (GO/BiOCl) nanocomposite film was prepared *via* a spread coating method. In visible-light photocatalytically degrading Rhodamine B (RhB) experiments, 2 wt% GO/BiOCl could degrade 99% of RhB within 1.5 h and the rate constant was 12.2 times higher than that of pure BiOCl. The degradation efficiency still kept at 80% even after 4 recycles, evidencing the relatively good recyclability. The enhancement was attributed to the improvement of visible light adsorption and charge separation. Holes and superoxide radicals·O_2^- played a major role as reactive species. The values of conduction band and valence band for GO and BiOCl were calculated and a new photocatalytic mechanism of GO/BiOCl nanocomposite was proposed.

Keywords: graphene, BiOCl, film, visible-light, photocatalytic activity

OPEN ACCESS

Edited by:
Zhimin Ao,
Guangdong University of Technology, China

Reviewed by:
Zhaohui Wang,
University of Newcastle, Australia
Daimei Chen,
China University of Geosciences, China

***Correspondence:**
Yi Zhu
tzhury@jnu.edu.cn

Specialty section:
This article was submitted to Green and Sustainable Chemistry, a section of the journal Frontiers in Chemistry

Received: *15 April 2018*
Accepted: *18 June 2018*
Published: *24 July 2018*

Citation:
Lin W, Yu X, Zhu Y and Zhang Y (2018) Graphene Oxide/BiOCl Nanocomposite Films as Efficient Visible Light Photocatalysts. Front. Chem. 6:274. doi: 10.3389/fchem.2018.00274

INTRODUCTION

The problems of environmental pollution have been becoming a major concern with industrial development, especially water pollution, which severely impacts our lives (Maeda et al., 2006; Zhao et al., 2015; Nie et al., 2018). The photocatalysis technique is often used in dealing with water pollution because of its low cost, chemical stability, and non-toxicity (Dong et al., 2015; Meng and Zhang, 2016; Yang G. et al., 2017; Jing et al., 2018; Wu et al., 2018). The conventional UV-light-driven photocatalytic semiconducting materials, such as TiO_2 and ZnO, can only be inspired by UV light accounting for <5% of sunlight (Liu et al., 2009; Yang et al., 2013; Chen et al., 2014a,b). Therefore, there is a need to exploit new visible-light photocatalysts with excellent photocatalytic performance. Among various photocatalytic materials, the bismuth compounds have attracted considerable attention for its relatively high photocatalytic activity (Li et al., 2014; Chen et al., 2018). As a V-VI-VII ternary semiconductor, bismuth oxychloxide (BiOCl) with a tetragonal crystal structure, consists of a tetragonal $[Bi_2O_2]^{2+}$ positive slabs interleaved by double negative slabs of Cl atoms, which provides the space large enough to polarize the related atoms and orbits (Long et al., 2015; Li M. et al., 2017) and leads to its relatively high photocatalytic activity (Cheng et al., 2014). Nevertheless, BiOCl has been prevented by low separation of the photogenerated electron–hole pairs and UV-light-driving, which make it difficult for practical applications. So it is urgent to further improve electron–hole pairs separation and its visible light adsorption to achieve a high photocatalytic activity. Methods have been applied to change this situation, such as morphology control (Zhu et al., 2010), crystal facet exposure (Wang D. H. et al., 2012), noble metal doping (Jiang et al., 2013), and so on. Among them, fabricating nanocomposites by hybridizing BiOCl with other materials is a practical way. Li et al. showed that novel BiOI/BiOCl nanocomposite demonstrated notably high photocatalytic activities over methyl orange (MO) and RhB in aqueous solution. The enhanced photocatalytic activities for BiOI/BiOCl composites

were ascribed to the matched conduction band and valence band level and effective separation of electron-hole pairs (Li et al., 2011). Wang et al. prepared the BiOCl-C_3N_4 heterojunction photocatalyst with high specific surface areas in a solvent-thermal way, which displayed notably high photocatalytic activity in decomposing MO under visible-light (Wang X. J. et al., 2013). Zhu and his coworkers reported N-doped carbon nanotube-BiOCl using a facile solvothermal method, exhibiting enhanced photocatalytic performance compared with pristine BiOCl for decomposition of RhB under UV-light (Zhu L. et al., 2016). Wang et al. successfully fabricated polyaniline/BiOCl photocatalysts with excellent visible-light photocatalytic activity toward MO. The enhancement of photocatalytic properties could be ascribed to the synergistic effect between BiOCl and polyaniline (Wang Q. et al., 2013).

Graphene, a new type of carbon material with monolayer of sp^2-hybridized carbon atoms in honeycomb structure, has aroused great attention in electronic, optical, and catalytic fields due to its good conductivity, optical and electrical properties (Berger et al., 2006; Geim, 2009; Xie et al., 2015; Xiong et al., 2015; Zhu S. et al., 2016). Recently, graphene exhibits wide applications in photocatalysis including photocatalytic water-splitting to produce hydrogen and photo-degradation for organic pollutants because of its outstanding mobility of charge carriers and much higher theoretical specific surface area (Xiang et al., 2012a,b; Cao et al., 2014; Feng J. et al., 2017). Many studies have been focused on fabricating GO/semiconductor composites to achieve enhanced visible light photocatalytic activities (Yang et al., 2015). For example, Xu et al. reported an efficient graphene hybridized with ZnO photocatalyst for the improved UV light photocatalytic activity (Xu et al., 2011). Ai and her partners fabricated BiOBr-graphene nanocomposites and investigated the excellent visible-light photodegradation on gaseous nitrogen monoxide (Ai et al., 2011). Zhang et al. synthesized a P25-graphene nanocomposite using a facile one-step hydrothermal method and observed significant enhancement photocatalytic activities in degradation of MO (Zhang et al., 2010). Better photocatalytic performances may be obtained by combining remarkable properties of GO and BiOCl to form GO/BiOCl nanocomposites. Up to now, there have been only few investigations on graphene oxides (GO) or reduced graphene oxides (rGO)/BiOCl nanocomposites. Tian et al. prepared rGO-BiOCl hybrid materials *via* a facile solvothermal method. The 0.73% rGO-BiOCl hybrid showed the best photocatalytic degradation performance for RhB (Tian L. et al., 2013). Gao et al. reported chemically bonded graphene/BiOCl composites by a facile chemical-bath method, which exhibited the degradation rate twice as much as that of pure BiOCl over methylbenzene removal under UV-light (Gao et al., 2012). Kang et al. prepared size-controlled rGO-BiOCl with PVP using a hydrothermal method at low temperatures, which showed much higher visible-light photocatalytic activity toward RhB degradation, compared with pure BiOCl (Kang et al., 2015). But only GO/BiOCl nanocomposite powders were reported, which were hard to be separated and recycled. Synthesis of composite films is the most effective way to deal with these problems (Mu et al., 2012). However, there is no report on GO/BiOCl films, which are easy to be separated and recycled.

In our work, GO/BiOCl films were successfully fabricated by a spread coating method at room temperature. The prepared samples were characterized, and the photocatalytic properties were studied by degrading RhB under visible light irradiation. Accordingly, a new photocatalytic mechanism was also presented.

EXPERIMENTAL

Synthesis of GO/BiOCl

The GO/BiOCl was synthesized on a FTO in a facile process. 1.5 g $BiCl_3$ and 0.25 mL HCl were dissolved in 50 mL ethanol by ultrasonication for 30 min. After that, GO was added into the mixture, which was magnetically stirred at room temperature. Few milliliter of mixture was sucked and smeared homogeneously on FTO, and then dried at 80°C for 30 min. Finally, the FTO was immerged in distilled water, and then dried at 60°C. The approach of fabricating GO/BiOCl film was shown in **Scheme 1**. Different amounts (0.8, 2, 4, and 5 wt%) of GO were added. For comparison, BiOCl without GO was prepared in the similar way.

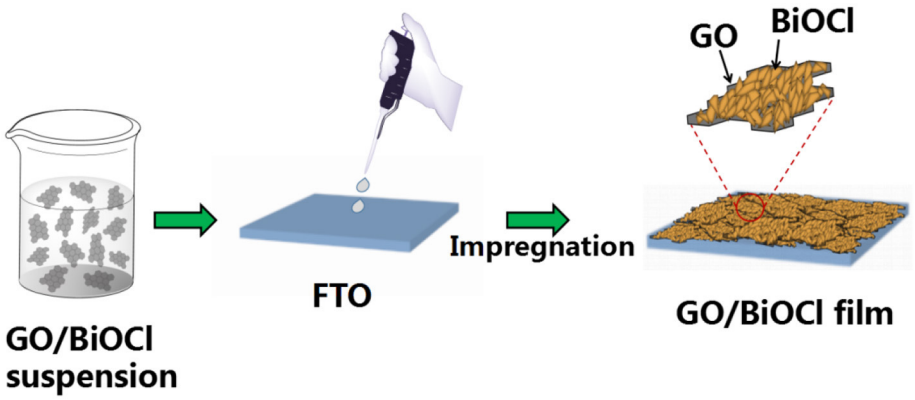

SCHEME 1 | Schematic procedure for fabricating GO/BiOCl film.

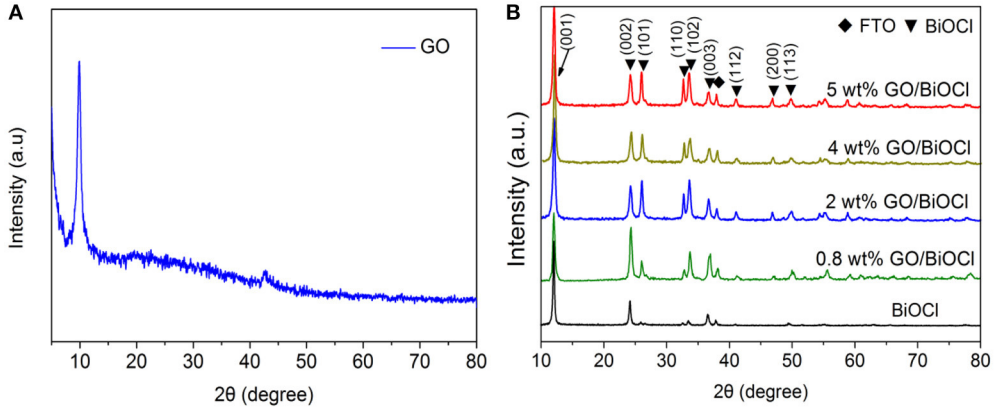

FIGURE 1 | XRD patterns of **(A)** GO, **(B)** pure BiOCl and GO/BiOCl with different GO contents.

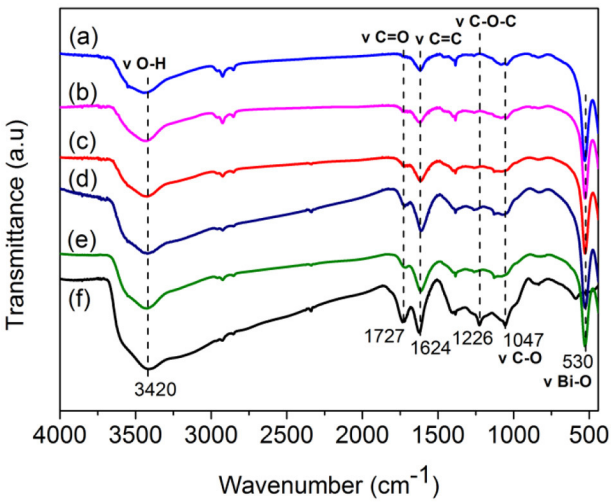

FIGURE 2 | FT-IR spectra of **(a)** BiOCl; **(b)** 0.8 wt% GO/BiOCl; **(c)** 2 wt% GO/BiOCl, **(d)** 4 wt% GO/BiOCl; **(e)** 5 wt% GO/BiOCl; **(f)** GO.

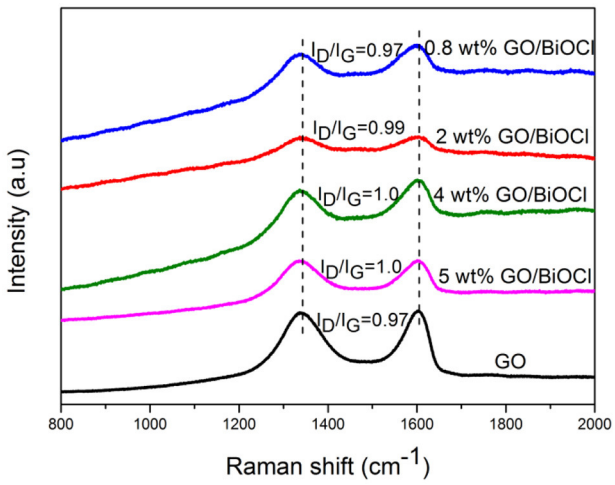

FIGURE 3 | Raman spectra of GO and GO/BiOCl composites.

Characterization

The structure and phase characterization of the as-prepared samples were recorded on an X-ray diffractometer (XD-2) at the scanning rate of $8°min^{-1}$. The morphologies of the samples were characterized by FE-SEM (Zeiss ULTRA 55) and FE-TEM (JEOL 2010F). EDS spectra were obtained using Bruker/Quanta 200 instrument. The ESCALab250 instrument was utilized to record the XPS spectra, which could be used to analyze the surface properties and chemical statement. The BET surface areas and N_2 adsorption-desorption isotherms of the samples were investigated on a TriSTRA 3000 at 77.3 K. The light absorption of the samples was investigated with a UV-Vis diffuse reflectance spectrum (DRS, Hitachi UV-3010) with $BaSO_4$ take for a reference. The photoluminescence (PL) spectra were performed by a RF-5301PC fluorescence spectrophotometer.

Photocatalytic Activity Tests

The photocatalytic properties of the as-fabricated GO/BiOCl were assessed by visible-light degradation of RhB under room temperature (a 350-W Xe lamp with a cut-off filter, λ>420 nm). In the photocatalytic test, the GO/BiOCl photocatalyst was added into a breaker with 100 mL 2.5 mg/L RhB aqueous solution. In order to establish the adsorption-desorption equilibrium, the mixture was stirred for 30 min in dark before the start of photocatalytic experiment. At given intervals, 5 mL suspension was collected and examined by the UV-vis spectrophotometer.

Photoelectrochemical Measurements

The transient photocurrent responses and electrochemical impedance spectroscopy (EIS) measurements were measured in an electrochemical workstation (SP-150, France). The platinum wire was used as the counter electrode and the saturated Ag/AgCl electrode used as the reference electrode. The photo

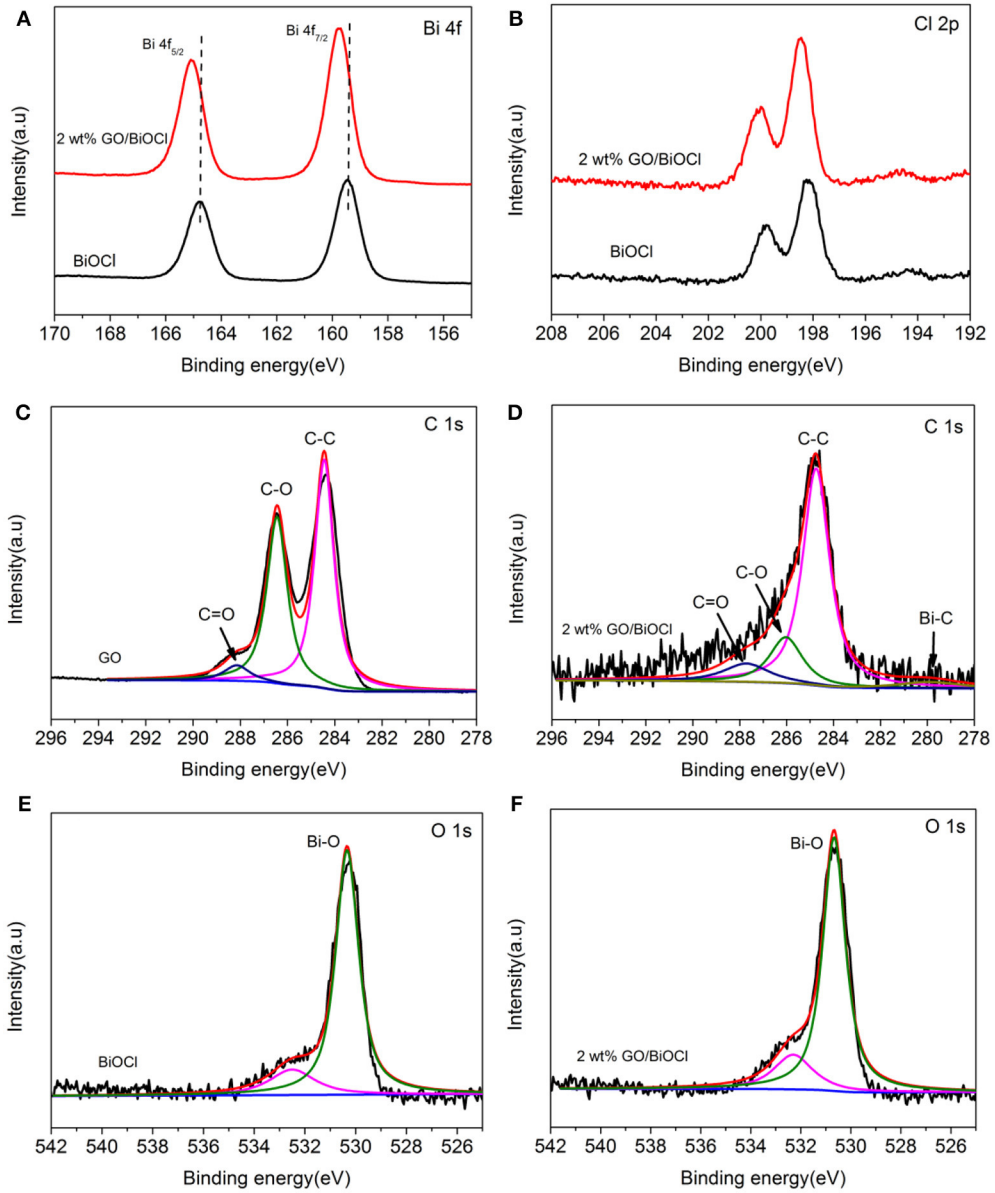

FIGURE 4 | XPS spectra of BiOCl and 2 wt% GO/BiOCl: **(A)** Bi 4f; **(B)** Cl 2p; **(C)** C 1s of GO; **(D)** C 1s of 2 wt% GO/BiOCl; **(E)** O 1s of BiOCl; **(F)** O 1s of 2 wt% GO/BiOCl.

electrochemical experiments were conducted in 0.1 M Na_2SO_4 electrolyte solution.

RESULTS AND DISCUSSION

Characterization of the GO/BiOCl

XRD patterns of GO, pure BiOCl and the as-prepared GO/BiOCl with different GO contents was shown in **Figure 1**. In **Figure 1A**, the peak at 10.6° belonged to GO, which was agreed with the reported results (Shin et al., 2009). The diffraction peaks of BiOCl were identical to those of tetragonal BiOCl, which suggested the high purity (**Figure 1B**). However, peaks of GO in the GO/BiOCl samples could not be observed, which owes to the low GO content in GO/BiOCl (Du et al., 2011). It was noticed that the peaks of BiOCl for GO/BiOCl samples obviously increased, suggesting that BiOCl grown on GO adopted a better crystallinity. The similar phenomenon was also observed in the previous report (Gao et al., 2012).

The FT-IR spectra of BiOCl, GO and GO/BiOCl with different GO contents were shown in **Figure 2**. The characteristic peaks of oxygen-containing functional groups of GO were observed, such as C=O stretching vibration at 1,727 cm^{-1} from carboxyl or carbonyl groups, C=C skeletal vibration at 1,624 cm^{-1} from un-oxidized graphitic domains, epoxide C—O—C, or phenolic C—O—H stretching at 1,226 cm^{-1}, and C—O stretching vibration at 1,047 cm^{-1} from epoxy groups (Szabó et al., 2006; Fu and Wang,

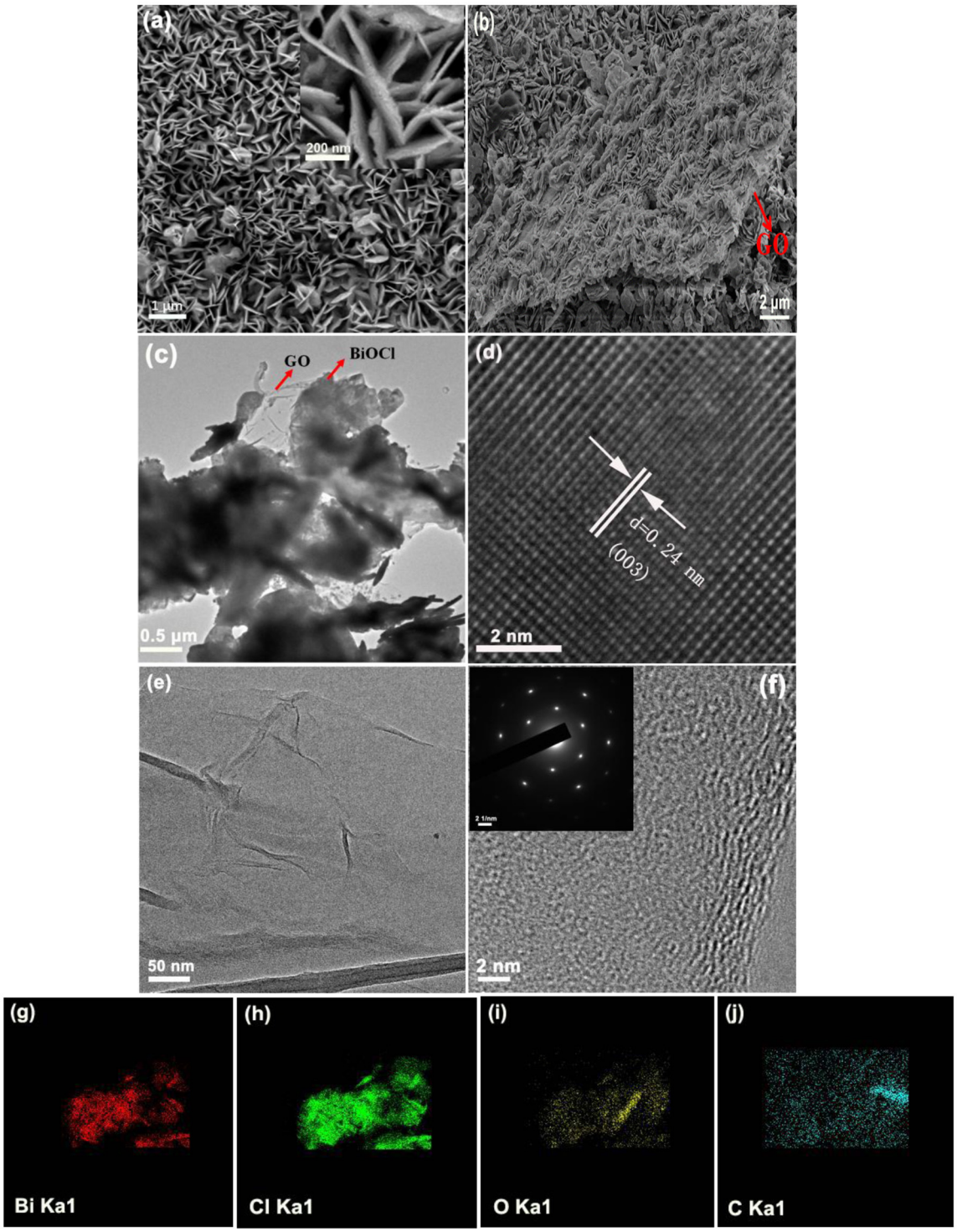

FIGURE 5 | (a,b) FE-SEM image of BiOCl and 2 wt% GO/BiOCl; **(c)** TEM image of 2 wt% GO/BiOCl; **(d)** HRTEM image of BiOCl; **(e,f)** FE-SEM and HRTEM images of GO; **(g–j)** chemical element mapping data of 2 wt% GO/BiOCl.

2011; Chen et al., 2012; Wang P. et al., 2013). The peak at 3,420 cm^{-1} was ascribed to the absorption of water or O—H groups (Liu et al., 2013). The GO/BiOCl samples had similar spectrum of GO but with lower peak intensity, which indicated the partial reduction of GO (Chen et al., 2012). In all the GO/BiOCl samples, the prominent peaks at about 530 cm^{-1} corresponded

to Bi—O vibration (Chou et al., 2013). The appearance of the broad absorption at 1,150 cm^{-1} referring to Bi—C vibration, suggested a chemical bonding between GO and BiOCl (Tu et al., 2012).

Raman spectroscopy was an important technique to study the structural properties of crystal and carbon materials. **Figure 3** showed the Raman spectra of GO and GO/BiOCl composites. As shown, GO displayed two characteristic peaks at around 1,340 and 1,600 cm^{-1}, which were ascribed to the D band and G band of graphite structures. However, in the GO/BiOCl composites, the D band shifted to around 1,334 cm^{-1} and G band moved to around 1,602 cm^{-1}, which could be attributed to the chemical interaction between GO and BiOCl (Hu et al., 2014). I_D/I_G ratio was used to represent the degree of graphitization. The I_D/I_G intensity of GO was 0.97, but the I_D/I_G intensity ratio increased with the increase of GO content, which suggested the reduction of GO during the procedure (Liu et al., 2014).

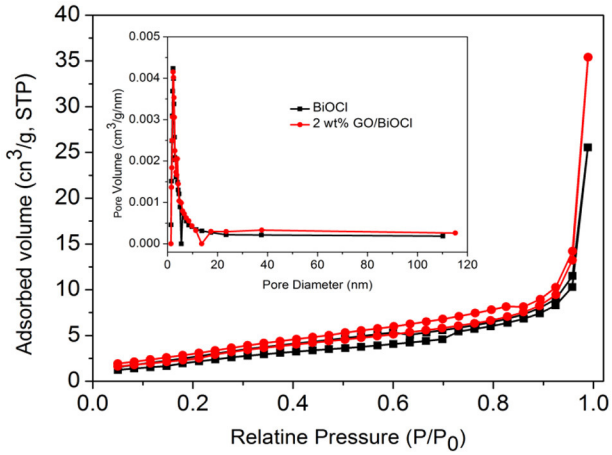

FIGURE 6 | Nitrogen adsorption-desorption isotherm plot and corresponding pore-size distributions (inset) of BiOCl and 2 wt% GO/BiOCl.

TABLE 1 | Summarized BET surface areas and catalytic properties of the photocatalysts.

Sample	S_{BET} (m^2 g^{-1})	k (h^{-1})
BiOCl	3.49	0.24
GO	21.68	0.52
0.8 wt% GO/BiOCl	7.22	0.41
2 wt% GO/BiOCl	11.16	2.93
4 wt% GO/BiOCl	11.29	1.92
5 wt% GO/BiOCl	12.73	1.84

The XPS spectra provided the information for chemical state and surface properties of the 2 wt% GO/BiOCl film. According to **Figure 4A**, two strong peaks centered at 159.7 eV and 165.0 eV in 2 wt% GO/BiOCl were ascribed to Bi $4f_{7/2}$ and Bi $4f_{5/2}$, suggesting Bi^{3+} in the GO/BiOCl (Ai et al., 2011). The peaks of Bi 4f in the 2 wt% GO/BiOCl shifted slightly toward higher binding energies compared with pristine BiOCl, due to the strong interaction between BiOCl and GO (Tian L. et al., 2013). The Cl 2p of XPS spectra were displayed in **Figure 4B**. The peaks located at 198.4 eV and 199.9 eV, corresponded to Cl $2p_{3/2}$ and Cl $2p_{1/2}$, which were characteristics of Cl^- in GO/BiOCl (Cheng et al., 2013). The XPS spectrum of C1s on GO was shown in **Figure 4C**. The peak at 284.7 eV was ascribed to C-C bond with sp^2 orbital. The peaks located at 286.5 eV and 288.4 eV were attributed to the C-O and C=O suggesting the existence of oxygen-containing functional groups in the GO (Liu et al., 2014). In the spectrum of 2 wt% GO/BiOCl (**Figure 4D**), the peak of C-O and C=O showed lower intensities than those of GO, suggesting the partial reduction of GO, which corresponded to the FTIR spectra (Liu et al., 2014). Besides, a new peak at 281.7 eV appeared, which was related to carburetion, and referred to the existence of Bi-C in 2 wt% GO/BiOCl. The result was in accordance with the FTIR spectrum (Akhavan and Ghaderi, 2009). The O 1s region of XPS spectra for BiOCl and 2 wt% GO/BiOCl were depicted in **Figures 4E,F**. The peak at 532 eV could be ascribed to the Bi-O bond in $[Bi_2O_2]$ slabs of BiOX layered structure. The peak centered at 530.3 eV was related to

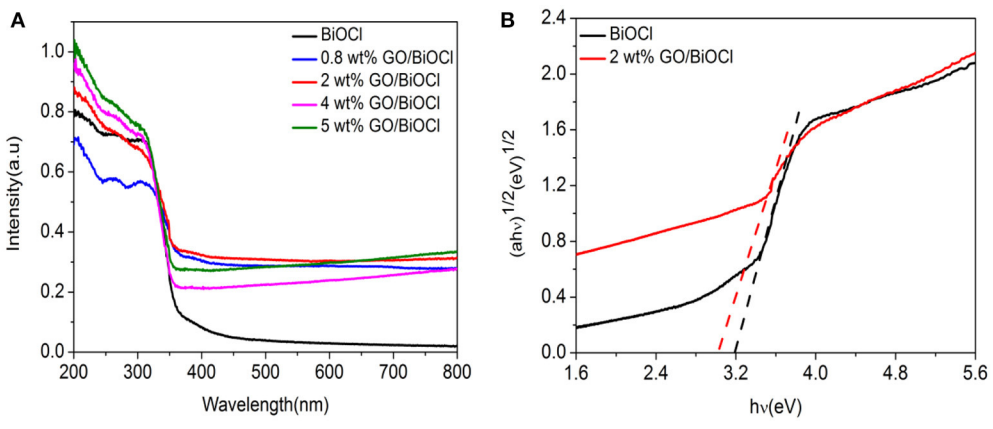

FIGURE 7 | (A) UV-visdiffuse reflectance of the as-prepared samples; **(B)** the band gaps energies (Eg) of pure BiOCl and 2 wt% GO/BiOCl.

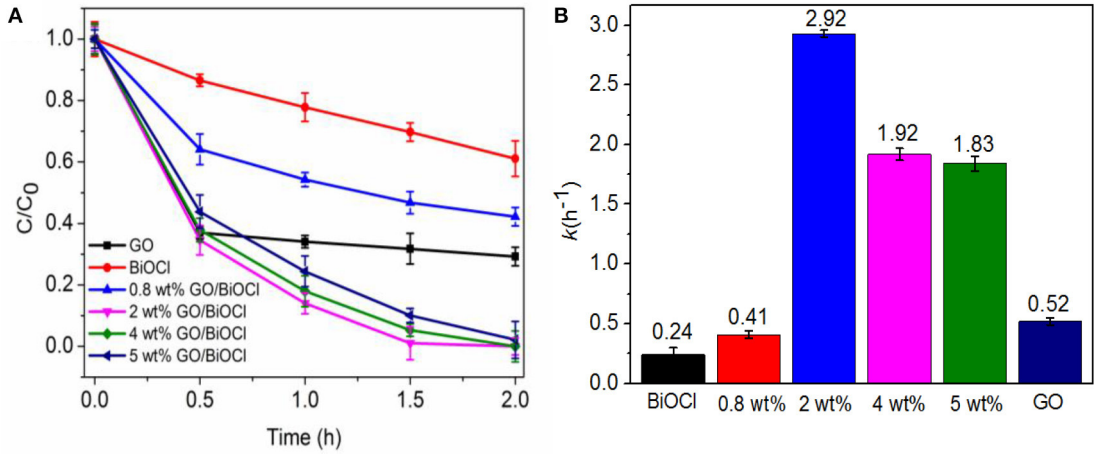

FIGURE 8 | (A) Comparison of photocatalytic activities of the as-prepared samples on the degradation of RhB under visible-light irradiation (λ>420 nm); **(B)** Reaction kinetics of RhB degradation under visible light irradiation by pure BiOCl, GO and GO/BiOCl composites.

TABLE 2 | Photocatalytic activities of various filmphotocatalysts on the degradation of RhB.

Photocataltsts	Dye concentration (mg/L)	Photocatalytic activity	References
Films			
TiO_2	10	50% degraded within 5 h (UV-light)	Wang C. et al., 2012
BiOCl	1.0	52.5% degraded within 8 h (visible-light)	Liang et al., 2013
BiOBr	5.0	80% degraded within 8 h (visible-light)	Cuellar et al., 2015
ZnO:I/TiO_2	2.4	97% degraded within 6 h (visible-light)	Wang et al., 2015
Bi_2WO_6	5.0	53% degraded within 12 h (visible-light)	Zhao et al., 2007
$Bi_2O(OH)_2SO_4$	1.0	92% degraded within 7 h (visible-light)	Zhang et al., 2015
GO/BiOCl	2.5	99% degraded within 1.5 h (visible-light)	This work

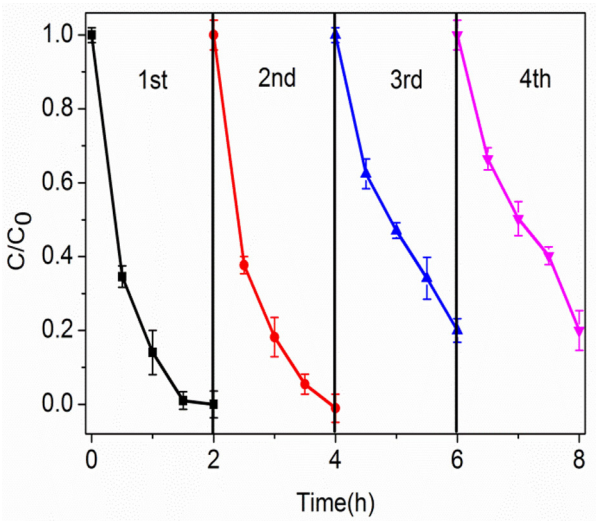

FIGURE 9 | Recycling tests of 2 wt% GO/BiOCl for the degradation of RhB under visible light irradiation.

the hydroxyl groups or water molecules absorbed on the surface of the sample (Liu et al., 2012). The peak of hydroxyl in the 2 wt% GO/BiOCl showed higher intensities than that of BiOCl, indicating more oxygen-containing groups on the GO/BiOCl.

The morphology and structure of 2 wt% GO/BiOCl were evaluated by SEM and TEM. **Figure 5a** showed the nanosheet-like morphology of the BiOCl with the size of 400–600 nm. **Figure 5b** showed that nanosheet-like BiOCl distribute uniformly onto the framework of GO in GO/BiOCl. **Figure 5c** depicted the TEM image of 2 wt% GO/BiOCl. As shown, the GO sheets were not very flat but displayed wrinkles. The structure of GO was shown in **Figures 5e,f**. A high-resolution TEM (HRTEM) image of BiOCl nanosheet (**Figure 5d**) exhibited the lattice spacing of 0.24 nm corresponding to (003) plane. As shown in **Figures 5g–j**, the signals of element Bi, Cl, O and C were clearly observed respectively, evidencing that the samples was GO/BiOCl.

Nitrogen Adsorption-Desorption Analysis

Figure 6 presented the N_2 adsorption-desorption isotherm and corresponding pore size distribution (PSD) cures of BiOCl and 2 wt% GO/BiOCl. Both of them were of type IV isotherms with a hysteresis loop within the range from 0.4 to 0.9 (P/P_0), confirming the mesoporous structure. The BET surface areas of the composites were exhibited in **Table 1**. The S_{BET} of the GO/BiOCl composites were much larger than the pure BiOCl, indicating GO could improve the surface area of the GO/BiOCl composites, which was a significant factor leading to

the enhanced photocatalytic activity. As shown in the inset of **Figure 6**, the pore sizes of the samples were found to be at about 2–11 nm.

Optical Absorption Properties

Figure 7 revealed the UV-vis DRS of pure BiOCl and GO/BiOCl composites. It was noticed that pure BiOCl showed absorption only in UV region. With the introduction of GO, the absorption intensity in the visible-light region of the GO/BiOCl samples was improved. This result indicated that GO played a major role in utilizing sunlight and worked as an electron reservoir to trap the electrons under irradiation (Wei et al., 2014), leading to better photocatalytic performance consequently. The Eg of the GO/BiOCl could be figured out according to previous report (Xie et al., 2013). As can be seen in **Figure 7B**, the band gap energy of pure BiOCl and 2 wt% GO/BiOCl were estimated to be 3.2 and 2.9 eV. It could be seen that the estimated band gap energy of the 2 wt% GO/BiOCl film was lower than that of pristine BiOCl, suggesting that hybridizing BiOCl with GO could enhance the optical absorption property of BiOCl in visible-light region.

Photocatalytic Properties

The photocatalytic performance of the as-fabricated GO/BiOCl was studied by visible-light degradation toward RhB in an aqueous solution. As can be seen in **Figure 8A**, GO/BiOCl displayed higher photodegradation efficiency compared to pure BiOCl. Along with the increase of GO content, the degradation efficiency of GO/BiOCl increased at first, but then decreased while the GO content was larger than 2 wt%. So the highest photocatalytic activity of GO/BiOCl was gained with the optimum content of GO located at 2 wt%, which led to 99% visible-light degradation of RhB within 1.5 h. The degradation rate constants (k, h^{-1}) were calculated to be 0.24, 0.41, 2.93, 1.92, 1.84 and 0.52 h^{-1} for pure BiOCl, 0.8, 2, 4 wt%, 5 wt% GO/BiOCl and GO respectively (**Figure 8B**). It could be seen that all GO/BiOCl showed much higher k-values compared to pristine BiOCl, and 2 wt% GO/BiOCl was about 12 times that of pristine BiOCl. As GO content further increased, the photocatalytic activity of RhB degradation obviously decreased, suggesting that suitable content of the GO was important to improve the photocatalytic activity.

The photocatalytic activity was also compared with other film photocatalysts (**Table 2**). The as-prepared 2 wt% GO/BiOCl film had a higher photocatalytic activity than those photocatalysts, which indicated that it had great prospect for practical applications in degrading pollutants.

The stability and regeneration of the photocatalyst are important to the practical applications. Due to immobilization, the GO/BiOCl samples could be directly separated from the aqueous solution for next recycle. **Figure 9** depicted the photocatalytic activities of 2 wt% GO/BiOCl for degradation of RhB within four cycles. It could be seen that the visible-light photodegradation efficiencies of RhB can reach 80%. These results suggested that the GO/BiOCl had excellent stability and regeneration and could be used as an effective photocatalyst in practical application.

Possible Photocatalytic Mechanism of GO/BiOCl

PL emission spectra have also been regarded as an efficient way to discuss the charge transportation and separation of photocatalysts. As we know, a lower PL intensity correlated with a higher separation efficiency of electron-hole pairs (Tian G. et al., 2013). As was depicted in **Figure 10A**, the emission spectra of pristine BiOCl and 2 wt% GO/BiOCl were similar, but the intensity for 2 wt% GO/BiOCl was lower than pure BiOCl, which implied that 2 wt% GO/BiOCl had a lower recombination rate of photogenerated charge carriers resulting in enhanced photocatalytic activities.

The transient photocurrent responses of BiOCl, GO and 2 wt% GO/BiOCl under visible light irradiation in on-off cycles were investigated. In **Figure 10B**, 2 wt% GO/BiOCl exhibited a significantly increased photocurrent density, which was about much stronger than that of BiOCl and GO, implying that the recombination of photogenerated carriers in 2 wt% GO/BiOCl composite was suppressed (Fan et al., 2016; Feng Y. et al., 2017). **Figure 10C** depicted the corresponding EIS of pure BiOCl, GO and 2 wt% GO/BiOCl. 2 wt% GO/BiOCl exhibited the smallest diameter of the Nyquist circle, demonstrating that the transfer efficiency of photoinduced carriers was improved in 2 wt% GO/BiOCl (Hao et al., 2017). All the PL, transient photocurrent response and EIS results suggested that the separation and transfer efficiency of electron-hole pairs were substantially improved by the addition of GO.

In order to further reveal the photocatalytic mechanism of 2 wt% GO/BiOCl in the photocatalytic degradation process, the trapping experiments of 2 wt% GO/BiOCl were conducted using different scavengers. As shown in **Figure 10D**, isopropanol (IPA), benzoquinone (BQ), and triethanolamine (TEOA) were used as the scavenger for hydroxyl radicals, superoxide radicals and holes (Li et al., 2017a,b,c). On one hand, the photodegradation efficiency of RhB was slightly decreased by adding IPA, which indicated that ·OH was not a major active species. On the other hand, with the addition of benzoquinone or triethanolamine into the system, the photodegradation of RhB decreased obviously suggesting that $\cdot O_2^-$ radicals and h^+ played a dominant part in the visible-light degradation process. This was different from the conclusions that e^- was the main active species for GO/BiOX composites in other relative reports.

Figure 11 showed the Mott-Schottlyplots for BiOCl and GO. The positive slope of the C^{-2}-E indicated the expected n-type BiOCl and GO of the film (Kong, 2008; Weng et al., 2013). The extrapolations of the Mott-Schottly plots provided a good approximation of the flat band potential, the value of which were about −0.26 and −0.27 eV for BiOCl and GO respectively. The measured potentials could be converted to the reversible hydrogen electrode scale *via* the Nernst equation (Yang G. et al., 2017; Yang J. et al., 2017), so the conduction band edges were calculated to be 0.36 and 0.34 eV. Based on the values of conduction band and the band gap, the valence band positions could be calculated to be 3.56 eV and 1.80 eV *via* $E_{CB} = E_{VB} - Eg$ (Duo et al., 2015), in which Eg was about 3.2 eV (**Figure 7B**) and 1.46 eV (**Figure 11A**) for BiOCl and GO.

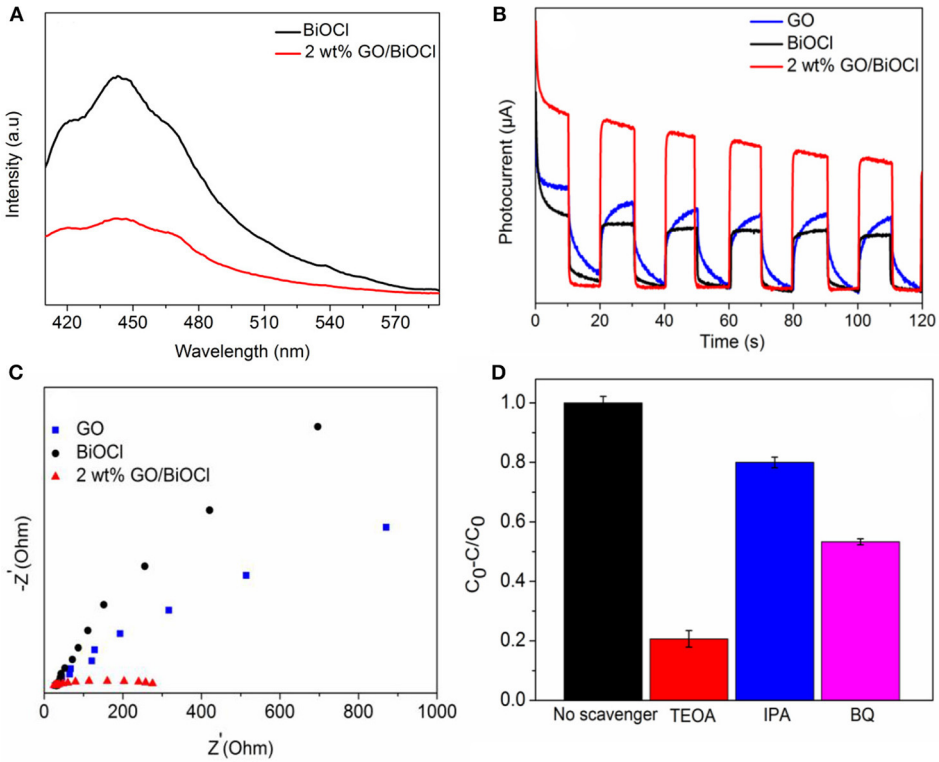

FIGURE 10 | (A) PL spectra of pure BiOCl and 2 wt% GO/BiOCl; **(B)** transient photocurrent response of pure BiOCl, GO and 2 wt% GO/BiOCl; **(C)** electrochemical impedance spectra of pure BiOCl, GO and 2 wt% GO/BiOCl; **(D)** the effect of reactive species in the photogradation process of RhB over 2 wt% GO/BiOCl.

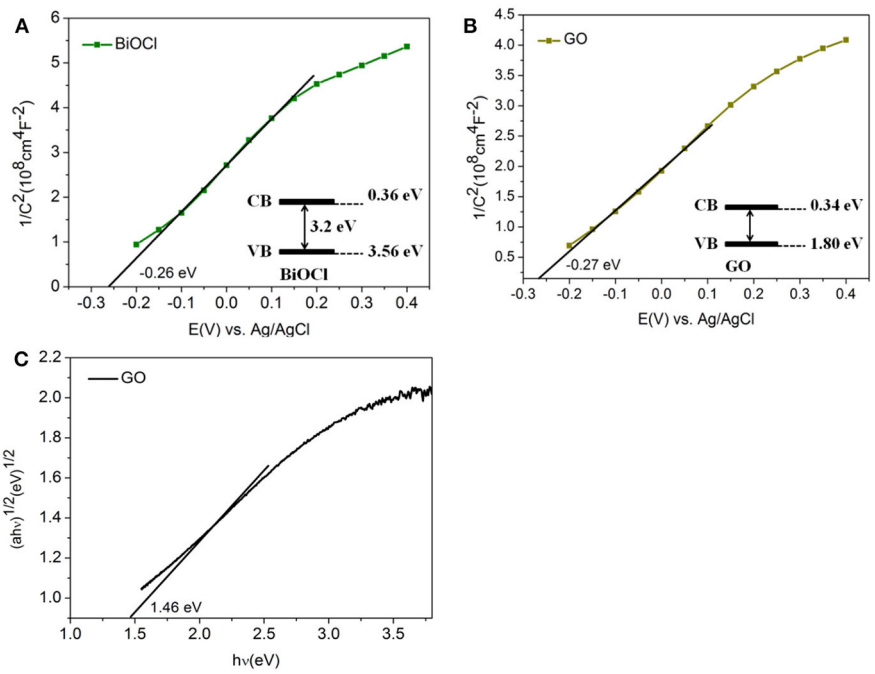

FIGURE 11 | (A) Mott-Schottky plots of BiOCl; **(B)** Mott-Schottky plots of GO; **(C)** band gaps energies (Eg) of GO.

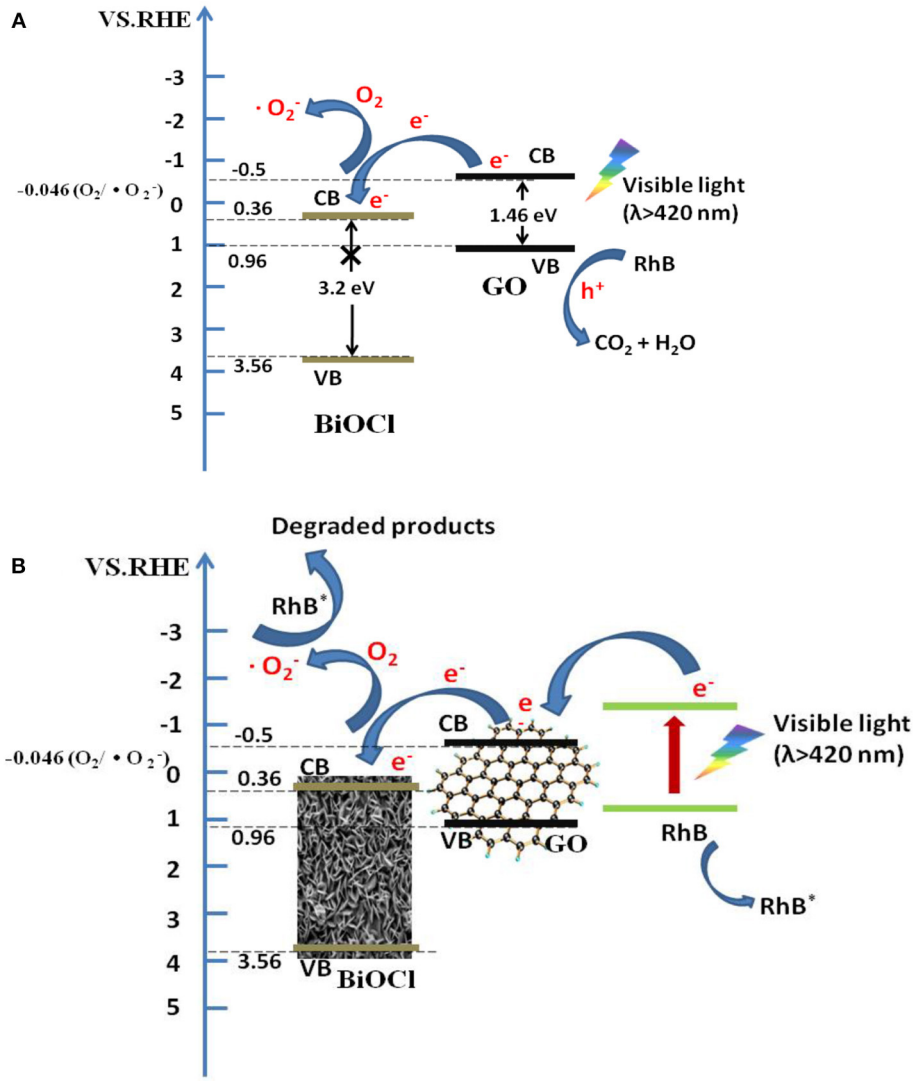

FIGURE 12 | Schematic illustration of the proposed photocatalytic mechanism for GO/BiOCl composites degrading RhB under visible light irradiation: photodegradation **(A)** and photosensitization **(B)**.

According to the above results, a new photocatalytic mechanism of GO/BiOCl nanocomposite including photodegradation and photosensitization at the same time, which was totally different from relevant reports, could be proposed as follows. (1) Holes played a dominant part in the visible-light degrading RhB process, suggesting that photodegradation was an important mechanism. Under visible light irradiation, GO was inspired and gave photo-generated electrons and holes. Electrons flew into the CB of BiOCl, which reacted with O_2 to generate $\cdot O_2^-$. $\cdot O_2^-$ and the holes on the VB of GO degraded the contaminant (**Figure 12A**). (2) Salicylic acid was slightly degraded under visible light irradiation (Figure S1), indicating photosensitization was another important mechanism. Under visible light irradiation, RhB was excited to produce electrons, which flew into the CB of GO, leaving the activated RhB molecules (RhB*). And the electrons on the CB of GO would further transfer to BiOCl, which reacted with O_2 to generate $\cdot O_2^-$, and degraded RhB^* directly (**Figure 12B**). During the photosensitization process, holes are not detected to be a major active species.

CONCLUSION

In summary, GO/BiOCl composite films were successfully prepared *via* a facile spread coating method. The GO/BiOCl films especially 2 wt% GO/BiOCl exhibited a much higher photocatalytic activity compared with pristine BiOCl and many other film photocatalysts, which could be mainly ascribed to the improved light adsorption and separation of photoinduced electrons and holes both resulting from GO. A new photocatalytic mechanism totally different from relevant reports, was revealed to include photodegradation and photosensitization

at the same time. In addition, their recycle was much easier and realizable owing to the immobilization of GO/BiOCl on FTO, and excellent recyclability under visible light was obtained. This work could provide a new way to developing novel composite film photocatalysts and studying new photocatalytic mechanisms for similar GO/BiOX nanocomposites.

AUTHOR CONTRIBUTIONS

WL conceived and designed the experiments, performed the experiments, analyzed the data, and drafted the manuscript. WL and YiZ revised the manuscript. XY and YuZ contributed significantly to the manuscript preparation.

ACKNOWLEDGMENTS

This work was supported by National Natural Science Foundation of China (21706091) and GuangDong Provincial Department of Science and Technology Application Research and Development Supporting Special Fund Project (2015B020235007).

SUPPLEMENTARY MATERIAL

The Supplementary Material for this article can be found online at: https://www.frontiersin.org/articles/10.3389/fchem.2018.00274/full#supplementary-material

REFERENCES

Ai, Z., Ho, W., and Lee, S. (2011). Efficient visible light photocatalytic removal of NO with BiOBr-Graphene nanocomposites. *J. Phys. Chem. C* 115, 25330–25337. doi: 10.1021/jp206808g

Akhavan, O., and Ghaderi, E. (2009). Photocatalytic reduction of graphene oxide nanosheets on TiO_2 thin film for photoinactivation of bacteria in solar light irradiation. *J. Phys. Chem. C* 113, 20214–20220. doi: 10.1021/jp906325q

Berger, C., Song, Z., Li, X., Wu, X., Brown, N., Naud, C., et al. (2006). Electronic confinement and coherence in patterned epitaxial graphene. *Science* 312, 1191–1196. doi: 10.1126/science.1125925

Cao, X., Tian, G., Chen, Y., Zhou, J., Zhou, W., Tian, C., et al. (2014). Hierarchical composites of TiO_2 nanowire arrays on reduced graphene oxide nanosheets with enhanced photocatalytic hydrogen evolution performance. *J. Mater. Chem. A* 2, 4366–4374. doi: 10.1039/c3ta14272h

Chen, C.-M., Zhang, Q., Yang, M. G., Huang, C. H., Yang, Y. G., and Wang, M. Z. (2012). Structural evolution during annealing of thermally reduced graphene nanosheets for application in supercapacitors. *Carbon* 50, 3572–3584. doi: 10.1016/j.carbon.2012.03.029

Chen, D., Wang, K., Xiang, D., Zong, R., Yao, W., and Zhu, Y. (2014a). Significantly enhancement of photocatalytic performances via core–shell structure of ZnO@mpg-C_3N_4. *Appl. Catalysis B* 147, 554–561. doi: 10.1016/j.apcatb.2013.09.039

Chen, D., Wang, Z., Ren, T., Ding, H., Yao, W., Zong, R., et al. (2014b). Influence of defects on the photocatalytic activity of ZnO. *J. Phys. Chem. C* 118, 15300–15307. doi: 10.1021/jp5033349

Chen, D., Yang, J., Zhu, Y., Zhang, Y., and Zhu, Y. (2018). Fabrication of BiOI/graphene Hydrogel/FTO photoelectrode with 3D porous architecture for the enhanced photoelectrocatalytic performance. *Appl. Catalysis B* 233, 202–212. doi: 10.1016/j.apcatb.2018.04.004

Cheng, G., Xiong, J., and Stadler, F. J. (2013). Facile template-free and fast refluxing synthesis of 3D desertrose-like BiOCl nanoarchitectures with superior photocatalytic activity. *New J. Chem.* 37:3207. doi: 10.1039/c3nj00413a

Cheng, H., Huang, B., and Dai, Y. (2014). Engineering BiOX (X = Cl, Br, I) nanostructures for highly efficient photocatalytic applications. *Nanoscale* 6, 2009–2026. doi: 10.1039/c3nr05529a

Chou, Y., Shao, C., Li, X., Su, C., Xu, H., Zhang, M., et al. (2013). BiOCl nanosheets immobilized on electrospun polyacrylonitrile nanofibers with high photocatalytic activity and reusable property. *Appl. Surf. Sci.* 285, 509–516. doi: 10.1016/j.apsusc.2013.08.085

Cuellar, E. L., Martínez-de la Cruz, A., Torres, N. C., and Cortez, J. O. (2015). Deposition of BiOBr thin films by thermal evaporation and evaluation of its photocatalytic activity. *Catalysis Today* 252, 2–6. doi: 10.1016/j.cattod.2015.01.013

Dong, Y., Feng, C., Zhang, J., Jiang, P., Wang, G., Wu, X., et al. (2015). A new p-metal-n structure AgBr-Ag-BiOBr with superior visible-light-responsive catalytic performance. *Chem. An Asian J.* 10, 687–693. doi: 10.1002/asia.201403217

Du, J., Lai, X., Yang, N., Zhai, J., Kisailus, D., Su, F., et al. (2011). Hierarchically ordered macro-mesoporous TiO(2)-graphene composite films: improved mass transfer, reduced charge recombination, and their enhanced photocatalytic activities. *ACS Nano* 5, 590–596. doi: 10.1021/nn102767d

Duo, F., Wang, Y., Mao, X., Zhang, X., Wang, Y., and Fan, C. (2015). A $BiPO_4$/BiOCl heterojunction photocatalyst with enhanced electron-hole separation and excellent photocatalytic performance. *Appl. Surf. Sci.* 340, 35–42. doi: 10.1016/j.apsusc.2015.02.175

Fan, W., Li, H., Zhao, F., Xiao, X., Huang, Y., Ji, H., et al. (2016). Boosting the photocatalytic performance of (001) BiOI: enhancing donor density and separation efficiency of photogenerated electrons and holes. *Chem. Commun.* 52, 5316–5319. doi: 10.1039/c6cc00903d

Feng, J., Ding, H., Yang, G., Wang, R., Li, S., Liao, J., et al. (2017). Preparation of black-pearl reduced graphene oxide-sodium alginate hydrogel microspheres for adsorbing organic pollutants. *J. Coll. Interface Sci.* 508, 387–395. doi: 10.1016/j.jcis.2017.07.113

Feng, Y., Ling, L., Wang, Y., Xu, Z., Cao, F., Li, H., et al. (2017). Engineering spherical lead zirconate titanate to explore the essence of piezo-catalysis. *Nano Energy* 40, 481–486. doi: 10.1016/j.nanoen.2017.08.058

Fu, Y., and Wang, X. (2011). Magnetically Separable $ZnFe_2O_4$-Graphene Catalyst and its High Photocatalytic Performance under Visible Light Irradiation. *Indus. Eng. Chem. Res.* 50, 7210–7218. doi: 10.1021/ie200162a

Gao, F., Zeng, D., Huang, Q., Tian, S., and Xie, C. (2012). Chemically bonded graphene/BiOCl nanocomposites as high-performance photocatalysts. *Phys. Chem. Chem. Phys.* 14:10572. doi: 10.1039/c2cp41045a

Geim, A. K. (2009). Graphene: status and prospects. *Science* 324, 1530–1534. doi: 10.1126/science.1158877

Hao, Q., Wang, R., Lu, H., Xie, C., Ao, W., Chen, D., et al. (2017). One-pot synthesis of C/Bi/Bi_2O_3 composite with enhanced photocatalytic activity. *Appl. Catalysis B* 219, 63–72. doi: 10.1016/j.apcatb.2017.07.030

Hu, C., Chen, F., Lu, T., Lian, C., Zheng, S., Hu, Q., et al. (2014). Water-phase strategy for synthesis of TiO_2-graphene composites with tunable structure for high performance photocatalysts. *Appl. Surf. Sci.* 317, 648–656. doi: 10.1016/j.apsusc.2014.08.161

Jiang, J., Zhang, L., Li, H., He, W., and Yin, J. J. (2013). Self-doping and surface plasmon modification induced visible light photocatalysis of BiOCl. *Nanoscale* 5:10573. doi: 10.1039/c3nr03597b

Jing, B., Ao, Z., Teng, Z., Wang, C., Yi, J., and An, T. (2018). Density functional theory study on the effects of oxygen groups on band gap tuning of graphitic carbon nitrides for possible photocatalytic applications. *Sustainable Mater. Technol.* 16, 12–22. doi: 10.1016/j.susmat.2018.04.001

Kang, S., Pawar, R. C., Pyo, Y., Khare, V., and Lee, C. S. (2015). Size-controlled BiOCl–RGO composites having enhanced photodegradative properties. *J. Exp. Nanosci.* 11, 259–275. doi: 10.1080/17458080.2015.1047420

Kong, D. S. (2008). The influence of fluoride on the physicochemical properties of anodic oxide films formed on titanium surfaces. *Langmuir* 24, 5324–5331. doi: 10.1021/la703258e

Li, J., Yu, Y., and Zhang, L. (2014). Bismuth oxyhalide nanomaterials: layered structures meet photocatalysis. *Nanoscale* 6, 8473–8488. doi: 10.1039/c4nr02553a

Li, M., Zhang, Y., Li, X., Yu, S., Du, X., Guo, Y., et al. (2017). In-depth insight into facet-dependent charge movement behaviors and photo-redox catalysis: a case of {001} and {010} facets BiOCl. *J. Coll. Interface Sci.* 508, 174–183. doi: 10.1016/j.jcis.2017.08.042

Li, S., Hu, S., Jiang, W., Liu, Y., Liu, J., and Wang, Z. (2017a). Facile synthesis of flower-like Ag_3VO_4/Bi_2WO_6 heterojunction with enhanced visible-light photocatalytic activity. *J. Coll. Interface Sci.* 501, 156–163. doi: 10.1016/j.jcis.2017.04.057

Li, S., Hu, S., Jiang, W., Liu, Y., Liu, J., and Wang, Z. (2017b). Synthesis of n -type TaON microspheres decorated by p-type Ag_2O with enhanced visible light photocatalytic activity. *Mol. Catalysis* 435, 135–143. doi: 10.1016/j.mcat.2017.03.027

Li, S., Hu, S., Xu, K., Jiang, W., Liu, J., and Wang, Z. (2017c). A Novel Heterostructure of BiOI nanosheets anchored onto MWCNTs with excellent visible-light photocatalytic activity. *Nanomaterials* 7:22. doi: 10.3390/nano7010022

Li, T. B., Chen, G., Zhou, C., Shen, Z. Y., Jin, R. C., and Sun, J. X. (2011). New photocatalyst BiOCl/BiOI composites with highly enhanced visible light photocatalytic performances. *Dalton Trans.* 40:6751. doi: 10.1039/c1dt10471c

Liang, Y., Guo, C., Cao, S., Tian, Y., and Lui, Q. (2013). A High Quality BiOCl film with petal-like hierarchical structures and its visible-light photocatalytic property. *J. Nanosci. Nanotechnol.* 13, 919–923. doi: 10.1166/jnn.2013.5972

Liu, G., Yang, H. G., Wang, X., Cheng, L., Pan, J., Lu, G. Q., et al. (2009). Visible light responsive nitrogen doped anatase TiO_2 sheets with dominant {001} facets derived from TiN. *J. Am. Chem. Soc.* 131, 12868–12869. doi: 10.1021/ja903463q

Liu, H., Cao, W. R., Su, Y., Chen, Z., and Wang, Y. (2013). Bismuth oxyiodide-graphene nanocomposites with high visible light photocatalytic activity. *J. Coll. Interface Sci.* 398, 161–167. doi: 10.1016/j.jcis.2013.02.007

Liu, H., Su, Y., Chen, Z., Jin, Z., and Wang, Y. (2014). Graphene sheets grafted three-dimensional $BiOBr_{0.2}I_{0.8}$ microspheres with excellent photocatalytic activity under visible light. *J. Hazard Mater.* 266, 75–83. doi: 10.1016/j.jhazmat.2013.12.013

Liu, Z., Xu, W., Fang, J., Xu, X., Wu, S., Zhu, X., et al. (2012). Decoration of BiOI quantum size nanoparticles with reduced graphene oxide in enhanced visible-light-driven photocatalytic studies. *Appl. Surf. Sci.* 259, 441–447. doi: 10.1016/j.apsusc.2012.07.063

Long, B., Huang, Y., Li, H., Zhao, F., Rui, Z., Liu, Z., et al. (2015). Carbon Dots Sensitized BiOI with Dominant {001} facets for superior photocatalytic performance. *Indus. Eng. Chem. Res.* 54, 12788–12794. doi: 10.1021/acs.iecr.5b02780

Maeda, K., Teramura, K., Lu, D., Takata, T., Saito, N., Inoue, Y., et al. (2006). Photocatalyst releasing hydrogen from water. *Nature* 440:295. doi: 10.1038/440295a

Meng, X., and Zhang, Z. (2016). Bismuth-based photocatalytic semiconductors: Introduction, challenges and possible approaches. *J. Mol. Catalysis A* 423, 533–549. doi: 10.1016/j.molcata.2016.07.030

Mu, Q., Zhang, Q., Wang, H., and Li, Y. (2012). Facile growth of vertically aligned BiOCl nanosheet arrays on conductive glass substrate with high photocatalytic properties. *J. Mater. Chem.* 22:16851. doi: 10.1039/c2jm32781c

Nie, C., Ao, Z., Duan, X., Wang, C., Wang, S., and An, T. (2018). Degradation of aniline by electrochemical activation of peroxydisulfate at MWCNT cathode: the proofed concept of nonradical oxidation process. *Chemosphere* 206, 432–438. doi: 10.1016/j.chemosphere.2018.04.173

Shin, H. J., Kim, K. K., Benayad, A., Yoon, S. M., Park, H. K., Jung, I. S., et al. (2009). Efficient reduction of graphite oxide by sodium borohydride and its effect on electrical conductance. *Adv. Funct. Mater.* 19, 1987–1992. doi: 10.1002/adfm.200900167

Szabó, T., Tombácz, E., Illés, E., and Dékány, I. (2006). Enhanced acidity and pH-dependent surface charge characterization of successively oxidized graphite oxides. *Carbon* 44, 537–545. doi: 10.1016/j.carbon.2005.08.005

Tian, G., Chen, Y., Zhai, R., Zhou, J., Zhou, W., Wang, R., et al. (2013). Hierarchical flake-like Bi_2MoO_6/TiO_2 bilayer films for visible-light-induced self-cleaning applications. *J. Mater. Chem. A* 1:6961. doi: 10.1039/c3ta10511c

Tian, L., Liu, J., Gong, C., Ye, L., and Zan, L. (2013). Fabrication of reduced graphene oxide–BiOCl hybrid material via a novel benzyl alcohol route and its enhanced photocatalytic activity. *J. Nanoparticle Res.* 15:1917. doi: 10.1007/s11051-013-1917-6

Tu, X., Luo, S., Chen, G., and Li, J. (2012). One-pot synthesis, characterization, and enhanced photocatalytic activity of a BiOBr-graphene composite. *Chemistry* 18, 14359–14366. doi: 10.1002/chem.201200892

Wang, C., Zhang, X., Zhang, Y., Jia, Y., Yuan, B., Yang, J., et al. (2012). Morphologically-tunable TiO_2 nanorod film with high energy facets: green synthesis, growth mechanism and photocatalytic activity. *Nanoscale* 4, 5023–5030. doi: 10.1039/c2nr31127e

Wang, D. H., Gao, G. Q., Zhang, Y. W., Zhou, L. S., Xu, A. W., and Chen, W. (2012). Nanosheet-constructed porous BiOCl with dominant {001} facets for superior photosensitized degradation. *Nanoscale* 4:7780. doi: 10.1039/c2nr32533k

Wang, P., Wang, J., Wang, X., Yu, H., Yu, J., Lei, M., et al. (2013). One-step synthesis of easy-recycling TiO_2-rGO nanocomposite photocatalysts with enhanced photocatalytic activity. *Appl. Catalysis B* 132–133, 452–459. doi: 10.1016/j.apcatb.2012.12.009

Wang, Q., Hui, J., Li, J., Cai, Y., Yin, S., Wang, F., et al. (2013). Photodegradation of methyl orange with PANI-modified BiOCl photocatalyst under visible light irradiation. *Appl. Surf. Sci.* 283, 577–583. doi: 10.1016/j.apsusc.2013.06.149

Wang, X. J., Wang, Q., Li, F. T., Yang, W. Y., Zhao, Y., Hao, Y. J., et al. (2013). Novel BiOCl–C_3N_4 heterojunction photocatalysts: *in situ* preparation via an ionic-liquid-assisted solvent-thermal route and their visible-light photocatalytic activities. *Chem. Eng. J.* 234, 361–371. doi: 10.1016/j.cej.2013.08.112

Wang, Y., Zheng, Y. Z., Lu, S., Tao, X., Che, Y., and Chen, J. F. (2015). Visible-light-responsive TiO_2-coated ZnO:I nanorod array films with enhanced photoelectrochemical and photocatalytic performance. *ACS Appl. Mater,. Interfaces* 7, 6093–6101. doi: 10.1021/acsami.5b00980

Wei, X. X., Chen, C. M., Guo, S. Q., Guo, F., Li, X. M., Wang, X.-X., et al. (2014). Advanced visible-light-driven photocatalyst BiOBr–TiO_2-graphene composite with graphene as a nano-filler. *J. Mater. Chem. A* 2:4667. doi: 10.1039/c3ta14349j

Weng, S., Chen, B., Xie, L., Zheng, Z., and Liu, P. (2013). Facile *in situ* synthesis of a Bi/BiOCl nanocomposite with high photocatalytic activity. *J. Mater. Chem. A* 1:3068. doi: 10.1039/c2ta01004f

Wu, M., Lv, H., Wang, T., Ao, Z., Sun, H., Wang, C., et al. (2018). Ag 2 MoO 4 nanoparticles encapsulated in g-C_3N_4 for sunlight photodegradation of pollutants. *Catalysis Today*. doi: 10.1016/j.cattod.2018.01.019. [Epub ahead of print].

Xiang, Q., Yu, J., and Jaroniec, M. (2012a). Graphene-based semiconductor photocatalysts. *Chem. Soc. Rev.* 41, 782–796. doi: 10.1039/c1cs15172j

Xiang, Q., Yu, J., and Jaroniec, M. (2012b). Synergetic effect of MoS2 and graphene as cocatalysts for enhanced photocatalytic H_2 production activity of TiO_2 nanoparticles. *J. Am. Chem. Soc.* 134, 6575–6578. doi: 10.1021/ja302846n

Xie, T., Liu, C., Xu, L., Yang, J., and Zhou, W. (2013). Novel Heterojunction $Bi_2O_3/SrFe_{12}O_{19}$ magnetic photocatalyst with highly enhanced photocatalytic activity. *J. Phys. Chem. C* 117, 24601–24610. doi: 10.1021/jp408627e

Xie, X., Ao, Z., Su, D., Zhang, J., and Wang, G. (2015). MoS_2/Graphene composite anodes with enhanced performance for sodium-ion batteries: the role of the two-dimensional heterointerface. *Adv. Funct. Mater.* 25, 1393–1403. doi: 10.1002/adfm.201404078

Xiong, T., Dong, F., Zhou, Y., Fu, M., and Ho, W. K. (2015). New insights into how RGO influences the photocatalytic performance of $BiOIO_3$/RGO nanocomposites under visible and UV irradiation. *J. Coll. Interface Sci.* 447, 16–24. doi: 10.1016/j.jcis.2015.01.068

Xu, T., Zhang, L., Cheng, H., and Zhu, Y. (2011). Significantly enhanced photocatalytic performance of ZnO via graphene hybridization and the mechanism study. *Appl. Catalysis B* 101, 382–387. doi: 10.1016/j.apcatb.2010.10.007

Yang, G., Daimei, C., Hao, D., Feng, J., Zhang, J. Z., Zhu, Y., et al. (2017). Well-designed 3D $ZnIn_2S_4$ nanosheets/TiO_2 nanobelts as direct Z-scheme photocatalysts for CO_2 photoreduction into renewable hydrocarbon fuel with high efficiency. *Appl. Catalysis B* 219, 611–618. doi: 10.1016/j.apcatb.2017.08.016

Yang, J., Chen, D., Zhu, Y., Zhang, Y., and Zhu, Y. (2017). 3D-3D porous Bi_2WO_6/graphene hydrogel composite with excellent synergistic effect of

adsorption-enrichment and photocatalytic degradation. *Appl. Catalysis B Environ.* 205, 228–237. doi: 10.1016/j.apcatb.2016.12.035

Yang, T. H., Huang, L. D., Harn, Y. W., Lin, C. C., Chang, J. K., Wu, C. I., et al. (2013). High density unaggregated Au nanoparticles on ZnO nanorod arrays function as efficient and recyclable photocatalysts for environmental purification. *Small* 9, 3169–3182. doi: 10.1002/smll.201300424

Yang, Z., Cheng, F., Dong, X., and Cui, F. (2015). Controllable *in situ* synthesis of $BiOBr_xI_{1-x}$solid solution on reduced graphene oxide with enhanced visible light photocatalytic performance. *RSC Advances* 5, 68151–68158. doi: 10.1039/c5ra08416d

Zhang, H., Lv, X., Li, Y., Wang, Y., and Li, J. (2010). P25-graphene composite as a high performance photocatalyst. *ACS Nano* 4, 380–386. doi: 10.1021/nn901221k

Zhang, J., Gu, H., Yang, X., Chen, M., Yang, Z., and Zhang, W. (2015). Large-scale synthesis of self-assembled ultralong cannonite nanobelt film as a visible-light photocatalyst. *RSC Adv.* 5, 8537–8543. doi: 10.1039/c4ra10916c

Zhao, H., Dong, Y., Jiang, P., Wang, G., Miao, H., Wu, R., et al. (2015). Light-Assisted Preparation of a ZnO/CdS nanocomposite for enhanced photocatalytic H_2 evolution: an insight into importance of *in situ* Generated ZnS. *ACS Sustain. Chem. Eng.* 3, 969–977. doi: 10.1021/acssuschemeng.5b00102

Zhao, X., Wu, Y., Yao, W., and Zhu, Y. (2007). Photoelectrochemical properties of thin Bi_2WO_6 films. *Thin Solid Films* 515, 4753–4757. doi: 10.1016/j.tsf.2006.11.017

Zhu, L. P., Liao, G. H., Bing, N. C., Wang, L. L., Yang, Y., and Xie, H. Y. (2010). Self-assembled 3D BiOCl hierarchitectures: tunable synthesis and characterization. *CrystEngComm* 12:3791. doi: 10.1039/c0ce00038h

Zhu, L., Wang, L., Bing, N., Li, P., Wang, L., Huang, C., et al. (2016). *In situ* synthesis of N-doped carbon nanotubes–BiOCl nanocomposites and their synergistic photocatalytic performance. *RSC Adv.* 6, 2926–2934. doi: 10.1039/c5ra24149a

Zhu, S., Dong, Y., Xia, X., Liu, X., and Li, H. (2016). Synthesis of Mo-doped TiO_2 nanowires/reduced graphene oxide composites with enhanced photodegradation performance under visible light irradiation. *RSC Adv.* 6, 23809–23815. doi: 10.1039/c5ra 24164b

Conflict of Interest Statement: The authors declare that the research was conducted in the absence of any commercial or financial relationships that could be construed as a potential conflict of interest.

frontiers in Chemistry

ORIGINAL RESEARCH
published: 19 September 2018
doi: 10.3389/fchem.2018.00415

Adsorption and Photocatalytic Processes of Mesoporous SiO_2-Coated Monoclinic $BiVO_4$

Duangdao Channei[1,2]*, *Auppatham Nakaruk*[3,4], *Wilawan Khanitchaidecha*[4,5], *Panatda Jannoey*[6] *and Sukon Phanichphant*[7]

[1] Department of Chemistry, Faculty of Science, Naresuan University, Phitsanulok, Thailand, [2] Research Center for Academic Excellence in Petroleum, Petrochemicals and Advanced Materials, Naresuan University, Phitsanulok, Thailand, [3] Department of Industrial Engineering, Faculty of Engineering, Naresuan University, Phitsanulok, Thailand, [4] Centre of Excellence for Innovation and Technology for Water Treatment, Naresuan University, Phitsanulok, Thailand, [5] Department of Civil Engineering, Faculty of Engineering, Naresuan University, Phitsanulok, Thailand, [6] Department of Biochemistry, Faculty of Medical Science, Naresuan University, Phitsanulok, Thailand, [7] Materials Science Research Center, Faculty of Science, Chiang Mai University, Chiang Mai, Thailand

The silicon dioxide (SiO_2)–coated bismuth vanadate ($BiVO_4$) composites as visible–driven–photocatalysts were successfully synthesized by the co–precipitation method. The effects of SiO_2 coating on the structure, optical property, morphology and surface properties of the composites were investigated by X–ray diffraction (XRD), UV–visible diffuse reflectance spectroscopy (DRS), transmission electron microscopy (TEM) and Brunauer–Emmette–Teller (BET) measurements. The photocatalytic activity of monoclinic $BiVO_4$ and $BiVO_4/SiO_2$ composites were evaluated according to the degradation of methylene blue (MB) dye aqueous solution under visible light irradiation. The SiO_2–coated $BiVO_4$ composites showed the enhancing photocatalytic activity approximately threefold in comparison with the single phase $BiVO_4$.

Keywords: composite materials, photocatalysis, $BiVO_4$, BET isotherms, SiO_2

OPEN ACCESS

Edited by:
Hongqi Sun,
Edith Cowan University, Australia

Reviewed by:
Priyabrat Mohapatra,
C. V. Raman College of Engineering, India
M. Nageeb Rashed,
Aswan University, Egypt

***Correspondence:**
Duangdao Channei
duangdaoc@nu.ac.th

Specialty section:
This article was submitted to Green and Sustainable Chemistry, a section of the journal Frontiers in Chemistry

Received: *09 March 2018*
Accepted: *23 August 2018*
Published: *19 September 2018*

Citation:
Channei D, Nakaruk A, Khanitchaidecha W, Jannoey P and Phanichphant S (2018) Adsorption and Photocatalytic Processes of Mesoporous SiO_2-Coated Monoclinic $BiVO_4$. Front. Chem. 6:415. doi: 10.3389/fchem.2018.00415

INTRODUCTION

Nowadays, the advanced oxidation process is known as an effective method for water purification and wastewater treatment. One of the most famous advanced oxidation process is heterogeneous photocatalysis; the contaminant (i.e., organic compounds) containing in the water and wastewater is finally degraded to carbon dioxide (Legrini et al., 1993; Mukherjee and Ray, 1999). This process can remove the organic contaminant perfectly and does not generate the second contaminant (i.e., sludge and other organic compounds) which are required the further treatment and disposal. According to the heterogeneous photocatalysis, the titanium dioxide (TiO_2) has been played a role as the important catalyst to promote the photocatalytic activity. Due to its wide band gap of 3.2 eV, the photocatalyst of TiO_2 is typically activated under the UV light (the wavelength $<$390 nm is required), which accounts for 45–50% of solar radiation (Linsebigler et al., 1995; Bahnemann et al., 2007; Devipriya et al., 2012). This theoretical fact becomes the limitation and non-cost-effectiveness of actual photocatalytic system for purifying the water at the site.

Another catalyst of monoclinic bismuth vanadate ($BiVO_4$) has been proposed to overcome the drawback of photocatalytic system using TiO_2 and together with enhance the photocatalytic activity during implementation. Since $BiVO_4$ has narrow band gaps of 2.4 to 2.8 eV (Kudo et al., 2001; Xie et al., 2006; Li et al., 2008), this photocatalyst can be activated by the visible light and consequences

the effective use of solar energy. However, the low specific surface area and poor surface textural property are the significant disadvantages of using $BiVO_4$ as the catalyst. Its low surface area and adsorption capacity cause the low efficiency of photocatalytic system for organic contaminant removal and also the long treatment period required. Therefore, the increase in specific surface area of $BiVO_4$ catalyst is necessary prior to imply the photocatalytic system to the actual wastewater.

Recently, alternative composite materials have been synthesized by combining metal oxide and porous materials (i.e., alumina, silica, zeolites, carbon black, charcoal) (Belessi et al., 2007; Wang et al., 2012; Xing et al., 2016) with the aim of improving the specific surface area, pore structure, and photocatalytic activity of catalysts (Gan et al., 2003; Kimura et al., 2003). For example, the enhancement of Ag–doped TiO_2 photocatalytic activity was suggested by adding the mesoporous SiO_2; the excellent efficiency of methyl orange (MO) removal was achieved by 2.5 h (Roldan et al., 2015). The increasing adsorption capacity of TiO_2 catalyst was observed when the catalyst was combined with SiO_2; the adsorption capacity was increased (Hu et al., 2012). The SiO_2 addition also enhance the separation rate of electron–hole pairs under UV excitation. Further, the deposition of gold nanoparticles (Au) on the porous SiO_2-WO_3 composite can enhance the methylene blue (MB) adsorption capacity; the adsorption capacity of Au–SiO_2-WO_3 was greater than SiO_2-WO_3 and WO_3 respectively (DePuccio et al., 2015). The complete MB removal was achieved by 300 min under visible light, and the fast kinetic of MB removal was found in Au–SiO_2-WO_3 catalyst, following by Au–WO_3 and WO_3 catalysts.

As all the above mentions, this study aimed to improve the surface morphology and photocatalytic activity of $BiVO_4$ catalyst by coating SiO_2. Various analytical techniques including X–ray diffraction (XRD), transmission electron microscopy (TEM), Brunauer–Emmett–Teller (BET) and UV–vis diffuse reflectance spectra (DRS) were used to clarify the better property of $BiVO_4$/SiO_2 composite rather than $BiVO_4$ and SiO_2. Further, the performance of $BiVO_4$/SiO_2 composites on wastewater treatment was preliminary studied in the batch test under visible light irradiation, and its performance was compared to the other two materials of $BiVO_4$ and SiO_2.

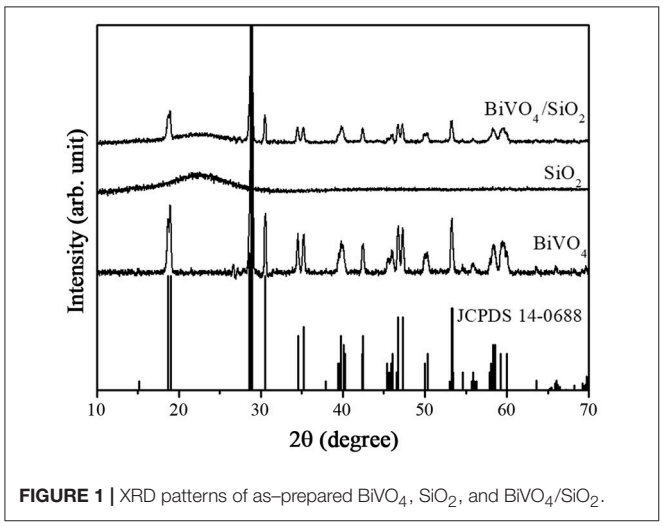

FIGURE 1 | XRD patterns of as–prepared $BiVO_4$, SiO_2, and $BiVO_4$/SiO_2.

EXPERIMENTAL PROCEDURE

All chemicals used were of analytical grade and were used as received without any further purification. The chemicals including tetraethyl orthosilicate (TEOS), bismuth (III) nitrate pentahydrate [$Bi(NO_3)_3{\cdot}5H_2O$], ammonium metavanadate (NH_4VO_3), methylene blue powder, sodium hydroxide pellet (NaOH), ammonia solution (28%) and nitric acid (37% HNO_3) were obtained from Sigma-Aldrich. All solutions were prepared with deionized water.

Preparation of SiO_2 Particles

SiO_2 particles were prepared by the sol–gel method. Ammonia solution (28%) was added in 100 mL of a mixed solution of absolute ethanol/DI water (80: 20 v/v) and stirred under ultrasonic dispersion for 60 min. Then, 20 mL of tetraethyl

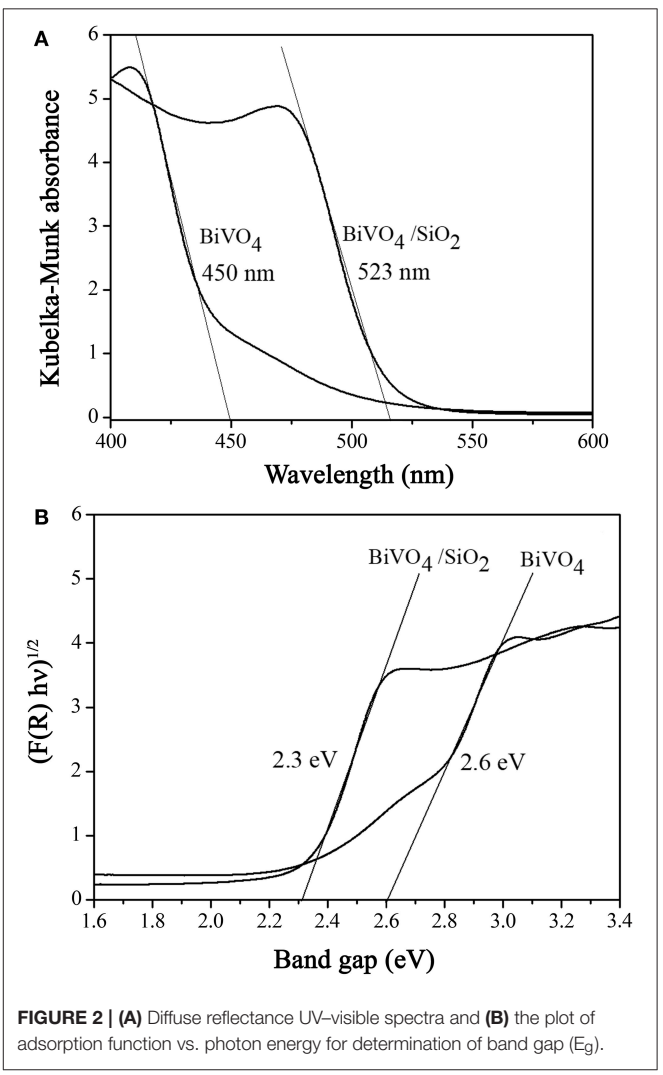

FIGURE 2 | (A) Diffuse reflectance UV–visible spectra and **(B)** the plot of adsorption function vs. photon energy for determination of band gap (E_g).

orthosilicate (TEOS) was added drop by drop to the mixed solution and stirred for 120 min at room temperature. After the reaction was homogenized, the fine particles were separated by centrifugation with typical rotating speed of 6,000 rpm for 15 min, washed by DI water and dried at 80°C for 24 h in a hot air oven. Fine particles of SiO_2 were obtained as a white powder following heat treatment at 500°C for 1 h in ambient.

Preparation of Monoclinic $BiVO_4$ and SiO_2-Coated $BiVO_4$ Composites

Monoclinic $BiVO_4$ were obtained by the co–precipitation method. Firstly, 12 mmol of bismuth (III) nitrate pentahydrate $[Bi(NO_3)_3{\cdot}5H_2O]$ and the same volume of ammonium metavanadate (NH_4VO_3) were dissolved in 100 mL of 2 M nitric acid (HNO_3) under vigorous stirring. The pH of the mixed solution was adjusted to 9 by adding 3 M sodium hydroxide (NaOH). The yellow precipitate was then separated by centrifugation at 6,000 rpm for 15 min, washed thoroughly with distilled water and ethanol and finally dried in a hot air oven at 80°C for 24 h. Crystalline monoclinic $BiVO_4$ was formed after calcination at 550°C for 4 h.

$BiVO_4$-coated SiO_2 composites were also prepared by the same method for comparison with an additional step of adding SiO_2 powder to 100 mL of 2 M HNO_3.

Photocatalytic Reaction

Photocatalytic activities of the $BiVO_4$, SiO_2 and $BiVO_4/SiO_2$ composites were evaluated through degradation of methylene blue (MB) dye as a model organic pollutant under visible light. A total of 0.20 g of photocatalyst was added to 100 mL MB aqueous solution (initial concentration $C_0 = 20$ ppm) under magnetic stirring in darkness for 60 min to achieve adsorption–desorption equilibrium. The system was irradiated by three 18 W halogen lamps (Essential MR, Philips, Thailand) to investigate photocatalytic degradation. Reduction of MB concentration over time (C_t) was recorded every 15 min by measuring the intensity change of the characteristic absorption peak at 664 nm using UV–vis double beam spectroscopy (UV−6100, Mapada).

Characterisation

Crystal phase and structure of the prepared samples were characterized by powder X–ray diffraction (XRD, Philips X'Pert MPD) using Cu K_α ($\lambda = 1.54056$ Å) radiation. Morphological changes in the composite materials were monitored by transmission electron microscopy (TEM, JSM−2010, JEOL). Brunauer–Emmett–Teller (BET) measurements (Adtosorb 1 MP, Quantachrome) were performed to compare the specific surface area of the $BiVO_4$ and $BiVO_4/SiO_2$ composites. Measurement of UV–vis diffuse reflectance spectroscopy (DRS UV–vis, Shimadzu UV−3101PC) was carried out at room temperature to detect reflectance and absorbance spectra.

RESULTS AND DISCUSSION

In **Figure 1**, the broad XRD peak at $2\theta = 22$–$23°$ corresponded to the amorphous SiO_2. The XRD pattern of $BiVO_4$ without SiO_2 was assigned to the standard monoclinic $BiVO_4$ (JCPDS no. 14–0688) (Gotić et al., 2005). After coating $BiVO_4$ with

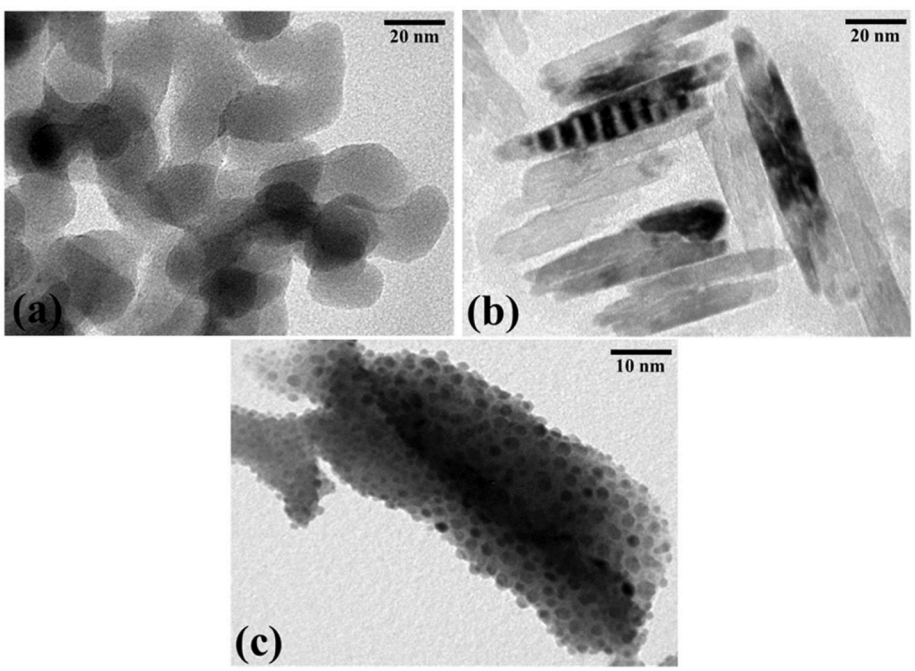

FIGURE 3 | TEM images of **(a)** SiO_2, **(b)** $BiVO_4$, and **(c)** SiO_2-coated $BiVO_4$.

SiO_2, the diffraction peaks matched well with the pure phase monoclinic $BiVO_4$ and no peaks of any other phases or impurities were recorded. However, the diffraction intensity of $BiVO_4$ decreased after coating SiO_2, because the amorphous substance had the negative effect on crystallinity. Alternatively, self–doped Si^{4+} ions in the $BiVO_4$ crystal structure might cause the decreasing crystallinity of $BiVO_4/SiO_2$ composites, and resulted in the broader peaks of the composite samples, which are similar to those reported by Phanichphant et al. (2016) for the binary composite CeO_2/SiO_2 photocatalyts and Kumar et al. for TiO_2/SiO_2 nanocomposites in solar cell applications (Arun Kumar et al., 2012).

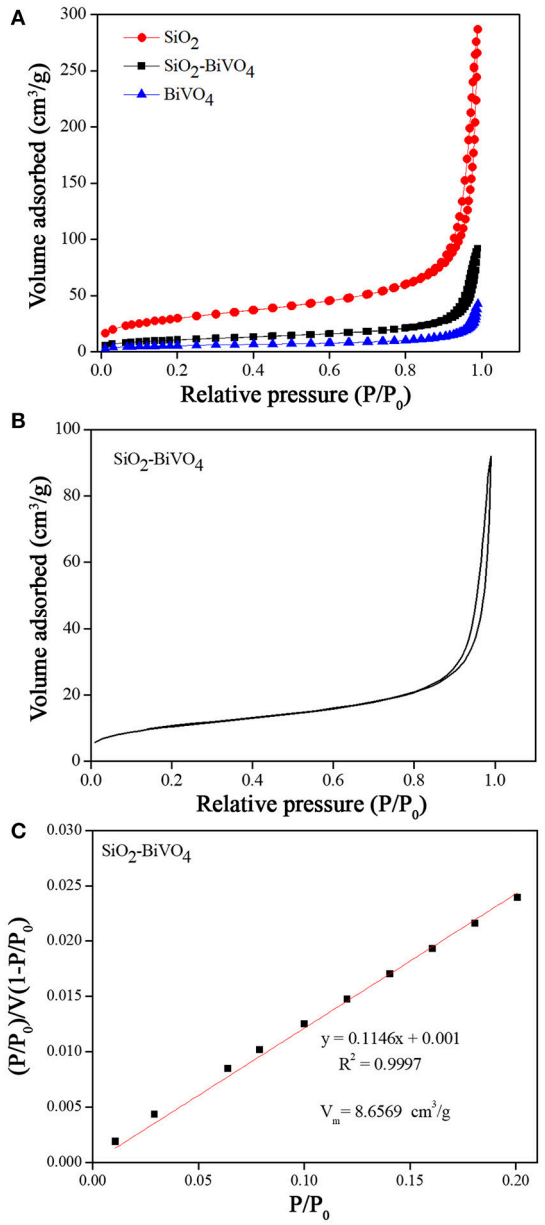

FIGURE 4 | (A), **(B)** N_2 adsorption-desorption isotherms, and **(C)** BET linear plot of relative pressure.

As shown in **Figure 2a**, the $BiVO_4$ demonstrated the absorption edge of the visible region at 450 nm, corresponding to the optical band gap (E_g) of 2.60 eV which was calculated by the Kubelka–Munk function (see **Figure 2b**) (Sirita et al., 2007). Compared to $BiVO_4/SiO_2$ composites, the value of the graph intercept was estimated at 2.30 eV, corresponding to the strong absorption edge in the visible region at 523 nm. The band gap energy of $BiVO_4$ decreased from 2.60 to 2.30 eV in the composite materials, due to the influence of Si^{4+} ions doping into the lattice of $BiVO_4$ which created the abundant doping energy levels. The estimated band gap values in this study was similar to those of $BiVO_4$ reported by Jiang et al. (2012), who prepared the $BiVO_4$ photocatalysts with different morphologies using the hydrothermal method. Liu et al. (2015) observed that the band gap energy of $BiVO_4/SiO_2$ catalyst estimated to be 2.32 eV, which was almost the same as that of calculate by this study.

The TEM images of SiO_2, $BiVO_4$ and $BiVO_4/SiO_2$ composites are presented in **Figure 3**. The SiO_2 image shows the aggregation of spherical–shaped particles with diameters ranging of 20–30 nm (**Figure 3a**), while **Figure 3b** shows the rod–like nanostructures of monoclinic $BiVO_4$ with the diameter of 10 nm and the length of 60 nm. Typical TEM images are used for characterizing the composite materials and proving the heterojunction formation between $BiVO_4$ and SiO_2, which demonstrated that the rod–like $BiVO_4$ core was covered by the SiO_2 particles growing on the surface (**Figure 3c**).

The N_2 adsorption-desorption isotherms (**Figure 4a**) show that the N_2 adsorption of $BiVO_4/SiO_2$ composites were relatively higher than that of the pure $BiVO_4$, however the value was much lower than that of the SiO_2. The specific surface areas of SiO_2, $BiVO_4/SiO_2$ composites, and $BiVO_4$ were found to be 106.9959, 37.6851, and 19.4964 m^2/g, respectively. In the meanwhile, the pore size was calculated by using the BJH method, and the results were 9.0316, 11.0776, and 11.8111 nm for SiO_2, $BiVO_4/SiO_2$, and $BiVO_4$ respectively (as summarized in **Table 1**). The surface area and pore size are positively related to the photocatalytic activity, therefore the photocatalytic activity of $BiVO_4/SiO_2$ composites were higher than that of pure $BiVO_4$. Even though the surface area of SiO_2 was higher than the $BiVO_4/SiO_2$ composite, the adsorption of pollutant by SiO_2 with high specific surface area have only the ability to transfer pollutants to alternative phases, but not completely get rid of them. Therefore, the photocatalytic process based on using the hydroxyl radicals is required in this study.

TABLE 1 | Surface properties of the prepared samples.

Sample	Specific surface area (m^2/g)	Average pore size diameter (nm)
SiO_2	106.9959	9.0316
$BiVO_4/SiO_2$	37.6851	11.0776
$BiVO_4$	19.4964	11.8111

Figure 4b shows the N_2 adsorption-desorption isotherms of $BiVO_4/SiO_2$ composites in the relative pressure (P/P_0) range 0.00–1.00. The curve exhibited Type IV isotherm characteristic with a small hysteresis loop at the relative pressure of 0.80–1.00. This indicated the existence of mesopores in the sample with the pore diameter ranging of 2–50 nm (Brunauer et al., 1940; Bae et al., 2010).

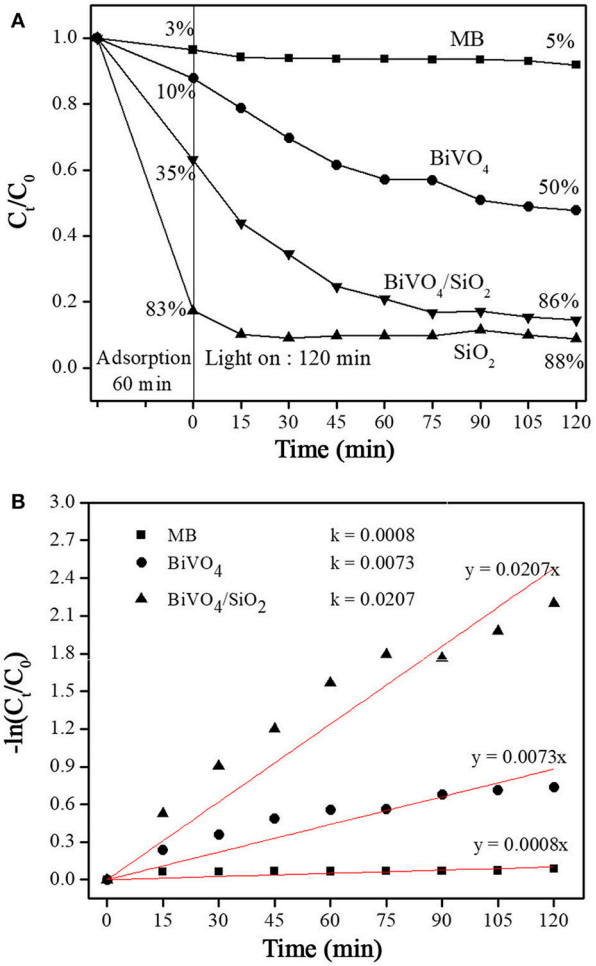

FIGURE 5 | MB concentration changes with irradiation time **(A)** C_t/C_0 and **(B)** $-\ln C_t/C_0$.

The information from the isotherm can be used to determine the specific surface area from the mathematical relations in Equation (1) and Equation (2) below (Itodo et al., 2010; Thommes et al., 2015)

$$\frac{P/P_0}{V(1-P/P_0)} = \frac{1}{V_m C} + \frac{(C-1)}{V_m C}\frac{P}{P_0} \quad (1)$$

where,

P_0, Initial pressure of N_2; P, Equilibrium pressure of N_2 adsorption; V_m, Monolayer capacity; V, Amount of N_2 adsorbed at standard temperature and pressure (STP).

$$\text{Specific Surface area} = \frac{V_m N_a \times A}{m \times 22400} \quad (2)$$

where,

A, Cross-sectional area of the adsorbed N_2; m, Adsorbate molecular weight; N_a, Avogadro's number.

The intercept and slope of the plot in **Figure 4c** were used to calculate the maximum volume of gas adsorbed at the monolayer (V_m), it was 8.6569 cm^3/g. The specific surface area was also calculated via the V_m value (see Equation 2). The result showed that the surface area of $BiVO_4/SiO_2$ composites was 37.6851 m^2/g.

Figure 5a presents the degradation efficiency of MB as a function of C_t/C_0 and visible irradiation time. The C_0 was the initial concentration of MB before irradiation and C_t was the MB concentration at the interval irradiation time (t, min). For using the SiO_2 as catalyst, the MB was removed of 83% under the dark adsorption, and only 5% of MB was further degraded under the visible light. For using the single phase monoclinic $BiVO_4$, the MB was removed around 10% under the dark adsorption, and 40% of MB was further degreased under the visible light irradiation. When the $BiVO_4/SiO_2$ composites was used, the MB removal efficiency reached 35 and 86% under

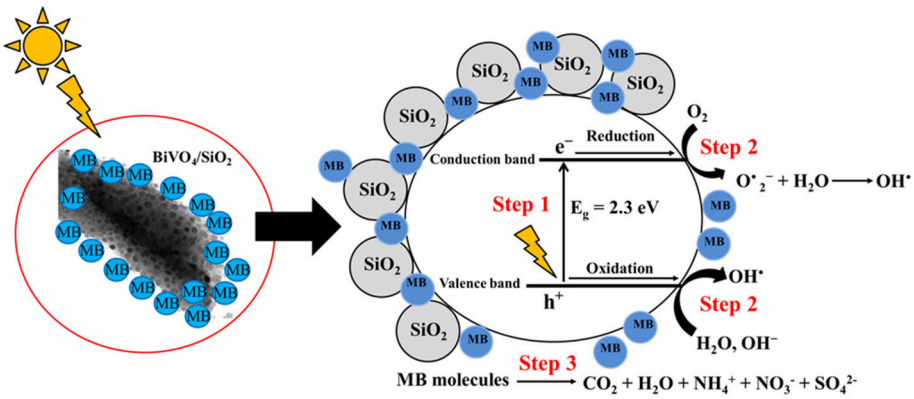

FIGURE 6 | The proposed mechanism of photogenerated charge carriers of $BiVO_4$ in $BiVO_4/SiO_2$ heterojunction.

the dark adsorption and visible light irradiation. As above explanation, the specific surface area of $BiVO_4/SiO_2$ composites were increased from $BiVO_4$, due to the SiO_2 coating. The increasing specific surface area resulted in the high adsorption of MB molecules during 60 min of the darkness, and then the adsorbed MB was continuously degraded by photocatalytic activity during visible light. These results illustrated that the photocatalytic activity of $BiVO_4$ was enhanced by coating the SiO_2 particles.

The kinetics of MB degradation was analyzed using the pseudo–first order model, which was given in Equation (3) (Yetim and Tekin, 2017). In **Figure 5b**, the correlation of–ln C_t/C_0 and t were positive with linear equation; the kinetic constant (k) were 0.0073 min^{-1} for $BiVO_4$ and 0.0207 min^{-1} for $BiVO_4/SiO_2$ composites. The kinetic constant of MB degradation using $BiVO_4/SiO_2$ composites was approximately threefold higher than that using the single phase $BiVO_4$.

$$-\ln(C_t/C_0) = kt \quad (3)$$

where k is the apparent rate constant of the pseudo–first order reaction (min^{-1}).

Since the photocatalytic degradation of dyes is associated with dye adsorption onto the surface of $BiVO_4/SiO_2$. Furthermore, photocatalytic degradation occurs at or near the surface of the catalyst rather than in the bulk solution. Thus the higher photocatalytic activity of $BiVO_4/SiO_2$ is consistent with the higher adsorption of MB on the surface of $BiVO_4/SiO_2$ photocatalyst. Mesoporous SiO_2 adsorbent enriches the MB molecules around the $BiVO_4$ surface as shown in **Figure 6** and the visible–light photocatalytic activity of the $BiVO_4$ interface in the composite materials is then excited to generate electrons (e–) and holes (h^+). Subsequently, photoexcited electrons in the valance band and hole in the conduction band of $BiVO_4$ react with oxygen, water and hydroxide ions to produce free superoxide radicals ($O_2^{-\bullet}$) and hydroxyl radicals ($OH^\bullet$) as the main active oxidizing species, which then react with MB molecules during the photocatalytic process (Lin et al., 2014; Zhou et al., 2014). The final products of MB aqueous solution photocatalytic degradation are oxidized to CO_2, H_2O, CO_2, NH_4^+, NO_3^-, and SO_4^{2-} (Houas et al., 2001; Luan and Hu, 2012).

CONCLUSIONS

$BiVO_4/SiO_2$ composites consisting of spherical SiO_2 particles coated on $BiVO_4$ nanorods were successfully prepared by co–precipitation. The composites exhibited higher photocatalytic activity compared to single monoclinic $BiVO_4$ by degrading MB under visible–light irradiation due to the greater surface area of mesoporous SiO_2. Fabrication of heterogeneous semiconductors using mesoporous materials can produce promising alternative photocatalysts for wastewater treatment under light irradiation by combining adsorption and photocatalytic processes.

AUTHOR CONTRIBUTIONS

DC designed and performed the experiments and wrote the manuscript. SP, AN advised the data analysis and edited manuscript. PJ and WK advised the data analysis. All authors reviewed the approved the manuscript.

ACKNOWLEDGMENTS

This work has been supported by grant from the National Research Council of Thailand (NRCT) under Grant No. R2561B075. The Office of the Higher Education Commission and the Thailand Research Fund (TRF) under Grant No. MRG6080097 is also acknowledged for financial support.

REFERENCES

Arun Kumar, D., Merline Shyla, J., and Xavier, F. P. (2012). Synthesis and characterization of TiO_2/SiO_2 nano composites for solar cell applications. *Appl. Nanosci.* 2, 429–436. doi: 10.1007/s13204-012-0060-5

Bae, Y. S., Snurr, R. Q., and Yazaydin, O. (2010). Evaluation of the BET method for determining surface areas of MOFs and zeolites that contain ultra-micropores. *Langmuir* 26, 5479–5483. doi: 10.1021/la100449z

Bahnemann, W., Muneer, M., and Haque, M. M. (2007). Titanium dioxide-mediated photocatalysed degradation of few selected organic pollutants in aqueous suspensions. *Catal. Today* 124, 133–148. doi: 10.1016/j.cattod.2007.03.031

Belessi, V., Lambropoulou, D., and Konstantinou, I. (2007). Structure and photocatalytic performance of TiO_2/clay nanocomposites for the degradation of dimethachlor. *Appl. Catal. B.* 73, 292–299. doi: 10.1016/j.apcatb.2006.12.011

Brunauer, S., Deming, L. S., Deming, W. E., Teller, E. (1940). On a theory of the van der waals adsorption of gases. *J. Am. Chem. Soc.* 62, 1723–1732. doi: 10.1021/ja01864a025

DePuccio, D. P., Botella, P., O'Rourke, B., and Landry, C. C. (2015). Degradation of methylene blue using porous WO_3, SiO_2–WO_3, and their Au-loaded analogs: adsorption and photocatalytic studies. *ACS Appl. Mater. Interfaces* 7, 1987–1996. doi: 10.1021/am507806a

Devipriya, S. P., Yesodharan, S., and Yesodharan, E. P. (2012). Solar photocatalytic removal of chemical and bacterial pollutants from water using Pt/TiO_2-coated ceramic tiles. *Int. J. Photoenergy* 1–8. doi: 10.1155/2012/970474

Gan, L., Chen, L., and Zhang, X. (2003). Preparation of silica aerogels by non-supercritical drying. *Acta Phys. Chim. Sin.* 19, 504–508. doi: 10.3866/PKU.WHXB20030605

Gotić, M., Musić, S., Ivand, M., Šoufek, M., and Popovi, S. (2005). Synthesis and characterisation of bismuth (III) vanadate. *J. Mol. Struct.* 744, 535–540. doi: 10.1016/j.molstruc.2004.10.075

Houas, A., Lachheb, H., Ksibi, M., Elaloui, E., Guillard, C., and Herrmann, J. (2001). Photocatalytic degradation pathway of methylene blue in water. *Appl. Catal. B* 31, 145–157. doi: 10.1016/S0926-3373(00)00276-9

Hu, S., Li, F., and Fan, Z. (2012). Preparation of SiO_2-coated TiO_2 composite materials with enhanced photocatalytic activity under UV Light. *Bull. Korean Chem. Soc.* 33, 1895–1899. doi: 10.5012/bkcs.2012.33.6.1895

Itodo, A. U., Itodo, H. U., Gafar, M. K. (2010). Estimation of specific surface area using langmuir isotherm method. *J. Appl. Sci. Environ. Manage.* 14, 141–145.

Jiang, H., Meng, X., Dai, H., Deng, J., Liu, Y., Zhang, L., et al. (2012). High performance porous spherical or octapod-like single-crystalline $BiVO_4$ photocatalysts for the removal of phenol and methylene blue under visible-light illumination. *J. Hazard. Mater.* 217–218, 92–99. doi: 10.1016/j.jhazmat.2012.02.073

Kimura, I., Kase, T., Taguchi, Y., and Tanaka, M. (2003). Preparation of titania/silica composite microspheres by sol–gel process in reverse suspension. *Mater. Res. Bull.* 38, 585–597. doi: 10.1016/S0025-5408(03)00027-8

Kudo, A., Tokunaga, S., Kato, H. (2001). Selective preparation of monoclinic and tetragonal BiVO4 with scheelite structure, and their photocatalytic properties. *Chem. Mater.* 13, 4624–4628. doi: 10.1021/cm0103390

Legrini, O., Oliveros, E., and Braun, A. M. (1993). Photochemical processes for water treatment. *Chem. Rev.* 93, 671–698. doi: 10.1021/cr00018a003

Li, G., Zhang, D., and Yu, J. C. (2008). Ordered Mesoporous BiVO4 through nanocasting: a superior visible light-driven photocatalyst. *Chem. Mater.* 20, 3983–3992. doi: 10.1021/cm800236z

Lin, H., Ye, H., Chen, S., and Chen, Y. (2014). One-pot hydrothermal synthesis of BiPO4/BiVO4 with enhanced visible-light photocatalytic activities for methylene blue degradation. *RSC Adv.* 4, 10968–10974. doi: 10.1039/c3ra45288c

Linsebigler, A. L., Lu, G., and Yates, J. T. (1995). Photocatalysis on TiO2 surfaces: principles, mechanisms, and selected results. *Chem. Rev.* 95, 735–758. doi: 10.1021/cr00035a013

Liu, B., Wang, Z., Zhou, S., and He, J. (2015). Synthesis and characterization of a novel $BiVO_4/SiO_2$ nanocomposites. *Mater. Lett.* 160, 218–221. doi: 10.1016/j.matlet.2015.07.104

Luan, J., and Hu, Z. (2012). Synthesis, property characterization, and photocatalytic activity of novel visible light-responsive photocatalyst Fe2BiSbO7. *Int. J. Photoenergy* 2012, 1–11.

Mukherjee, P. S., and Ray, A. K. (1999). Application photocatalysis for treatment of industrial waste water-A short review. *Chem. Eng. Technol.* 22, 253–260. doi: 10.1002/(SICI)1521-4125(199903)22:3<253::AID-CEAT253>3.0.CO;2-X

Phanichphant, S., Nakaruk, A., and Channei, D. (2016). Photocatalytic activity of the binary composite CeO_2/SiO_2 for degradation of dye. *Appl. Surf. Sci.* 387, 214–220. doi: 10.1016/j.apsusc.2016.06.072

Roldan, M. V., Castro, Y., Pellegri, N., and Duran, A. (2015). Enhanced photocatalytic activity of mesoporous SiO_2/TiO_2 sol–gel coatings doped with Ag nanoparticles. *J. Sol–Gel Sci. Technol.* 76, 180–194. doi: 10.1007/s10971-015-3765-6

Sirita, J., Phanichphant, S., and Meunier, F. C. (2007). Quantitative analysis of adsorbate concentrations by diffuse reflectance FT-IR. *Anal. Chem.* 79, 3912–3918. doi: 10.1021/ac0702802

Thommes, M., Kaneko, K., Neimark, A. V., Olivier, J. P., Reinoso, F. R., Rouquerol, J., et al. (2015). Performance of an activated carbon-ammonia adsorption refrigeration system. *Pure Appl. Chem.* 87, 1051–1069.

Wang, X. D., Shi, F., Huang, W., and Fan, C. M. (2012). Synthesis of high quality TiO2 membranes on alumina supports and their photocatalytic activity. *Thin Solid Films* 520, 2488–2492. doi: 10.1016/j.tsf.2011.10.023

Xie, B., Zhang, H., Cai, P., Qiu, R., and Xiong, Y. (2006). Simultaneous photocatalytic reduction of Cr(VI) and oxidation of phenol over monoclinic $BiVO_4$ under visible light irradiation. *Chemosphere* 63, 956–963. doi: 10.1016/j.chemosphere.2005.08.064

Xing, B., Shi, C., Zhang, C., Yi, G., Chen, L., Guo, H., et al. (2016). Preparation of TiO2/activated carbon composites for photocatalytic degradation of RhB under UV light irradiation. *J. Nanomater.* 2016, 1–10. doi: 10.1155/2016/8393648

Yetim, T., and Tekin, T. (2017). A kinetic study on photocatalytic and sonophotocatalytic degradation of textile dyes, Period. *Polytech. Chem. Eng.* 61, 102–108.

Zhou, P., Yu, J. G., and Jaroniec, M. (2014). All-solid-state Z-scheme photocatalytic systems. *Adv. Mater.* 26, 4920–4935. doi: 10.1002/adma.201400288

Conflict of Interest Statement: The authors declare that the research was conducted in the absence of any commercial or financial relationships that could be construed as a potential conflict of interest.

frontiers in Chemistry

ORIGINAL RESEARCH
published: 20 December 2018
doi: 10.3389/fchem.2018.00632

Catalytic and Photocatalytic Nitrate Reduction Over Pd-Cu Loaded Over Hybrid Materials of Multi-Walled Carbon Nanotubes and TiO_2

Cláudia G. Silva, Manuel F. R. Pereira, José J. M. Órfão, Joaquim L. Faria and Olívia S. G. P. Soares*

Laboratory of Separation and Reaction Engineering-Laboratory of Catalysis and Materials (LSRE-LCM), Faculdade de Engenharia, Universidade do Porto, Porto, Portugal

TiO_2 and carbon nanotube-TiO_2 hybrid materials synthesized by sol-gel and loaded with 1%Pd−1%Cu (%*wt*.) were tested in the catalytic and photocatalytic reduction of nitrate in water in the presence of CO_2 (buffer) and H_2 (reducing agent). Characterization of the catalysts was performed by UV-Vis and fluorescence spectroscopy, X-ray diffraction, temperature programed reduction, N_2 adsorption, and electron microscopy. The presence of light produced a positive effect in the kinetics of nitrate removal. Higher selectivity toward nitrogen formation was observed under dark condition, while the photo-activated reactions showed higher selectivity for the production of ammonium. The hybrid catalyst containing 20 %wt. of carbon nanotubes shows the best compromise between activity and selectivity. A mechanism for the photocatalytic abatement of nitrate in water in the presence of the hybrid materials was proposed, based in the action of carbon nanotubes as light harvesters, dispersing media for TiO_2 particles and as charge carrier facilitators.

Keywords: photocatalysis, catalytic reduction, nitrate, titanium dioxide, carbon nanotubes, palladium, copper

OPEN ACCESS

Edited by:
Zhimin Ao,
Guangdong University of Technology, China

Reviewed by:
Priyabrat Mohapatra,
C. V. Raman College of Engineering, India
Miguel Angel Centeno,
Instituto de Ciencia de Materiales de Sevilla (ICMS), Spain

****Correspondence:***
Cláudia G. Silva
cgsilva@fe.up.pt

Specialty section:
This article was submitted to Green and Sustainable Chemistry, a section of the journal Frontiers in Chemistry

Received: *01 August 2018*
Accepted: *05 December 2018*
Published: *20 December 2018*

Citation:
Silva CG, Pereira MFR, Órfão JJM, Faria JL and Soares OSGP (2018) Catalytic and Photocatalytic Nitrate Reduction Over Pd-Cu Loaded Over Hybrid Materials of Multi-Walled Carbon Nanotubes and TiO_2. Front. Chem. 6:632. doi: 10.3389/fchem.2018.00632

INTRODUCTION

Nitrate is a naturally occurring ion that is part of the nitrogen cycle, in which nitrogen species are switched between organisms and the environment. The increasing use of inorganic nitrogenous fertilizers, the disposal of wastes (mainly from oxidation of nitrogenous waste products in human and animal excreta) and changes in land use are the main causes accounting for the progressively increasing levels of this pollutant in groundwater supplies. Nitrate ion (NO_3^-) is the stable form of combined nitrogen for oxygenated systems and is potentially hazardous for humans, since it can be transformed into nitrite in the human body, which may cause the blue baby syndrome, being also a precursor of carcinogenic nitrosamines (Kapoor and Viraraghavan, 1997). Moreover, it may cause the eutrophication of rivers and lakes. The maximum contaminant level in drinking water of nitrogen species as nitrate, nitrite, and ammonium is 50, 0.5, and 0.5 mg/L, respectively (EU Water Framework Directive[1]).

[1]EU Water Framework Directive (2000). Available online at: http://ec.europa.eu/environment/water/water-framework/index_en.html (Accessed 2018).

The removal of nitrate from water constitutes a great challenge to safeguarding drinking water resources of suitable quality. In this context, a great effort has been put in the development of water technologies capable to address the environmental and health concerns. Conventional methods are based in physical-chemical treatment processes (reverse osmosis, ion exchange, and electrodialysis) and biological denitrification.

Heterogeneous catalytic systems like catalytic and photocatalytic reduction of nitrate have been shown to be promising processes compared to conventional treatments (Sá et al., 2009; Soares et al., 2011a, 2014; Luiz et al., 2012; Shand and Anderson, 2013). Catalytic nitrate reduction occurs by consecutive and parallel reactions where nitrate is reduced to nitrite, which is converted to ammonium, as undesired by-product, and to nitrogen, as desired product. The main issue of this process is the selectivity toward nitrogen, which is often compromised. Bimetallic catalysts composed by a noble metal (Pd, Pt, or Rh) and a promoter metal (Cu, Sn, or In) supported on different materials are the most used for catalytic hydrogenation of nitrate (Soares et al., 2009; Calvo et al., 2010; Marchesini et al., 2010; Wada et al., 2012), although monometallic catalysts also present some activity depending on the support (Barrabés et al., 2010; Anderson, 2011; Devadas et al., 2011). Pd-Cu catalysts are normally the most efficient, Pd-Sn and Pd-In also presenting good performances (Martínez et al., 2017). In the case of photocatalytic reduction, besides the type of metal catalysts, several other conditions such as the catalyst support, the pH of the solution, the irradiation source, nature of the reducing agent or electron donor (hole scavenger) also affect the performance of the process. H_2 and CO_2 are usually used in catalytic reduction reactions, in which H_2 serves as reductant and CO_2 as buffer (Prusse et al., 2000). In the case of the photo-assisted catalytic process, oxalic acid, formic acid, or methanol are the most used hole scavengers (Zhang et al., 2005; Doudrick et al., 2013).

Titanium dioxide-based materials are the most widely used catalysts for the photocatalytic reduction of nitrate, the bimetallic Pd-Cu/TiO_2 and Pt-Cu/TiO_2 being the ones showing most promising results. On the other hand, Pd-Cu catalysts supported on carbon materials and also in metal oxides are the most used for nitrate catalytic reduction. TiO_2-based catalysts are normally highly active for nitrate removal, yet, due to their capacity to drive hydrogenation, low nitrogen selectivity is reached (Sá et al., 2005). It has been reported that the activity of Pd-Cu bimetallic catalysts supported on carbon materials was higher than the same Pd-Cu catalyst supported on a metal oxide, such as TiO_2, Al_2O_3, SiO_2, or ZrO_2, at the same operating conditions, due to their surface chemistry and higher metals dispersion (Sakamoto et al., 2006; Soares et al., 2011a). Moreover, the coupling of carbon nanotubes with TiO_2 has proved to induce a positive effect in the activity and selectivity of Pd-Cu catalysts for the catalytic reduction of nitrate into N_2 (Soares et al., 2011a).

Following the previous findings, in the present work we explored the synergies between carbon nanotubes (CNT) and titanium dioxide in both catalytic and photocatalytic reduction of nitrate in water. For that purpose, hybrid materials of TiO_2 with different CNT contents, and loaded with 1%Pd and 1%Cu (wt.%) were evaluated as catalysts. Hydrogen and carbon dioxide were used as reducing and pH buffer agents, respectively. The materials were tested under the same experimental conditions, the only difference between the two processes being the introduction of a near-UV to visible light source in the case of the photocatalytic reactions.

EXPERIMENTAL

Catalysts Preparation

Multi-walled carbon nanotubes synthesized by catalytic decomposition of CH_4 were purchased from Shenzhen Nanoport Co. Ltd (purity > 95%, diameter < 10 nm; length = 5–15 μm). TiO_2 and CNT–TiO_2 composite catalysts were prepared through an acid-catalyzed sol–gel procedure, as described elsewhere (Silva and Faria, 2010). Briefly, TiO_2 was prepared by dissolving $Ti(OC_3H_7)_4$ (Aldrich 97%) in ethanol. The solution was magnetically stirred for 30 min, and then nitric acid (Fluka 65%) was added.

For the composite catalysts preparation, a certain amount of CNT was added to the $Ti(OC_3H_7)_4$ ethanol solution. The mixture was kept stirring until a homogenous gel was formed. The gel was left aging in air for 5 days. The resulting material was then crushed into a fine powder (particle size < 100 μm). The powders were calcined at 400°C under a flow of N_2 for 2 h to obtain TiO_2 or CNT–TiO_2 hybrid materials. Catalysts were labeled as XCNT–TiO_2, where X (5, 10, 20, 50, 70, and 90) corresponds to the weight percentage of CNT in the material.

The monometallic (Pd) and bimetallic (Pd-Cu) catalysts were prepared by incipient wetness impregnation and co-impregnation, respectively. Briefly, aqueous solutions containing the proper mass of the corresponding salts [$PdCl_2$, Alfa Aesar 99.9%; $Cu(NO_3)_2$, Riedel-de Haen 99%] were added dropwise to TiO_2 and CNT-TiO_2 materials. In the case of the bimetallic catalyst, the materials were co-impregnated with a solution containing both precursor salts. The palladium and copper contents were fixed at 1%Pd-1%Cu and 1%Pd (weight percentages). After impregnation, the metal-loaded materials were dried in an oven at 100°C for 24 h. Then, the catalysts were heat treated under a nitrogen flow at 200°C for 1 h. At the end of this period, the gas stream was switched to hydrogen for 3 h to promote metals reduction. Finally, the materials were left to cool down to room temperature under a nitrogen flow.

Catalysts Characterization

Powder X-ray Diffraction (XRD) analysis was performed on a Philips X'PertMPD diffractometer (Cu-Ka = 0.15406 nm). The Brunauer-Emmett-Teller (BET) specific surface area (S_{BET}) was determined from N_2 adsorption-desorption isotherms at 196°C, in a Quantachrome Nova 4200e apparatus. Temperature programmed reduction (TPR) was carried out in an AMI-200 (Altamira Instruments) system. The H_2 consumption was followed by a thermal conductivity detector (TCD) and by a mass spectrometer (Dymaxion 200 amu, Ametek). Transmission electron microscopy (TEM) micrographs were obtained using a LEO 906E microscope operating with an accelerating voltage of 120 kV. Diffuse reflectance (DR) UV-Vis spectra of the powder samples were recorded on a JASCO V-560 UV-Vis spectrophotometer, equipped with an integrating sphere attachment (JASCO ISV-469). The

reflectance spectra were converted by the instrument software (JASCO) to equivalent absorption Kubelka–Munk units. Steady-state photoluminescence (PL) spectra were recorded at room temperature on a JASCO FP-8300 spectrofluorometer equipped with a 150 W Xe lamp. The morphology and elemental mapping of the materials was obtained by SEM/EDXS analysis using a FEI Quanta 400FEG ESEM/EDAX Genesis X4M instrument.

Catalytic and Photocatalytic Nitrate Reduction Experiments

The catalytic and photocatalytic experiments were carried out in a glass cylindrical reactor. Initially, 190 mL of deionised water and 100 mg of catalyst were fed into the reactor. When used, a gas mixture of H_2 and CO_2 [1:1 flow rate = 200 cm^3 (STP) min^{-1}] was passed through the reactor to remove the dissolved oxygen; CO_2 acts as pH buffer (pH = 5.5). A Heraeus TQ 150 medium pressure mercury vapor lamp (λ_{exc} = 254, 313, 365, 436, and 546 nm) was used as radiation source. The lamp was located axially in the reactor and held in a quartz immersion tube. A DURAN® glass jacket was used as water circulating cooling system (temperature maintained at 25°C) and as a filter for cutting-off low wavelength UV lines and letting pass radiation in the near-UV to visible light range ($\lambda_{exc} \geq$ 365 nm). Before turning illumination on, the solution was magnetically stirred in the dark for 15 min. After that period, 10 mL of a nitrate solution, prepared from $NaNO_3$ (Sigma-Aldrich 99%), was added to the reactor, in order to obtain an initial NO_3^- concentration of 100 mg L^{-1}. The first sample was taken out just before the light was turned on, in order to determine the initial nitrate concentration in solution. The catalytic (dark) experiments were carried out under the same experimental conditions, but in the absence of light.

Samples were withdrawn regularly from the reactor, and centrifuged before determination of NO_3^-, NO_2^-, and NH_4^+ concentrations. NO_3^- and NO_2^- were simultaneously determined by HPLC using a Hitachi Elite Lachrom system equipped with a diode array detector. The stationary phase was a Hamilton PRP-X100 column (150 × 4.1 mm) working at room temperature, under isocratic conditions. The mobile phase was a solution of 0.1 M NaCl:CH_3OH (45:55). The concentration of NH_4^+ was determined by potentiometry.

Palladium and copper leaching was assessed after each experiment by atomic absorption spectrometry (UNICAM 939/959), the absence of metals (within the experimental error) being confirmed for all the cases.

Reproducibility tests were performed for selected experiments, the results being in agreement with a maximum error of about 2.5%. NO_3^- conversion and the selectivity to NO_2^- and NH_4^+ were calculated as described elsewhere (Soares et al., 2014).

RESULTS AND DISCUSSION

Catalysts Characterization

XRD patterns of neat CNT, Pd-Cu/TiO_2, and Pd-Cu/20CNT-TiO_2 are displayed in **Figure 1**. Typical (002) and (100) diffraction lines are evident in the XRD pattern of CNT. XRD

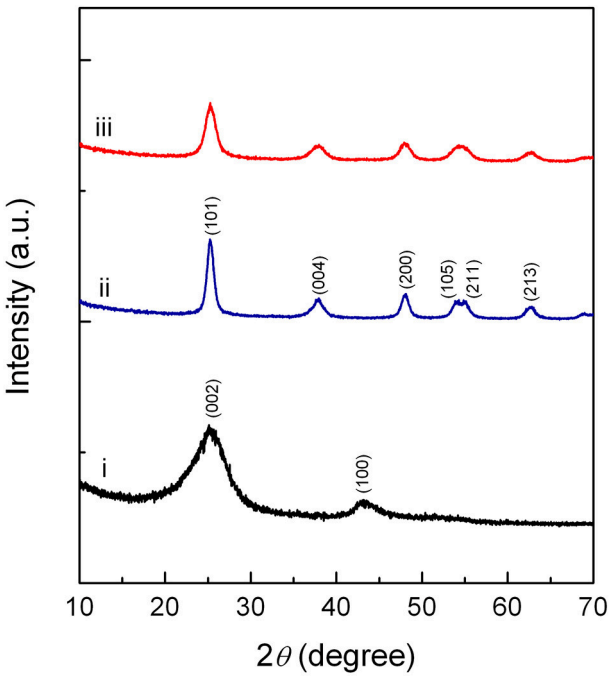

FIGURE 1 | X-ray diffraction patterns of neat CNT (i), Pd-Cu/TiO_2 (ii), and Pd-Cu/20CNT-TiO_2 (iii).

analysis of TiO_2 and CNT-TiO_2 composites revealed that only anatase phase is present in neat TiO_2 and composite catalysts. The XRD patterns of the Pd-Cu loaded CNT–TiO_2 materials are very similar to the one of Pd-Cu/TiO_2, with the CNT contribution hardly been identified. The Cu and Pd phases were not detected by XRD, which must be related to the low metal percentages (1%wt.). Anatase crystallites of 8.5 nm average size were found for neat TiO_2, as determined by the Scherrer equation and confirmed by TEM (**Figure 2a**). The sizes of the anatase crystallites present at the composite catalysts decreased with increasing carbon content, suggesting that CNT may act as dispersing medium for TiO_2 particle precursors during the crystallization process (**Table 1**).

The BET surface areas (S_{BET}) of TiO_2 and CNT-TiO_2 materials are listed in **Table 1**. Materials with lower carbon content, namely 5CNT–TiO_2 and 10CNT–TiO_2 composites, showed surface areas lower than the ones estimated through the mass composition of the composites ($S_{BET,calc}$) and even lower than for neat TiO_2. These results indicate that the presence of low amounts of CNT induces the formation of big TiO_2 crystallite agglomerates, therefore decreasing the surface area of the composite catalyst (**Figure 2b**).

With the carbon content increasing up to 20% (20CNT–TiO_2), the presence of a larger amount of CNT seems to prevent TiO_2 particles from agglomerating, thus increasing the surface area, which was even higher than the calculated ($S_{BET,calc}$). This was confirmed by TEM (**Figure 2c**), where TiO_2 particles of very small dimensions can be observed surrounding the sidewalls of CNT. In the case of the composite with

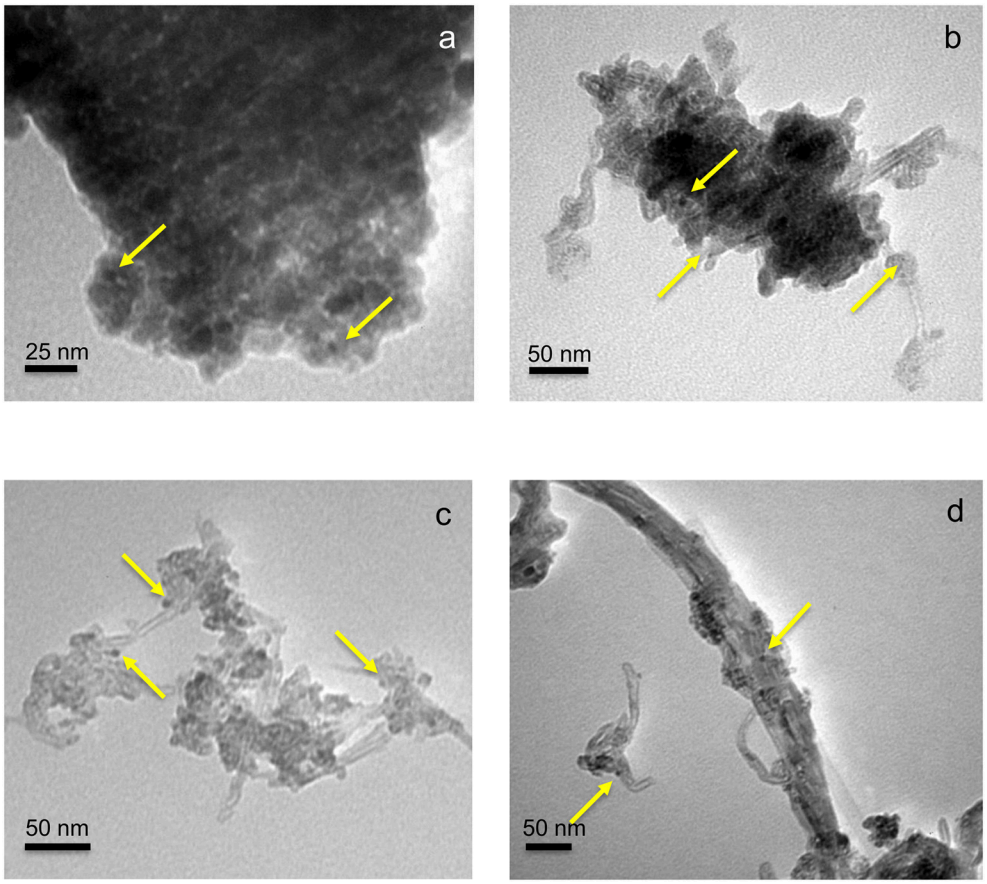

FIGURE 2 | TEM micrographs of TiO_2 **(a)**, 5CNT-TiO_2 **(b)**, 20CNT-TiO_2 **(c)**, and 70CNT-TiO_2 **(d)** loaded with 1% Cu and 1% Pd (*wt.* %). The arrows indicate the presence of metal nanoparticles.

similar amounts of TiO_2 and CNT phases (50CNT-TiO_2), the values for S_{BET} and $S_{BET,calc}$ were similar. Nevertheless, a further increase on the amount of CNT revealed to have a detrimental effect on the surface area of the resulting composites. A decrease in the S_{BET} in relation to the calculated values of 15 and 40% was observed for 70CNT-TiO_2 and 90CNT-TiO_2 materials, respectively, which may be attributed to the formation of CNT bundles decreasing the accessible surface area, as could be visualized by TEM for 70CNT-TiO_2 (**Figure 2d**). Due to the low amount of metals used, the textural properties of the metal-loaded catalysts remained practically unchanged compared to the pristine supports. The presence of metal particles of very small dimensions (lower than 10 nm) loaded on the TiO_2-based materials could be observed by TEM (**Figure 2**).

SEM-EDXS analysis of Pd-Cu/TiO_2 (**Figure 3a**) and Pd-Cu/20CNT-TiO_2 (**Figure 3b**) revealed that Pd and Cu nanoparticles are well dispersed in the catalysts, with no apparent prevalence of one of the metals.

The carbon content of the CNT-TiO_2 composites determined by TG analysis (C_{TG}) agrees fairly well with the nominal percentage, indicating negligible gasification of CNT during the calcination step (**Table 1**).

TABLE 1 | Surface area, carbon content, and dimensions of the anatase crystallites of TiO_2 and CNT-TiO_2 composites.

Catalyst	S_{BET} ($m^2\ g^{-1}$)	$S_{BET,calc}$ ($m^2\ g^{-1}$)	C_{TG} (%)	d_A (nm)
TiO_2-SG	107	–	–	8.5
CNT	185	–	–	-
5CNT-TiO_2	70	110	3.5	11.2
10CNT-TiO_2	94	113	7.6	9.4
20CNT-TiO_2	131	120	17	8.3
50CNT-TiO_2	147	143	46	7.2
70CNT-TiO_2	111	130	71	6.5[a]
90CNT-TiO_2	104	174	86	*n.d.*

[a] *Determined by TEM; n.d., not determined.*

Figure 4 shows the TPR profiles for both TiO_2 and 20CNT-TiO_2 materials, which were obtained before heat-treating the metal salt-loaded supports. Both materials show a reduction peak centered at 150°C, assigned to the reduction of Cu oxides promoted by the presence of Pd (Soares et al., 2011a). The thermal treatment under

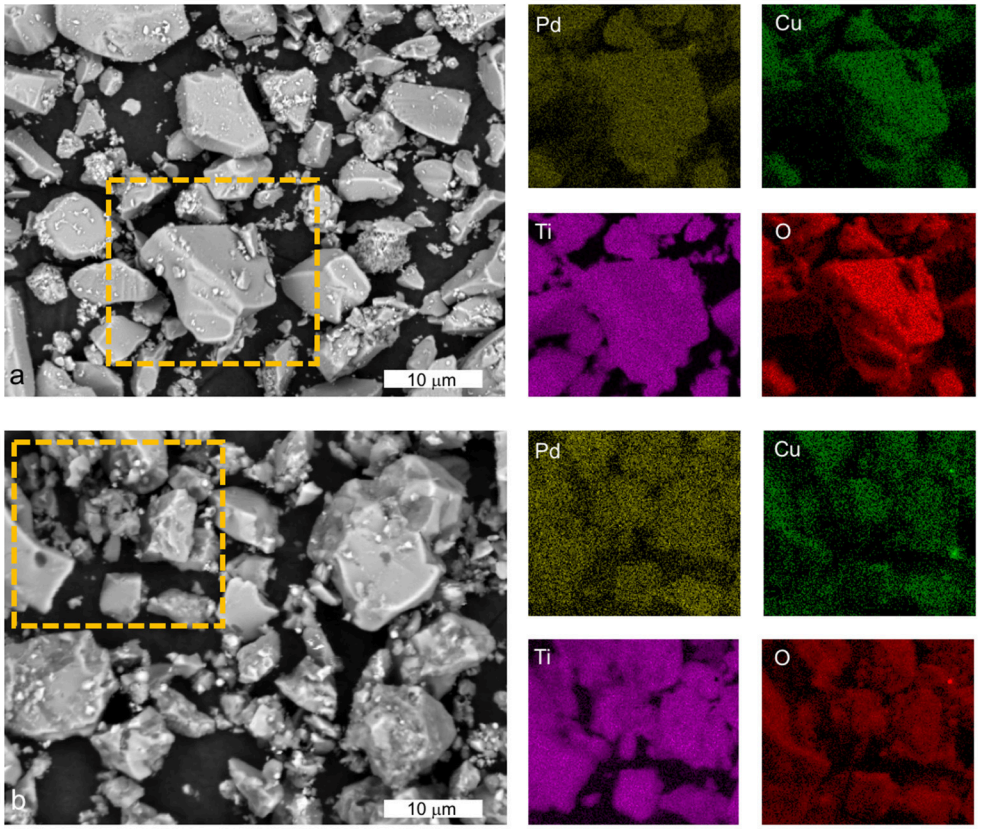

FIGURE 3 | SEM-EDX analysis of Pd-Cu/TiO_2 **(a)** and Pd-Cu/20CNT-TiO_2 **(b)** with the respective elemental mapping for Pd, Cu, Ti, and O in the selected regions (dashed rectangle).

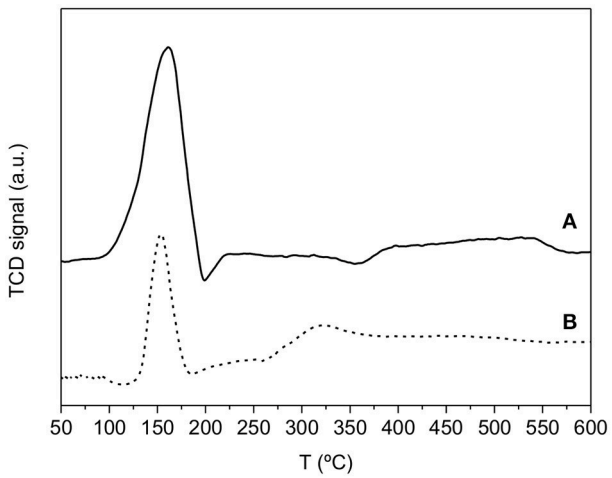

FIGURE 4 | TPR profiles of Pd-Cu loaded on TiO_2 **(A)** and on 20CNT-TiO_2 **(B)**.

H_2 should produce Pd and Cu particles in the reduced form, i.e., Pd^0 and Cu^0 (Soares et al., 2010, 2011a). Similar results were obtained for the remaining CNT-TiO_2 composite materials.

DR UV-Vis analysis of Pd-Cu/TiO_2 (**Figure 5A**) shows the TiO_2 characteristic absorption band at wavelength below 400 nm, a band peaking at c.a. 480 nm attributed to the presence of Pd and a broad absorption band rising from 550 nm due to the occurrence of Cu species (López et al., 2009; Wu et al., 2009; Soares et al., 2014).

As expected, the presence of CNT led to a rise of light absorption in the visible spectral region, increasing with the CNT content on the composite catalysts up to a CNT load of 50 wt.%. This behavior has been attributed not only to the capacity of CNT to absorb visible light but also to an increment of surface electronic species availability and mobility in the composite catalysts due to the introduction of CNT, as already reported in previous studies (Silva and Faria, 2010; Dai et al., 2014). A further increase in the CNT content did not produce any effect on the optical absorption of the composite materials. Moreover, the absorption peaks of the metal species could not be identified in the UV-Vis spectra of the composite materials, which may be attributed to a higher dispersion of the metal particles when supported on the composite materials.

The photoluminescence (PL) spectra were performed for having an insight in the behavior of light-generated electronic species in photocatalysts, since PL emission results from the recombination of electrons and holes. The PL emission spectra

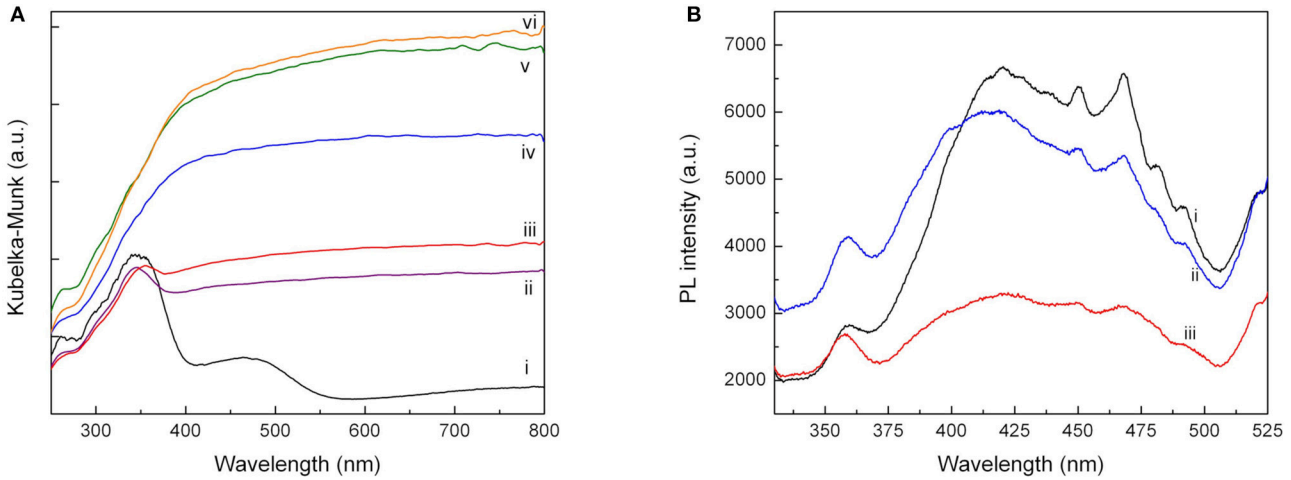

FIGURE 5 | (A) Diffuse reflectance UV-Vis spectra of Pd-Cu-loaded TiO_2 (i); 5CNT-TiO_2 (ii); 10CNT-TiO_2 (iii); 20CNT-TiO_2 (iv); 50CNT-TiO_2 (v); CNT (vi); **(B)** PL spectra of neat TiO_2 (i), Pd-Cu/TiO_2 (ii) and Pd-Cu/20CN-TiO_2 (iii).

of the pure neat TiO_2 and Pd-Cu loaded TiO_2 and 20CNT-TiO_2 materials excited at 280 nm are shown in **Figure 5B**. The PL signal observed for neat TiO_2 can be attributed to the transition of electrons from the oxygen vacancies to TiO_2 valence band (Tahir et al., 2017). After loading TiO_2 with Pd and Cu, an increase in the PL intensity was observed in the range from 330 to 400 nm, which may be attributed to the higher availability of photoexcited electrons in the bimetallic catalyst. Yet, a decrease in the PL signal intensity in the 400–525 nm range is observed, meaning that electron-hole recombination was decreased by the presence of the metal nanoparticles. Pd-Cu/20CNT-TiO_2 shows a very significant decrease in the PL intensity as compared with bare and metal loaded TiO_2, indicating highly efficient inhibition of charge carriers recombination and suggesting the existence of electronic synergies between the metals and the hybrid CNT-TiO_2 material (Zhang et al., 2012).

Catalytic and Photocatalytic Nitrate Reduction

TiO_2 and CNT-TiO_2 composites loaded with 1%Pd and 1%Cu (wt.%) were used for catalytic and photocatalytic reduction of nitrate in aqueous suspensions. Monometallic Pd-TiO_2 was used for comparison purposes. H_2 and CO_2 were continuously added to the reaction media, acting as reducing agent and pH buffer, respectively. The materials were tested under the same experimental conditions, the only difference between the two processes being the introduction of a near-UV to visible light source in the case of the photocatalytic reactions.

The performances of the different catalysts for the (dark) catalytic reduction process are presented in **Figure 6A**. Very low nitrate conversion (4%) was achieved using the monometallic Pd-TiO_2 catalyst, the presence of Cu being fundamental for the reaction to occur. Moreover, as expected, it can be observed that the support has a crucial influence on the performance of the bimetallic catalysts.

In the case of the catalytic reduction process, Pd-Cu/TiO_2 was the most efficient catalyst in terms of the kinetics of nitrate removal, with total nitrate conversion being achieved at the end of 90 min of reaction. Similar kinetic behavior was observed for nitrate reduction reactions using the composite materials with a CNT load (Y) of 5, 10, and 20%, leading to total nitrate removal at the end of 120 min of reaction. For higher CNT loads, a progressive detrimental effect in the kinetics of nitrate removal has been observed. Nitrate conversions of 95, 79, and 27% have been obtained at the end of 240 min when using composites with Y = 50, 70, and 90%, respectively. For the Pd-Cu/CNT catalyst only 12% nitrate removal was achieved at the end of the catalytic run.

In general, the presence of light promotes a positive effect in nitrate removal (**Figure 6B**). As in the case of the (dark) catalytic process, the simultaneous presence of Pd and Cu was a *sine qua non* condition for nitrate conversion to occur. The composite material with the lowest CNT content (Y = 5%) produced a decrease in the efficiency of nitrate abatement compared to Pd-Cu/TiO_2. Yet, a further increase in the CNT load up to Y = 20% lead to a rise in the rate of nitrate removal. For the composites with higher CNT content (Y = 50, 70, and 90%) a progressive loss in the efficiency toward NO_3^- conversion was observed.

The conversion of nitrate at 60 min of reaction was calculated in order to get a better understanding of the effect of CNT load in the kinetics of NO_3^- removal by both catalytic and photocatalytic routes (**Figure 6C**). It is notorious that the amount of CNT plays a role in the efficiency of the composite materials. As already mentioned, composite materials underperformed TiO_2 in catalytic nitrate reduction with a decrease in the nitrate conversion with increasing CNT load. Yet, for the photocatalytic process a positive effect was observed using 10CNT-TiO_2 and, in particular, 20CNT-TiO_2 comparing with the experiments using TiO_2 as support. On the other hand, the bimetallic catalyst supported on 20CNT-TiO_2 promotes total conversion of nitrate at 60 min of reaction. Reutilization tests were performed

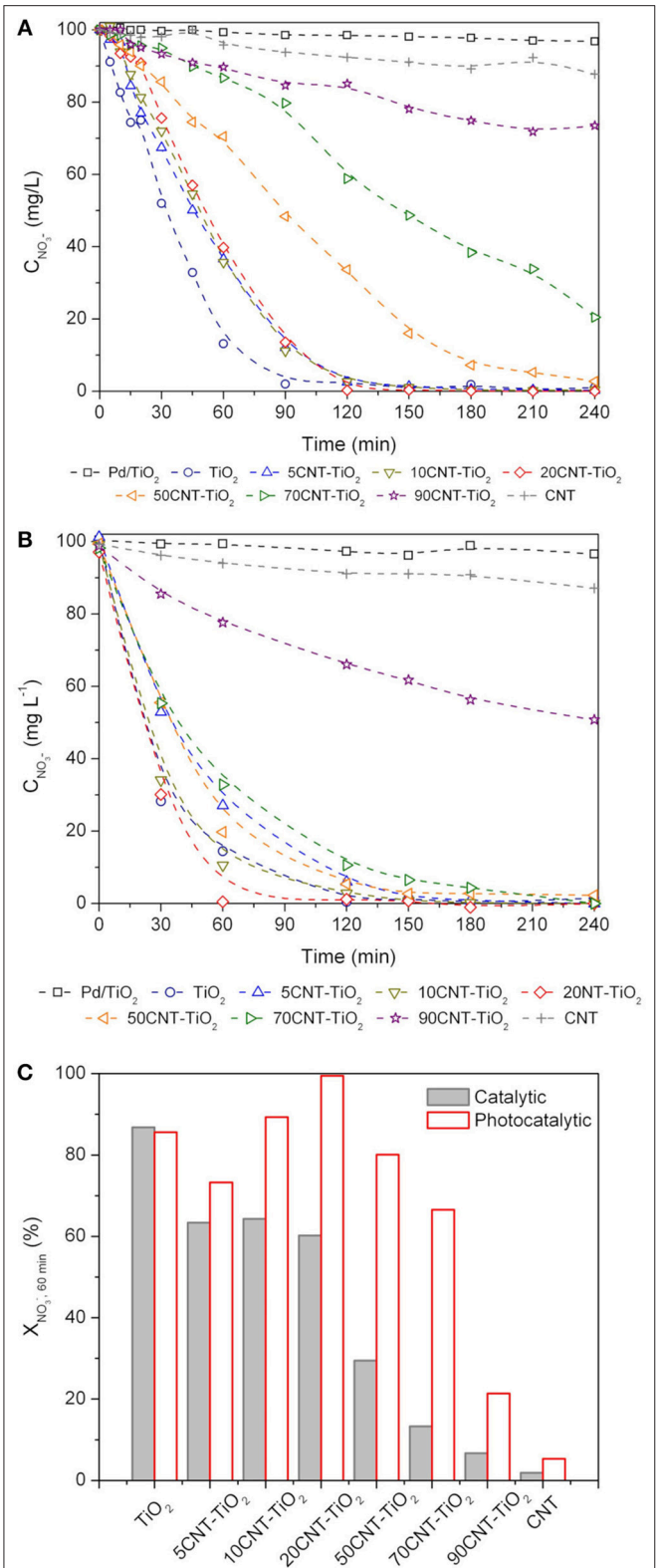

FIGURE 6 | Nitrate concentration ($C_{NO_3^-}$) during catalytic **(A)** and photocatalytic **(B)** reactions. Pd/TiO_2 refers to the monometallic catalyst while all other results refer to Pd-Cu bimetallic catalysts. Nitrate conversion at 60 min ($X_{NO_3^-,60\ min}$) using Pd-Cu loaded materials **(C)**.

using Pd-Cu/20CNT-TiO_2 and Pd-Cu/TiO_2 under catalytic and photocatalytic conditions. In both cases the results indicate that the performance of the catalysts was maintained within 5% variation over 3 consecutive runs.

Figure 7 shows the nitrite and ammonium profiles during catalytic and photocatalytic reactions using Pd-Cu loaded TiO_2, CNT, and 20CNT-TiO_2 catalysts. Residual amounts of NO_2^- and NH_4^+ were produced using Pd-Cu/CNT during both catalytic and photocatalytic processes. When Pd-Cu/TiO_2 was used as catalyst, nitrite is partially transformed into ammonia during the reaction, which is accumulated in the aqueous media. It was found that for the catalytic process, the formation of nitrite and conversion into ammonium is slower than for the photocatalytic process. Also, lower amounts of ammonia were produced in the presence of light, using Pd-Cu/TiO_2 and Pd-Cu/CNT, meaning a higher selectivity of the photocatalytic process toward N_2 formation.

For the reactions using Pd-Cu/20CNT-TiO_2 higher amounts of NO_2^- were found during the catalytic and photocatalytic reactions, which were completely depleted at the end of 180 and 60 min of reaction, respectively (**Figure 7A**). Yet, contrarious to what was observed for the reactions using Pd-Cu/TiO_2 and Pd-Cu/CNT, the use of the metal-loaded 20CNT-TiO_2 catalyst under irradiation lead to the formation of higher amounts of ammonia when compared to the catalytic process (**Figure 7B**).

Catalytic and Photocatalytic Nitrate Reduction Mechanisms Using CNT-TiO_2 Catalysts

As described above, nitrate reduction over CNT-TiO_2 hybrid materials behave very differently in dark conditions and under irradiation. Although the photo-assisted process provide a quicker depletion of NO_3^-, the selectivity toward N_2 is greatly affected by the use of CNT-TiO_2 hybrid materials as Pd-Cu supports (**Figure 8**).

In the case of the catalytic reduction process, an increase in N_2 selectivity is observed with increasing CNT content up to 20 wt.%. A further increase in the amount of CNT led to a progressive decrease in the selectivity toward N_2 formation (**Figure 8A**). On the other hand, the photocatalytic reduction of NO_3^- using CNT-TiO_2 catalysts appeared to be more selective for the reduction of nitrate into ammonia (**Figure 8B**).

It is well accepted that during the (dark) catalytic reduction over bimetallic catalysts, using hydrogen as reducing agent, NO_3^- is converted into NO_2^- according to a redox reaction on the promoter metal (Cu). The role of the noble metal is to activate hydrogen, reducing the promoter metal, completing the catalytic cycle (Epron et al., 2001; Soares et al., 2011b; Zhang et al., 2013), being also active for the NO_2^- reduction.

In the case of the photocatalytic process using metal-loaded TiO_2, the mechanism generally proposed is based on the role of metal nanoparticles as electron sinks. Since the Fermi levels of noble metals are lower than that of TiO_2, the photo-excited electrons can be transferred from the conduction band of the semiconductor to the metal nanoparticles deposited on its surface, being then available for NO_3^- reduction (Kominami

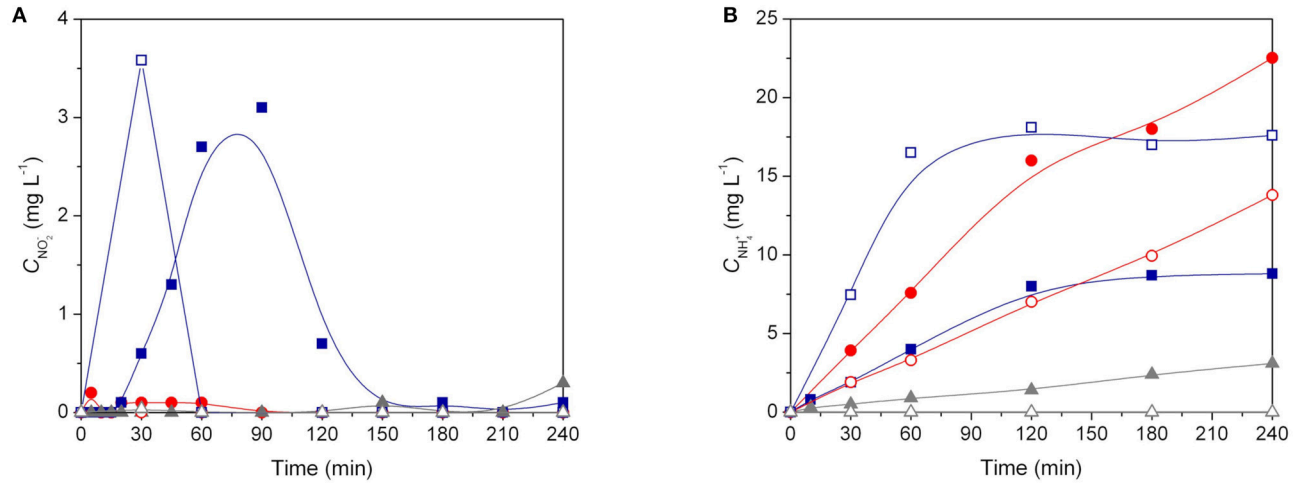

FIGURE 7 | (A) NO_2^- and **(B)** NH_4^+ concentrations as a function of time during nitrate reduction over Pd–Cu loaded TiO_2 (● and ○), 20CNT-TiO_2 (■ and □) and CNT (▲ and △) under dark catalytic (solid symbols) and photocatalytic (open symbols) conditions.

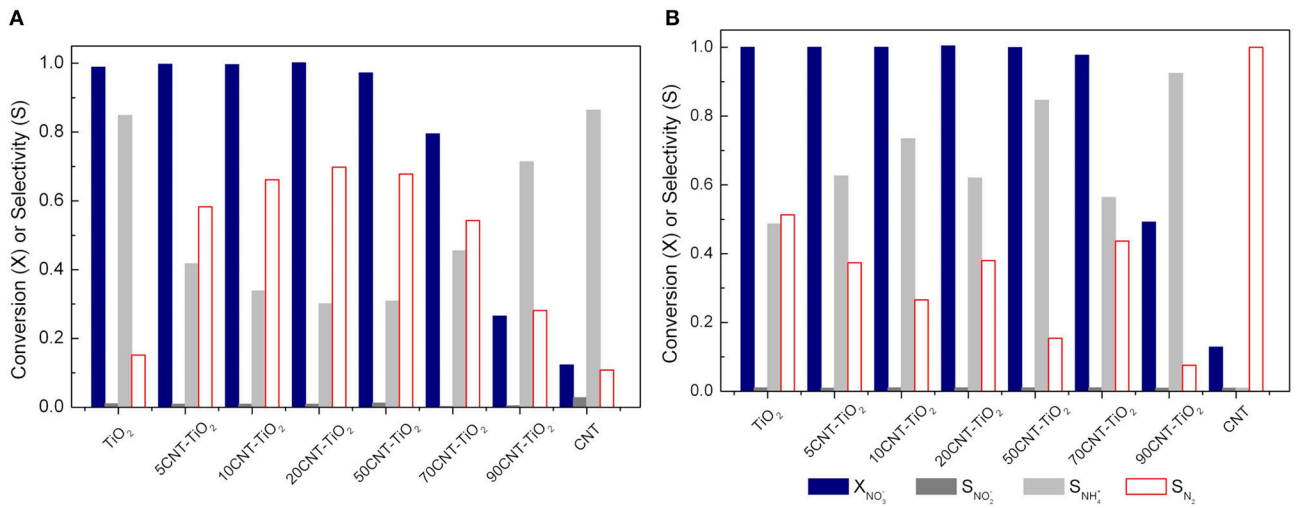

FIGURE 8 | Nitrate conversion ($X_{NO_3^-}$) and nitrite, ammonium and nitrogen selectivity ($S_{NO_2^-}$, $S_{NH_4^+}$, S_{N_2}) using Pd-Cu loaded TiO_2 and CNT-TiO_2 catalysts after 4 h of catalytic **(A)** and photocatalytic **(B)** reactions.

et al., 2005; Anderson, 2012; Soares et al., 2014). Hole scavengers are generally used, acting as sacrificial electron donors, avoiding electron-hole recombination. Yet, in the present work, no scavengers were added to the reaction medium.

The role played by CNT in CNT-TiO_2 hybrids has been discussed in previous works reporting the use of this type of materials as photocatalysts for environmental applications (Silva and Faria, 2010; Silva et al., 2015; Zeng et al., 2015; Yang and Park, 2017). CNT may act as adsorbent, as dispersing medium for TiO_2 nanoparticles, it may span light absorption into the visible and may retard electron hole recombination. Although the surface area of the hybrid materials increased with CNT content, the first is not likely to be the most important effect, since no significant adsorption was observed whether the catalyst used. TEM images of CNT-TiO_2 hybrids show that CNT promote the dispersion of TiO_2 avoiding particle agglomeration (**Figure 2**). Moreover, the introduction of CNT increased the absorption of the resulting materials in the visible range, as shown by the UV-Vis spectra (**Figure 5A**), and lead to a decrease in the electron-hole recombination (**Figure 5B**).

Based in our findings, and considering the operation conditions used in this study, the following photocatalytic reaction mechanism is proposed. Since the irradiation source emits in the near UV to visible range, it is expected that TiO_2 and CNT could be photoexcited simultaneously (**Figure 9**, steps 1 and 1*).

After charge separation, electrons are transferred to Pd and Cu nanoparticles that are supported over TiO_2 and also over

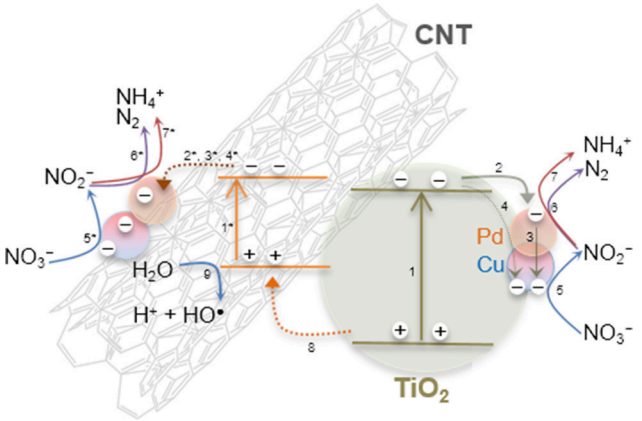

FIGURE 9 | Schematic representation of the photocatalytic reduction of nitrate over Pd–Cu/CNT-TiO_2 catalysts in the presence of H_2 and CO_2, under near UV to visible light irradiation.

CNTs (**Figure 9**, steps 2–4), as observed by TEM (**Figure 2**). Photogenerated electrons may reduce both nitrate and nitrite adsorbed on Cu and Pd, respectively (**Figure 9**, steps 5–7). On the other hand, positively charged holes may migrate from TiO_2 to the CNT phase, where, in the absence of sacrificial electron donors, water can be oxidized to H^+ and $HO^•$ (**Figure 9**, steps 8 and 9). Hydroxyl radicals may indirectly re-oxidize byproducts to NO_3^- (Tugaoen et al., 2017), while $CO_2^{•-}$, which can be generated from the reduction of CO_2 (used as pH buffer) by available electrons, may play a role as reducing mediator (Zhang et al., 2005; Sá et al., 2009). The higher selectivity toward NH_4^+ production obtained using CNT-TiO_2 catalysts when irradiated may be rationalized by the excess of H^+ in the reaction medium, resulting from step 9 in **Figure 9**. Yet, no direct correlation between the CNT load in the hybrid materials and the selectivity toward NH_4^+ could be found (**Figure 8B**), which may derive from the complexity and simultaneity of the reactions involved in the mechanism of the photocatalytic process.

Although the photocatalytic process appears more advantageous in terms of kinetics of nitrate removal, the (dark) catalytic reactions using CNT-TiO_2 hybrid materials revealed to be more selective toward N_2 formation. Nevertheless, the possibility of using this type of materials may be envisioned as a cleaner route for the production of ammonia, comparing with the conventional fossil fuel based process (Yamauchi et al., 2011; Hirakawa et al., 2017).

CONCLUSION

TiO_2 and CNT-TiO_2 loaded with 1%Pd−1%Cu show high catalytic activity in the dark and under near UV to visible light irradiation, in the presence of H_2 and CO_2. The presence of light promotes faster NO_3^- conversion, due to the higher availability of reducing species. Carbon nanotubes induce to a positive effect in the selectivity of the catalytic reduction process toward N_2 formation. In the case of the photocatalytic process, the hybrid materials lead to an increase in the yield of the reduction of NO_3^- to NH_4^+, due to the high availability of H^+. The efficiency of the hybrid materials depends on the CNT load, the best performing material being that composed by 20 wt.% of carbon nanotubes. In the case of the dark catalytic process, the synergic effect observed by the introduction of CNT in the TiO_2 matrix is mainly ascribed to the action of the carbon phase as dispersing medium to metal oxide particles, while under irradiation, CNT produce an increase in the efficiency of charge separation and mobility in the composite material.

AUTHOR CONTRIBUTIONS

CS and OS conceived the research work, prepared and characterized the catalysts, performed the activity tests and drafted the manuscript. JÓ, MP, and JF provided the means for the realization of this work and contributed to the interpretation of the experimental results. All authors read and approved the final manuscript.

FUNDING

This work was financially supported by Project POCI-01-0145-FEDER-006984—Associate Laboratory LSRE-LCM funded by FEDER through COMPETE2020—Programa Operacional Competitividade e Internacionalização (POCI)—and by national funds through FCT—Fundação para a Ciência e a Tecnologia, and by the project AIProcMat@N2020—Advanced Industrial Processes and Materials for a Sustainable Northern Region of Portugal 2020, with the reference NORTE-01-0145-FEDER-000006, supported by Norte Portugal Regional Operational Programme (NORTE 2020), under the Portugal 2020 Partnership Agreement, through the European Regional Development Fund (ERDF). CGS acknowledges the FCT Investigator Programme (IF/00514/2014) with financing from the European Social Fund and the Human Potential Operational Programme.

REFERENCES

Anderson, J. A. (2011). Photocatalytic nitrate reduction over Au/TiO_2. *Catal. Today* 175, 316–321. doi: 10.1016/j.cattod.2011.04.009

Anderson, J. A. (2012). Simultaneous photocatalytic degradation of nitrate and oxalic acid over gold promoted titania. *Catal. Today* 181, 171–176. doi: 10.1016/j.cattod.2011.05.027

Barrabés, N., Dafinov, A., Medina, F., and Sueiras, J. E. (2010). Catalytic reduction of nitrates using Pt/CeO_2 catalysts in a continuous reactor. *Catal. Today* 149, 341–347. doi: 10.1016/j.cattod.2009.05.029

Calvo, L., Gilarranz, M. A., Casas, J. A., Mohedano, A. F., and Rodriguez, J. J. (2010). Denitrification of water with activated carbon-supported metallic catalysts. *Ind. Eng. Chem. Res.* 49, 5603–5609. doi: 10.1021/ie100838r

Dai, K., Zhang, X., Fan, K., Zeng, P., and Peng, T. (2014). Multiwalled carbon nanotube-TiO_2 nanocomposite for visible-light-induced photocatalytic hydrogen evolution. *J. Nanomater.* 2014:8. doi: 10.1155/2014/694073

Devadas, A., Vasudevan, S., and Epron, F. (2011). Nitrate reduction in water: influence of the addition of a second metal on the performances of the Pd/CeO_2 catalyst. *J. Hazard. Mater.* 185, 1412–1417. doi: 10.1016/j.jhazmat.2010.10.063

Doudrick, K., Yang, T., Hristovski, K., and Westerhoff, P. (2013). Photocatalytic nitrate reduction in water: managing the hole scavenger and reaction by-product selectivity. *Appl. Catal. B* 136–137, 40–47. doi: 10.1016/j.apcatb.2013.01.042

Epron, F., Gauthard, F., Pineda, C., and Barbier, J. (2001). Catalytic reduction of nitrate and nitrite on Pt-Cu/Al_2O_3 catalysts in aqueous solution: role of the interaction between copper and platinum in the reaction. *J. Catal.* 198, 309–318. doi: 10.1006/jcat.2000.3138

Hirakawa, H., Hashimoto, M., Shiraishi, Y., and Hirai, T. (2017). Photocatalytic conversion of nitrogen to ammonia with water on surface oxygen vacancies of titanium dioxide. *J. Am. Chem. Soc.* 139, 10929–10936. doi: 10.1021/jacs.7b06634

Kapoor, A., and Viraraghavan, T. (1997). Nitrate removal from drinking water-review. *J. Environ. Eng.* 123, 371–380. doi: 10.1061/(ASCE)0733-9372(1997)123:4(371)

Kominami, H., Nakaseko, T., Shimada, Y., Furusho, A., Inoue, H., Murakami, S., et al. (2005). Selective photocatalytic reduction of nitrate to nitrogen molecules in an aqueous suspension of metal-loaded titanium(IV) oxide particles. *Chem. Commun.* 23, 2933–2935. doi: 10.1039/b502909k

López, R., Gómez, R., and Llanos, M. E. (2009). Photophysical and photocatalytic properties of nanosized copper-doped titania sol-gel catalysts. *Catal. Today* 148, 103–108. doi: 10.1016/j.cattod.2009.04.001

Luiz, D. D. B., Andersen, S. L. F., Berger, C., José, H. J., and Moreira, R. D. F. P.M. (2012). Photocatalytic reduction of nitrate ions in water over metal-modified TiO_2. *J. Photochem. Photobiol. A* 246, 36–44. doi: 10.1016/j.jphotochem.2012.07.011

Marchesini, F. A., Gutierrez, L. B., Querini, C. A., and Mir,ó, E. E. (2010). Pt,In and Pd,In catalysts for the hydrogenation of nitrates and nitrites in water. FTIR characterization and reaction studies. *Chem. Eng. J.* 159, 203–211. doi: 10.1016/j.cej.2010.02.056

Martínez, J., Ortiz, A., and Ortiz, I. (2017). State-of-the-art and perspectives of the catalytic and electrocatalytic reduction of aqueous nitrates. *Appl. Catal. B* 207, 42–59. doi: 10.1016/j.apcatb.2017.02.016

Prusse, U., Hahnlein, M., Daum, J., and Vorlop, K. D. (2000). Improving the catalytic nitrate reduction. *Catal. Today* 55, 79–90. doi: 10.1016/S.0920-5861(99)00228-X

Sá, J., Aguera, C. A., Gross, S., and Anderson, J. A. (2009). Photocatalytic nitrate reduction over metal modified TiO_2. *Appl. Catal. B* 85, 192–200. doi: 10.1016/j.apcatb.2008.07.014

Sá, J., Berger, T., Fottinger, K., Riss, A., Anderson, J. A., and Vinek, H. (2005). Can TiO_2 promote the reduction of nitrates in water? *J. Catal.* 234, 282–291. doi: 10.1016/j.jcat.2005.06.015

Sakamoto, Y., Kamiya, Y., and Okuhara, T. (2006). Selective hydrogenation of nitrate to nitrite in water over Cu-Pd bimetallic clusters supported on active carbon. *J. Mol. Catal. A Chem.* 250, 80–86. doi: 10.1016/j.molcata.2006.01.041

Shand, M., and Anderson, J. A. (2013). Aqueous phase photocatalytic nitrate destruction using titania based materials: routes to enhanced performance and prospects for visible light activation. *Catal. Sci. Technol.* 3, 879–899. doi: 10.1039/c3cy20851f

Silva, C. G., and Faria, J. L. (2010). Photocatalytic oxidation of benzene derivatives in aqueous suspensions: synergic effect induced by the introduction of carbon nanotubes in a TiO_2 matrix. *Appl. Catal. B* 101, 81–89. doi: 10.1016/j.apcatb.2010.09.010

Silva, C. G., Sampaio, M. J., Marques, R. R. N., Ferreira, L. A., Tavares, P. B., Silva, A. M. T., et al. (2015). Photocatalytic production of hydrogen from methanol and saccharides using carbon nanotube-TiO_2 catalysts. *Appl. Catal. B* 178, 82–90. doi: 10.1016/j.apcatb.2014.10.032

Soares, O. S. G. P., Órfão, J. J. M., and Pereira, M.F.R. (2009). Bimetallic catalysts supported on activated carbon for the nitrate reduction in water: optimization of catalysts composition. *Appl. Catal. B* 91, 441–448. doi: 10.1016/j.apcatb.2009.06.013

Soares, O. S. G. P., Órfão, J. J. M., and Pereira, M.F.R. (2011a). Nitrate reduction in water catalysed by Pd-Cu on different supports. *Desalination* 279, 367–374. doi: 10.1016/j.desal.2011.06.037

Soares, O. S. G. P., Órfão, J. J. M., and Pereira, M.F.R. (2011b). Nitrate reduction with hydrogen in the presence of physical mixtures with mono and bimetallic catalysts and ions in solution. *Appl. Catal. B* 102, 424–432. doi: 10.1016/j.apcatb.2010.12.017

Soares, O. S. G. P., Órfão, J. J. M., Ruiz-Martínez, J., Silvestre-Albero, J., Sepúlveda-Escribano, A., and Pereira, M.F.R. (2010). Pd-Cu/AC and Pt-Cu/AC catalysts for nitrate reduction with hydrogen: influence of calcination and reduction temperatures *Chem. Eng. J.* 165, 78–88. doi: 10.1016/j.cej.2010.08.065

Soares, O. S. G. P., Pereira, M. F. R., Órfão, J. J. M., Faria, J. L., and Silva, C.G. (2014). Photocatalytic nitrate reduction over Pd-Cu/TiO_2. *Chem. Eng. J.* 251, 123–130. doi: 10.1016/j.cej.2014.04.030

Tahir, M., Tahir, B., and Amin, N. A. S. (2017). Synergistic effect in plasmonic Au/Ag alloy NPs co-coated TiO_2 NWs toward visible-light enhanced CO_2 photoreduction to fuels. *Appl. Catal. B* 204, 548–560. doi: 10.1016/j.apcatb.2016.11.062

Tugaoen, H. O., Garcia-Segura, S., Hristovski, K., and Westerhoff, P. (2017). Challenges in photocatalytic reduction of nitrate as a water treatment technology. *Sci. Total Environ.* 599–600, 1524–1551. doi: 10.1016/j.scitotenv.2017.04.238

Wada, K., Hirata, T., Hosokawa, S., Iwamoto, S., and Inoue, M. (2012). Effect of supports on Pd-Cu bimetallic catalysts for nitrate and nitrite reduction in water. *Catal. Today* 185, 81–87. doi: 10.1016/j.cattod.2011.07.021

Wu, Z., Sheng, Z., Wang, H., and Liu, Y. (2009). Relationship between Pd oxidation states on TiO_2 and the photocatalytic oxidation behaviors of nitric oxide. *Chemosphere* 77, 264–268. doi: 10.1016/j.chemosphere.2009.07.060

Yamauchi, M., Abe, R., Tsukuda, T., Kato, K., and Takata, M. (2011). Highly selective ammonia synthesis from nitrate with photocatalytically generated hydrogen on CuPd/TiO_2. *J. Am. Chem. Soc.* 133, 1150–1152. doi: 10.1021/ja106285p

Yang, H. M., and Park, S. J. (2017). Effect of incorporation of multiwalled carbon nanotubes on photodegradation efficiency of mesoporous anatase TiO_2 spheres. *Mater. Chem. Phys.* 186, 261–270. doi: 10.1016/j.matchemphys.2016.10.052

Zeng, Q., Li, H., Duan, H., Guo, Y., Liu, X., Zhang, Y., et al. (2015). A green method to prepare TiO2/MWCNT nanocomposites with high photocatalytic activity and insights into the effect of heat treatment on photocatalytic activity. *RSC Adv.* 5, 13430–13436. doi: 10.1039/C4RA13809K

Zhang, F., Jin, R., Chen, J., Shao, C., Gao, W., Li, L., et al. (2005). High photocatalytic activity and selectivity for nitrogen in nitrate reduction on Ag/TiO_2 catalyst with fine silver clusters. *J. Catal.* 232, 424–431. doi: 10.1016/j.jcat.2005.04.014

Zhang, R., Shuai, D., Guy, K. A., Shapley, J. R., Strathmann, T. J., and Werth, C. J. (2013). Elucidation of nitrate reduction mechanisms on a Pd-In bimetallic catalyst using isotope labeled nitrogen species. *ChemCatChem* 5, 313–321. doi: 10.1002/cctc.201200457

Zhang, Y., Zhang, N., Tang, Z. R., and Xu, Y. J. (2012). Improving the photocatalytic performance of graphene–TiO_2 nanocomposites via a combined strategy of decreasing defects of graphene and increasing interfacial contact. *Phys. Chem. Chem. Phys.* 14, 9167–9175. doi: 10.1039/c2cp41318c

Conflict of Interest Statement: The authors declare that the research was conducted in the absence of any commercial or financial relationships that could be construed as a potential conflict of interest.

frontiers in Chemistry

ORIGINAL RESEARCH
published: 14 June 2018
doi: 10.3389/fchem.2018.00216

Hydrodeoxygenation of Bio-Derived Phenol to Cyclohexane Fuel Catalyzed by Bifunctional Mesoporous Organic–Inorganic Hybrids

Liuye Mo[1]*, *Wanjin Yu*[2]*, *Huangju Cai*[3], *Hui Lou*[3] and *Xiaoming Zheng*[3]

[1] Institute of Innovation & Application, Zhejiang Ocean University, Zhoushan, China, [2] State Key Laboratory of Fluorinated Greenhouse Gases Replacement and Control Treatment, Zhejiang Research Institute of Chemical Industry, Hangzhou, China, [3] Key Lab of Applied Chemistry of Zhejiang Province, Department of Chemistry, Zhejiang University, Hangzhou, China

In this work, mesoporous silica materials SBA-15 functionalized with propyl/phenyl-sulfonic acid group were synthesized and loaded with Pt to form bifunctional catalysts. SAXRD, WAXRD, N_2 adsorption-desorption, TEM techniques were used to characterize the above bifunctional catalysts. These bifunctional catalysts were applied to the reaction of hydrodeoxygenation (HDO) of bio-derived phenol (PhOH) to produce cyclohexane fuel and showed very good catalytic performances. There were strong synergies between the metal sites and the acid sites on the bifunctional catalysts. This reaction of phenol HDO provides a model system for the catalytic upgrading of biomass-derived fuel.

Keywords: mesoporous silica, bifunctional catalyst, hydrodeoxygenation, bio-oil, phenol, cyclohexane

OPEN ACCESS

Edited by:
Zhimin Ao,
Guangdong University of Technology, China

Reviewed by:
Yiming Tang,
South China Normal University, China
Jun Huang,
The University of Sydney, Australia

***Correspondence:**
Liuye Mo
liuyemo@zjou.edu.cn
Wanjin Yu
yuwanjin1@sinochem.com

Specialty section:
This article was submitted to Green and Sustainable Chemistry, a section of the journal Frontiers in Chemistry

Received: *21 March 2018*
Accepted: *25 May 2018*
Published: *14 June 2018*

Citation:
Mo L, Yu W, Cai H, Lou H and Zheng X (2018) Hydrodeoxygenation of Bio-Derived Phenol to Cyclohexane Fuel Catalyzed by Bifunctional Mesoporous Organic–Inorganic Hybrids. Front. Chem. 6:216. doi: 10.3389/fchem.2018.00216

INTRODUCTION

Due to its abundance (15–30 wt % of wood-based biomass) and remarkably lower oxygen content than polysaccharides, lignin is a favorable feedstock for the production of biofuel, which is regarded as a promising energy alternative for fossil fuels (Huber et al., 2006). Currently, two-step processes are typical strategies to utilize lignin for biofuel production. In the first step, lignin is hydrolyzed (Kudsy and Kumazawa, 1999; Shabtai et al., 1999; Hepditch and Thring, 2000; Liu et al., 2008) or fast pyrolyzed (Meier et al., 1994; Thring and Breau, 1996; Britt et al., 2000; Dobele et al., 2007; Boateng et al., 2008; Ingram et al., 2008; French and Czernik, 2010) to depolymerize into a mixture of simple aromatic compounds (mostly phenols). Unfortunately, large quantities of reactive, unstable, and corrosive oxygenate compounds are contained in crude biofuel, which cannot be used directly as a vehicle fuel (Garcia-Perez et al., 2007). Therefore, the crude mixture from the first step must be upgraded into fuels in the second step. In order to simultaneously stabilize two main kind of reactive components, aldehydes and organic acids, in the bio-oil, we have newly developed a reaction system named one-step hydrogenation-esterification (OHE) reaction as a possible approach for biofuel upgrading (Tang et al., 2008; Yu et al., 2011). However, phenols with poor combustion performance could not be converted effectively during the OHE process (Yu et al., 2011). Therefore, the conversion of phenolic compounds into hydrocarbon fuels remains a challenge (Crossley et al., 2010). Hydrodeoxygenation (HDO) is regarded as a most attractive and effective method to convert phenolic compounds to alkanes for bio-oil upgrading

(Huber et al., 2006). Traditional catalysts for HDO reaction were sulfide CoMo and NiMo/γ-Al_2O_3 catalysts, which are used in the hydrodesulfurization or hydrodenitrogenation process in petroleum refineries (Senol et al., 2005; Bui et al., 2009). However, it is well known that the fuels produced by sulfide catalysts will be contaminated as sulfur may be leached into the reaction liquids, and the catalysts will suffer from deactivation by water induction and coke accumulation (Yan et al., 2010). Lercher and Kou groups have reported a new highly efficient one-pot route for HDO of aqueous phenolic bio-oil to cycloalkanes over catalysts combining the noble catalysts with mineral acids or Brønsted acidic ionic liquids (Zhao et al., 2009, 2010; Yan et al., 2010). New progresses have been made over noble metal and transition metal catalysts combined with liquid acids or solid acids to upgrade biofuels via HDO of bio-derived phenolic compounds (Luska et al., 2015; Dongil et al., 2016; Lee et al., 2016). The good catalytic performance of the catalysts using mesoporous acidic solid materials as supports can be expected, as the bulky molecular of bio-derived phenolic compounds can easily access the active sites in the mesopores. Furthermore, the environmental benign solid acids can be recovered simply by filtration. Bifunctional catalysts of Pt/HY and Pt/HBeta were successfully used for phenolics HDO to produce hydrocarbons in fixed-bed configurations (Hong et al., 2010; Zhu et al., 2011). However, utilization of the bifunctional catalysts using mesoporous solid acid materials as supports for HDO of bio-derived phenolics was rarely reported. More recently, Xiao group has developed mesoporous zeolite ZSM-5 supported Ru to convert efficiently both small and bulky phenolic biomolecules via HDO to the corresponding alkanes owing to the open mesopores with abundant exposed acidic sites in the catalysts (Wang L. et al., 2015).

This paper focuses on the conversion of bio-derived phenol to cyclohexane via HDO reaction, a liquid fuel with good combustion properties, under mild reaction conditions over Pt bifunctional catalysts which possess functions of both hydrogenation and dehydration. The support of SBA-15 functionalized with organosulfonic acid was used, showing strong acidity and accessibility for bulky bio-derived molecules, may overcome the disadvantages both of the liquid acids and microporous solid acids.

EXPERIMENTAL SECTION

Catalyst Preparation

The catalysts used in this work were organic-inorganic hybrid SBA-15 materials, which were functionalized with propylsulfonic (arenesulfonic) acid groups and loaded with platinum. Organosulfonic acid-functionalized SBA-15 materials were synthesized as described elsewhere (Mbaraka and Shanks, 2006; Tang et al., 2010) with only slight modifications. Tetraethoxysilane (TEOS, 98%, Aldrich) and (3-mercaptopropyl)trimethoxysilane (MPTMS, 85 wt. %, Acros) or 2-(4-chloro-sulfonyl-phenyl) ethyl trimethoxysilane (CSPTMS, 50 wt. % in CH_2Cl_2, Acros) were adopted directly without further purification as the silica and the organosulfonic acid sources. Pluronic P123 (Aldrich), a triblock copolymer of polyethylene oxide-polypropylene oxide-polyethylene oxide with the molecular structure PEO_{20}-PPO_{70}-PEO_{20} (Mw = 5800), was used as a structure template to synthesizethe SBA-15. H_2PtCl_6 solution used as the platinum precursor was provided by Hangzhou Kaiming Catalyst Co., Ltd. Formaldehyde (HCHO, 37 wt.%, aqueous solution, Sinopharm Chemical reagents Co., China) was used as reducing agents. The functionalized SBA-15 hybrids with propylsulfonic or arenesulfonic acid groups were abbreviated as SBA-Pr and SBA-Ar, respectively. The nominal loading of platinum on the catalysts was fixed at 1 wt%.

Synthesis of 1%Pt/SBA-Pr and 1%Pt/SBA-Ar

In a typical synthesis of SBA-Pr, Pluronic P123 (4.00 g, 0.69 mmol) was dissolved in HCl solution (1.9 M, 125 mL) at room temperature. Then, keeping stirring the solution was heated to 40°C before the addition of TEOS (8.23 mL, 36.74 mmol). Before the addition of MTPMS (3.674 mmol) and H_2O_2 (12.86 mmol), ∼45 min was allowed for prehydrolysis of TEOS. The resulting mixture was agitated for 24 h at 40°C and then aged for another 24 h at 110°C under static conditions. After that, the resulting solids were separated by filteration, washed with D.I. water and dried at 100°C in an oven for 8 h. The template in the as-synthesis samples was extracted by 10% v/v HCl in ethanol and refluxing for 36 h. To ensure complete removal of the template, fresh ethanol would be introduced after every 12 h.

Pt was loaded on SBA-Pr by reduction-deposition method. 1.00 g SBA-Pr was added into the aqueous solution containing 30.0 mL of D.I. water and 0.021 g of H_2PtCl_6. The Formaldehyde solution (10 mL) was used as reducing agent and added dropwise into the above aqueous suspension with vigorous stirring () at 60°C. The suspension was stirred for 24 h at 60°C to allow the reduction of Pt^{4+} to Pt^0. After that, the suspension was filtered at room temperature and thoroughly washed with D.I. water until free of Cl^- in the filtrate (tested with silver nitrate solution). The wet filter cake was re-suspended in 50 mL of 1 wt% H_2SO_4 solution for 4 h for acidification. Finally, the solid was treated by filtering, washing, and vacuum drying at 110°C. The synthesis procedures of SBA-Ar and **1%Pt/SBA-Ar were** the same as the synthesis of SBA-Pr and 1%Pt/SBA-Pr described above, besides CSPTMS was used instead of MPTMS.

Catalyst Characterization

Small angle XRD (SAXRD) patterns were recorded for SBA-Pr, SBA-Ar, 1%Pt/SBA-Pr, and 1%Pt/SBA-Ar powder in order to confirm the hexagonal structure of samples. Wide angle XRD (WAXRD) was used to analyze the 1%Pt/SBA-Pr and 1%Pt/SBA-Ar. The above XRD measurements were performed on the Rigaku D/MAX-RB.

A Philips-FEI transmission electron microscope (Tecnai G2 F30 S-Twin, The Netherlands), operating at 300- kV, was used to obtain the HRTEM images of catalysts. Samples were mounted on copper grid-supported carbon films by dropping a few droplets of ultrasonically dispersed suspensions of samples in ethanol on the grids, followed by drying at ambient conditions.

CO chemisorption measurements were carried out at 25°C on a CHEMBET-3000 pulse flow system. Prior to measurements, the catalysts were tableted formed, crushed and sieved to 40–60 mesh. To remove any oxygen from the samples, pretreatments

were done at 250°C for 1 h with a ramp of 10°C/min from room temperature under 30 mL/min of 5 vol. % H_2/He up to 250°C. After that, the adsorbed hydrogen on samples was removed by purging with 30 mL/min helium gas for 2 h at 250°C. Finally, the catalysts were cooled down to 25°C under He flow and 5 vol% CO in helium were pulsed into the catalysts until the CO peak areas appeared to be identical.

The real weight percentages of Pt on the supports of SBA-Pr and SBA-Ar were determined by inductively coupled plasma-mass spectroscopy (ICP-MS) on a PS1000 instrument from American LEEMAN LABS INC.

The N_2 adsorption/desorption method was adopted to measure the textural properties of the catalytic materials on an automated adsorption apparatus (OMNIISORP 100CX) at−196°C. Prior to the adsorption/desorption measurement, all samples were degassed for 2 h at 195°C in the pretreated chamber of the adsorption apparatus. The surface area, pore volume (Vp) were calculated by the Brunauer-Emmett-Teller (BET) and Barret-Joyner-Hallenda (BJH) methods. The mean pore diameter (MPD) of the samples was analyzed by the BJH method based on the adsorption branch of the N_2 adsorption-desorption isotherms.

The decomposition of organic moiety and the thermal stability of the solids were examined by thermogravimetric analysis (TGA) on a Perkin-Elmer TGA7 instrument. The samples were heated under a stream of air (20 mL/min) from 50 to 700°C with a ramp rate of 10°C/min.

The acidic properties (strength and amount of acid sites) of the catalysts were determined by acid-base titration. The relative pKa values of the samples were estimated using the Gran plot analysis. Typically, 0.1 g of the sample was weighted and suspended in 10 ml of D.I. water, and then was titrated potentiometrically by continuous addition of 5 mM KOH aqueous solution.

Catalytic Evaluation

All the HDO of phenol experiments were performed in a 100 mL stainless steel batch autoclave reactor. In a typical experiment, a certain mass of phenol dissolved in a certain volume of dichloromethane was added into the reactor with a certain amount of catalysts. Before each run, the reactor was purged with hydrogen for five times, 2.0 MPa at a time, to remove air from the setup. Then hydrogen was introduced into the reactor with a certain pressure ranged from 1.0 to 4.0 MPa. The reaction system would be heated to reaction temperatures (80–200°C) within half an hour. The stirring speed and the granule size were adopted at 800 rpm and smaller than 400 mesh to ensure that the mass transfer on catalytic performances was excluded. After reactions, the reactor was put into ice water and quickly cooled down to room temperature. Subsequently, the gas in the reactor was released very slowly to a sampling gas bag that was purged in advance with H_2 for five times. The products in gas phase were analyzed using a gas chromatography (GC) equipped with a Porapak Q packed column and a TCD. The products in liquid phase were identified and quantified by a GC-MS and a GC (equipped with an SE-30 nonpolar capillary column and a flame ionization detector, FID), and the internal standard method was applied.

Reproducibility of experiment results was carried out by repeating each run for three times at least until the results were within acceptable limits. The conversion of PhOH (X(PhOH)), yield of i (Y(i)) and the selectivity to i (S(i)) were calculated based on the following Equations. (1–3):

$$X(PhOH) = \frac{m(PhOH, in) - m(PhOH, out)}{m(PhOH, in)} \times 100\% \quad (1)$$

$$Y(i) = \frac{\frac{m(i)}{M(i)} \times M(PhOH)}{m(PhOH, in)} \times 100\% \quad (2)$$

$$S(i) = \frac{Y(i)}{X(PhOH)} \times 100\% \quad (3)$$

RESULTS AND DISCUSSION

Characterization Results

XRD Results

Figure 1 is small-angle XRD spectra of freshly prepared SBA-Pr, SBA-Ar, Pt/SBA-Pr, and Pt/SBA-Ar. Three well-resolved peaks were observed in each sample, which were indexed to the (100), (110), and (200) reflections of the hexagonal space group P6 mm (Zhao et al., 1998; Yue et al., 1999). All the diffraction patterns suggested that the SBA-15 structure was well preserved in the process of synthesis of SBA-Pr, SBA-Ar by co-condensation method and in the process of introduction of Pt by reduction-deposition method. The addition of precursors of MPTMS, CSPTMS and H_2PtCl_6 did not destroy the structure of the SBA-15. Figure S1 presents wide-angle XRD spectra of Pt/SBA-Pr and Pt/SBA-Ar. Only the characteristic diffraction peaks of metallic Pt, (111), (200), (220), were detected for the two samples, demonstrating that the Pt species were primarily present in metallic form after reduction by formaldehyde. According to calculation based on the Scherrer equation, the average Pt particle size of 1%Pt/SBA-Pr was 8.9 nm, while that of 1% Pt/SBA-Ar was 9.7 nm. This illustrated that Pt particles were highly dispersed on these supports.

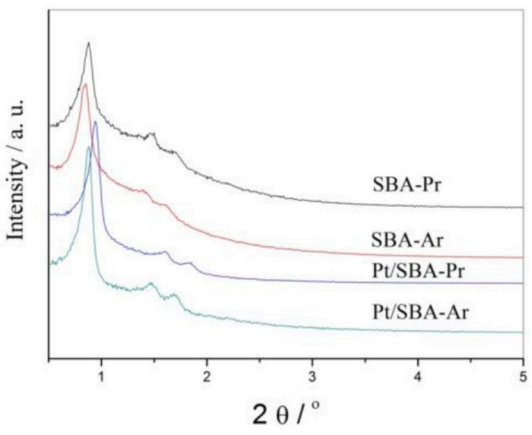

FIGURE 1 | SAXRD patterns of the catalyst samples.

DTG Characterization

The differential thermogravimetric (DTG) analysis was used to determine the thermal decomposition behaviors of the tethered organic moieties in the catalyst samples, as determined by differential thermogravimetric (DTG) analysis, (shown in Figure S2). For SBA-Pr without extraction by ethanol, three peaks centered at about 110, 250, and 460°C were observed, which were resulted from the desorption of water, the decomposition of template and the decomposition of propylsulfonic acid, respectively. No weight loss peak appears in the vicinity of the 350°C (which was attributed to the decomposition of the propylthiol groups, MPTMS) (Tang et al., 2010), meaning the effective oxidation of MPTMS to propylsulfonic acid by hydrogen peroxide added during the preparation of SBA-Pr. For SBA-Pr after ethanol extraction, only weight loss peak of propyl sulfonic acid (around 470°C) was observed on DTG curves, indicating complete removal of the template P123 by ethanol extraction method. The results of DTGclearly showed that the propylsulfonic acid groups in the catalysts did not occur decomposition while using the catalyst under 350°C owing to the higher thermal stability of tethered propylsulfonic acid.

ICP-MS and CO Chemisorptions Results

The properties of the metal sites of two catalysts, including metal loading, and dispersion, were characterized by ICP-MS and CO chemisorption techniques. The results are listed in **Table 1**. ICP results showed that the real loading of Pt was smaller than the theoretical loading of 1 wt.%, demonstrating loss of metal during the preparation process. When Pt was loaded on SBA-Pr, the highest load efficiency of 84% and the highest dispersion (D_{Pt}) of 53% were obtained. The metal particle sizes (d_{Pt}) showed in **Table 1** were calculated from the CO chemisorptions results according literature (Wang and Yeh, 2001). All the metal particles of Pt were highly dispersed over the SBA-Pr and the SBA-Ar with $d_{Pt} < 3.0$ nm. Noticeably, the d_{Pt} was as small as 2.1 nm on the Pt/SBA-Pr. Evidently, the particle sizes calculated from chemisorptions was quite smaller than the aforementioned data derived from XRD. It is well known that the XRD can only be sensitive the big crystallines but not the highly dispersed particles.

TABLE 1 | Metal sites properties of the catalysts.

Catalysts	Metal content/wt.%	D_{Pt}/%	d_{Pt}/nm
Pt/SBA-Pr	0.84	53	2.1
Pt/SBA-Ar	0.60	41	2.7

TEM Characterization Results

TEM is a useful technique to characterize the structure of mesoporous materials. From **Figures 2**, **3**, it can be seen, the organic sulfonic acid functionalized SBA-15 materials have regular one-dimensional pore structure preserving the characteristic pore structure of SBA-15. **Figure 4** shows that after loading of Pt the mesoporous structure of the carriers were still well preserved and the Pt particles were dispersed well on the supports. It could be observed that a lot of Pt particles were as small as <2 nm located in the mesopores.

N_2 Adsorption–Desorption Characterization Results

The N_2 adsorption-desorption isotherms of the samples of SBA-Pr, SBA-Ar, Pt/SBA-Pr, and Pt/SBA-Ar are shown in Figure S3. The observed isotherms of the four samples were obviously classified as IV type isotherms, which was consistent with the mesoporous structure directed by non–ionic surfactant (Buchmeiser, 2003). All the isotherms had Type-H 1 hysteresis loops, and the capillary condensation occured at higher relative pressures (0.7–0.8). This illustrated the synthesized mesoporous materials possessing regular pore arrangements and narrow pore size distributions (Schmidt et al., 1995). The nitrogen

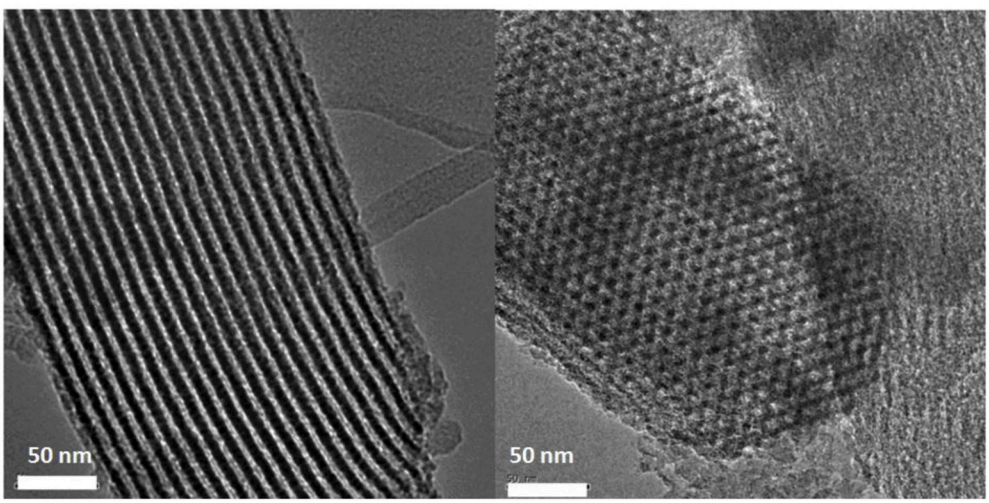

FIGURE 2 | TEM images of sample of SBA-Pr.

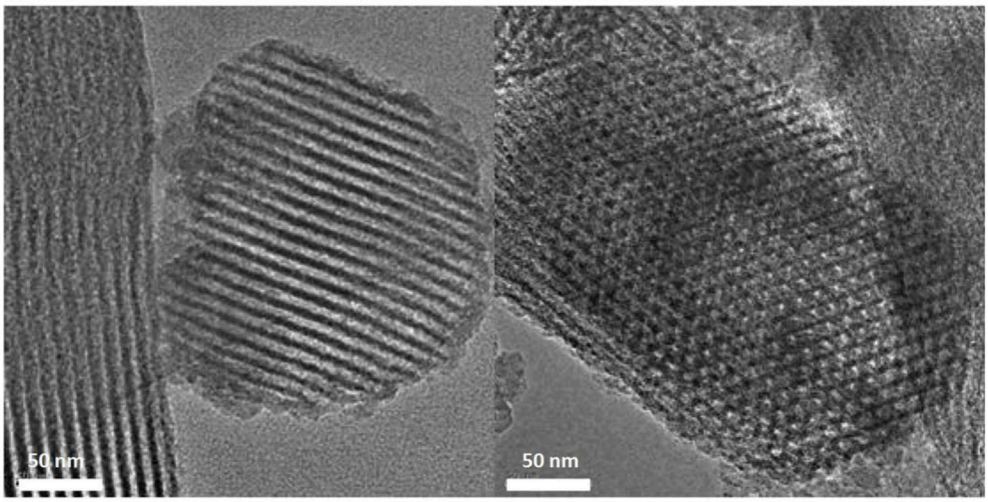

FIGURE 3 | TEM images of sample of SBA-Ar.

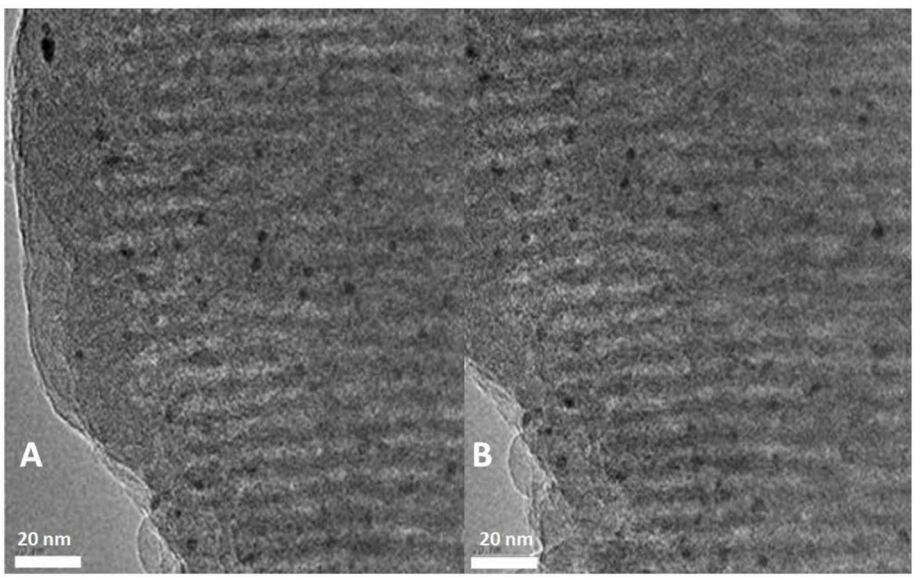

FIGURE 4 | TEM images of 1%Pt/SBA-Pr **(A)** and 1%Pt/SBA-Ar **(B)**.

sorption isotherms also revealed that no partial pore blocking has occurred upon incorporation of platinum, as the adsorption and desorption branches were almost parallel and exhibited narrow hysteresis. After loading of platinum the pore diameter, pore volume, and surface area of SBA-15 were waned showing in Table S1. After functionalization with organosulfonic acid and loading of Pt, the specific surface area and pore size of the samples were decreased compared to SBA-15, but still remained at a high level. These data also showed that the organic and inorganic functional groups did not cause remarkable clogging of pores. The structure of SBA-15 remained stable during the functionalization.

Catalytic Testing Results

Pt Based Organic-Inorganic Hybrid Materials Catalyzed HDO Reaction of Phenol

The catalytic results of phenol HDO catalyzed by bifunctional Pt/SBA-Pr, as well as the relevant control experiment results are presented in **Table 2**. From Entry 1, a good result of phenol HDO reaction was achieved over the bifunctional catalyst of 1%Pt/SBA-Pr with high conversion of phenol (X(PhOH) = 94.1%) and high selectivity to target product of cyclohexane ($S(C_6H_{12}) = 98.6\%$). From Entry 3 and 5, it could be seen that when there is no catalyst or SBA-Pr is used alone phenol did not convert at all. Surprisingly, in Entry 2, over the catalysts of 1% Pt/SBA-15 the

product of cyclohexane was also formed and the selectivity was as high as 63.8%. In entry 4, 1%Pt/SBA-15 and SBA-Pr was physically mixed to form bifunctional catalyst. It was found that both of X(PhOH) and S(C_6H_{12}) were significantly improved over the physically mixed catalyst compared to the 1%Pt/SBA-15 catalyst (entry 2). From above results, it could be considered that the metal sites of catalysts alone catalyze the HDO of phenol with the aid of negligible acidity sites of silanol groups on SBA-15 support, but the stronger acid sites would greatly enhance the HDO reaction activity of the catalyst. Compared to the physical mixed bifunctional catalyst (entry 4), the composite bifunctional catalyst (entry 1) owed the highest conversion of phenol and the best selectivity to cyclohexane. The above results exhibited that there was a synergistic effect between metal sites and acid sites for HDO reaction of phenol. Huang and Baiker group also found that the proper acid sites properties could significantly enhance the catalytic performance for the reaction of hydrogenation of acetophenone on the Pt/[Al]MCM-41 (Wang Z. et al., 2015).

Effect of Supports on Catalyst Performances

Pt was supported on SBA-Pr and SBA-Ar to form bifunctional catalysts of 1%Pt/SBA-Pr and 1%Pt/SBA-Ar. Their catalytic results for HDO of phenol are listed in **Table 3**. 1%Pt/SBA-Pr exhibited higher conversion of phenol (94.1%) and higher selectivity to cyclohexane (98.6%), compared to SBA-Ar supported Pt catalyst with X(PhOH) = 35.0% and S(C_6H_{12}) = 67.4%. According to the characterization results (**Table 1**), though the two catalysts had the same nominal Pt loading, they actually had different Pt content. In order to exclude the influence of the metal content on the results, the TON calculated based on the target product of cyclohexane are also shown in **Table 3**. Pt/SBA-Pr shows higher TON (103.3 mol cyclohexane/mol Pt) in comparison with Pt/SBA-Ar (14.5 mol cyclohexane/mol Pt). Since the impact of metal sites on HDO reaction was excluded, only the acidities of the supports affected the HDO reaction.

The acidities of the catalysts, including the amount and strength of the acid sites, were characterized by means of acid-base titration. The results are shown in **Table 4**. In spite of the same nominal loading, the real amount of acid sites of SBA-Ar was smaller than that of SBA-15-Ar. This might be related to the fact that the molecule of arenesulfonic acid had bigger size and rigidity compared to propylsulfonic acid, which was not conducive to effective loading of arenesulfonic acid. The data also showed that the pKa value of SBA-Ar was smaller than that of SBA-Ar, i.e., SBA-Ar exhibited stronger acid sites. According to Shanks (Mbaraka and Shanks, 2006), the arenesulfonic acid-functionalized samples had lower pKa values as the sulfonate ions in the phenyl group were more stablethan that in aliphatic carbon chain of propylsulfonic acid groups after deprotonation.

Pt/SBA-Pr had more acid sites but lower acid strength compared to Pt/SBA-Ar (**Table 4**). The catalytic activity of Pt/SBA-Pr was higher than that of Pt/SBA-Ar (**Table 3**). Therefore, it was concluded that the acid sites amount of the supports may be a dominant factor to affect the activity of a bifunctional catalyst. The more the acid sites was, the higher activity of the HDO reaction was. In addition, from Table S1, the pore volume of Pt/SBA-Pr and Pt/SBA-Ar is 0.91 and 0.78 cm^3/g, respectively. Obviously, from perspective of mass diffusion the former was in favor of the reaction.

Screening of Solvents

Solvent always plays an important role in a liquid phase reaction. **Table 5** presents the results of phenol hydrodeoxygenation in different solvents. The catalytic activity of 1%Pt/SBA-Pr was the lowest (X(PhOH)∼5.0%) as the solvent of water with high polarity was used, while the solvent of dicloromethane with low polarity was adopted both the X(PhOH) and the S(C_6H_{12}) reaches a maximum with 63.0 and 95.9%, respectively. From

TABLE 2 | Catalytic performance for HDO of phenol.

Entry	Catalysts	X(PhOH)/%	Y(C_6H_{12})/%	S(C_6H_{12})/%
1	1%Pt/SBA-Pr	94.1	92.8	98.6
2	1%Pt/SBA-15	44.8	28.6	63.8
3	SBA-Pr	0	0	–
4	1%Pt/SBA-15+SBA-Pr	74.5	63.3	84.9
5	Catalyst-free	0	0	–

Reaction conditions: T_R, 200°C; P_{H2}, 4.00 MPa; t_R, 8 h, 800 rpm, 0.0125 mol PhOH in 25.0 mL CH_2Cl_2, 0.9756 g catalyst (0.05 mmol Pt, except for entry 3 and 5).

TABLE 3 | Pt supported on different carriers for HDO of phenol.

Support	X(PhOH)/%	Y(C_6H_{12})/%	S(C_6H_{12})/%	TON(480 min)
SBA-Pr	94.1	92.8	98.6	103.3
SBA-Ar	35.0	23.6	67.4	14.5

Reaction conditions: T_R, 200°C; P_{H2}, 4.0 MPa; t_R, b8 h, 800 rpm; t_R, 4 h, 0.0125 mol PhOH in 25.0 mL CH_2Cl_2, 0.9756 g catalyst (n_{Pt}:n_{PhOH} = 1:250).

TABLE 4 | Acidities of the catalysts and the supports.

Catalysts	Acid Sites/(μmol/g)	pKa
SBA-Pr	810	3.72
Pt/SBA-Pr	790	3.61
SBA-Ar	560	3.26
Pt/SBA-Ar	470	3.18

TABLE 5 | HDO of phenol over 1%Pt/SBA-Pr in different solvents.

Solvent	X(PhOH)/%	Y(C_6H_{12})/%	S(C_6H_{12})/%
H_2O	5.0	3.7	74.0
EtOH	6.7	3.5	52.2
Dioxane	25.0	19.4	77.6
CH_2Cl_2	63.0	60.4	95.9

Reaction conditions: T_R, 200°C; P_{H2}, 3.0 MPa, 800 rpm; t_R, 4 h, 0.0250 mol PhOH in 50.0 mL solvent, 0.4878 g 1%Pt/SBA-Pr (n_{Pt}:n_{PhOH} = 1:1000).

the above results, solvents had significant effects for HDO of phenol, the catalytic activities increased as the polarity of a solvent lowered. The solvent of dichloromethane with the lowest polarity was the best reaction solvent among the solvents tested, including H_2O, EtOH, dioxane, and dicloromethane solvents. So the optimization work was carried out in the solvent of dichloromethane.

Optimization of Reaction Conditions

Figure 5 shows the effects of reaction temperature (TR) on the HDO reaction of phenol over the 1%Pt/SBA-Pr catalyst. Both conversion of phenol and selectivity to cyclohexane increased with the T_R increasing. In the evaluation range of temperature, at 200°C the X(PhOH) and the S(C_6H_{12}) reaches maximum, 63.0 and 95.5%, respectively. The main byproduct was cyclohexanol.

Figure 6 presents the effects of hydrogen pressure (P_{H2}) on the HDO reaction of phenol over the 1% Pt/SBA-Pr catalyst. In the evaluation range the initial hydrogen pressure had little effect on the conversion of phenol, it mainly affected the selectivity to the desired product cyclohexane. The X(PhOH) increased from 56.6 to 69.7% while increasing the P_{H2} from 1.0 MPa to 4.0 MPa. However, the S(C_6H_{12}) increased remarkably from 60.9 to 97.4%. The higher the initial hydrogen pressure was, the larger the concentration of adsorbed active hydrogen on the catalyst surface was, and thus the more conducive to the generation of the target product of cyclohexane.

The effects of the catalyst amount on the HDO reaction of phenol was also investigated over the 1% Pt/SBA-Pr catalyst (**Figure 7**). At the certain reaction condition (P_{H2} = 4.00 MPa, T_R = 200°C, 800 rpm, t_R = 4 h), the conversion of phenol increased with the n_{Pt}/n_{PhOH} increasing from 1:1000 to 1:250, while the selectivity to the target product of cyclohexane remains almost unchanged, meaning that the selectivity to cyclohexane was independent on the amount of Pt metal sites under this reaction condition.

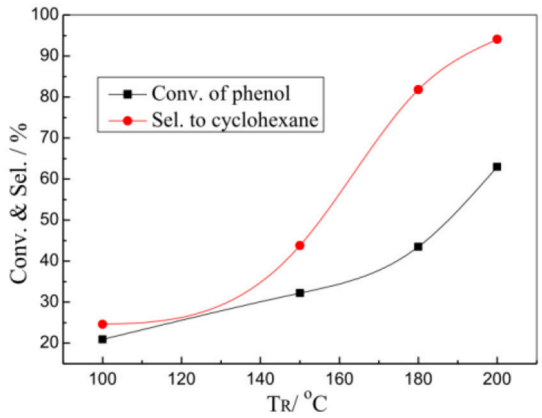

FIGURE 5 | Effect of T_R on the HDO of phenol over 1%Pt/SBA-Pr. Reaction conditions: P_{H2}, 3.00 MPa; 800 rpm; t_R, 4 h, 0.0250 mol PhOH in 50.0 mL CH_2Cl_2, 0.4878 g 1%Pt/SBA-Pr (n_{Pt}:n_{PhOH} = 1:1,000).

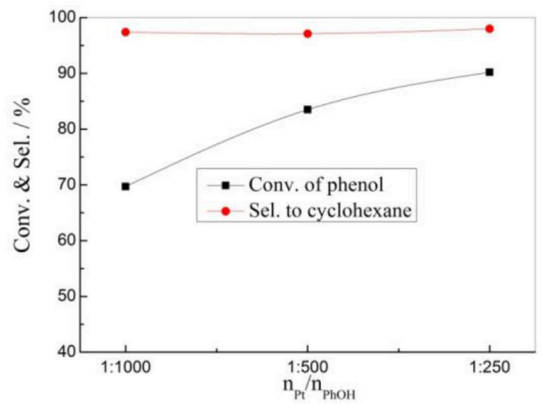

FIGURE 7 | Effect of n_{Pt}/n_{PhOH} on the HDO of phenol over 1%Pt/SBA-Pr. Reaction conditions: P_{H2}, 4.00 MPa; T_R, 200°C; 800 rpm, t_R, 4 h.

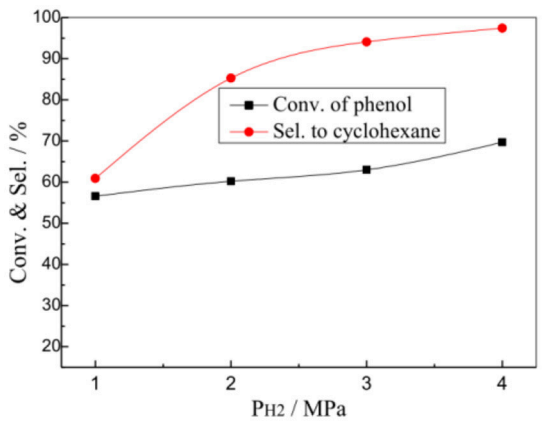

FIGURE 6 | Effect of P_{H2} on the HDO of phenol over 1%Pt/SBA-Pr. Reaction conditions: T_R, 200°C, 800 rpm; t_R, 4 h, 0.0250 mol PhOH in 50.0 mL CH_2Cl_2, 0.4878 g 1%Pt/SBA-Pr (n_{Pt}:n_{PhOH}) = 1:1000).

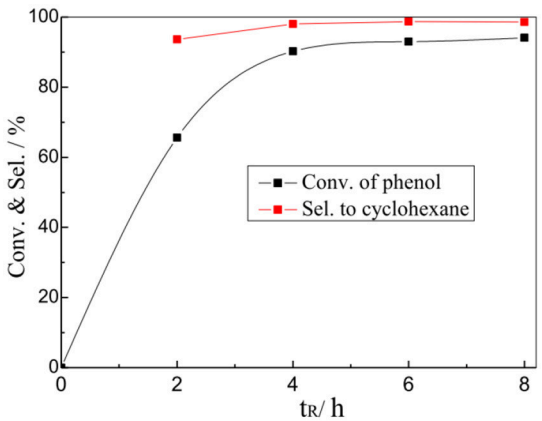

FIGURE 8 | Effect of t_R on the HDO of phenol over 1%Pt/SBA-Pr. Reaction conditions: P_{H2}, 4.0 MPa, TR, 200°C; 800 rpm, 0.0125 mol PhOH in 25.0 mL CH_2Cl_2, 0.9756 g 1%Pt/SBA-Pr (n_{Pt}:n_{PhOH} = 1:250).

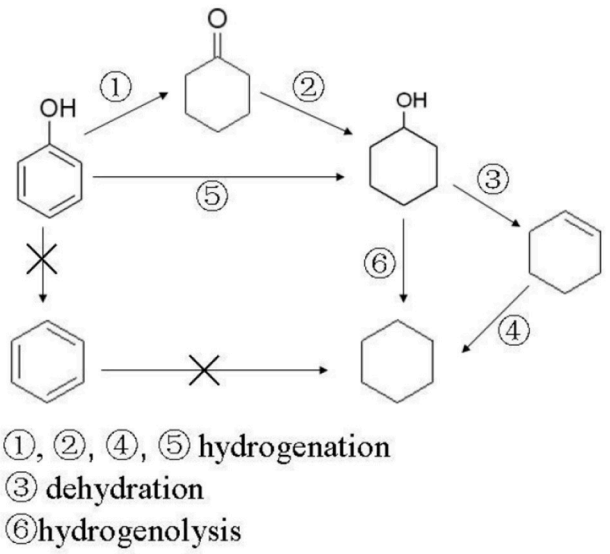

SCHEME 1 | Proposed reaction mechanism for HDO of phenol.

The effect of reaction time on the catalytic performance of 1%Pt/SBA-Pr was also investigated. Most of the phenol was converted within the first 2 h (**Figure 8**). When increasing the reaction time from 4 h to 8 h, the conversion of phenol slightly increased from 90.2 to 94.1%, with the selectivity to cyclohexane almost unchanged.

By screening the reaction temperature, the initial hydrogen pressure, reaction time and the relative content of the catalyst and the reaction solvent, the optimal reaction condition was obtained: $T_R = 200°C$, $P_{H2} = 3.00$ MPa, 800 rpm, $t_R = 4$ h, 0.0125 mol PhOH in 25.0 mL CH_2Cl_2, 0.9756 g 1%Pt/SBA-Pr (n_{Pt}:n_{PhOH}) = 1:250. Under these conditions, the conversion of phenol was 94.1%, and the selectivity to desired product of cyclohexane reached to 98.6%.

Possible Reaction Mechanism

Based on the experimental results a possible reaction mechanism for HDO of phenol was proposed as **Scheme 1**. Experimental results of Kou et al (Yan et al., 2010; Zhao et al., 2010) showed that cyclohexanol can exist stably under acid catalysts below 180°C. Once the temperature was above 180°C under acid catalysts it dehydrated rapidly to produce cyclohexene. But in our reaction conditions, cyclohexene was never detected as, cyclohexene might be easily hydrogenated to cyclohexane in the reaction system. At lower reaction temperatures (below 180°C), or when there are no acidic sites on the catalyst, cyclohexanol cannot dehydrate to form cyclohexene, so hydrogenation reaction is conducted by path ①② or ⑤ to generate cyclohexanol, hydrogenolysis of which takes place to form cyclohexane follow the path of ⑥. Different from the literatures (Hong et al., 2010; Zhu et al., 2011) performing with gas phase reactants in fixed bed reactor, aromatic hydrocarbons, which were produced from hydrogenolysis (direct deoxygenation), could not be found in this work. The difference might result from the different reaction conditions and catalyst systems. Therefore, the reaction pathways might be proposed as the **Scheme 1**.

CONCLUSIONS

In this work, organic-inorganic hybrid materials of SBA-Pr and SBA-Ar were synthesized and loaded with Pt to form bifunctional catalysts. These bifunctional catalysts had good catalytic activities for HDO of phenol to produce cyclohexane, a model reaction of biofuel upgrading. Under optimal reaction conditions, the conversion of phenol was 94.1%, with 98.6% selectivity to the target product of cyclohexane. The metal sites and the acid sites on bifunctional catalysts displayed significant synergistic effect for the HDO of PhOH. The bifunctional catalysts using in this work may be potentially applied to the upgrading of bio-fuel derived from lignin or biomass.

AUTHOR CONTRIBUTIONS

LM was in charge of the writting and designing the experiments. WY and HC performed the experiments. XZ and HL were consultants to the project.

FUNDING

We thank the financial support from Zhejiang Ocean University Research Startup Founding (Q1538) and Department of Education of Zhejiang Province (507300-G21513).

ACKNOWLEDGMENTS

We thank Dr. Yang Tang's benificial discussion in the manuscript.

SUPPLEMENTARY MATERIAL

The Supplementary Material for this article can be found online at: https://www.frontiersin.org/articles/10.3389/fchem.2018.00216/full#supplementary-material

REFERENCES

Boateng, A. A., Mullen, C. A., Goldberg, N., Hicks, K. B., Jung, H. G., and Lamb, J. F. S. (2008). Production of bio-oil from alfalfa stems by fluidized-bed fast pyrolysis. *Ind. Eng. Chem. Res.* 47, 4115–4122. doi: 10.1021/ie800096g

Britt, P. F., Buchanan, A. C., Cooney, M. J., and Martineau, D. R. (2000). Flash vacuum pyrolysis of methoxy-substituted lignin model compounds. *J. Org. Chem.* 65, 1376–1389. doi: 10.1021/jo991479k

Buchmeiser, M. R. (2003). *Polymeric Materials in Organic Synthesis and Catalysis*. Weinheim: WILEY-VCH.

Bui, V. N., Toussaint, G., Laurenti, D., Mirodatos, C., and Geantet, C. (2009). Co-processing of pyrolisis bio oils and gas oil for new generation of bio-fuels: hydrodeoxygenation of guaiacol and SRGO

mixed feed. *Catal. Today* 143, 172–178. doi: 10.1016/j.cattod.2008.11.024

Crossley, S., Faria, J., Shen, M., and Resasco, D. E. (2010). Solid nanoparticles that catalyze biofuel upgrade reactions at the water/oil interface. *Science* 327, 68–72. doi: 10.1126/science.1180769

Dobele, G., Urbanovich, I., Volpert, A., Kampars, V., and Samulis, E. (2007). Fast pyrolysis – effect of wood drying on the yield and properties of bio-oil. *BioResources* 2, 699–706.

Dongil, A. B., Ghampson, I. T., Garc'ia, R., Fierro, J. L. G., and Escalon, N. (2016). Hydrodeoxygenation of guaiacol over Ni/carbon catalysts: effect of the support and Ni loading. *RSC Adv.* 6, 2611–2623. doi: 10.1039/C5RA22540J

French, R., and Czernik, S. (2010). Catalytic pyrolysis of biomass for biofuels production. *Fuel Process Technol.* 91, 25–32. doi: 10.1016/j.fuproc.2009.08.011

Garcia-Perez, M., Chaala, A., Pakdel, H., Kretschmer, D., and Roy, C. (2007). Characterization of bio-oils in chemical families. *Biomass Bioenergy* 31, 222–242. doi: 10.1016/j.biombioe.2006.02.006

Hepditch, M. M., and Thring, R. W. (2000). Degradation of solvolysis lignin using Lewis acid catalysts. *Can. J. Chem. Eng.* 78, 226–231. doi: 10.1002/cjce.5450780129

Hong, D. Y., Miller, S. J., Agrawal, P. K., and Jones, C. W. (2010). Hydrodeoxygenation and coupling of aqueous phenolics over bifunctional zeolite-supported metal catalysts. *Chem. Commun.* 46, 1038–1040. doi: 10.1039/B918209H

Huber, G. W., Iborra, S., and Corma, A. (2006). Synthesis of transportation fuels from biomass: chemistry, catalysts, and engineering. *Chem. Rev.* 106, 4044–4098. doi: 10.1021/cr068360d

Ingram, L., Mohan, D., Bricka, M., Steele, P., Strobel, D., Crocker, D., et al. (2008). Pyrolysis of wood and bark in an auger reactor: physical properties and chemical analysis of the produced bio-oils. *Energ. Fuel.* 22, 614–625. doi: 10.1021/ef700335k

Kudsy, M., and Kumazawa, H. (1999). Pyrolysis of kraft lignin in the presence of molten ZnCl2-KCl mixture. *Can. J. Chem. Eng.* 77, 1176–1184. doi: 10.1002/cjce.5450770614

Lee, E. H., Park, R., Kim, H., Park, S. H., Jung, S. C., Jeon, J. K., et al. (2016). Hydrodeoxygenation of guaiacol over Pt loaded zeolitic materials. *J. Ind. Eng. Chem.* 37, 18–21. doi: 10.1016/j.jiec.2016.03.019

Liu, Q., Wang, S. R., Zheng, Y., Luo, Z. Y., and Cen, K. F. (2008). Mechanism study of wood lignin pyrolysis by using TG–FTIR analysis. *J. Anal. Appl. Pyrol.* 82, 170–177. doi: 10.1016/j.jaap.2008.03.007

Luska, K. L., Migowski, P., Sayed, S. E., and Leitner, W. (2015). Synergistic interaction within bifunctional ruthenium nanoparticle/SILP catalysts for the selective hydrodeoxygenation of phenols. *Angew. Chem. Int. Ed.* 54, 15750–15755. doi: 10.1002/anie.201508513

Mbaraka, I. K., and Shanks, B. H. (2006). Acid strength variation due to spatial location of organosulfonic acid groups on mesoporous silica. *J. Catal.* 244, 78–85. doi: 10.1016/j.jcat.2006.09.001

Meier, D., Berns, J., Faix, O., Balfanz, U., and Baldauf, W. (1994). Hydrocracking of organocell lignin for phenol production. *Biomass Bioenergy* 7, 99–105.

Schmidt, R., Hansen, E. W., Stöcker, M., Akporiaye, D., and Ellestad, O. H. (1995). Pore size determination of MCM-51 mesoporous materials by means of 1H NMR spectroscopy, N2 adsorption, and HREM. A preliminary study. *J. Am. Chem. Soc.* 117, 4049–4056.

Senol, O. I., Viljava, T. R., and Krause, A. O. I. (2005). Hydrodeoxygenation of methyl esters on sulphided NiMo/gamma-Al2O3 and CoMo/gamma-Al2O3 catalysts. *Catal. Today* 100, 331–335. doi: 10.1016/j.cattod.2004.10.021

Shabtai, J. S., Zmierczak, W. W., and Chornet, E. (1999). *Process for Conversion of Lignin to Reformulated Hydrocarbon Gasoline*. Salt Lake City, UT: United States Patent and Trademark Office. 5959167.

Tang, Y., Miao, S. J., Shanks, B. H., and Zheng, X. M. (2010). Bifunctional mesoporous organic–inorganic hybrid silica for combined one-step hydrogenation/esterification. *Appl. Catal. A Gen.* 375, 310–317. doi: 10.1016/j.apcata.2010.01.015

Tang, Y., Yu, W. J., Mo, L. Y., Lou, H., and Zheng, X. M. (2008). One-step Hydrogenation–Esterification of aldehyde and acid to ester over bifunctional Pt catalysts: a model reaction as novel route for catalytic upgrading of fast pyrolysis bio-Oil. *Energy Fuels* 22, 3484–3488. doi: 10.1021/ef800148q

Thring, R. W., and Breau, J. (1996). Hydrocracking of solvolysis lignin in a batch reactor. *Fuel* 75, 795–800. doi: 10.1016/0016-2361(96)00036-1

Wang, C. B., and Yeh, C. T. (2001). Oxidation behavior of alumina-supported platinum metal catalysts. *Appl. Catal. A Gen.* 209, 1–9. doi: 10.1016/S0926-860X(00)00746-8

Wang, L., Zhang, J., Yi, X. F., Zheng, A. M., Deng, F., Chen, C. Y., et al. (2015). Mesoporous ZSM-5 zeolite-supported Ru nanoparticles as highly efficient catalysts for upgrading phenolic biomolecules. *ACS Catal.* 5, 2727–2734. doi: 10.1021/acscatal.5b00083

Wang, Z., Kim, K. D., Zhou, C., Chen, M., Maeda, N., Liu, Z., et al. (2015). Influence of support acidity on the performance of size-confined Pt nanoparticles in the chemoselective hydrogenation of acetophenone. *Catal. Sci. Technol.* 5, 2788–2797. doi: 10.1039/C5CY00214A

Yan, N., Yuan, Y., Dykeman, R., Kou, Y., and Dyson, P. J. (2010). Hydrodeoxygenation of lignin-derived phenols into alkanes by using nanoparticle catalysts combined with Brønsted acidic ionic liquids. *Angew. Chem. Int. Ed.* 49, 5549–5553. doi: 10.1002/anie.201001531

Yu, W. J., Tang, Y., Mo, L. Y., Chen, P., Lou, H., and Zheng, X. M. (2011). One-step hydrogenation–esterification of furfural and acetic acid over bifunctional Pd catalysts for bio-oil upgrading. *Bioresour. Technol.* 102, 8241–8246. doi: 10.1016/j.biortech.2011.06.015

Yue, Y., Gédéon, A., Bonardet, J. L., Melosh, N., D'Espinose, J. B., and Fraissard, J. (1999). Direct synthesis of AlSBA mesoporous molecular sieves: characterization and catalytic activities. *Chem. Commun.* 1967–1968. doi: 10.1039/a904467a

Zhao, C., Kou, Y., Lemonidou, A. A., Li, X., and Lercher, J. A. (2009). Highly selective catalytic conversion of phenolic bio-oil to alkanes. *Angew. Chem. Int. Ed.* 48:3987. doi: 10.1002/anie.200900404

Zhao, C., Kou, Y., Lemonidou, A. A., Li, X., and Lercher, J. A. (2010). Hydrodeoxygenation of bio-derived phenols to hydrocarbons using RANEY Ni and Nafion/SiO2 catalysts. *Chem. Commun.* 46, 412–414. doi: 10.1039/B916822B

Zhao, D., Feng, J., Huo, Q., Melosh, N., Fredrickson, G. H., Chmelka, B. F., et al. (1998). Triblock copolymer syntheses of mesoporous silica with periodic 50 to 300 angstrom pores. *Science* 279, 548–552. doi: 10.1126/science.279.5350.548

Zhu, X., Lobban, L. L., Mallinson, R. G., and Resasco, D. E. (2011). Bifunctional transalkylation and hydrodeoxygenation of anisole over a Pt/HBeta catalyst. *J. Catal.* 281, 21–29. doi: 10.1016/j.jcat.2011.03.030

Conflict of Interest Statement: The authors declare that the research was conducted in the absence of any commercial or financial relationships that could be construed as a potential conflict of interest.

frontiers in Chemistry

ORIGINAL RESEARCH
published: 07 February 2018
doi: 10.3389/fchem.2018.00017

The Correlation of Adsorption Behavior between Ciprofloxacin Hydrochloride and the Active Sites of Fe-doped MCM-41

Ying Wu[1], *Yiming Tang*[1,2,3]*, *Laisheng Li*[1,2,3], *Peihong Liu*[1,2,3], *Xukai Li*[1,2,3], *Weirui Chen*[1] and *Ying Xue*[1]

[1] School of Chemistry and Environment, South China Normal University, Guangzhou, China, [2] Guangdong Provincial Engineering Technology Research Center for Drinking Water Safety, Guangzhou, China, [3] Guangdong Provincial Key Lab of Functional Materials for Environmental Protection, Guangzhou, China

HIGHLIGHTS

- Fe incorporation significantly accelerated the adsorption of CPX on MCM-41.
- Fe leaching can be ignored when pH was higher than 4.0.
- pH played an important role in CPX adsorption on Fe-MCM-41.
- Co-effect of CPX and metal cations on Fe-MCM-41 was investigated.

Fe-MCM-41s with various molar ratios of silicon to iron (20, 40, 80, and 160) were prepared to investigate adsorption properties of ciprofloxacin hydrochloride (CPX) in aqueous solutions. Fe-MCM-41s were characterized by transmission electron microscope (TEM), X-ray diffraction (XRD), X-ray photoelectron spectroscopy (XPS), nitrogen adsorption/desorption isotherms, and infrared spectroscopy (FT-IR). Effects of silicon-iron ratio, adsorbent dosage, pH, and temperature were conducted to explore the adsorption mechanism of CPX on Fe-MCM-41. The results showed that the introduction of iron facilitated the absorption quantity for CPX from 20.04 to 83.33 mg g^{-1} at 120 min of reaction time, which was mainly attributed to surface complexation. The promotion of hydrophobic effect, electrostatic interactions, and π-π electron donor-acceptor interaction also played coordinate roles in the adsorption process. The experimental kinetic data followed both the pseudo-second-order and intra-particle diffusion models, while the adsorption isotherm data fit well to Freundlich model at high temperature. Thermodynamic study showed that the adsorption was spontaneous. Under the effect of electrostatic interaction, pH of the solution strongly affected CPX adsorption. Five representative metal cations (Ca, Cu, Ni, Pb, and Cd) were chosen to study the effects on CPX adsorption and their complexation. The inhibiting effect of metal cations on CPX adsorption was sequenced in the order of Cu > Ni > Pb > Cd > Ca, which followed the same order as the complexation stability constants between CPX and cations. The Fe-MCM-41 adsorbent possessed excellent reusability for 4 cycles use, suggesting a potential applicability of Fe-MCM-41 to remove CPX in water.

Keywords: ciprofloxacin hydrochloride, Fe-MCM-41, adsorption capacity, pH, complexation, metal cations

OPEN ACCESS

Edited by:
Zhimin Ao,
Guangdong University of Technology, China

Reviewed by:
Priyabrat Mohapatra,
C.V. Raman College of Engineering, Bhubaneswar, India
Sijie Lin,
Tongji University, China

***Correspondence:**
Yiming Tang
y.tang@m.scnu.edu.cn

Specialty section:
This article was submitted to Green and Environmental Chemistry, a section of the journal Frontiers in Chemistry

Received: *22 September 2017*
Accepted: *19 January 2018*
Published: *07 February 2018*

Citation:
Wu Y, Tang Y, Li L, Liu P, Li X, Chen W and Xue Y (2018) The Correlation of Adsorption Behavior between Ciprofloxacin Hydrochloride and the Active Sites of Fe-doped MCM-41. Front. Chem. 6:17. doi: 10.3389/fchem.2018.00017

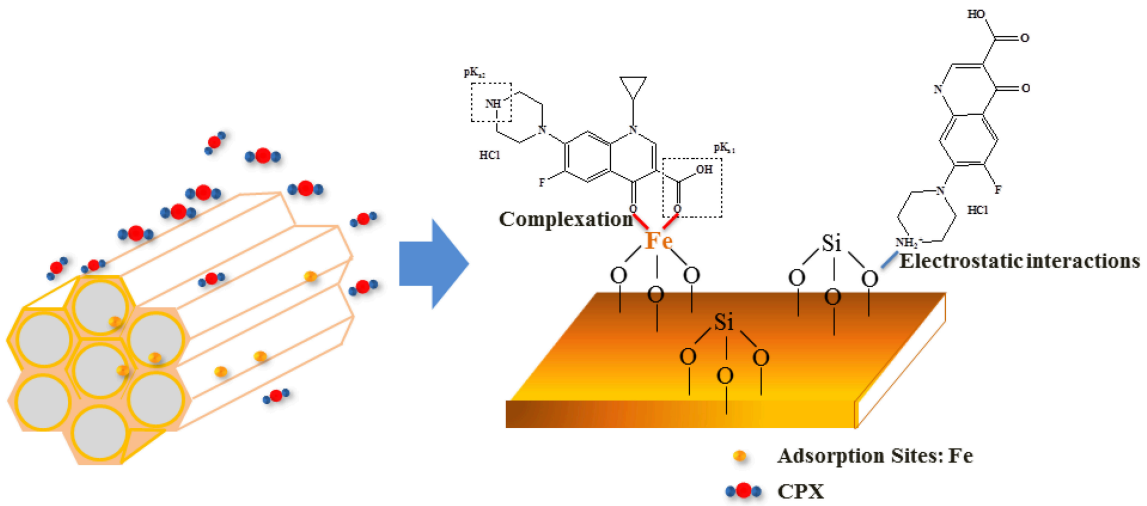

Graphical Abstract | Schematic diagram of adsorption process of CPX by Fe-doped MCM-41 catalyst.

INTRODUCTION

During the last decades, pharmaceuticals and personal care products (PPCPs) among the emerging contaminants have caused more concern of environmental research than the conventional priority pollutants (Arp, 2012; Liu and Wong, 2013; Hayat and Marty, 2014; Montes-Grajales et al., 2017). With abusive use of various antibiotics, large quantity of pharmaceutical wastewater (Cardoso et al., 2014), hospital effluents (Ory et al., 2016; Verlicchi and Zambello, 2016), and excreta-urine (Zheng et al., in press) containing antibiotics have been discharged into environment and regarded as an emerging issue around the world. As a high-use second generation fluoroquinolone, ciprofloxacin hydrochloride (CPX) has the strongest antimicrobial activity and has the highest water concentration in Pearl River of Guangzhou (Bu et al., 2013). Similar to other antibiotics, CPX can transfer in natural environments either as the parent compound or its hydrolysis products, conjugates, oxides when excrete from a target organism (Sarmah et al., 2006) and bring great threats to the ecosystem and human health by inducing proliferation of drug-resistance bacteria (Johnson et al., 2015; Wang et al., 2017b). Therefore, the removal of CPX from water has become a pressing problem. Various methods have been attempted for the removal of CPX from water, such as ultrasound decomposition (Xiao et al., 2013), photocatalytic degradation (Bojer et al., 2017), membrane bioreactor (Hamjinda et al., 2017), ozonation (Gomes et al., 2017), and adsorption on bamboo-based activated carbon (Carabineiro et al., 2012; Peng et al., 2015; Wang et al., 2015), goethite (Gu et al., 2015), graphene oxide (Chen et al., 2015; Fei et al., 2016), Aluminum and Iron hydrous oxides (Gu and Karthikeyan, 2005), and palygorskite-montmorillonite (Berhane et al., 2016). Adsorption technique is widely applied to remove antibiotics from wastewater as a promising method due to its simple theoretical design, ease of operability, relatively low costs and lower amounts of toxic byproducts.

As a member of the M41S family, MCM-41 applied to adsorption area has attracted more awareness because of its hexagonal arrays of uniform channels, high surface area and pore volume and hydrothermal stability (Lee et al., 2007; Jiang et al., 2012). However, hydrophobicity of CPX limits the adsorption capacity by highly hydrophilic MCM-41. Therefore, functional modifications are desired to improve its performance. In the former research, CPX adsorption process can be influenced by metal cations which has been demonstrated that many cations have complexation ability to CPX (Turel et al., 1996). It has been reported that the environmental fate of CPX can be affected by coexisting cations such as Ca and Cu (Pei et al., 2010; Chen et al., 2013). Hence, on the one hand, the introduction of metal ingredient to MCM-41 leads to cation bridging and hydrophobic enhancement, which is beneficial to material for better absorbability. On the other hand, there are few investigations dealing with the different impacts of various free heavy metals on CPX adsorption by comparison.

The main objectives of this paper are to prepare an adsorbent which can enhance the adsorption capacity of CPX by modifying the pure MCM-41 with Fe, to evaluate the effects of various factors including silicon-iron ratio, adsorbent dosage, pH, contact time, temperature, and to study the adsorption mechanisms. Specifically, when CPX coexists with heavy metals in the aqueous phase, the relationship of the formation of Metal cations/CPX complex and the adsorption abilities of CPX is presented to estimate the optimal condition of Fe-MCM-41 adsorbent in practical use.

EXPERIMENTAL SECTION

Materials

These reagents were used to synthesize and modify MCM-41: cetyltrimethyl ammonium bromide (CTAB), sodium silicate ($NaSiO_3 \cdot 9H_2O$) and ferric nitrate ($Fe(NO_3)_3 \cdot 9H_2O$)

were obtained from Sinopharm Chemical Reagent Co. Ltd. (Shanghai, China). For the adsorption experiments, ciprofloxacin hydrochloride (CPX) was obtained from Macklin Biochemical Co. Ltd. (Shanghai, China). Acetonitrile was chromatography grade and was purchased from Tianjin Kemiou Chemical Reagent Co. Ltd. (Tianjin, China). All the other metals were nitrate salt species and analytical grades. Deionized water was used throughout the study. pH value of the solution was adjusted with 0.1 M hydrochloric acid (HCl) and sodium hydroxide (NaOH).

Synthesis of Adsorbent

MCM-41 was prepared via a hydrothermal treatment using $Na_2SiO_3 \cdot 9H_2O$ as silicon source and CTAB as the structure-directing group. Briefly, dissolved sodium silicate (0.1 mol) was stirred at 313 K for 15 min. H_2SO_4 (2 M) was added dropwise to form a gel. After adding CTAB (7.28 g dissolved in 25 ml water at 338 K) to the gel, the mixed solution was stirring for 30 min, and then aged at 418 K for 48 h. The product gotten was filtered after natural cooling, washed with deionized water and dried. Finally, the sample was calcined for 6 h at 823 K to obtain MCM-41. Fe-MCM-41 was prepared from the same route besides adding $Fe(NO_3)_3 \cdot 9H_2O$ as iron modification to the solution before pH adjustment. The samples were designated as Fe-MCM-41(x) (x = 20, 40, 80, and 160), where x was denoted as different molar ratios of Si to Fe for as-synthesized materials.

Analytical Procedures

The low-angle XRD measurements (D8 ADVANCE, BRUKER, German) were carried out in the 2θ ranges of 1.0–8.0°. The N_2 adsorption/desorption isotherms (ASAP2020, Micromeritics, USA) was used to calculate the surface area. The pH_{pzc} value was measured by potentiometric titration. The leaching iron content of the solution was determined by atomic absorption Spectrophotometer (AA-7020, EWAI, China). The FT-IR absorption spectra (6700, Nicolet, USA) was obtained over the range 4,000–400 cm^{-1}.

The concentration of CPX was quantified using HPLC (LC10A, Shimadzu) consisting of a UV detector (SPD-10AV) at 278 nm and a Diamonsil C18 column (250 × 4.6 mm, 5 μm, Dikmate technologies). The mobile phase used for detection of CPX was acetonitrile/0.01 M potassium dihydrogen phosphate (23:77, v/v) and the flow rate was 1.0 mL min^{-1}.

Batch Adsorption Experiments

For adsorption experiments, 0.04 g of adsorbent was mixed with 200 mL of CPX solution (20 mg L^{-1}, initial pH = 5.40) in flasks and the mixture stirred at 303 K up to beyond the equilibrium time. The rotating speed was set to 175 rpm. Additional experiments were also performed to study the effects of equilibrium time, dosage, pH, temperature and metal cations on the adsorption properties. To study the impact of various metal cations on the adsorption behavior of CPX, predetermined amounts of Ca(II), Cu(II), Ni(II), Pb(II), Cd(II) were introduced to obtain 0.01 M ionic strength solutions at 303 K, respectively. Controls without Fe-MCM-41 were considered to explain losses from adsorption to flasks. All experiments were run in triplicate under the same conditions.

A series of adsorbent doses from 30 to 60 mg were selected to discuss the effect of dosage. The pH effects experiments were conducted by adjusting the pH between 3 and 11. To study the impact of various metal cations on the adsorption behavior of CPX, predetermined amounts of Ca(II), Cu(II), Ni(II), Pb(II), Cd(II) were added to obtain 0.01 M ionic strength solutions at 303 K, respectively. The isotherms were obtained by batch experiments performed at 293 ± 0.5, 303 ± 0.5, 313 ± 0.5 K, respectively. The initial concentrations of CPX (varying from 20 to 80 mg L^{-1}) were chosen based on preliminary experiments, which controlled the adsorbed amount of CPX between 30 and 90% of the initial amounts. A study of reusability was carried out by adsorption/desorption for four times.

RESULTS AND DISCUSSION

Characterization of Adsorbents Used in This Work

Figure 1 showed the low angle XRD patterns of all absorbents at different molar ratios of Si to Fe and pure sample. All absorbents had three well-resolved peaks indexed to (100), (110), and (200) diffraction planes, indicating a highly ordered hexagonal mesostructure (Li et al., 2012). When the silicon-iron ratio decreased, iron content became higher, the intensity of the peaks diminished and the peak width increased. This meant the introduction of excess iron could reduce ordering of the structure. The result of the segment was consistent with the TEM exhibited in Figure S1.

All isotherms in **Figure 2** belonged to type IV isotherm according to IUPAC classification. Compared with the other four absorbents, the BET curve and the BJH pore size distribution curve of Fe-MCM-41(20) exhibited obviously different. The position closed to $p/p_0 = 0.9$ showed a distinct region of steep increase, which was corresponding to the capillary condensation in the pristine silica gel pores (Kolesnikov et al., 2017). This

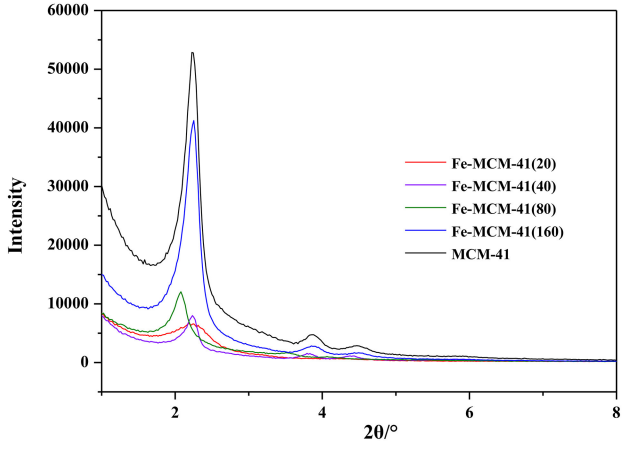

FIGURE 1 | The XRD pattern of Fe-MCM-41(x) (x = 20, 40, 80, and 160, x was denoted as molar ratio of Si to Fe).

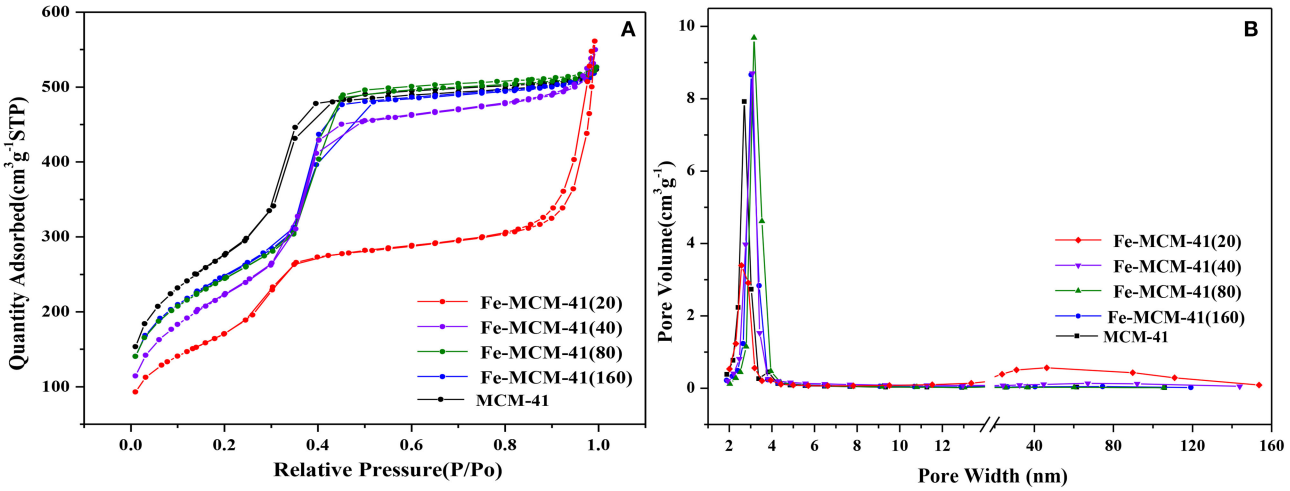

FIGURE 2 | (A) The nitrogen adsorption/desorption isotherms, and **(B)** pore size distributions of Fe-MCM-41(x) (x = 20, 40, 80, and 160, x was denoted as molar ratio of Si to Fe).

was similar to the above discussion of XRD that the pores size increased after iron-doping during aging process gradually. Except for tiny amounts of macroporous structures, the vast majority of pore widths were below 5 nm. It could be seen from the structural properties of all absorbents in Table S1. The pore diameters increased from 3.15 to 4.33 nm and the BET surface area decreased from 1002.1 to 625.6 m^2 g^{-1}. Note that by replacing Si^{4+} (0.40 Å) with Fe^{3+} (0.63 Å) in the structure of material, the extension of radius enlarged the pore sizes and decreased surface area. Moreover, XPS was provided to clarify the chemical phase of Fe species in the synthesized Fe-MCM-41. XPS spectrum in **Figure 3** gave a description that the peaks at 712 and 725 eV for the binding energies of $Fe2p_{3/2}$ and $Fe2p_{1/2}$, reflecting iron species existed as Fe^{3+} in Fe-MCM-41 (Nie et al., 2015).

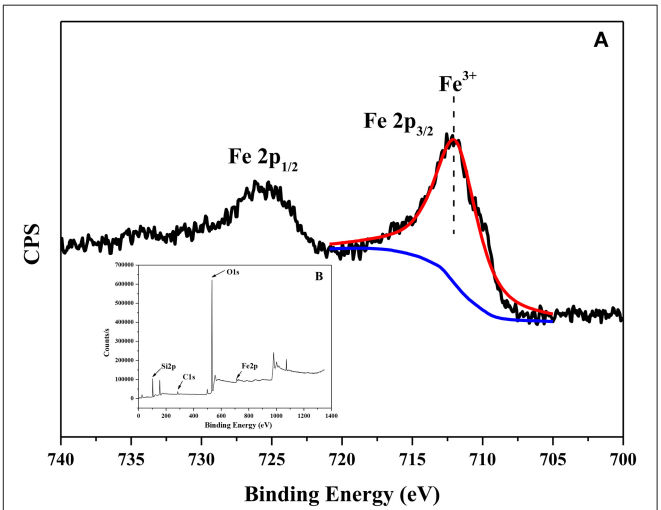

FIGURE 3 | XPS spectrum of Fe-MCM-41.

Effect of Silicon-Iron Ratio

In **Figure 4**, the removal efficiency for CPX decreased with the increasing surface area of Fe-MCM-41. Hydrophobic compound was difficult to be adsorbed on the surface of mesoporous MCM-41 silica which contained large amounts of Si–OH (Hu et al., 2014), and iron doping strengthened the surface hydrophobicity. More importantly, CPX with the numerous reactive functional groups like carboxyl, keto, and piperazine could form complexes with majority of metal cations (Turel, 2002; Sun et al., 2014). As seen in **Figure 5**, the interactions between CPX and Fe-MCM-41 were investigated by comparing the FT-IR spectra of CPX, fresh and used Fe-MCM-41 in the range of 1250–1800 cm^{-1}, which included the main characteristic peaks (Full scale FT-IR curve could be found in Figure S2 in Supplementary Information). The band positions and their corresponding band assignments were listed in **Table 1** (Gu and Karthikeyan, 2005; Trivedi and Vasudevan, 2007; Wang et al., 2011; Peng et al., 2012). The position of C=O stretching vibration of pyridine-keto upshifted slightly to a higher frequency of 1631.4 cm^{-1} after adsorption and the 9.4 cm^{-1} shift indicated reinforcement of the C=O bond. That was ascribed to the release of intramolecular hydrogen bond between the ortho substituted carboxylate group and Fe-MCM-41 which was an indirect evidence for ferric-ciprofloxacin interactions. Meanwhile, the intensity of this peak was much weaker, suggesting that the fraction of pyridine-keto group interacted with Fe-MCM-41. The most significant feature of CPX adsorbed on Fe-MCM-41 was the complete disappearance of the peak at 1698.7 cm^{-1}, which indicated that all the carboxyl groups participated in the binding reaction with Fe-MCM-41. The band shifting from 1382.8 to 1384.2 cm^{-1} demonstrated that electrostatic interactions were occurred between the negative sites on the absorbent surface and the protonated amine group. The shift exhibited by the band between 1445.8 to 1474.6 cm^{-1} meant the C–N bond of amine group also supported this assumption. Overall, it was almost certain that iron doping added the sites of adsorption

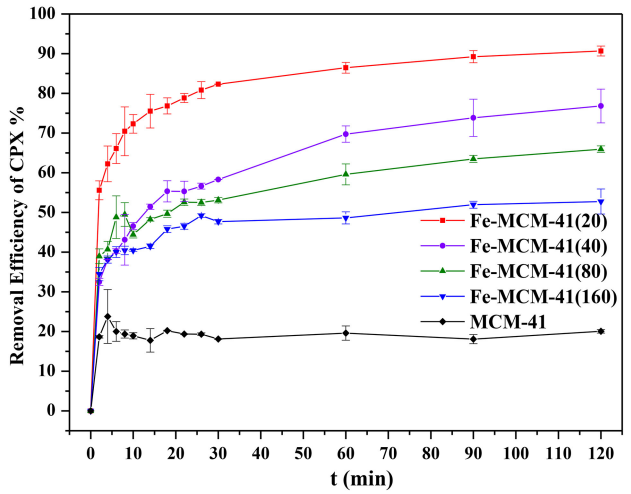

FIGURE 4 | Adsorption of CPX on Fe-MCM-41(x) (x = 20, 40, 80, and 160, x was denoted as molar ratio of Si to Fe; volume of CPX solution: 200 mL; rotating speed: 175 rpm/min; initial pH value: 5.40; equilibrium time: 120 min).

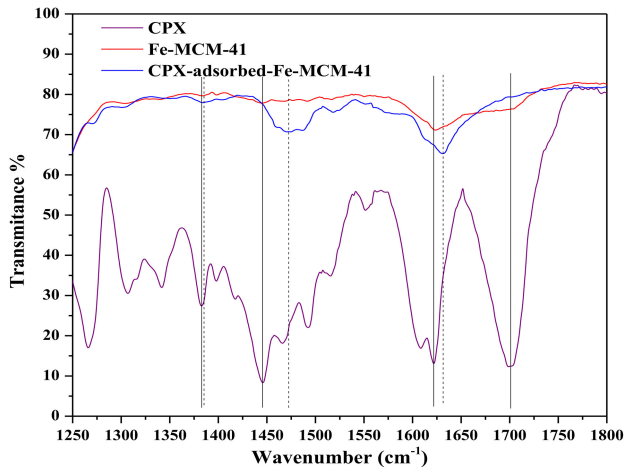

FIGURE 5 | FT-IR spectra of CPX, Fe-MCM-41 and CPX-adsorbed Fe-MCM-41. The characteristic band positions of pure CPX were marked by black lines. The distinctive band positions of CPX as a result of adsorption on Fe-MCM-41 were denoted by dashed lines.

(see **Graphical Abstract**). The complex was present through the cation bridging of Fe(III) with the adjacent carbonyl oxygen and the oxygen from the deprotonated carboxylate group. The other absent peaks after adsorption might show signs of other adsorption affinity, for instance, hydrophobic effect and π-π interaction (discussed later). Fe-MCM-41 (20) was chosen as the adsorbent for the subsequent research.

Influence of Adsorbent Dose and Kinetics of Adsorption

Figure 6 illustrated the influence of adsorbent dose on the uptake of CPX. It was displayed that the removal efficiency

TABLE 1 | FT-IR band positions (cm^{-1}) and suggested assignments for CPX and CPX-adsorbed samples.

CPX	CPX-adsorbed samples	Band assignment
1621.85	1631.24	υ (pyridine-keto C=O)
1698.69	–	υ (carboxylic acid C=O)
1445.81	1474.64	υ (Stretching of C–N)
1382.75	1384.16	Protonation of amine group in the piperazine moiety

υ, stretching; δ, bending.

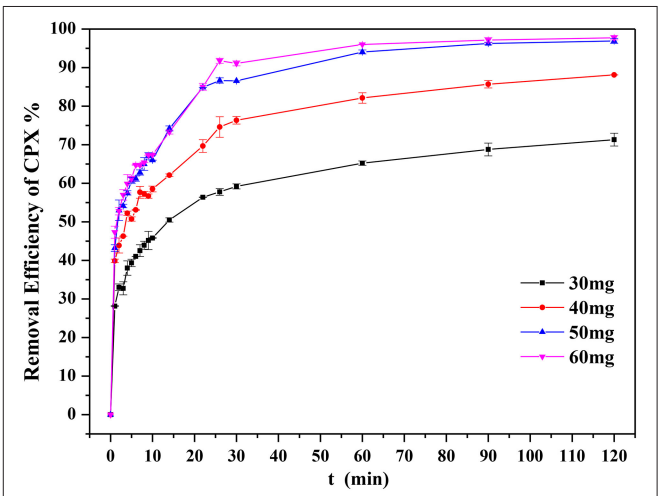

FIGURE 6 | Influence of adsorbent dosage (volume of CPX solution: 200 mL; initial concentration = 20 mg L^{-1}; rotating speed: 175 rpm/min; temperature: 303 K; initial pH-value: 5.40).

increased with adsorbent dose. This behavior could be explained by adsorption mainly occurring at active sites when the adsorbent dose was large. The high removal efficiency for CPX reflected the satisfactory textural and structural properties of the adsorbent. Therefore, 40 mg adsorbent dose was chosen for the following study.

The kinetics could be employed to evaluate the performance of the adsorbent and give the underlying adsorption mechanisms. Three available kinetic models were examined as follows:

Pseudo-first-order kinetic equation:

$$\frac{1}{q_t} = \frac{k_1}{q_e} \times \frac{1}{t} + \frac{1}{q_e} \quad (1)$$

Pseudo-second-order kinetic equation:

$$\frac{t}{q_t} = \frac{t}{q_e} + \frac{1}{k_2 \times {q_e}^2} \quad (2)$$

Where q_e and q_t were the adsorption amounts at equilibrium and time t, respectively. k_1 and k_2 were defined as reaction rate constants.

Intra-particle diffusion model:

$$q_t = k_i \times t^{1/2} + c_i \quad (3)$$

Where k_i was defined as rate constant at stage i, k_i could be obtained by plotting q_t vs. $t^{1/2}$.

The avidity of three kinetic models was analyzed by fitting straight lines in **Figures 7A–C**. **Table 2** listed the kinetics parameters for three reaction orders. It was obvious that the experimental data of CPX adsorbed by Fe-MCM-41 were more accurately simulated by pseudo-second-order model with higher correlation coefficients (R^2) value. Also, based on the second-order model, the calculated q_e ($q_{e,cal}$) was a good agreement with the experimental q_e ($q_{e,exp}$) values, besides q_e ($q_{e,exp}$) increased from 20.12 to 95.24 mg g^{-1} with Fe content. Compared the various adsorption capacities of CPX with those reported adsorbents such as Graphene oxide/calcium alginate (GO/CA) (Wu et al., 2013), Carbon nanofibers (Li et al., 2015), Goethite (MacKay and Seremet, 2008) and Illite (Wang et al., 2011), $H_2Ti_2O_5{\cdot}H_2O$ (Wu et al., 2014), and Fe_3O_4/C (Shi et al., 2013) as showed in **Table 3**, Fe-MCM-41 showed better adsorption property which required a shorter time to reach adsorption equilibrium and possessed a higher adsorption capacity.

The models discussed above were not able to describe the phenomena of intraparticle or pore diffusion, which were often the rate-limiting steps in an adsorption process. With the intra-particle diffusion model, **Figure 7C** exhibited that the adsorption plots of adsorbents were not linear and could be divided into three linear regions, denoting that the multi stages of the intraparticle adsorption (Ghaedi et al., 2012). The first-stage portion was sharper and did not pass through zero point, which was due to the diffusion of adsorbents through the bulk solution to the external surface. It demonstrated that particle diffusion was not only the sole rate-limiting step, but also controlled by boundary layer in the initial phase of the adsorption. These results could be validated by further analyzing data with Boyd's mode which was expressed as follows:

$$F = 1 - \frac{6}{\pi^2}\exp(-Bt) \tag{4}$$

$$F = \frac{q_t}{q_e} \tag{5}$$

$$Bt = -0.4977 - \ln(1 - F) \tag{6}$$

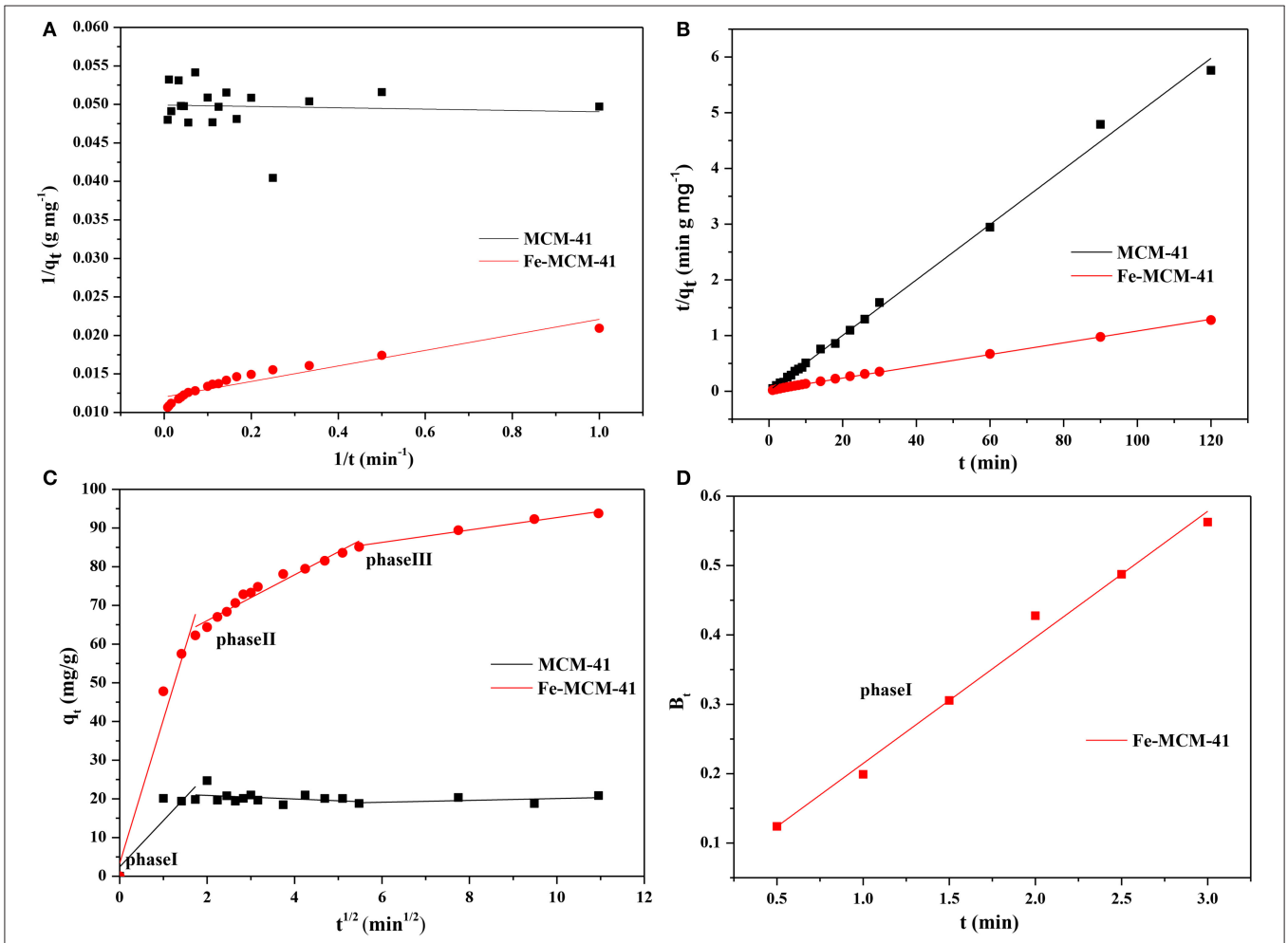

FIGURE 7 | The adsorption Kinetics of CPX by MCM-41 and Fe-MCM-41 **(A)** pseudo-first-order model, **(B)** pseudo-second-order model, **(C)** intra-particle diffusion model and **(D)** Boyd plots for CPX adsorption at different temperatures.

TABLE 2 | Kinetic parameters for the adsorption of CPX on MCM-41 and Fe-MCM-41.

Kinetic model	Parameters	Values	
		MCM-41	Fe-MCM-41
Pseudo-first-order	$q_{e,cal}$ (mg g^{-1})	20.0361	83.3333
	k_1 (min^{-1})	−0.0175	0.8417
	R^2	−0.0573	0.8950
Pseudo-second-order	k_2 (g mg^{-1} min^{-1})	0.2775	0.0043
	R^2	0.9996	0.9993
	$q_{e,exp}$ (mg g^{-1})	20.8354	93.7965
	$q_{e,cal}$ (mg g^{-1})	20.1207	95.2381
Intra-particle diffusion	K_I	11.9766	37.1644
	C_I	2.4231	3.3595
	R^2	0.7465	0.9408
	K_{II}	−0.4644	5.9203
	C_{II}	21.8282	54.2310
	R^2	0.0572	0.9603
	K_{III}	0.2410	1.6064
	C_{III}	17.6776	76.6507
	R^2	−0.0625	0.9796

TABLE 3 | Adsorption capacities of CPX on various adsorbents.

Adsorbents	Adsorption amounts (mg g^{-1})	Rate constant of Pseudo second-order kinetic equation (g mg^{-1} min^{-1})	References
Illite	36.781	0.00449	Wang et al., 2011
Graphene oxide/calcium alginate (GO/CA)	12.1124	0.1604	Wu et al., 2013
Carbon nanofibers	639.602	0.00093	Li et al., 2015
Goethite	3.678	–	MacKay and Seremet, 2008
$H_2Ti_2O_5{\cdot}H_2O$	14.81	–	Wu et al., 2014
Fe_3O_4/C	38.61	–	Shi et al., 2013
Fe-MCM-41	93.7965	0.0043	This work

Where q_t and q_e were the adsorption amounts at any time t and equilibrium, F given by Equation (5) was the fraction at time t, B_t denoted a mathematical function of F.

The linearity of the plot was applied to differentiate the controlled rates of adsorption between external transport and intra-particle diffusion. The plot in **Figure 7D** were linear and did not move toward the zero point, demonstrating that external transfer governed adsorption process at the start and then the intra-particle diffusion.

The second-stage portion became slower than first stage due to the weak adsorption between CPX and the surface atoms of the solid. The third-stage portion tended to ease up and reached final equilibrium. It could be attributed to the smaller pores, lower concentration of CPX and enhanced electrostatic repulsion (between CPX and the adsorbents surface). What's more, comparisons of the values of k_i also proved that the adsorption rate became slower during the adsorption process. It concluded that the intraparticle diffusion was present while some other mechanisms might be involved.

Effect of the Temperature

The adsorption isotherm in **Figure 8** described the equilibrium relationships between the liquid-phase CPX concentration and the amount of CPX on the Fe-MCM-41. The adsorption capacities of the CPX increased with temperature, indicating that adsorption process on Fe-MCM-41 was favored at higher temperatures. The phenomenon could be ascribed to promote mobility of the CPX molecules in solution and increased new active sites on the Fe-MCM-41 for adsorption (Ghaedi et al., 2012). The results also suggested that it was an endothermic process in nature.

For further examining the impact of temperature on adsorption process, thermodynamic parameters was determined at three temperatures (Ao et al., 2009). As listed in **Table 4**, the adsorption parameters were fitted by the most frequently utilized adsorption isotherms models named Langmuir and Freundlich models at 293, 303, and 313 K. It was apparent that the Langmuir isotherm better represented the experimental data with higher value of the determination coefficient ($R^2 = 0.9459$) at 293 K while Freundlich model yielded the best fit at temperatures 303 K ($R^2 = 0.9544$) and 313 K ($R^2 = 0.9675$). This implied monolayer adsorption with a value of 133.33 mg g^{-1} obtained for q_{max} and evenly distribution of the adsorption sites at low temperature. However, as temperature rose, the Freundlich equation became even more accurate to assess the adsorption process. It was possible to deduce that the thermal treatments activated more active sites for adsorption as described above. Molecules of CPX retained two monolayer adsorptions when the pore diameter of Fe-MCM-41 was greater than molecule diameter of CPX, and despite reversible adsorption occurred meanwhile (Song et al., 2013; Wang et al., 2017a). This non-linear adsorption also demonstrated that the adsorption process was the result of interaction of various forces. The increased values of K_F with temperature demonstrated the endothermic adsorption process. The n-values were more than 1, revealing a beneficial adsorption system and heterogeneity of Fe-MCM-41 adsorption sites (Wu et al., 2017).

As listed in **Table 5**, the thermodynamic parameters, such as enthalpy change (ΔH), entropy change (ΔS), and the Gibb's free energy (ΔG), were evaluated to obtain insights into the changes of adsorption processes using the Van't Hoff equation (Jiang et al., 2013). The value of K_d, an equilibrium constant, was obtained by dividing q_e and C_e. The thermodynamic parameters of adsorption could be determined by using Equations (7) and (8):

$$\Delta G = -R \times T \times \ln K_d \tag{7}$$

$$\ln K_d = \frac{\Delta S}{R} - \frac{\Delta H}{R \times T} \tag{8}$$

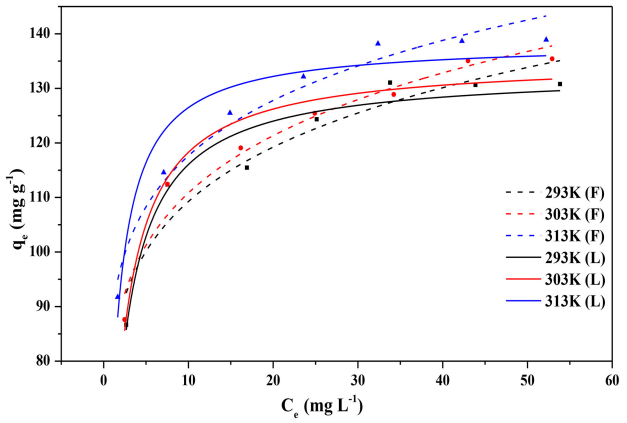

FIGURE 8 | The adsorption isotherm of CPX on Fe-MCM-41(20), solid lines represent Langmuir model fits to the data, dotted lines represent Freundlich model fits to the data (volume of CPX solution: 200 mL; rotating speed: 175 rpm/min; initial pH-value: 5.40; equilibrium time: 120 min).

TABLE 4 | Adsorption isotherms constants and correlation coefficients.

T (K)	Langmuir $\frac{1}{q_e} = \frac{1}{q_m \times k_L \times Ce} + \frac{1}{q_m}$			Freundlich $q_e = K_F \times C_e^{1/n}$		
	K_L (L mg^{-1})	q_m (mg g^{-1})	R^2	K_F (mg g^{-1}) /(mg L^{-1})$^{1/n}$	n	R^2
293	0.701	133.333	0.9459	71.4140	7.513	0.9080
303	0.74	135.135	0.9497	70.8384	7.337	0.9544
313	1.177	136.986	0.9167	78.3907	8.071	0.9675

TABLE 5 | Thermodynamic parameters for the adsorption under different temperature.

T (K)	ΔG (KJ mol^{-1})	ΔH (KJ mol^{-1})	ΔS (KJ mol^{-1} K^{-1})
293	−7.5041	9.926	59.2
303	−7.8718		
313	−8.6888		

The negative ΔG-values were obtained in the range of 293–313 K, revealing the feasible and spontaneous of adsorption process. The positive ΔH-value demonstrated an endothermic process while the positive value of ΔS indicated that the organization of the CPX molecular at the solid- liquid interface became more random than low temperature.

Effect of pH on the Adsorption of CPX

The pH_{pzc} of Fe-MCM-41(20) was estimated to be around 5.4, the surface charge of Fe-MCM-41(20) remained negative over the range of pH (5.4 < pH < 11.0) in this study. Therefore, the speciation of CPX molecules were regarded as the mainly factor to this pH range (5.4 < pH < 11.0) influence on the adsorption level. **Figure 9** indicated the pH dependency of CPX adsorption on Fe-MCM-41(20). As seen there, a bell-shaped adsorption envelop was noticed. Initially, adsorption increased with pH from 5 to 10 and reached to a maximum value. At pH values >10, adsorption decreased sharply with increasing pH. The acid dissociation constants pK_{a1} and pK_{a2} values of CPX were 6.1 and 8.7, respectively. Most of CPX molecular were in cationic form with protonated amine group in the piperazine moiety when pH was less than 6.1. Cationic CPX generated electrostatic attraction with negatively charged Fe-MCM-41(20) on the surface, accordingly promoting the adsorption. As displayed in **Figure 9B**, a great amount of Fe leached and the structure of adsorbent collapsed at strong acidic environment (pH < 4), which greatly reduced the adsorption ability. When 6.1 < pH < 8.7, CPX removal efficiency increased with its zwitterion form. The zwitterionic CPX was least soluble at pH 7.5 in water for its neutral charge (Roca Jalil et al., 2015). In other word, it could be assumed that hydrophobic effect had played an important role in the adsorption process. When pH value was above 8.7, the anionic form could induce the electrostatic repulsion between CPX and Fe-MCM-41. When 8.7 < pH < 10, another force might exist to balance the hydrophobic effect and electrostatic repulsion which suggested as π-electron-donor–acceptor (EDA) interaction between CPX and Fe-MCM-41(20). The aromatic ring could serve as π-electron acceptors due to the strong electron-withdrawing ability of fluorine group on the benzene ring of CPX. In this, the hydroxyl groups on adsorbent surface acting as electron-donors interacted strongly with the π-acceptor compound. When pH > 10, a drastic decrease of CPX adsorption amount was due to the strong electrostatic repulsion effect. Therefore, strong chemical interactions were of vital importance for CPX adsorption on Fe-MCM-41(20).

The Effect of Metal Cations

Metal cations with relatively high concentration could impact CPX adsorption. The presence of Cu(II) facilitated the adsorption of CPX on montmorillonite at pH > 6.0 (Pei et al., 2010). Similar conclusion was also given on activated carbon at pH 3.4–6.5 (Sun et al., 2014). As depicted in **Figure 10**, all metal cations suggested a significantly decline to the adsorption property of CPX, whether it be Ca represented alkaline earth element or those metals which were common divalent metals (Cu, Ni, Pb, and Cd) in water. The influence of five metal cations on removal efficiency followed a decreasing order of Cu (52.3%) > Ni (49.0%) > Pb (28.3%) >Cd (21.9%) >Ca (18.7%). This phenomenon could be assumed that metal cations screened negative charged sites of adsorbent surface. Metal cations had a relatively strong affinity to CPX. In order to make a thorough exploration about the complexing ability of five metal ions, the complexation stability constants were listed in **Table 6** (combined with the prior results). Some conclusions can be drawn from the values. On the basis of the liberation degrees of CPX, which complexed with metal cations mainly in three forms: $[M(AH)]^{2+}$, $[M(AH)_2]^{2+}$, $[M(AH)A]^{+}$. Because of the solution under neutral conditions, $[M(AH)]^{2+}$ was the main form. Compared to other divalent metals, the complexation ability of CPX with Cu was much stronger, and the result agreed with the heavy metals which exhibited different removal efficiency.

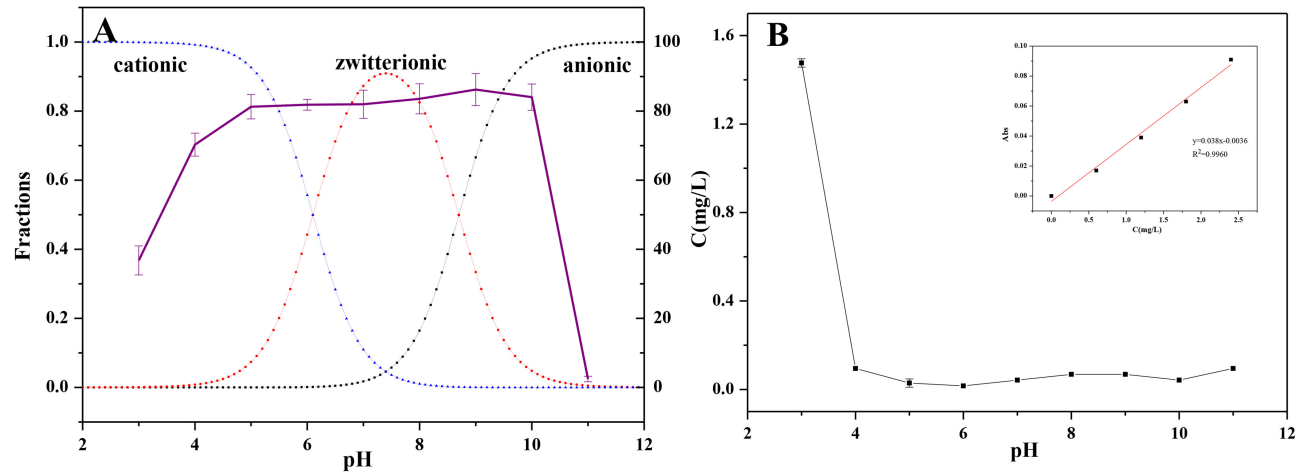

FIGURE 9 | (A) The relation of removal efficiency of CPX to the pH values of Fe-MCM-41 at 298 K (The dotted lines represented the fraction of cationic, zwitterionic, and anionic forms of CPX), **(B)** the leaching of Fe content at different pH-value.

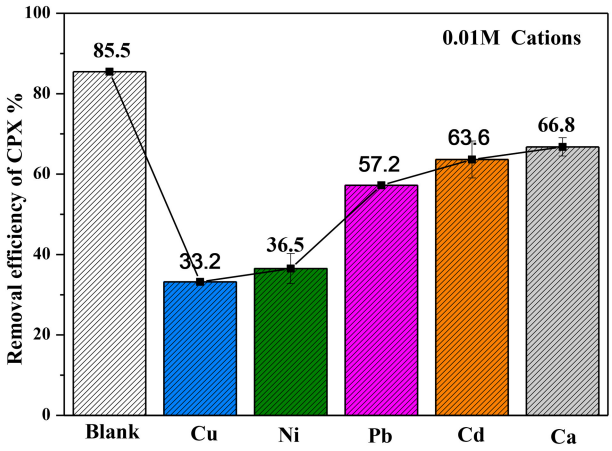

FIGURE 10 | Influence of metal cations on removal efficiency of CPX (volume of CPX solution: 200 mL; rotating speed: 175 rpm/min; initial pH-value: 5.40; equilibrium time: 120 min).

TABLE 6 | Complexation constants of CPX with metals found in the literature.

Equilibria	Ca	Cu	Ni	Cd	Pb	References
$M^{2+}+HA^{\pm} = [M(AH)]^{2+}$	2.75	6.19	4.39			Turel et al., 1996
$[M(AH)]^{2+}+HA^{\pm} = [M(AH)_2]^{2+}$		5.26	4.3			
$[M(AH)_2]^{2+} = [M(AH)A]^{+}+H^{+}$		−6.6	−7.35			
$M^{2+}+HA^{\pm} = [M(AH)]^{2+}$	2.75	6.14		3.14	3.86	Tan et al., 2014
$[M(AH)]^{2+}+HA^{\pm} = [M(AH)_2]^{2+}$		10.49		5.01	7.51	
$[M(AH)_2]^{2+} = [M(AH)A]^{+}+H^{+}$		3.32		−1.12	0.38	

Regeneration of the Adsorbent

It was important for an adsorbent with good reuse performance in practical application. According to the investigation of pH influence, the adsorption capacity of CPX on Fe-MCM-41 was negligible when the pH was above 10. It indicated that of CPX could desorbed from the absorbent surface using 0.1 M NaOH solution as the desorption agents possibly, then the adsorbent was filtered, washed and dried at 358 K. The regenerated adsorbent was tested by four cycles of adsorption/desorption process under the same conditions. **Figure 11** presented the removal efficiency of CPX on the recycled Fe-MCM-41, exhibiting slightly decline with a loss of 23.6% after four cycles, which might due to the damage of adsorption sites. Therefore, Fe-MCM-41 could be recycled as an efficient absorbent for practical application.

CONCLUSIONS

Fe-MCM-41s prepared from a hydrothermal process were used as adsorbents to adsorb the CPX in aqueous solutions. Experimental results described that Fe-MCM-41 with Si/Fe = 20 exhibited the best CPX removal efficiency. The XRD and TEM results confirmed that the hexagonal mesoporous structure maintained after iron doping. A combination of multiple effects including electrostatic interaction, surface complexation, hydrophobic effect and π-π interaction on the adsorption process were confirmed under different reaction conditions. The experimental kinetic data showed that the adsorption was a chemical-controlling and multi-step process, Fe-MCM-41 showed the better adsorption property. Strong acidic/alkaline environment was not conducive to the adsorption process. The adsorption performed a higher adsorption affinity at higher temperature was a spontaneous exothermic process. Moreover,

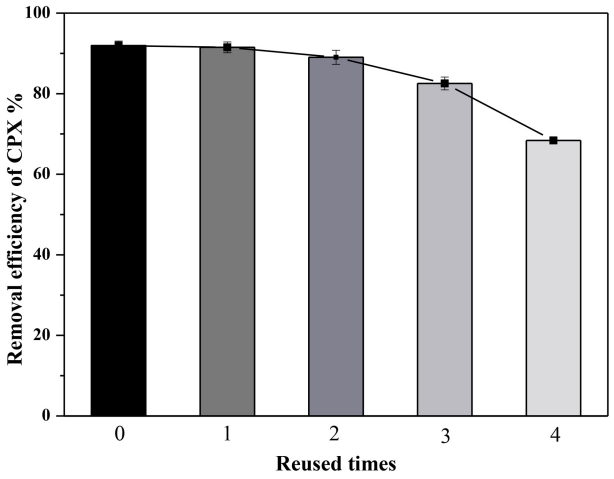

FIGURE 11 | Regenerated use of Fe-MCM-41 adsorbent for removal of CPX (volume of CPX solution: 200 mL; rotating speed: 175 rpm/min; initial pH-value: 5.40; equilibrium time: 120 min).

due to the depression of Me-CPX complex, metal cations decreased CPX adsorption on Fe-MCM-41 surface. As the same order as the complexation stability constants of CPX, Cu impacted CPX adsorption most. Fe-MCM-41 exhibited stable performances for 4 cycles use without deterioration which could possibly applied to wastewater treatment including POPs.

AUTHOR CONTRIBUTIONS

YW: Conducted all the experiments; YT: Supervised the project; LL: Revised the manuscript; PL and XL: Provided assistance in setting up the gears; WC and YX: Helped analysis the data.

ACKNOWLEDGMENTS

This work was supported by the project of the Science Technology Office of Guangzhou (201607010276), China Postdoctoral Science Foundation (2016M602483) and the Ph.D. start-up Fund of Natural Science Foundation of Guangdong Province, China (2017A030310420).

SUPPLEMENTARY MATERIAL

The Supplementary Material for this article can be found online at: https://www.frontiersin.org/articles/10.3389/fchem.2018.00017/full#supplementary-material

REFERENCES

Ao, Z. M., Li, S., and Jiang, Q. (2009). Thermal stability of interaction between the CO molecules and the Al doped graphene. *Phys. Chem. Chem. Phys*. 11, 1683–1687. doi: 10.1039/b812188e

Arp, H. P. (2012). Emerging decontaminants. *Environ. Sci. Technol.* 46, 4259–4260. doi: 10.1021/es301074u

Berhane, T. M., Levy, J., Krekeler, M. P. S., and Danielson, N. D. (2016). Adsorption of bisphenol A and ciprofloxacin by palygorskite-montmorillonite: effect of granule size, solution chemistry and temperature. *Appl. Clay Sci.* 132–133, 518–527. doi: 10.1016/j.clay.2016.07.023

Bojer, C., Schöbel, J., Martin, T., Ertl, M., Schmalz, H., and Breu, J. (2017). Clinical wastewater treatment: photochemical removal of an anionic antibiotic (ciprofloxacin) by mesostructured high aspect ratio ZnO nanotubes. *Appl. Catal. B Environ*. 204, 561–565. doi: 10.1016/j.apcatb.2016.12.003

Bu, Q., Wang, B., Huang, J., Deng, S., and Yu, G. (2013). Pharmaceuticals and personal care products in the aquatic environment in China: a review. *J. Hazard. Mater*. 262, 189–211. doi: 10.1016/j.jhazmat.2013.08.040

Carabineiro, S. A. C., Thavorn-Amornsri, T., Pereira, M. F. R., Serp, P., and Figueiredo, J. L. (2012). Comparison between activated carbon, carbon xerogel and carbon nanotubes for the adsorption of the antibiotic ciprofloxacin. *Catal. Today* 186, 29–34. doi: 10.1016/j.cattod.2011.08.020

Cardoso, O., Porcher, J. M., and Sanchez, W. (2014). Factory-discharged pharmaceuticals could be a relevant source of aquatic environment contamination: review of evidence and need for knowledge. *Chemosphere* 115, 20–30. doi: 10.1016/j.chemosphere.2014.02.004

Chen, H., Gao, B., and Li, H. (2015). Removal of sulfamethoxazole and ciprofloxacin from aqueous solutions by graphene oxide. *J. Hazard. Mater*. 282, 201–207. doi: 10.1016/j.jhazmat.2014.03.063

Chen, H., Ma, L. Q., Gao, B., and Gu, C. (2013). Influence of Cu and Ca cations on ciprofloxacin transport in saturated porous media. *J. Hazard. Mater*. 262, 805–811. doi: 10.1016/j.jhazmat.2013.09.034

Fei, Y., Li, Y., Han, S., and Ma, J. (2016). Adsorptive removal of ciprofloxacin by sodium alginate/graphene oxide composite beads from aqueous solution. *J. Colloid Interface Sci.* 484, 196–204. doi: 10.1016/j.jcis.2016.08.068

Ghaedi, M., Sadeghian, B., Pebdani, A. A., Sahraei, R., Daneshfar, A., and Duran, C. (2012). Kinetics, thermodynamics and equilibrium evaluation of direct yellow 12 removal by adsorption onto silver nanoparticles loaded activated carbon. *Chem. Eng. J.* 187, 133–141. doi: 10.1016/j.cej.2012.01.111

Gomes, J., Costa, R., Quinta-Ferreira, R. M., and Martins, R. C. (2017). Application of ozonation for pharmaceuticals and personal care products removal from water. *Sci. Total Environ.* 586, 265–283. doi: 10.1016/j.scitotenv.2017.01.216

Gu, C., and Karthikeyan, K. G. (2005). Sorption of the antimicrobial ciprofloxacin to aluminum and iron hydrous oxides. *Environ. Sci. Technol.* 39, 9166–9173. doi: 10.1021/es051109f

Gu, X., Tan, Y., Tong, F., and Gu, C. (2015). Surface complexation modeling of coadsorption of antibiotic ciprofloxacin and Cu(II) and onto goethite surfaces. *Chem. Eng. J.* 269, 113–120. doi: 10.1016/j.cej.2014.12.114

Hamjinda, N. S., Chiemchaisri, W., and Chiemchaisri, C. (2017). Upgrading two-stage membrane bioreactor by bioaugmentation of *Pseudomonas putida* entrapment in PVA/SA gel beads in treatment of ciprofloxacin. *Int. Biodeterior. Biodegrad.* 119, 595–604. doi: 10.1016/j.ibiod.2016.10.020

Hayat, A., and Marty, J. L. (2014). Aptamer based electrochemical sensors for emerging environmental pollutants. *Front. Chem*. 2:41. doi: 10.3389/fchem.2014.00041

Hu, Y., He, Y., Wang, X., and Wei, C. (2014). Efficient adsorption of phenanthrene by simply synthesized hydrophobic MCM-41 molecular sieves. *Appl. Clay Sci.* 311, 825–830. doi: 10.1016/j.apsusc.2014.05.173

Jiang, C., Su, A., Li, X., Zhou, T., and He, D. (2012). Study on the hydrothermal stability of MCM-41 via secondary restructure. *Powder Technol.* 221, 371–374. doi: 10.1016/j.powtec.2012.01.028

Jiang, Q. G., Ao, Z. M., and Jiang, Q. (2013). First principles study on the hydrophilic and conductive graphene doped with Al atoms. *Phys. Chem. Chem. Phys.* 15, 10859–10865. doi: 10.1039/c3cp00128h

Johnson, A. C., Keller, V., Dumont, E., and Sumpter, J. P. (2015). Assessing the concentrations and risks of toxicity from the antibiotics ciprofloxacin, sulfamethoxazole, trimethoprim and erythromycin in European rivers. *Sci. Total Environ.* 511, 747–755. doi: 10.1016/j.scitotenv.2014.12.055

Kolesnikov, A. L., Uhlig, H., Möllmer, J., Adolphs, J., Budkov, Y. A., Georgi, N., et al. (2017). Pore size distribution of MCM-41-type silica materials

from pseudomorphic transformation - A minimal input data approach based on excess surface work. *Micropor. Mesopor. Mater.* 240, 169–177. doi: 10.1016/j.micromeso.2016.11.017

Lee, C. K., Liu, S. S., Juang, L. C., Wang, C. C., Lin, K. S., and Lyu, M. D. (2007). Application of MCM-41 for dyes removal from wastewater. *J. Hazard. Mater.* 147, 997–1005. doi: 10.1016/j.jhazmat.2007.01.130

Li, B., Wu, K., Yuan, T., Han, C., Xu, J., and Pang, X. (2012). Synthesis, characterization and catalytic performance of high iron content mesoporous Fe-MCM-41. *Micropor. Mesopor. Mater.* 151, 277–281. doi: 10.1016/j.micromeso.2011.10.024

Li, X., Chen, S., Fan, X., Quan, X., Tan, F., Zhang, Y., et al. (2015). Adsorption of ciprofloxacin, bisphenol and 2-chlorophenol on electrospun carbon nanofibers: in comparison with powder activated carbon. *J. Colloid Interface Sci.* 447, 120–127. doi: 10.1016/j.jcis.2015.01.042

Liu, J. L., and Wong, M. H. (2013). Pharmaceuticals and personal care products (PPCPs): a review on environmental contamination in China. *Environ. Int.* 59, 208–224. doi: 10.1016/j.envint.2013.06.012

MacKay, A. A., and Seremet, D. E. (2008). Probe compounds to quantify cation exchange and complexation interactions of ciprofloxacin with soils. *Environ. Sci. Technol.* 42, 8270–8276. doi: 10.1021/es800984x

Montes-Grajales, D., Fennix-Agudelo, M., and Miranda-Castro, W. (2017). Occurrence of personal care products as emerging chemicals of concern in water resources: a review. *Sci. Tot. Environ.* 595, 601–614. doi: 10.1016/j.scitotenv.2017.03.286

Nie, Y., Li, N., and Hu, C. (2015). Enhanced inhibition ofbromate formation in catalytic ozonation of organic pollutants over Fe-Al LDH/Al2O3. *Sep. Purif. Technol.* 151, 256–261. doi: 10.1016/j.seppur.2015.07.057

Ory, J., Bricheux, G., Togola, A., Bonnet, J. L., Donnadieu-Bernard, F., Nakusi, L., et al. (2016). Ciprofloxacin residue and antibiotic-resistant biofilm bacteria in hospital effluent. *Environ. Pollut.* 214, 635–645. doi: 10.1016/j.envpol.2016.04.033

Pei, Z., Shan, X. Q., Kong, J., Wen, B., and Owens, G. (2010). Coadsorption of ciprofloxacin and Cu(II) on montmorillonite and kaolinite as affected by solution pH. *Environ. Sci. Technol.* 44, 915–920. doi: 10.1021/es902902c

Peng, H., Feng, S., Zhang, X., Li, Y., and Zhang, X. (2012). Adsorption of norfloxacin onto titanium oxide: effect of drug carrier and dissolved humic acid. *Sci. Total Environ.* 438, 66–71. doi: 10.1016/j.scitotenv.2012.08.045

Peng, X., Hu, F., Lam, F. L., Wang, Y., Liu, Z., and Dai, H. (2015). Adsorption behavior and mechanisms of ciprofloxacin from aqueous solution by ordered mesoporous carbon and bamboo-based carbon. *J. Colloid Interface Sci.* 460, 349–360. doi: 10.1016/j.jcis.2015.08.050

Roca Jalil, M. E., Baschini, M., and Sapag, K. (2015). Influence of pH and antibiotic solubility on the removal of ciprofloxacin from aqueous media using montmorillonite. *Appl. Clay Sci.* 114, 69–76. doi: 10.1016/j.clay.2015.05.010

Sarmah, A. K., Meyer, M. T., and Boxall, A. B. (2006). A global perspective on the use, sales, exposure pathways, occurrence, fate and effects of veterinary antibiotics (VAs) in the environment. *Chemosphere* 65, 725–759. doi: 10.1016/j.chemosphere.2006.03.026

Shi, S., Fan, Y., and Huang, Y. (2013). Facile low temperature hydrothermal synthesis of magnetic mesoporous carbon nanocomposite for adsorption removal of ciprofloxacin antibiotics. *Ind. Eng. Chem. Res.* 52, 2604–2612. doi: 10.1021/ie303036e

Song, X., Zhang, Y., Yan, C., Jiang, W., and Chang, C. (2013). The Langmuir monolayer adsorption model of organic matter into effective pores in activated carbon. *J. Colloid Interface Sci.* 389, 213–219. doi: 10.1016/j.jcis.2012.08.060

Sun, Y., Yue, Q., Gao, B., Gao, Y., Xu, X., Li, Q., et al. (2014). Adsorption and cosorption of ciprofloxacin and Ni(II) on activated carbon-mechanism study. *J. Taiwan Inst. Chem. E.* 45, 681–688. doi: 10.1016/j.jtice.2013.05.013

Tan, Y., Guo, Y., Gu, X., and Gu, C. (2014). Effects of metal cations and fulvic acid on the adsorption of ciprofloxacin onto goethite. *Environ. Sci. Pollut.* 22, 609–617. doi: 10.1007/s11356-014-3351-4

Trivedi, P., and Vasudevan, D. (2007). Spectroscopic investigation of ciprofloxacin speciation at the goethite-water interface. *Environ. Sci. Technol.* 41, 3153–3158. doi: 10.1021/es061921y

Turel, I. (2002). The interactions of metal ions with quinolone antibacterial agents. *Coord. Chem. Rev.* 232, 27–47. doi: 10.1016/S0010-8545(02)00027-9

Turel, I., Bukovec, N., and Farkas, E. (1996). Complex formation between some metals and a quinolone family member (ciprofloxacin). *Polyhedron* 15, 269–275. doi: 10.1016/0277-5387(95)00231-G

Verlicchi, P., and Zambello, E. (2016). Predicted and measured concentrations of pharmaceuticals in hospital effluents. Examination of the strengths and weaknesses of the two approaches through the analysis of a case study. *Sci Tot. Environ.* 565, 82–94. doi: 10.1016/j.scitotenv.2016.04.165

Wang, C., Boithias, L., Ning, Z., Han, Y., Sauvage, S., Sánchez-Pérez, J.-M., et al. (2017a). Comparison of Langmuir and Freundlich adsorption equations within the SWAT-K model for assessing potassium environmental losses at basin scale. *Agr. Water Manage.* 180, 205–211. doi: 10.1016/j.agwat.2016.08.001

Wang, C.-J., Li, Z., and Jiang, W.-T. (2011). Adsorption of ciprofloxacin on 2:1 dioctahedral clay minerals. *Appl. Clay Sci.* 53, 723–728. doi: 10.1016/j.clay.2011.06.014

Wang, J., Li, Y., Xu, X., Liang, B., Wu, F., Yang, X., et al. (2017b). Antimicrobial resistance of Salmonella enterica Serovar Typhimurium in Shanghai, China. *Front. Microbiol.* 8:510. doi: 10.3389/fmicb.2017.00510

Wang, Y. X., Ngo, H. H., and Guo, W. S. (2015). Preparation of a specific bamboo based activated carbon and its application for ciprofloxacin removal. *Sci. Tot. Environ.* 533, 32–39. doi: 10.1016/j.scitotenv.2015.06.087

Wu, Q., Yang, X., Liu, J., Nie, X., Huang, Y., Wen, Y., et al. (2014). Topotactic growth, selective adsorption, and adsorption-driven photocatalysis of protonated layered titanate nanosheets. *ACS Appl. Mater. Interfaces* 6, 17730-17739. doi: 10.1021/am5041847

Wu, S., Zhao, X., Li, Y., Zhao, C., Du, Q., Sun, J., et al. (2013). Adsorption of ciprofloxacin onto biocomposite fibers of graphene oxide/calcium alginate. *Chem. Eng. J.* 230, 389–395. doi: 10.1016/j.cej.2013.06.072

Wu, Y., Ma, Y., Pan, J., Gu, R., and Luo, J. (2017). Porous and magnetic molecularly imprinted polymers via pickering high internal phase emulsions polymerization for selective adsorption of λ-cyhalothrin. *Front. Chem.* 5:18. doi: 10.3389/fchem.2017.00018

Xiao, R., Diazrivera, D., and Weavers, L. K. (2013). Factors influencing pharmaceutical and personal care product degradation in aqueous solution using pulsed wave ultrasound. *Ind. Eng. Chem. Res.* 52, 2824–2831. doi: 10.1021/ie303052a

Zheng, W., Zhang, Z., Liu, R., and Lei, Z. (in press). Removal of veterinary antibiotics from anaerobically digested swine wastewater using an intermittently aerated sequencing batch reactor. *J. Environ. Sci-China.* doi: 10.1016/j.jes.2017.04.011

Conflict of Interest Statement: The authors declare that the research was conducted in the absence of any commercial or financial relationships that could be construed as a potential conflict of interest.

frontiers in Chemistry

ORIGINAL RESEARCH
published: 29 May 2018
doi: 10.3389/fchem.2018.00187

First Principles Study on the CO Oxidation on Mn-Embedded Divacancy Graphene

Quanguo Jiang[1], Jianfeng Zhang[1], Zhimin Ao[2]*, Huajie Huang[1], Haiyan He[1] and Yuping Wu[1]*

[1] College of Mechanics and Materials, Hohai University, Nanjing, China, [2] Guangzhou Key Laboratory of Environmental Catalysis and Pollution Control, Institute of Environmental Health and Pollution Control, School of Environmental Science and Engineering, Guangdong University of Technology, Guangzhou, China

The CO oxidation mechanism on graphene with divacancy (DG) embedded with transition metal from Sc to Zn has been studied by using first principles calculations. The results indicate that O_2 molecule is preferentially adsorbed on Sc, Ti, V, Cr, Mn, and Fe-DG, which can avoid the CO poisoning problem that many catalysts facing and is beneficial to the CO oxidation progress. Further study indicates that Mn-DG shows the best catalytic properties for CO oxidation with consideration of both Langmuir-Hinshelwood (LH) and Eley-Rideal (ER) oxidation mechanisms. Along the ER mechanism, the reaction energy barrier for the first step ($CO_{\text{free}} + O_{2\ \text{pre-adsorbed}} \rightarrow OOCO$) is 0.96 eV. Along the LH mechanism, the energy barrier for the rate limiting step ($CO_{\text{adsorbed}} + O_{2\ \text{adsorbed}} \rightarrow OOCO$) is only 0.41 eV, indicating that the CO oxidation on Mn-DG will occur along LH mechanism. The Hirshfeld charge distributions of O_2 and CO molecules is tuned by the embedded Mn atom, and the charge transfer from the embedded Mn atom to the adsorbed molecules plays an important role for the CO oxidation. The result shows that the Mn-embedded divacancy graphene is a noble-metal free and efficient catalyst for CO oxidation at low temperature.

Keywords: graphene, divacancy, Mn-embedded, CO oxidation, first principles calculations

OPEN ACCESS

Edited by:
Philippe Vernoux, UMR5256 Institut de Recherches sur la Catalyse et l'Environnement de Lyon (IRCELYON), France

Reviewed by:
Xingang Li, Tianjin University, China
Jose Luis Valverde, Universidad de Castilla-La Mancha, Spain

****Correspondence:***
Jianfeng Zhang
jfzhang@hhu.edu.cn
Zhimin Ao
zhimin.ao@gdut.edu.cn

Specialty section:
This article was submitted to Green and Sustainable Chemistry, a section of the journal Frontiers in Chemistry

Received: *06 January 2018*
Accepted: *07 May 2018*
Published: *29 May 2018*

Citation:
Jiang Q, Zhang J, Ao Z, Huang H, He H and Wu Y (2018) First Principles Study on the CO Oxidation on Mn-Embedded Divacancy Graphene. Front. Chem. 6:187. doi: 10.3389/fchem.2018.00187

INTRODUCTION

Carbon monoxide (CO) is colorless, tasteless and toxic in air, while oxidation of CO is an efficient way to eliminate of the air pollutant (Xie et al., 2009). CO oxidation has important applications in atmosphere purification for hydrogen gas fuel in fuel cells as well (Qiao et al., 2015; Saavedra et al., 2016). Noble metals(Bleakley and Hu, 1999; Zhang and Hu, 2001; Liu et al., 2002; Gong et al., 2004; Dupont et al., 2006; Zhang et al., 2006; Liu, 2007) are common catalysts for the CO oxidation, where the rate limiting energy barriers are 0.46 eV (Liu et al., 2002) for Au(221), 0.91 eV (Gong et al., 2004) and 0.93 eV (Zhang and Hu, 2001) for Pd(111), 0.79 eV (Gong et al., 2004) and 0.82 eV (Dupont et al., 2006) for Pt(111), 1.17 eV (Gong et al., 2004) and 1.01 eV (Zhang et al., 2006) for Rh(111), 1.00 eV (Liu, 2007) for Rh(100). Due to the high cost and high reaction temperature of these noble metals, it is desirable to develop noble-metal-free catalysts for CO oxidation at low temperature. Noble metal clusters on supports are further studied to decrease the reaction barriers for CO oxidation (Tang et al., 2015; Ma et al., 2016; Wang et al., 2016; Ali et al., 2017; Chen et al., 2017). Furthermore, single atom catalyst decorated on appropriate matrix is attracted a lot of interests due to the excellent catalytic performance (Dvorák et al., 2016; Jones et al., 2016). The outstanding

physical properties (Novoselov et al., 2005; Balandin et al., 2008; Lee et al., 2008) and the large surface-to-volume ratio make graphene (Novoselov et al., 2004) to be a promising substrate to realize high performance single atom catalysis. However, the inert nature of pristine graphene usually causes clustering problems for the adsorbed metal atoms (Liu and Huang, 2017; Liu et al., 2017). The interactions between the pristine graphene and the adsorbed atoms can be enhanced by introducing different carbon vacancies. Experimentally, single carbon vacancy (SV) and double carbon vacancies (DV) are common point defects on graphene. Vacancies can be introduced into graphene by exposing it to the focussed electron beam, and the vacancy defects in graphene can be tailored by controlling the exposing time, where the DV is more often observed than SV due to the high energy of the SV under electron beam irradiation (Robertson et al., 2012). In addition, the concentration of DV changes from 0.1 to 0.5 nm^2 by controlling the total electron beam dose (Robertson et al., 2012). In addition, it is reported that the metal atoms resident on the SV and DV positions in graphene surfaces are stable in comparison to that on graphene edge (Robertson et al., 2013). Hence, it is important to evaluate the catalytic performance of a single atom supported on graphene with both SV and DV defects.

Many works about the CO oxidation have been reported for single atom decorated at the single carbon vacancy on graphene. Theoretically, Au- (Lu et al., 2009), Fe- (Li et al., 2010), Cu- (Song et al., 2011), Pt- (Tang et al., 2012), Si- (Zhao et al., 2012), and Al-embedded (Jiang et al., 2014) SV graphenes show high activity for the CO oxidation. Although the SV graphene with decorating metal atoms has high catalytic activity, decorating metal atom on the controllable carbon vacancies in graphene to realize different single atom catalyst is still highly desirable. The decorated metal atom is three-bond coordinated on SV graphene, while it is four-bond coordinated on DV graphene, indicating that the chemical activity of the decorated metal atom on different carbon vacancies should be different due to the different chemical environment. Furthermore, as mentioned above divacancy is commonly present in graphene obtained through chemical synthesis. However, only the catalytic activity of Fe-decorated DV graphene has been studied (Tang et al., 2016; Liu et al., 2017). Therefore, further research about the catalytic performance of DV graphene decorated with metal atom for CO oxidation is needed.

For the CO oxidation, Langmuir-Hinshelwood (LH) and Eley-Rideal (ER) are two mainly mechanisms. Along the ER mechanism, the activated O_2 molecule directly reacts with the free CO molecule, where the activation of O_2 is the rate-limiting step (Lu et al., 2009). Alone the LH mechanism, the CO and O_2 molecules are first coadsorbed, and then react to form OOCO intermediate, which is the rate-limiting step for the oxidation progress (Lu et al., 2009). In general, the reaction energy barriers are proportional to the adsorption energy of adsorbed molecules on supported catalyst (Gong et al., 2004), indicating that the adsorption energy of adsorbed CO and O_2 molecules could be a benchmark for the catalytic performance of graphene for CO oxidation. In addition, a larger adsorption energy for O_2 molecule than that of CO is desired during the CO oxidation progress, because the preferential adsorption of CO will block the active sites and prevent the continuous oxidation reaction (Jiang et al., 2014; Tang et al., 2016). Therefore, the adsorption energy for O_2 and CO on transition metals doped graphene is first calculated and the alternative decorating atom is chosen based on this rule.

In this work, by using first principles calculations, we will systematically study the CO oxidation mechanism on DV graphene decorated with transition metals from Sc to Zn, which are non-noble metals and commonly used to decorate two dimensional materials. The reaction barriers for each step are analyzed and the corresponding reaction mechanisms are discussed through analyzing the electronic property of the graphene systems.

Calculation Methods

The density functional theory (DFT) calculations are carried out by using $Dmol^3$ package (Delley, 2000). Exchange-correlation functions are taken as generalized gradient approximation (GGA) with Perdew-Burke-Ernzerhof (PBE) (Perdew et al., 1996). The selection of exchange–correlation functional has evidential effect on the result of adsorption energies, while has much smaller effect on the reaction energy barriers (Roldán et al., 2009). DFT semicore pseudopotentials (DSPPs) core treatment is implemented for relativistic effects. Double numerical plus polarization (DNP) is employed as the basis set. The convergence tolerance of energy of 10^{-5} Hartree is taken (1 Hartree = 27.21 eV), and the maximal allowed force and displacement are 0.002 Hartree/Å and 0.005 Å, respectively. Linear synchronous transit/quadratic synchronous transit (LST/QST) (Halgren and Lipscomb, 1977) and nudged elastic band (NEB) (Henkelman and Jonsson, 2000) tools in $Dmol^3$ module are used to investigate the minimum energy pathway for CO oxidation on graphene, which have been well validated to determine the transition state. Three-dimensional periodic boundary conditions are taken in the simulation. The simulation cell consists of a 4 × 4 graphene supercell with a vacuum width of 20 Å above the graphene layer to minimize the interlayer interaction. The *k*-point is set to 5 × 5 × 1, and all atoms are allowed to relax according to previous reports (Jiang et al., 2014). After structure relaxations, the density of states (DOS) are calculated with a finer *k*-point grid of 15 × 15 × 1. The DFT+D method within the Grimme scheme (Grimme, 2006) is used in all calculations to consider the van der Waals forces. The electron orbits of the free and adsorbed molecules are calculated with CASTEP code (Segall et al., 2002), where the ultrasoft pseudopotentials, GGA-PBE functional, an energy cutoff of 340 eV and 5 × 5× 1 *k*-point meshes are used. We have compared the total energy of the graphene system with different spin state, and choose the proper spin state for the graphene system with the smallest total energy.

The adsorption energy E_{ad} of molecules on graphene is determined by,

$$E_{ad} = E_{molecules/graphene} - (E_{graphene} + E_{molecules}) \quad (1)$$

where $E_{molecules/graphene}$, $E_{graphene}$, and $E_{molecule}$ are total energies of the adsorbed graphene system, the isolate graphene and molecules respectively.

RESULTS AND DISCUSSION

Adsorption of O_2 and CO on TM-DG

Based on the literature results in the introduction section, it is expected that transition-metal-embedded divacancy graphene (TM-DG) could also exhibit excellent catalytic behaviors for CO oxidation, similar to the cases of graphene with single vacancy systems. Herein, we present systematic DFT calculations on the adsorption energy of O_2 and CO molecules on the divacancy graphene embedded with transition metal (from Sc to Zn). To comprehensively understanding the adsorption behaviors of O_2 and CO molecules on transition metal decorated divacancy graphene, the adsorption energies of O_2 and CO, as well as the co-adsorption energy of O_2 and CO molecules on TM-DG are shown in **Figure 1**, where we can see that the adsorption energy of O_2 molecule is larger than that of CO molecule on TM-DG (from Sc to Fe), while the adsorption energy of CO molecule is larger than that of O_2 molecule on TM-DG (from Co to Zn). This result indicates that the O_2 molecule has priority during the adsorption progress and avoids the CO poisoning at the active sites on TM-DG (from Sc to Fe) during the CO oxidation. In addition, the co-adsorption energy of O_2 and CO molecules on TM-DG (from Sc to Fe) is also shown in **Figure 1**, where a local adsorption energy minimum on Mn-DG is found, which indicates that Mn-DG can facilitate the CO oxidation better, due to the fact that the energy barrier is proportional to the adsorption energy of molecules (Gong et al., 2004). Therefore, CO oxidation on Mn-DG is mainly studied in the following, and the CO oxidation on other TM-DG (Sc, Ti, V, Cr and Fe) is also studied for comparison purpose.

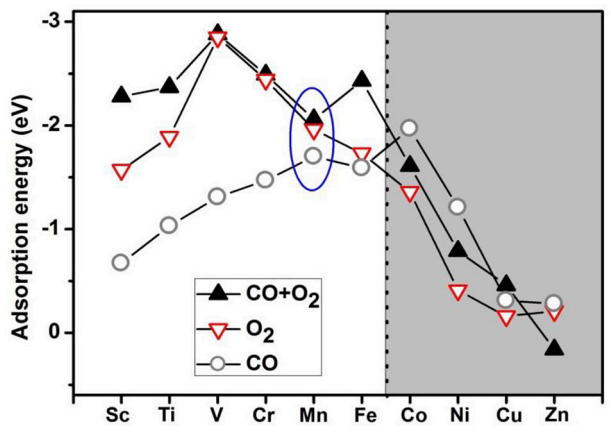

FIGURE 1 | The adsorption energies of O_2 and CO as well as the co-adsorption energy of O_2 and CO on TM-DG, where the light and dark areas indicate the preferential adsorption of O_2 and CO molecules, respectively.

Electronic Properties and Stability of Mn-DG

Before further study the catalytic properties of Mn-DG, the electronic properties and structure stability of Mn-DG are first studied in **Figure 2**. After embedding Mn atom into the divancancy graphene through substituting two carbon atoms, the reconstructed structure of graphene is shown in **Figure 2A**, where four chemical Mn-C bonds are formed in graphene with bond length $l_{Mn-C} = 1.99$ Å. Mn atom is out of the plane of graphene with a distance of 0.68 Å due to the larger atomic radius of 1.79 Å compared with that of C 0.91 Å. The adsorption energy of the Mn atom on the divacancy graphene is −6.81 eV. The Hirshfeld charge distributions near the dopant are also given in **Figure 2A**, where the electron-deficiency position is formed for the Mn atom with losing electrons of 0.284 *e*, which promotes the adsorption of O_2 and CO molecules. The differential charge density along C-Mn-C bonds for Mn-DG is further studied and is shown in **Figure 2B**, where the blue and red isosurfaces correspond to the increase in the number of electrons and the depletion zone, respectively. It shows that electrons accumulate near the doped Mn atom, indicating the high chemical active area.

The aggregation problems for the adsorbed metal atoms on substrate are significant for the catalytic performance, especially when the concentration of metal atom is high (Ao and Peeters, 2010a). To determine the possibility of aggregation for Mn atoms on divacancy graphene, the diffusion pathway of Mn atom to its neighboring positions is investigated based on DFT calculations (see **Figure 2C**), where the corresponding diffusion energy barrier for the decorated Mn atom is 5.91 eV. It is claimed that a surface reaction will occur when the reaction barrier is smaller than the critical value of $E_{cbar} = 0.91$ eV (Young, 2001), the decorated Mn atom on divacancy graphene is thus stable. In addition, the adsorption energy of Mn atom on divacancy graphene is −6.81 eV and it is much larger than the cohesive energy −2.92 eV/atom for Mn element (http://www.knowledgedoor.com/). Therefore, the Mn decorated divacancy graphene is quite stable without aggregation problems. Partial density of states (PDOS) are further analyzed to confirm the enhanced interactions between the Mn atom and graphene (**Figure 2D**), where the energy bands between the decorated Mn atom and carbon atoms overlap significantly. The electron-deficiency character is confirmed by the Fermi level crossing the valence band, and it is consistent with the Hirshfeld charge distributions. As shown in the insert of **Figure 2D**, the positive and negative spin density of Mn-DG is shown in green and red, respectively. Therefore, the magnetic moment of Mn-DG is 3.053 μ_B, which is mainly contributed by the Mn atom. The remaining unsaturated *d* orbital of Mn atom is reactive, which can adsorb small molecules and promote the subsequent reactions.

Adsorption of Molecules on Mn-DG

To investigate the oxidation of CO on Mn-embedded divacancy graphene, the adsorptions of O_2 and CO on Mn-DG are studied carefully. **Figure 3A** shows the most stable configuration for O_2 molecule adsorbed on Mn-DG ($E_{ad} = -1.96$ eV), where the

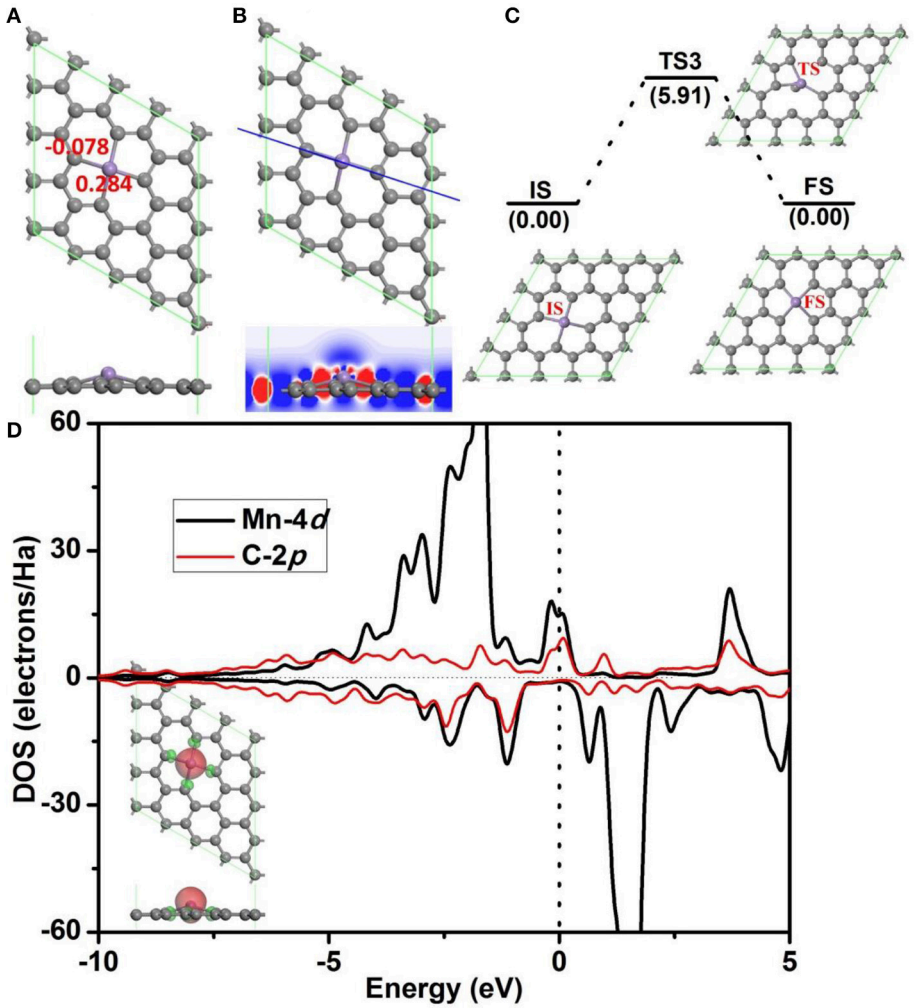

FIGURE 2 | (A) The atomic structure of divacancy graphene embedded with Mn atom (Mn-DG), where the gray and pink atoms are C and Mn atoms, respectively, in this and following figures. The atomic charge obtained by Hirshfeld analysis near the Mn dopant is also given. **(B)** The differential charge density along C-Mn-C bonds for Mn-DG is shown, where the blue and red isosurfaces correspond to the increase in the number of electrons and the depletion zone, respectively. **(C)** The diffusion pathway of the Mn atom on Mn-DG, where IS, TS, and FS represent initial, transition and final structures, respectively, in this and following figures. **(D)** PDOS of Mn atom and C atom on the Mn-DG, where the vertical line indicates the Fermi level. Inset is the positive and negative spin density of Mn-DG shown in green and red, respectively.

O-O bond is parallel to the graphene sheet, and ∼0.18 *e* is transferred from Mn-DG to O_2 molecule based on Hirshfeld charge analysis. To assess the stability of the adsorbed O_2 molecule, the dissociative adsorption of O_2 molecule on Mn-DG is then studied in **Figure 3B**. After NEB calculations, the dissociation reaction barrier for an O_2 molecule on the Mn-DG is 1.18 eV > E_{cbar} = 0.91 eV (Young, 2001), which indicates that the adsorbed O_2 molecule prefers to stay on Mn-DG in molecular state at room temperature. The PDOS of free O_2 molecule is shown in **Figure 3C**, where the 2π∗ anti-bond orbital is half filled (Honkala and Laasonen, 2000). Then, the PDOS of Mn atom and the adsorbed O_2 molecule is shown in **Figure 3D**, where all orbitals of the adsorbed O_2 molecule are also labeled to understand the interaction between the adsorbed O_2 and Mn-DG. About 0.18 *e* is transferred from Mn-DG to the adsorbed O_2 molecule based on Hirshfeld method, which occupies the O_2-2π∗ orbital above the Fermi level (see **Figure 3C**) and is confirmed by the new peaks for O_2-2π∗ orbital below the Fermi level (see **Figure 3D**). This charge transfer elongates the O-O bond from 1.23 Å in free O_2 to 1.40 Å in adsorbed O_2 molecule. The activated O_2 molecule with longer O-O bond will be beneficial for the subsequent CO oxidation. The O_2-2π∗ orbitals and Mn atom is strong hybridized near the Fermi level (see **Figure 3D**), which mainly responses for the chemical adsorption of O_2 molecule on Mn-DG.

The adsorption configuration of a CO molecule on Mn-DG is shown in **Figure 4A**, where the CO molecule is vertically

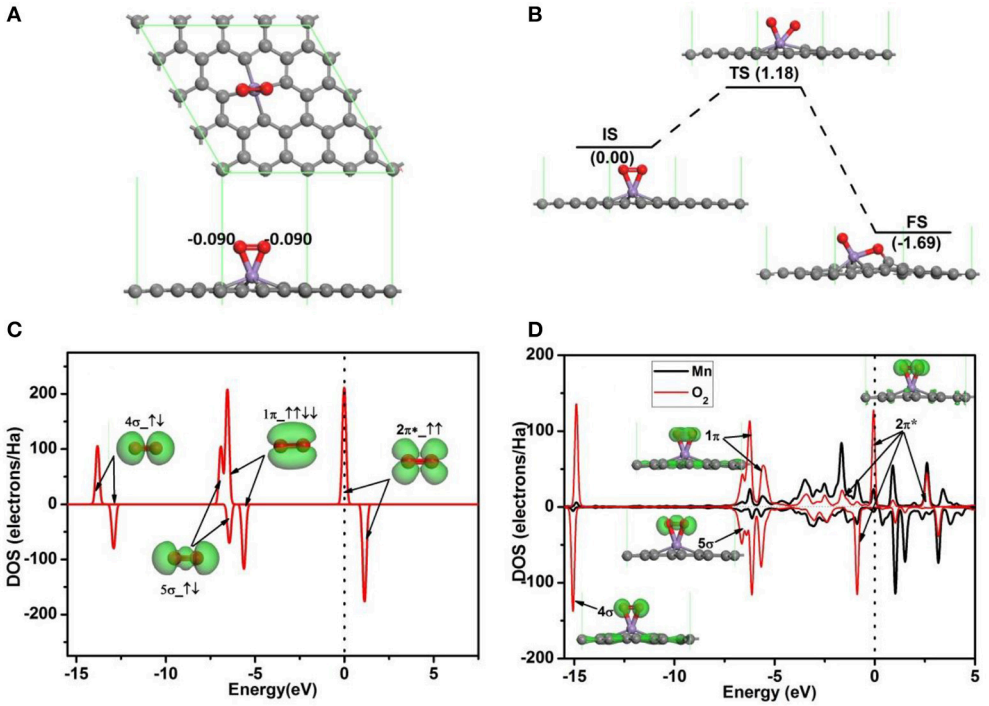

FIGURE 3 | (A) The most stable structure of O_2 adsorbed on Mn-DG. **(B)** The reaction pathway for the dissociative adsorption of O_2 molecule on Mn-DG. **(C)** PDOS and orbitals of the free O_2 molecule, where the number of electrons for each orbital is also shown by arrows. **(D)** PDOS of the adsorbed O_2 molecule and Mn atom for Mn-DG, inset is the charge density of 4s, 5s, 1p, and 2p* orbitals of the adsorbed O_2 molecule. The vertical lines indicate the Fermi level.

adsorbed on the top of the decorated Mn atom. CO is chemically adsorbed on Mn-DG, which is confirmed by the chemical bond between Mn atom and the carbon atom of CO molecule. The adsorption energy of a CO molecule on Mn-DG is $E_{ad} = -1.70$ eV, and CO molecule loses 0.006 e to the Mn-DG. The binding energy E_b of C-O bond is 11.57 eV, which is much larger than $E_b = 6.36$ eV for O-O bond based on DFT calculations. Thus CO should be more difficult to be dissociated, which is confirmed by the fact that the dissociative energy barrier for CO molecule on Mn-DG is 5.55 eV based on DFT calculation as shown in **Figure 4B**. The PDOS of free CO molecule is shown in **Figure 4C**, where all orbitals are labeled. **Figure 4D** shows the PDOS of the adsorbed CO molecule on Mn-embedded divacancy graphene, where the orbitals of adsorbed CO molecule are labeled and displayed. The 5σ peak of the CO molecule adsorbed on Mn-DG is significantly depressed than the free CO molecule due to the charge transfer. Although the 2π∗ anti-bond orbital far above Fermi level for free CO molecule is fully empty, Mn atom transfers some electrons to CO-2π∗ orbital due to the fact that CO-2π∗ is close to the Fermi level at absorbed state, which slightly elongates the C-O bond from 1.14 Å for free CO molecule to 1.16 Å for adsorbed CO molecule. In addition, CO molecules will act as a donor with the carbon atom near the graphene surface, dur to fact that the CO-5σ orbital locates on the carbon atom (Leenaerts et al., 2008). This agrees with the above Hirshfeld analysis result. The above discussions indicate that O_2 and CO have strong interactions with Mn-DG (corresponding adsorption energies are −1.96 and −1.70 eV, respectively), but the adsorption of O_2 is much stronger. The O_2 molecule is activated on Mn-DG, which will facilitate the CO oxidation progress on graphene.

CO Oxidation on Mn-DG

Two reaction mechanisms have been established for the oxidation of CO molecule: Langmuir-Hinshelwood (LH) mechanism and Eley-Rideal (ER) mechanism (Molina and Hammer, 2005; An et al., 2008; Lu et al., 2009; Li et al., 2010; Song et al., 2011; Tang et al., 2012; Zhao et al., 2012; Jiang et al., 2014). For the ER mechanism, the O_2 molecule is first adsorbed and activated by the Mn-DG, then a free CO molecule approaches the substrate to form an intermediate product. Along the LH mechanism, the O_2 and CO molecules first co-adsorb on the Mn-DG, and then form an intermediate product. Since O_2 has a larger adsorption energy (−1.96 eV) on Mn-DG than that of CO (−1.70 eV), the adsorption of O_2 on Mn-DG has higher priority, thus the ER mechanism for the CO oxidation seems to be favorable. However, the lower co-adsorption energy for O_2 and CO molecules (−2.06 eV) indicates that O_2 and CO may co-adsorb on Mn atom as discussed in literatures (Lu et al., 2009; Song et al., 2011; Tang et al., 2012; Jiang et al., 2014). Therefore, both mechanisms for CO oxidation will be discussed in the following.

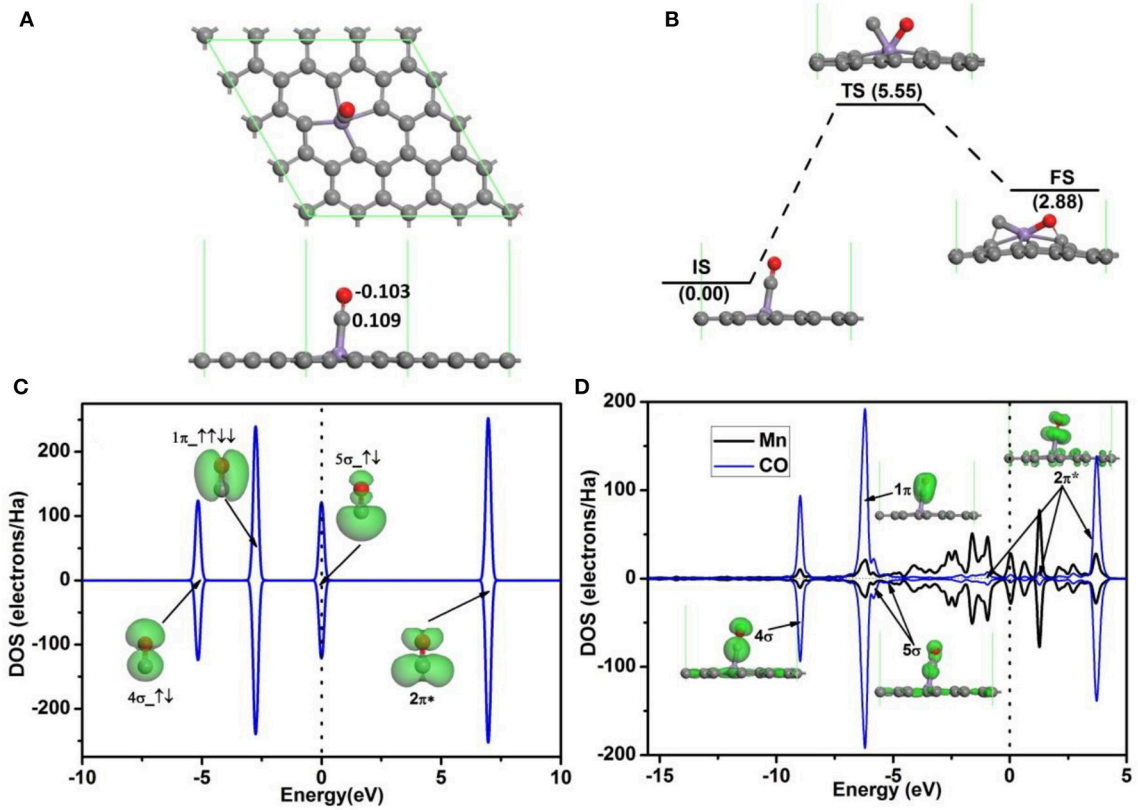

FIGURE 4 | (A) The most stable structure of CO adsorbed on Mn-DG. **(B)** The reaction pathway for the dissociative adsorption of CO molecule on Mn-DG. **(C)** PDOS and orbitals of the free CO molecule, where the number of electrons for each orbital is also shown by arrows. **(D)** PDOS of the adsorbed CO molecule and Mn atom for the Mn-DG, inset is the charge density of 4σ, 1π, 5σ, and 2π* orbitals of the adsorbed CO molecule. The vertical lines indicate the Fermi level.

In order to search the preferred reaction path for CO oxidation on Mn-DG, the first reaction step along both LH and ER mechanisms is studied in **Figure 5**. If the LH mechanism is more favorable, the free CO molecule will co-adsorb on Mn atom with pre-adsorbed O_2 molecule after overcoming a small reaction barrier. If the ER mechanism is more favorable, the free CO molecule will react with the O_2 molecule to form an intermediate (OOCO). The structure of physisorbed CO molecule on the Mn-DG with pre-adsorbed O_2 molecule was selected as the IS after studying all adsorption configurations as shown in **Figure 5A**. The reaction profile for the co-adsorption of CO and O_2 molecules on Mn atom is shown in **Figure 5A**, where the CO and O_2 are titled toward the graphene surface at TS state. After overcoming an energy barrier of 0.19 eV, the CO and O_2 co-adsorb on Mn-DG with releasing energy of 0.02 eV, as shown in **Figure 5A**.

Figure 5B shows the reaction profile for intermediate product along the ER mechanism. When the free CO approaches the Mn atom, the O-O bond is broken (see TS in **Figure 5B**). After overcoming a relative large energy barrier of 0.96 eV, the C atom from the CO binds with two O atoms from the dissociation of the O_2 molecule to form a OOCO complex over the Mn atom (see FS in **Figure 5B**). This exothermic process releases an energy of 3.39 eV.

The effect of temperature on the energy barriers is considered. The free energy change (ΔG) between the reactant and transition state is considered as the temperature-dependent energy barrier E'_{bar} and $\Delta G = \Delta H$ - TΔS, where ΔH is the enthalpy change, ΔS is the entropy change, and T is the room temperature (298.15 K). In addition, $\Delta H = (\Delta U + P\Delta V)$, $\Delta U = (\Delta E_{\mathrm{tot}} + \Delta E_{\mathrm{vib}} + \Delta E_{\mathrm{trans}} + \Delta E_{\mathrm{rot}})$ and $\Delta S = \Delta S_{\mathrm{vib}} + \Delta S_{\mathrm{trans}} + \Delta S_{\mathrm{rot}}$, where ΔU is the internal energy change, ΔE_{tot} is the change of total electronic energy, the *vib*, *trans* and *rot* indicate vibration, translation and rotation, respectively, which can be obtained through calculations of vibrational frequency. The temperature-dependent energy barriers at 298.15 K in **Figure 5** are: $E'_{\mathrm{bar}} =$ 0.33 eV in **Figure 5A** and $E'_{\mathrm{bar}} =$ 1.15 eV in **Figure 5B**. This indicates that the free CO molecule will desorb from substrate with increasing temperature, and the reaction is more difficult to occur. The co-adsorption of CO and O_2 on Mn-DG in **Figure 5A** will happen at 298.15 K due to the lower reaction barrier than the critical barrier of $E_{\mathrm{cbar}} =$ 0.91 eV (Young, 2001), thus the LH mechanism is mainly studied for the CO oxidation in the following.

For oxidation of CO on the Mn-DG along LH mechanism, several steps and also intermediate products (MS) for the oxidation procedure exist (Lu et al., 2009; Song et al., 2011; Tang et al., 2012; Jiang et al., 2014). For each step, e.g., from initial

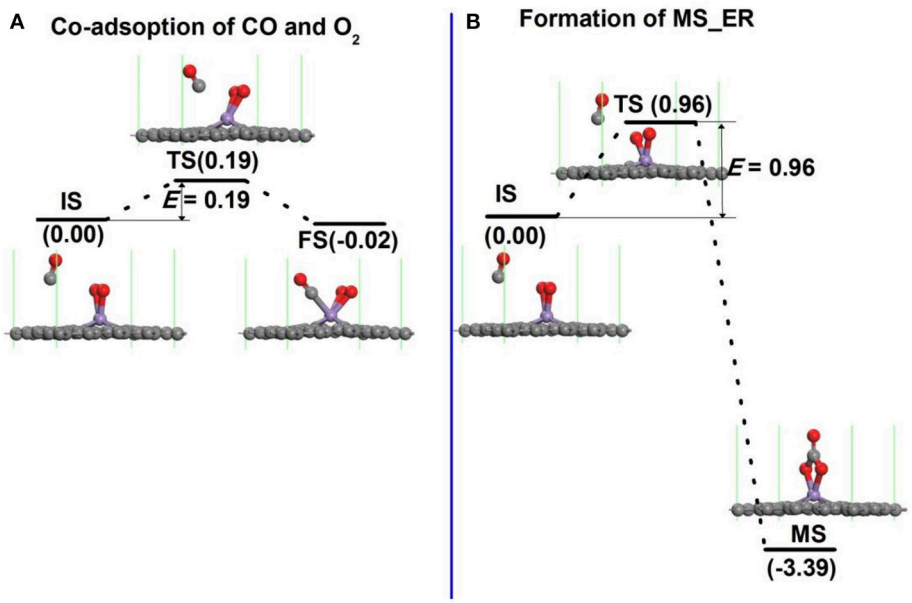

FIGURE 5 | (A) The reaction pathway for the adsorption of CO molecule on Mn-embedded graphene with pre-adsorbed O_2 molecule. **(B)** The primary reaction step for the oxidation of CO molecule on Mn-embedded graphene for ER mechanism.

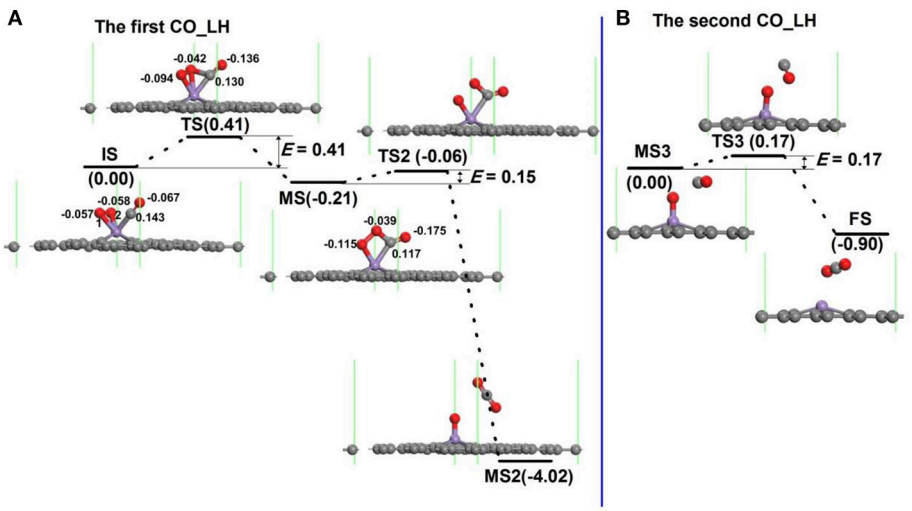

FIGURE 6 | The reaction pathway of CO oxidation on Mn-embedded graphene for LH mechanism: production of the first CO_2 molecule **(A)**, and the second CO_2 moelcule **(B)**. The energy profile for the formation of CO_2 molecule is also shown. The unit of *E* is eV, where *E* is the energy barrier. The Hirshfeld charge near the adsorbate is also shown.

state to intermediate state in **Figure 6**, a transition state also exists. The configuration of co-adsorbed CO and O_2 molecules on Mn-DG is taken as the reactant (IS in **Figure 6A**) based on the above discussions. At transition state, one O-Mn bond changes from 1.93 to 2.10 Å and a C-O bond between CO and O_2 is formed. After overcoming an energy barrier of 0.41 eV, an OOCO intermediate (MS in **Figure 6A**) is formed and the elongated O-Mn bond is cleaved. Then the first CO_2 molecule (MS2) is formed on Mn-DG after overcoming an energy barrier of 0.15 eV (see **Figure 6A**), where the CO_2 is physically adsorbed on Mn-DG and its adsorption energy is −0.20 eV. The reaction for this step can release a heat of 3.81 eV, which can sufficiently overcome the adsorption energy of CO_2, and the first produced CO_2 molecule would desorb from the Mn-DG efficiently. The O-O bond for OOCO configuration in MS is broken at TS2, and a CO_2 molecule with bond angle of 126.6° is formed. **Figure 6B** shows the formation of the second CO_2 molecule on Mn-embedded divacancy graphene. The subsequent CO molecule

TABLE 1 | The reaction energy barriers of each step for the CO oxidation on divacancy graphene decorated with transition metal (from Sc to Fe) along the LH mechanism, where E_{bar1}, E_{bar2}, and E_{bar3} are the energy barriers for step 1, step 2, and step 3 during CO oxidation, respectively.

	E_{bar1} (eV)	E_{bar2} (eV)	E_{bar3} (eV)
Sc-DG	1.15	0.38	0.15
Ti-DG	0.95	0.24	0.43
V-DG	0.65	0.25	0.85
Cr-DG	1.17	0.22	1.10
Mn-DG	0.41	0.15	0.17
Fe-DG	0.88	0.13	0.06

will react with the remaining O atom to produce CO_2 after surmounting an energy barrier of 0.17 eV (see **Figure 6B**), similar to the Au-embedded graphene (Lu et al., 2009). The reaction for this step releases a heat of 0.90 eV, which can also surmount the adsorption energy of CO_2 (−0.27 eV) in Mn-DG, and the second CO_2 molecule will desorb from Mn-DG efficiently. The reaction profile for the production of the two CO_2 molecules is shown in **Figure 6**, where the rate limiting step is the formation of OOCO intermediate and the energy barrier of 0.41 eV is quite small. Therefore, the CO oxidation reaction along the LH mechanism releases 0.21 eV, 3.81 eV, and 0.90 eV for step 1, step 2, and step 3, respectively, which indicates the favorable thermodynamics for the CO oxidation on Mn-DG. In addition, the small energy barrier of 0.41 eV for the rate limiting step indicates the favorable kinetics for the CO oxidation on Mn-DG.

The energy barrier of each step for the CO oxidation along LH mechanism on divacancy graphene decorated with transition metals (from Sc to Fe) are also studied as shown in **Table 1**, where the rate limiting energy barriers are 1.15, 0.95, 0.85, 1.17, 0.41, and 0.88 eV for Sc-, Ti-, V-, Cr-, Mn-, and Fe-DG, respectively. The reaction barrier is the smallest on Mn-DG, which confirms the fact that the reaction barriers of molecules are proportional to the adsorption energy on supported catalyst (Gong et al., 2004), and the co-adsorption energy of adsorbed CO and O_2 molecules can be a benchmark for the catalytic performance of the graphene for CO oxidation. Therefore, CO can be oxidized easily on Mn-DG at low temperature, indicating that Mn-DG is an excellent candidate during the catalysts for CO oxidation.

The energy barriers at 298.15 K for each step of CO oxidation on Mn-DG in **Figure 6** are: $E'_{bar} = 0.49$ eV for step 1, $E'_{bar} = 0.10$ eV for step 2, and $E'_{bar} = 0.25$ eV for step 3, where the energy barriers for step 1 and step 3 slightly increase than those

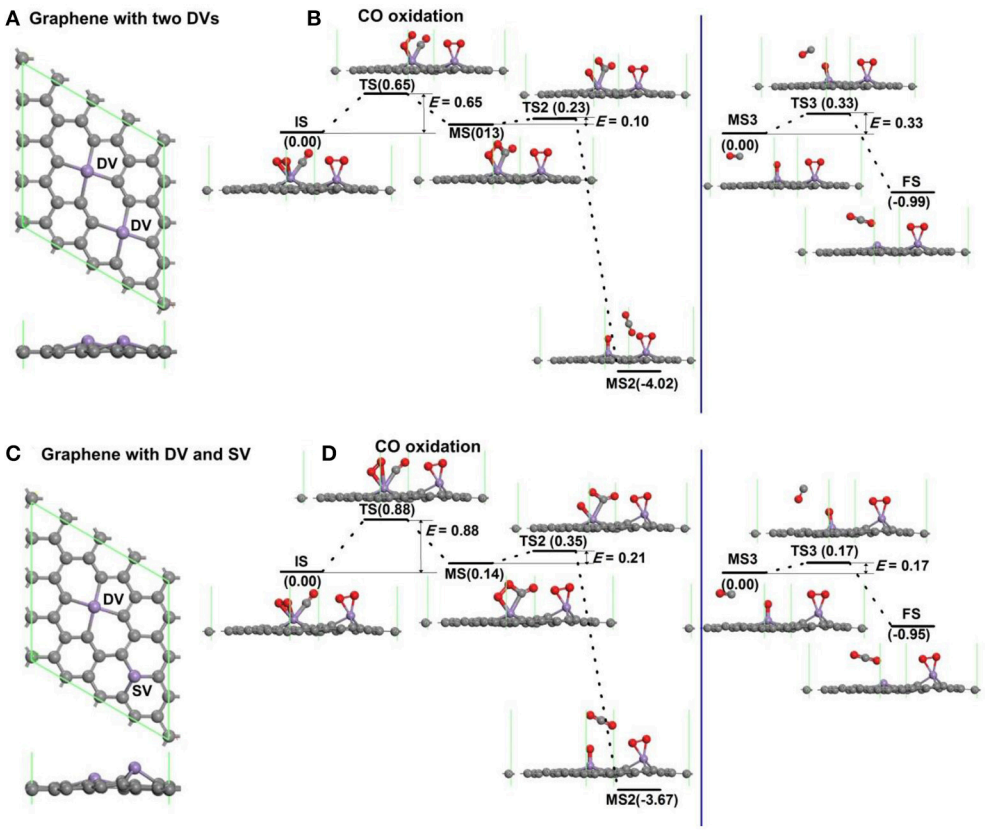

FIGURE 7 | The atomic structure of graphene with two divacancies embedded with Mn atoms **(A)**, and the corresponding reaction pathway of CO oxidation along LH mechanism **(B)**. The atomic structure of graphene with one divacancy and one single vacancy embedded with Mn atoms **(C)**, and the corresponding reaction pathway of CO oxidation along LH mechanism **(D)**.

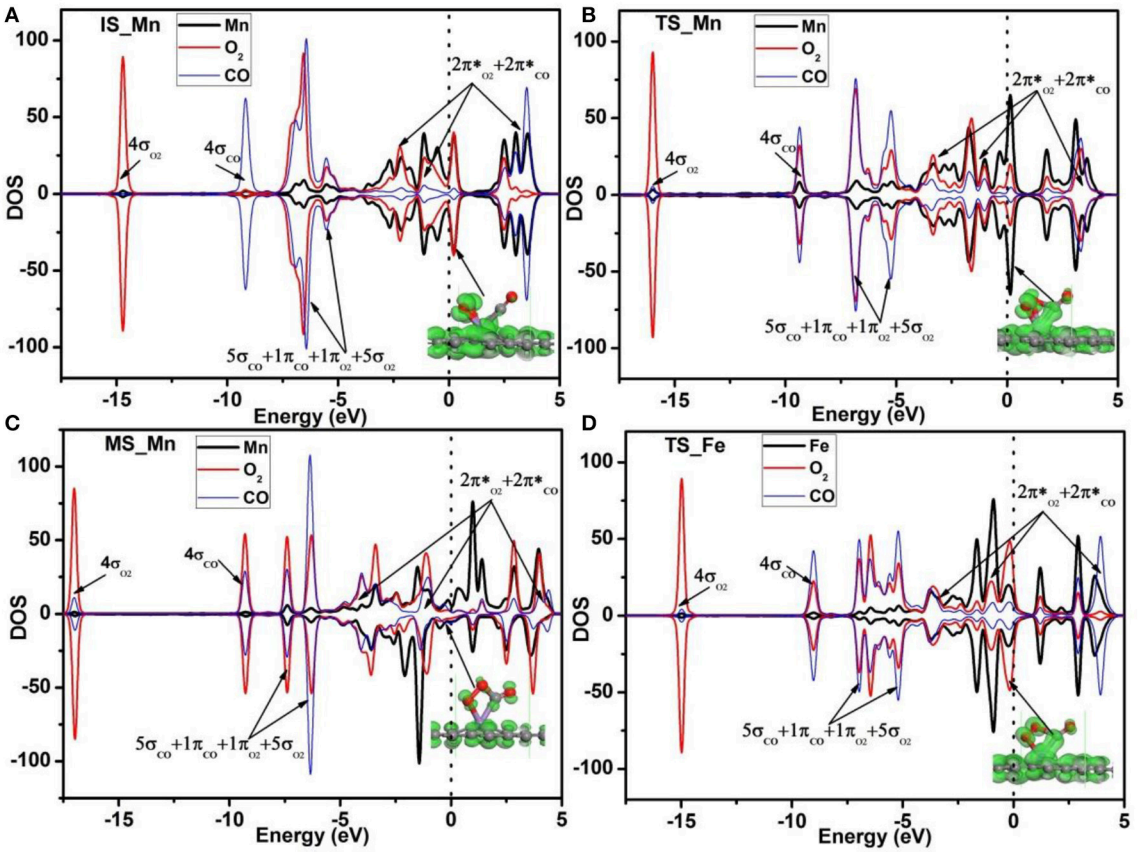

FIGURE 8 | PDOS of adsorbed O_2, CO, and Mn atom on Mn-DG for the IS **(A)**, TS **(B)**, and MS **(C)**. PDOS of adsorbed O_2, CO and Fe atom on Fe-DG for the TS state is also shown in **(D)**. Red, blue and black curves represent PDOS of adsorbed O_2, CO, and Mn (or Fe) atom, respectively. The orbitals of the adsorbed O_2 and CO molecules are roughly labeled. Inset is the charge density of orbitals near the Fermi level. The vertical lines indicate the Fermi level.

at 0 K. The reaction time for each step in **Figure 6** is calculated by Arrhenius equation (Pauling, 1988)

$$\tau = \frac{1}{\nu e^{\left(\frac{-E_{bar}}{K_B T}\right)}} \quad (2)$$

where K_B is the Boltzmann constant, ν is in order of 10^{12} Hz, and $T = 298.15$ K. $\tau_1 = 1.9 \times 10^{-4}$ s for step 1, $\tau_2 = 4.9 \times 10^{-11}$ s for step 2, and $\tau_3 = 1.7 \times 10^{-8}$ s for step 3, respectively. Therefore, the CO oxidation on Mn-DG along LH mechanism has fast kinetics.

The possibility for the reversing reaction of CO oxidation, i.e., for the dissociation of the first and the second CO_2 molecule into CO molecule and O atom on Mn-DG are further considered as shown in **Figure 6**. The reversing energy barriers for the step 1, step 2, and step 3 based on DFT calculations are 0.62, 3.96, and 1.07 eV, respectively. After considering the effect of temperature, the reversing energy barriers at 298.15 K are: $E'_{bar} = 0.69$ eV for step 1, $E'_{bar} = 4.05$ eV for step 2, $E'_{bar} = 1.01$ eV for step 3, while the corresponding reaction time is: $\tau_1 = 0.44$ s for step 1, $\tau_2 = 2.3 \times 10^{56}$ s for step 2, and $\tau_3 = 1.1 \times 10^5$ s for step 3. The long reaction time indicates that the reversing reactions for the CO oxidation on Mn-DG are hardly to occur and the CO oxidation can be finished thoroughly.

To consider the effect of interactions between vacancies on the oxidation of CO, the graphene with more vacancies in the 4 × 4 supercell is studied as shown in **Figure 7**. The atomic structure of graphene with two divacancies embedded with Mn atoms is shown in **Figure 7A**, and the corresponding reaction pathway of CO oxidation for LH mechanism is shown in **Figure 7B**, where the rate limiting energy barrier is 0.65 eV for the formation of OOCO complex. The atomic structure of graphene with one divacancy and one single vacancy embedded with Mn atoms is shown in **Figure 7C**, and the corresponding reaction pathway of CO oxidation for LH mechanism is shown in **Figure 7D**, where the rate limiting energy barrier is 0.88 eV for the formation of OOCO complex. Therefore, the reaction barriers on graphene with two double vacancies or one single and one double vacancies in the supercell in **Figure 7** are both large than that on graphene with one double vacancy in **Figure 6**. Considering that the distances between the nearest Mn dopants in **Figures 7A**,**B** are 4.295 Å and 5.062 Å, while that in the periodic supercell with one double vacancy in **Figure 2A** is

9.908 Å with E_{bar} = 0.41 eV, thus the relative larger distance between carbon vacancies is beneficial for the CO oxidation on Mn-DG.

Origin of the High Activity of Mn-DG

To further understand the high activity of the Mn-DG for CO oxidation, the Hirshfeld charge near the adsorbed molecules along the LH reaction path is shown in **Figure 6**, and the corresponding PDOS near the adsorbed molecules is shown in **Figure 8**. O_2 obtains 0.115 *e* while CO loses 0.076 *e* for the initial state in **Figure 6A**. The empty component of the O_2-2π∗ and CO-2π∗ orbitals are partially filled (see **Figure 8A**) due to the electron transformation during the adsorption, which causes the elongation of the O-O bond and C-O bond to 1.34 Å and 1.15 Å, respectively. At transition state, the charge of adsorbed O_2 is −0.136 *e* while that of adsorbed CO is −0.006 *e* in **Figure 6A**. This indicates that the O_2-2π∗ and CO-2π∗ orbitals are more filled as shown in **Figure 8B**, which is confirmed by the elongation of the O-O bond and C-O bond to 1.46 and 1.17 Å, respectively. After surmounting the energy barrier, more charge transfers from graphene to the adsorbed O_2 and CO, where the charge of O_2 is −0.154 *e* while that of CO is −0.058 *e* for MS in **Figure 6A**. The O_2-2p* and CO-2π∗ orbitals are more filled as shown in **Figure 8C**. Therefore, the Mn-DG can tune the charge distributions of the adsorbed O_2 and CO, and the charge transfer from Mn-DG to O_2 and CO molecules plays an important role for the OOCO intermediate formation.

Due to the fact that Fe is a commonly used dopant and the energy barrier for the first step on Fe-DG is 0.88 eV for CO oxidation, which is larger than that of 0.41 eV on Mn-DG, the PDOS of the TS configurations on Fe-DG is analyzed to further understood the mechanism for depressing the formation energy barrier of OOCO intermediate, as shown in **Figure 8D**. It can be seen that the overlapping area between O_2-2π∗ and Mn-3*d* orbitals at Fermi level on Mn-DG (see **Figure 8B**) becomes much weaker compared with that on Fe-DG (see **Figure 8D**), indicating that the interaction of Mn-O bond is significant weakened on Mn-DG. It is reported that weaker interaction nearby the Fermi level generally causes smaller reaction barrier (Arellano et al., 2000; Ao and Peeters, 2010b; Jiang et al., 2016). In addition, the interaction from −16 to −5 eV is strengthened on Mn-DG (see **Figures 8B,D**). Therefore, the enhanced interactions in the low energy range could lead to smaller reaction barrier for the CO oxidation on Mn-DG.

CONCLUSION

The oxidation of CO molecule on transition metals decorated graphene with divacancy (DG) has been studied by using DFT calculations. We found that Mn-DG has the best performance for the CO oxidation, while the LH mechanism is preferred, where the rate limiting energy barrier is only 0.41 eV, indicating the efficient oxidation process. The charge transfer from Mn-DG to the O_2-2p* and CO-2π∗ orbitals through the Mn atom along the LH mechanism plays a key role for depressing the energy barrier of the CO oxidation. The results indicate that Mn-DG can be a noble-metal-free and efficient catalyst for CO oxidation.

AUTHOR CONTRIBUTIONS

QJ, JZ, and ZA designed the research and wrote the paper. QJ carried out the simulation. HJH, HYH, and YW entered the discussion. All authors commented on the manuscript.

FUNDING

We acknowledge supports by the Fundamental Research Funds for National Natural Science Foundation of China (Grant No. 21703052), the Central Universities (Grant Nos. 2017B12914 and 2015B01914), China Postdoctoral Science Foundation (2015M571652), Natural Science Foundation of Jiangsu Province (BK20161506) and National 973 Plan Project (2015CB057803). ZA acknowledges the financial supports from National Natural Science Foundation of China (Grant No. 21607029, 21777033), Science and Technology Program of Guangdong Province (2017B020216003), Science and Technology Program of Guangzhou City (201707010359), and 1000 Plan for Young Professionals Program of China, 100 Talents Program of Guangdong University of Technology.

REFERENCES

Ali, S., Liu, T. F., Lian, Z., Li, B., and Su, D. S. (2017). The tunable effect of nitrogen and boron dopants on a single walled carbon nanotube support on the catalytic properties of a single gold atom catalyst: a first principles study of CO oxidation. *J. Mater. Chem. A* 5, 16653–16662. doi: 10.1039/C7TA03551A

An, W., Pei, Y., and Zeng, X. C. (2008). CO oxidation catalyzed by single-walled helical gold nanotube. *Nano Lett.* 8, 195–202. doi: 10.1021/nl072409t

Ao, Z. M., and Peeters, F. M. (2010a). High-capacity hydrogen storage in Al-adsorbed graphene. *Phys. Rev. B* 81:205406. doi: 10.1103/PhysRevB.81.205406

Ao, Z. M., and Peeters, F. M. (2010b). Electric field: A catalyst for hydrogenation of graphene. *Appl. Phys. Lett.* 96:253106. doi: 10.1063/1.3456384

Arellano, J. S., Molina, L. M., Rubio, A., and Alonso, J. A. (2000). Density functional study of adsorption of molecular hydrogen on graphene layers. *J. Chem. Phys.* 112:8114. doi: 10.1063/1.481411

Balandin, A. A., Ghosh, S., Bao, W., Calizo, I., Teweldebrhan, D., Miao, F., et al. (2008). Superior thermal conductivity of single-layer graphene. *Nano Lett.* 8, 902–907. doi: 10.1021/nl0731872

Bleakley, K., and Hu, P. (1999). A density functional theory study of the interaction between CO and O on a Pt Surface: CO/Pt (111), O/Pt (111), and CO/O/Pt (111). *J. Am. Chem. Soc.* 121, 7644–7652. doi: 10.1021/ja983363w

Chen, Z. W., Wen, Z., and Jiang, Q. (2017). Rational design of Ag_{38} cluster supported by graphdiyne for catalytic CO oxidation. *J. Phys. Chem. C* 121, 3463–3468. doi: 10.1021/acs.jpcc.6b12434

Delley, B. (2000). From molecules to solids with the $Dmol^3$ approach. *J. Chem. Phys.* 113:7756. doi: 10.1063/1.1316015

Dupont, C., Jugnet, Y., and Loffreda, D. (2006).Theoretical evidence of PtSn alloy efficiency for CO oxidation. *J. Am. Chem. Soc.* 128, 9129–9136. doi: 10.1021/ja061303h

Dvorák, F., Camellone, M. F., Tovt, A., Tran, N. D., Negreiros, F. R., Vorokhta, M., et al. (2016). Creating single-atom Pt-ceria catalysts by surface step decoration. *Nat. Commun.* 7:10801. doi: 10.1038/ncomms10801

Gong, X. Q., Liu, Z. P., Raval, R., and Hu, P. (2004). A systematic study of CO oxidation on metals and metal oxides: density functional theory calculations. *J. Am. Chem. Soc*. 126, 8–9. doi: 10.1021/ja030392k

Grimme, S. (2006). Semiempirical GGA-type density functional constructed with a long-range dispersion correction. *J. Comput. Chem.* 27, 1787–1799. doi: 10.1002/jcc.20495

Halgren, T. A., and Lipscomb, W. N. (1977). The synchronous-transit method for determining reaction pathways and locating molecular transition states. *Chem. Phys. Lett*. 49, 225–232. doi: 10.1016/0009-2614(77)80574-5

Henkelman, G., and Jonsson, H. (2000). A climbing image nudged elastic band method for finding saddle points and minimum energy paths. *J. Chem. Phys*. 113:9978. doi: 10.1063/1.1323224

Honkala, K., and Laasonen, K. (2000). Oxygen molecule dissociation on the Al (111) surface. *Phys. Rev. Lett.* 84:705. doi: 10.1103/PhysRevLett.84.705

Jiang, Q. G., Ao, Z. M., Li, S., and Wen, Z. (2014). Density functional theory calculations on the CO catalytic oxidation on Al-embedded graphene. *RSC Adv.* 4, 20290–20296. doi: 10.1039/C4RA01908C

Jiang, Q. G., Wu, W. C., Zhang, J. F., Ao, Z. M., Wu, Y. P., and H. J., Huang (2016). Defections induced hydrogenation of silicene: a density functional theory calculation study. *RSC Adv*. 6, 69861–69868. doi: 10.1039/C6RA11885B

Jones, J., Xiong, H. F., Delariva, A. T., Peterson, E. J., Pham, H., Challa, S. R., et al. (2016). Thermally stable single-atom platinum-on-ceria catalysts via atom trapping. *Science* 353, 150–154. doi: 10.1126/science.aaf8800

Lee, C. G., Wei, X. D., Kysar, J. W., and Hone, J. (2008). Measurement of the elastic properties and intrinsic strength of monolayer graphene. *Science* 321, 385–388. doi: 10.1126/science.1157996

Leenaerts, O., Partoens, B., and Peeters, F. M. (2008). Adsorption of H_2O, NH_3, CO, NO_2, and NO on graphene: a first-principles study. *Phys. Rev. B* 77:125416. doi: 10.1103/PhysRevB.77.125416

Li, Y. F., Zhou, Z., Yu, G. T., Chen, W., and Chen, Z. F. (2010). CO catalytic oxidation on iron-embedded graphene: computational quest for low-cost nanocatalysts. *J. Phys. Chem. C* 114, 6250–6254. doi: 10.1021/jp911535v

Liu, D. J.,(2007). CO oxidation on Rh (100): multisite atomistic lattice-gas modelling. *J. Phys. Chem. C* 111, 14698–14706. doi: 10.1021/jp071944e

Liu, S. G., and Huang, S. P. (2017). Theoretical insights into the activation of O_2 by Pt single atom and Pt_4 nanocluster on functionalized graphene support: critical role of Pt positive polarized charges. *Carbon* 115, 11–17. doi: 10.1016/j.carbon.2016.12.094

Liu, Z. P., Hu, P., and Alavi, A. (2002). Catalytic role of gold in gold-based catalysts: a density functional theory study on the CO oxidation on gold. *J. Am. Chem. Soc*. 124, 14770–14779. doi: 10.1021/ja0205885

Liu, Z. Y., He, T. W., Liu, K. K., Chen, W. G., and Tang, Y. N. (2017). Structural, electronic and catalytic performances of single-atom Fe stabilized by divacancy-nitrogen-doped graphene. *RSC Adv*. 7, 7920–7928. doi: 10.1039/C6RA28387J

Lu, Y. H., Zhou, M., Zhang, C., and Feng, Y. P. (2009). Metal-embedded graphene: a possible catalyst with high activity. *J. Phys. Chem. C* 113, 20156–20160. doi: 10.1021/jp908829m

Ma, L., Melander, M., Weckman, T., Laasonen, K., and Akola, J. (2016). CO oxidation on the $Au_{15}Cu_{15}$ cluster and the role of vacancies in the MgO(100) support. *J. Phys. Chem. C* 120, 26747–26758. doi: 10.1021/acs.jpcc.6b06876

Molina, L. M., and Hammer, B. (2005). The activity of the tetrahedral Au_{20} cluster: charging and impurity effects. *J. Catal*. 233, 399–404. doi: 10.1016/j.jcat.2005.04.037

Novoselov, K. S., Geim, A. K., Morozov, S. V., Jiang, D., Katsnelson, M. I., Grigorieva, I. V., et al. (2005). Two-dimensional gas of massless dirac fermions in graphene. *Nature* 438, 197–200. doi: 10.1038/nature04233

Novoselov, K. S., Geim, A. K., Morozov, S. V., Jiang, D., Zhang, Y., Dubonos, S. V., et al. (2004). Electric field effect in atomically thin carbon films. *Science* 306, 666–669. doi: 10.1126/science.1102896

Pauling, L. (1988). *General Chemistry*. New York, NY: Dover Publications.

Perdew, J. P., Burke, K., and Ernzerhof, M. (1996). Generalized gradient approximation made simple. *Phys. Rev. Lett*. 77:3865. doi: 10.1103/PhysRevLett.77.3865

Qiao, B. T., Liu, J. X., Wang, Y. G., Lin, Q. Q., Liu, X. Y., Wang, A. Q., et al. (2015). Highly efficient catalysis of preferential oxidation of CO in H_2-rich stream by gold single-atom catalysts. *ACS Catal.* 5, 6249–6254. doi: 10.1021/acscatal.5b01114

Robertson, A. W., Allen, C. S., Wu, Y. A., He, K., Olivier, J., Neethling, J., et al. (2012). Spatial control of defect creation in graphene at the nanoscale. *Nat. Commun.* 3:1144. doi: 10.1038/ncomms2141

Robertson, A. W., Montanari, B., He, K., Kim, J., Allen, C. S., Wu, Y. A., et al. (2013). Dynamics of single Fe atoms in graphene vacancies. *Nano Lett.* 13, 1468–1475. doi: 10.1021/nl304495v

Roldán, A., Ricart, J. M., and Illas, F. (2009). Influence of the exchange-correlation potential on the description of the molecular mechanism of oxygen dissociation by Au nanoparticles. *Theor. Chem. Acc.* 123, 119–126. doi: 10.1007/s00214-009-0540-1

Saavedra, J., Whittaker, T., Chen, Z. F., Pursell, C. J., Rioux, R. M., and Chandler, B. D. (2016). Controlling activity and selectivity using water in the Au-catalysed preferential oxidation of CO in H_2. *Nat. Chem.* 8, 584–589. doi: 10.1038/nchem.2494

Segall, M. D., Lindan, P. L. D., Probert, M. J., Pickard, C. J., Hasnip, P. J., Clark, S. J., et al. (2002). First-principles simulation: ideas, illustrations and the CASTEP code. *J. Phys.* 14, 2717–2744. doi: 10.1088/0953-8984/14/11/301

Song, E. H., Wen, Z., and Jiang, Q. (2011). CO catalytic oxidation on copper-embedded graphene. *J. Phys. Chem. C* 115, 3678–3683. doi: 10.1021/jp108978c

Tang, Y. A., Zhou, J. C., Shen, Z. G., Chen, W. G., Li, C. G., and Dai, X. Q. (2016). High catalytic activity for CO oxidation on single Fe atom stabilized in graphene vacancies. *RSC Adv.* 6, 93985–93996. doi: 10.1039/C6RA14476D

Tang, Y. N., Lu, Z. S., Chen, W. G., Li, W., and Dai, X. Q. (2015). Geometric stability and reaction activity of Pt clusters adsorbed graphene substrates for catalytic CO oxidation. *Phys. Chem. Chem. Phys.* 17, 11598–11608. doi: 10.1039/C5CP00052A

Tang, Y. N., Yang, Z. X., and Dai, X. Q. (2012). A theoretical simulation on the catalytic oxidation of CO on Pt/graphene. *Phys. Chem. Chem. Phys*. 14, 16566–16572. doi: 10.1039/c2cp41441d

Wang, Y. G., Cantu, D. C., Lee, M. S., Li, J., Glezakou, V. A., and Rousseau, R. (2016). CO oxidation on Au/TiO_2: condition-dependent active sites and mechanistic pathways. *J. Am. Chem. Soc.* 138, 10467–10476. doi: 10.1021/jacs.6b04187

Xie, X. W., Li, Y., Liu, Z. Q., Haruta, M., and Shen, W. J. (2009). Low-temperature oxidation of CO catalysed by Co_3O_4 nanorods. *Nature* 458, 746–749. doi: 10.1038/nature07877

Young, D. C. (2001). *Computational Chemistry: A Practical Guide for Applying Techniques to Real World Problems*. New York, NY: Wiley.

Zhang, A. H., Zhu, J., and Duan, W. H. (2006). Oxidation of carbon monoxide on Rh (111): a density functional theory study. *J. Chem. Phys*. 124:234703. doi: 10.1063/1.2209239

Zhang, C. J., and Hu, P. (2001). CO oxidation on Pd (100) and Pd (111): a comparative study of reaction pathways and reactivity at low and medium coverages. *J. Am. Chem. Soc.* 123, 1166–1172. doi: 10.1021/ja002432f

Zhao, J. X., Chen, Y., and Fu, H. G. (2012). Si-embedded graphene: an efficient and metal-free catalyst for CO oxidation by N_2O or O_2. *Theor. Chem. Acc*. 131:1242. doi: 10.1007/s00214-012-1242-7

Conflict of Interest Statement: The authors declare that the research was conducted in the absence of any commercial or financial relationships that could be construed as a potential conflict of interest.

frontiers in Chemistry

ORIGINAL RESEARCH
published: 12 September 2018
doi: 10.3389/fchem.2018.00351

The Activity Improvement of the TM_3(hexaiminotriphenylene)$_2$ Monolayer for Oxygen Reduction Electrocatalysis: A Density Functional Theory Study

Beibei Xiao[1]*, *Hui Zhu*[1], *HouYi Liu*[1], *XiaoBao Jiang*[2] and *Qing Jiang*[3]*

[1] School of Energy and Power Engineering, Jiangsu University of Science and Technology, Zhenjiang, China, [2] School of Materials Science and Engineering, Jiangsu University of Science and Technology, Zhenjiang, China, [3] Key Laboratory of Automobile Materials, Ministry of Education, School of Materials Science and Engineering, Jilin University, Changchun, China

OPEN ACCESS

Edited by:
Zhimin Ao,
Guangdong University of Technology, China

Reviewed by:
Aijun Du,
Queensland University of Technology, Australia
Simonetta Antonaroli,
Università degli Studi di Roma Tor Vergata, Italy

***Correspondence:**
Beibei Xiao
xiaobb11@mails.jlu.edu.cn
Qing Jiang
jiangq@jlu.edu.cn

Specialty section:
This article was submitted to Green and Sustainable Chemistry, a section of the journal Frontiers in Chemistry

Received: *19 May 2018*
Accepted: *25 July 2018*
Published: *12 September 2018*

Citation:
Xiao B, Zhu H, Liu H, Jiang X and Jiang Q (2018) The Activity Improvement of the TM_3(hexaiminotriphenylene)$_2$ Monolayer for Oxygen Reduction Electrocatalysis: A Density Functional Theory Study. Front. Chem. 6:351. doi: 10.3389/fchem.2018.00351

Polymer electrolyte membrane fuel cells (PEMFCs) are one of the most prominent clean energy technologies designed to achieve hydrogen utilization and solve problems such as low efficiency and high pollution associated with fossil fuel combustion. In order to bring about PEMFC commercialization, especially for automobile applications, developing high-activity and -selectivity catalysts for the oxygen reduction reaction (ORR) is of critical importance. Based on the density functional theory, the catalytic activity of the conductive, two-dimensional metal–organic frameworks $TM_3(HITP)_2$ monolayer (where HITP = hexaiminotriphenylene; TM = Ni, Co, Fe, Pd, Rh, Ru, Pt, Ir, and Os) for ORR has been investigated systematically. Furthermore, the classical volcano curves of the ORR activity, as a function of the OH binding, are found where the Ni, Pd, and Pt located at the weak binding side suffer from the sluggish *OOH formation and prefer the inefficient $2e^-$ mechanism, while for other elements belonging to the strong binding side, the reactions are hindered by the poison due to ORR intermediates. Based on the free energy profiles, the corresponding overpotentials μ_{ORR} exhibit the inverted volcano curve as a function of the atomic number of the 3*d*/4*d*/5*d* TM active center in the same period. Based on the μ_{ORR} data, ORR activity decreases in the order of Ir > Co ≈ Rh > Ni ≈ Pd > Pt ≈ Fe > Ru > Os. Herein, the Co, Rh, and Ir central atoms exhibit enhanced catalytic activity in combination with the desirable selectivity of the O_2 reduction to H_2O. This systematic work may open new avenues for the development of high-performance non-PGM catalysts for practical applications of ORR.

Keywords: oxygen reduction reaction, activity and selectivity, 2D materials, transition metal elements, DFT calculation

INTRODUCTION

Hydrogen is a potential candidate for future energy provision, as stated in the concept of the hydrogen economy, so as to solve the issues of the rising global energy demands, depletion of fossil fuel reserves, and associated environmental pollution issues. Due to its high efficiency, ease of operation, and low emission, the polymer electrolyte membrane fuel cell (PEMFCs) is the

most prominent technology to derive benefit from the proposed hydrogen cycle, which leads to the production of electricity from the electrochemical oxidation of hydrogen, with water as its endproduct (Colić and Bandarenka, 2016; Xia Z. et al., 2016; Chen et al., 2017, 2018). However, a critical obstacle to its commercialization is the dominant voltage loss associated with the sluggish oxygen reduction reaction (ORR), even when catalyzed by the noble Pt nanoparticle (Nørskov et al., 2004). In this regard, a significant amount of Pt is required to achieve the desirable power density, making the overall cost prohibitively high (Debe, 2012). In order to overcome the economic bottleneck, design, and application of earth-abundant alternatives for ORR electrocatalysis are at the heart of PEMFC research (Xia W. et al., 2016).

Inspired by the pioneering work on cobalt phthalocyanines acting as cathode catalysts (Jasinski, 1964), a tremendous amount of research is being performed on the TM–N_x carbon materials for ORR (TM denotes transition metals), especially TM–N_4 active motif. The intrinsic active characteristic of TM in N_x carbon materials is experimentally supported, where the presence of the TM atom would boost the ORR performance compared with the metal-free counterpart (Peng et al., 2013; Yin et al., 2016; Yang et al., 2017); the corresponding activity would be suppressed by adding the SCN^- ions and CO molecule (Zhang et al., 2016; Yang et al., 2017). Linear correlations between the content of TM–N_x and ORR activity have been observed (Yang et al., 2017). Furthermore, ORR activity shows its dependence on the TM center atom, and this is supported by the density functional theory (DFT), a theoretical work of Rossmeisl et al., where the ORR activity of the TM–N_4 embedded graphene has been systematically investigated, and where the Fe, Ir, Mn, Ru, and Rh doping is identified as boosting the ORR (Calle-Vallejo et al., 2011). Additionally, the ORR mechanism is sensitive to the TM–N_4 active motif. Liu et al. have synthesized the Fe–N_x and Co–N_x doped carbon nanofiber and realized that the Fe–N_4 promotes $4e^-$ ORR in comparison with the $2e^-$ pathway of the Co–N_4 one (Liu et al., 2016). The same conclusion has been achieved by Kattel et al., where the O–O bond scission is presented and the efficient $4e^-$ reduction of O_2 to $2H_2O$ is preferred on the Fe–N_4 sites, but the reduction of O_2 to H_2O_2 is found enhanced on the Co–N_4 motif (Kattel et al., 2013, 2014).

Despite these encouraging research works, such TM–N_4 carbon materials generally suffer from low activity caused by the relatively few catalytic sites as well as the experimental challenge of the well-controlled active motif (Liang et al., 2013; Peng et al., 2013; Palaniselvam et al., 2016), reducing the competition with the state-of-the-art Pt/C catalysts. Paying attention to the high TM–N_4 density in combination with the electronic conductivity, Miner et al. have developed the attractive $Ni_3(HITP)_2$ as ORR electrocatalyst (Miner et al., 2016). However, the performance is far from satisfying expectations, with its incomplete oxidation of O_2 and the predominant production of H_2O_2 under the working potential (Miner et al., 2016). In this regard, utilizing the aforementioned information, the development of the efficient $TM_3(HITP)_2$ catalysts can be achieved via the variation of metal nodes (Choi et al., 2015; Zhang et al., 2015). It has naturally raised the interest to search for the optimal combinations of the $TM_3(HITP)_2$, possessing superior ORR activity as well as selectivity.

In the manuscript, DFT calculations are used within an electrochemical framework to analyze the ORR electrocatalysis over the $TM_3(HITP)_2$monolayer. In particular, the stability of the ORR intermediates is calculated, which allows to evaluate the thermodynamic ORR free energy and its overpotentials. The data provide the fundamental understanding of the mechanism of $Ni_3(HITP)_2$ and further identify optimal candidates as catalysts. According the *d*–partial density of states, an atomistic insight of the activity origin has been provided by a thorough comparison among the considered systems. Herein, for simplification, our attention is mainly focused on the monolayer structure shown in **Figure 1** as a representative model due to the weak interaction between the interlayers of the 2D-layered materials (Sheberla et al., 2014; Chen et al., 2015; Miner et al., 2016).

METHODS

All calculations have been performed within the DFT framework, as implemented in the DMol^3 code (Delley, 1990, 2000). The generalized gradient approximation with the Perdew–Burke–Ernzerhof (PBE) functional is employed to describe exchange and correlation effects (Perdew et al., 1996). The DFT semicore pseudopotentials (DSPP) core treat method is implemented for relativistic effects, which replaces core electrons by a single effective potential and introduces some degree of relativistic correction into the core (Delley, 2002). The double numerical atomic orbital augmented by a polarization function (DNP) is chosen as the basis set (Delley, 1990). A smearing of 0.005 Ha (1 Ha = 27.21 eV) to the orbital occupation is applied to achieve accurate electronic convergence. In order to ensure high-quality results, the real-space global orbital cutoff radius is set as high as 5.2 Å. In order to accurately describe the long-range electrostatic interactions of the ORR intermediates with catalysts, the PBE-D method with the TS van der Waals (vdW) correction is employed. In the geometry optimization of structures, the convergence tolerances of energy, maximum force, and displacement are

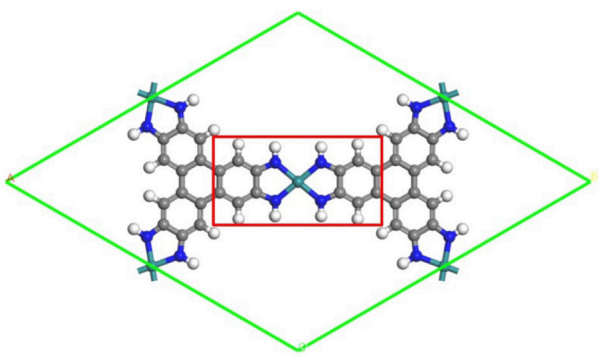

FIGURE 1 | The schematic structure of the $TM_3(HITP)_2$ monolayer. Green, blue, gray, and white denote the TM, N, C, and H atoms.

1.0×10^{-5} Ha, 0.002 Ha/Å, and 0.005 Å, respectively. The spin-unrestricted method is used for all calculations. A conductor-like screening model (COSMO) was used to simulate a H_2O solvent environment for all calculations (Todorova and Delley, 2008), which is a continuum model, where the solute molecule forms a cavity within the dielectric continuum. The DMol^3/COSMO method has been generalized to periodic boundary cases. The dielectric constant is set as 78.54 for H_2O. Some previous results have shown that this implicit solvation model is an effective method to describe solvation (Sha et al., 2011; Zhang et al., 2015). The 15 Å-thick vacuum is added to avoid the artificial interactions between the $TM_3(HITP)_2$ monolayer and its images. The proposed structure of the $TM_3(HITP)_2$ monolayer is shown in **Figure 1**, where the atoms in the red square are fixed in all of the structure-optimization calculations.

The adsorption energy (E_{ads}) of the reactant O_2 is calculated by the following,

$$E_{ads}(O_2) = E_{sys} - E_{substrate} - E_{O2} \quad (1)$$

The adsorption energy (E_{ads}) of the ORR intermediates are calculated relative to H_2O and H_2 (Calle-Vallejo et al., 2011), through,

$$E_{ads}(OOH) = E_{sys} - E_{substrate} - (2E_{H2O} - 3/2E_{H2}) \quad (2)$$

$$E_{ads}(O) = E_{sys} - E_{substrate} - (E_{H2O} - E_{H2}) \quad (3)$$

$$E_{ads}(OH) = E_{sys} - E_{substrate} - (E_{H2O} - 1/2E_{H2}) \quad (4)$$

where E_{sys}, $E_{substrate}$, E_{H2O}, and E_{H2} are the total energy of the adsorption systems, the $TM_3(HITP)_2$ monolayer, H_2O molecule, and H_2 molecule, respectively. The $E_{ads} < 0$ corresponds to an exothermic adsorption process.

The Gibbs free energy changes (ΔG) of the ORR elemental steps have been calculated according to the computational hydrogen electrode (CHE) model developed by Nørskov et al., where the chemical potential of the proton/electron ($H^+ + e^-$) in solution is equal to the half of the chemical potential of a gas-phase H_2 at the reference relative hydrogen electrode (RHE) potential (Nørskov et al., 2004). Herein, $G_{(H++e-)} = 1/2G_{(H2)}$. The variance of the proton–electron pair free energy with potential is simply determined using the linear free energy dependence of the electron energy on potential, shifting the electron energy $-eU$, where e is the elementary positive charge and U is the electrode potential of interest on the RHE scale (Nørskov et al., 2004; Nie et al., 2014). The total chemical potential of a proton–electron pair at the potential U is written as follows:

$$G(U)_{(H++e-)} = 1/2G_{(H2)} - eU \quad (5)$$

Therefore, for a general electrochemical reaction, the free energy change ΔG for every elemental step can be determined as following:

$$\Delta G = \Delta E + \Delta ZPE - T\Delta S + \Delta G_{pH} + \Delta G_U \quad (6)$$

where ΔE is the electronic energy difference based on DFT calculations, ΔZPE is the change in zero point energy, T is the temperature (equal to 298.15 K here), ΔS is the change in the entropy, and ΔG_{pH} and ΔG_U are the free energy contributions due to variation in pH value and electrode potential U, respectively. $\Delta G_U = -eU$, in which U is the potential related to the standard hydrogen electrode. $\Delta G_{pH} = -kT\ln10$ x pH, which is the corrected free energy of H^+ ions depending on the concentration. According to the previous works, pH is set as 0 in acid medium and 14 in alkaline medium. The zero-point energies and entropies of the ORR intermediates are calculated from the vibrational frequencies according to standard methods. Following the suggestion of Wilcox et al. (Lim and Wilcox, 2012), in order to reduce the calculation, the $TM_3(HITP)_2$ monolayer is fully constrained. The $\Delta G < 0$ corresponds to an exothermic adsorption process. The free energy G of O_2 is derived as $G(O_2) = 4.92+2G(H_2O)-2G(H_2)$ by utilizing OER equilibrium at the standard conditions; the G of H_2O_2 is derived similarly considering that the H_2O_2/O_2 standard equilibrium potential is 0.682 V vs. SHE (Sun et al., 2014). The CHE model has been successfully applied for developing the novel electrocatalysts with prominent ORR performances, where the DFT calculations are in line with the experimental results (Nørskov et al., 2004; Greeley et al., 2009; Favaro et al., 2015; Lang et al., 2015; Jia et al., 2016; Tang et al., 2016; Liu et al., 2017; Li et al., 2018; Xu et al., 2018). Furthermore, the PBE/DNP method in Dmol^3 code has been widely employed for evaluating the potential of the TM-based carbon electrocatalysts (Wang et al., 2015, 2016b; Hou et al., 2016; Xiao et al., 2017). Therefore, the reliability of the mentioned approach is confirmed.

RESULTS AND DISCUSSION

Prior to the investigation of the activity, the essential step is to determine the adsorption behavior of the ORR intermediates. For $Ni_3(HITP)_2$, the energetics of the O_2 adsorption is endothermic with the value of 0.13 eV, caused by the structure deformation as shown in the inset of **Figure 2A**, indicating no such adsorption has occurred on the Ni center atom. Besides the reactant, the corresponding E_{ads} of ORR intermediates are 4.08, 3.57, and 1.17 eV for OOH, O, and OH, respectively. In comparison with the Pt(111) (3.55 eV for OOH, 1.38 eV for O, and 0.64 eV for OH) (Xiao et al., 2016), the obviously weak adsorption ability of the center Ni atom has been observed.

Considering the low affinity of the ORR intermediates to the Ni center, it is expected that the ORR activity would be boosted by selecting suitable TMs. Indeed, the change of the TM center definitely exhibits different adsorption behaviors, as shown in **Figure 2**, where the corresponding E_{ads} data are given. From the figures, the E_{ads} of the reactant O_2 and the corresponding ORR intermediates decrease monotonically in the order of Ru ≈ Os > Fe > Co > Rh ≈ Ir > Ni > Pd ≈ Pt. It is obvious that the adsorption ability of the elements is weakened from group 8 to group 10. Carefully reviewing the O_2 adsorption as shown in the inset of **Figure 2A**, similar to Ni, no such adsorption behaviors have occurred at the Pd and Pt active centers due to the endothermic adsorption energies. The unfavorable adsorption behavior of group 10 implies the

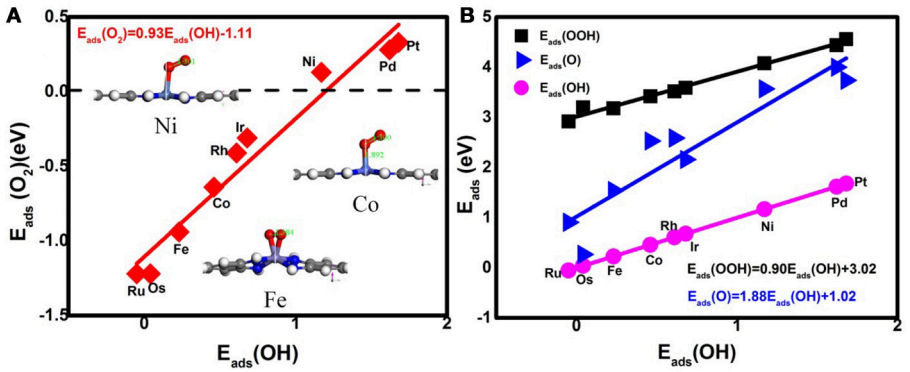

FIGURE 2 | The adsorption energies of the O_2 molecules **(A)** and the ORR intermediates **(B)**. Inset: the representative O_2 adsorption structure on Ni, Co, and Fe active centers.

underlying mechanism of the OOH formation, which originates from the long-range electron transfer from the catalyst to O_2 molecules at the outer Helmholtz plane (Choi et al., 2014). On the contrary, group 9 binds to the reactant suitably with the corresponding end-on structure and group 8 possesses a too strong O_2 adsorption with the side-on adsorption configuration. Herein, the mentioned adsorption capability is in line with the general prediction of the *d*-band model (Hammer and Nørskov, 2000). The corresponding evidences are provided by the *d*–partial density of states (*d*–PDOS) of the central TM atom plotted in **Figure 3**. As shown, the *d* band moves away from the Fermi energy as the TM atom changes from group 8 to group 10. The TM atom with the higher *d* states possesses stronger adsorption ability. Furthermore, due to the relationship between the adsorption behavior and the *d* band, the linear scaling relations between $E_{ads}(O_2)/E_{ads}(OOH)/E_{ads}(O)$ and $E_{ads}(OH)$ are observed, in accordance with the previous reports of other functionalized carbon materials (Calle-Vallejo et al., 2011; Baran et al., 2014). That is,

$$E_{ads}(O_2) = 0.93E_{ads}(OH) - 1.11, \quad (7)$$

$$E_{ads}(OOH) = 0.90E_{ads}(OH) + 3.02, \quad (8)$$

$$E_{ads}(O) = 1.88E_{ads}(OH) + 1.02. \quad (9)$$

To further evaluate the ORR activity of TM$_3$(HITP)$_2$, according to the experimental condition (Miner et al., 2016), the OOH associative mechanisms in the alkaline solution are taken into consideration, with the elemental steps R_i listed as follows (Wang et al., 2016a), where asterisks denote active TM sites. Due to the small barrier of proton transfer, which can be ignored at high applied voltages, our attention is only focused on the reaction energies (Nørskov et al., 2004; Calle-Vallejo et al., 2011; Zhang et al., 2015).

$$O_2(g) + * + H_2O(l) + e^- \rightarrow OOH^* + OH^-, (R_1)$$

$$OOH^* + e^- \rightarrow O^* + OH^-, \quad (R_{2a})$$

$$OOH^* + H_2O(l) + e^- \rightarrow H_2O_2^* + OH^-, \quad (R_{2b})$$

$$O^* + H_2O(l) + e^- \rightarrow OH^* + OH^-, \quad (R_3)$$

$$OH^* + e^- \rightarrow OH^-. \quad (R_4)$$

Analyzing the free energy plots of the complete $4e^-$ ORR pathway in **Figure 4A**, the endothermic processes of *OOH formation (R_1) and *O formation (R_{2a}) are observed even at $U = 0$ V. The corresponding values of the free energy change ΔG_i are 0.28 and 0.08 eV, respectively. The positive values indicate that the mentioned steps are thermodynamically unfavorable (Nørskov et al., 2004). When the ideal potential of 0.4 eV is applied, the mentioned reaction steps are even unfavorable with the increased ΔG_i of 0.68 and 0.48 eV, respectively. Based on the information, R_1 is determined as the rate-determining step (RDS), pointing to the fact that the Ni$_3$(HITP)$_2$ monolayer suffers from insufficient O_2 activation (Greeley et al., 2009), in accordance with the endothermic capture of the O_2 molecule as shown in **Figure 2A**. To clarify the selectivity of the $2/4e^-$ mechanism, the comparison between R_{2a} and R_{2b} is considered. In the alternative $2e^-$ pathway, the ΔG_{2b} of the H_2O_2 formation (R_{2b}) is increased from 0.01 to 0.41 eV as the *U* ranged from 0 to 0.4 V, being 0.07 eV lower than ΔG_{2a}, indicating the slightly energy favorable condition of R_{2b}. Herein, the predominant production of H_2O_2 would be expected on the Ni$_3$(HITP)$_2$ monolayer, which is in consistence with the experiment results of the 3D Ni$_3$(HITP)$_2$. In summary, the Ni$_3$(HITP)$_2$ monolayer slightly prefers the $2e^-$ mechanism, with the RDS located at the *OOH formation.

Owing to the different adsorption abilities of TM$_3$(HITP)$_2$, the suitable TM would boost the ORR activity as well as the selectivity of the $4e^-$ mechanism. In order to characterize the relationship between the ORR activity and the TM center atom, the reactive free energy change ΔG_i of the elementary steps R_i at $U = 0.4$ V as a function of $E_{ads}(OH)$ is plotted in **Figure 4B**. As the weakening of the $E_{ads}(OH)$ occurs with the values ranging from −0.05 to 1.68 eV, ΔG_1 and ΔG_{2a} increase from the negative to the positive values, while the opposite tendency is found for ΔG_3 and ΔG_4, which decrease from the positive to the negative values. That is, the steps R_1 and R_{2a} change from the exothermic to endothermic process, while the steps R_3 and R_4 become more thermodynamically favorable. Obviously, the RDS steps are identified as R_4 for group 8 and group 9 with the exception of Os, where the RDS step is R_3, while the RDS step is located at R_1 for group 10.

On the basis of the assumption that the activation barrier for the RDS is equal to ΔG_{max}, the activity variation of $TM_3(HITP)_2$ referred to as $Ni_3(HITP)_2$ is estimated by the rate constant k via the simple Arrhenius equation in the following,

$$k = A\exp(-\Delta G_{max}/k_BT) \quad (10)$$

$$\ln(k_{TM}/k_{Ni}) = [\Delta G_{max}(Ni) - \Delta G_{max}(TM)]/k_BT \quad (11)$$

where A is the prefactor, k_B is the Boltzmann constant, and T is the temperature (298.15 K). The classic volcano curve is observed in **Figure 5A**, where the $\ln(k_{TM}/k_{Ni})$ as a function of the E_{ads}(OH) is plotted. Based on our results, the adsorption ability is weakened as the atomic number increases from group 8 to group 10. The Ni/Pd/Pt active centers suffer from the too weak binding strength, leading to the energetically unfavorable process of the *OOH formation. Meanwhile, for the Fe/Ru/Os active centers, the too strong interaction with the ORR intermediates accounts for the poisoning of the O-containing intermediates. The suitable binding strength of Co/Rh/Ir active centers indicates the balance between the O_2 activation and the catalyst recovery.

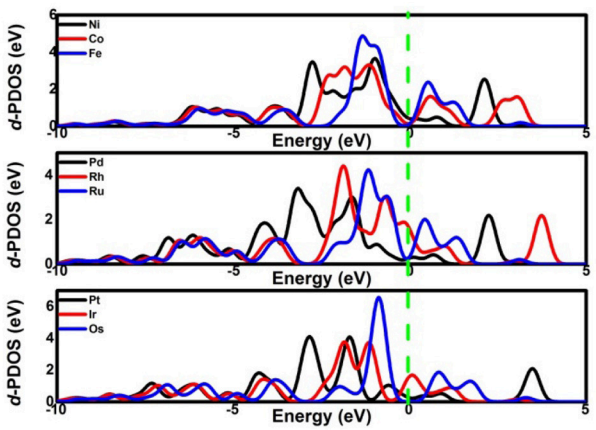

FIGURE 3 | The *d*-PDOS of the central TM atom.

As discussed by the previous reports (Calle-Vallejo et al., 2011; Viswanathan et al., 2012a; Baran et al., 2014; Zhang et al., 2015), the ORR activity depends on the adsorption of the intermediates. Our results are in accordance with the previous reports in that the bond strength should be compromised in the case of the effective ORR catalysts on the basis of Sabatier principle (Greeley et al., 2009; Gao et al., 2017, 2018); this is similar with the previous studies on metal (Stephens et al., 2012), functional graphene (Calle-Vallejo et al., 2011), metal porphyrine (Baran et al., 2014) as well as the 2D MOF (Gao et al., 2017). Herein, in comparison with the $Ni_3(HITP)_2$ monolayer (0.68 eV), group 9 possesses superior catalytic performance with the smaller ΔG_{max} of 0.50, 0.52, and 0.22 eV for the Co, Rh, and Ir center atoms, respectively. By contrast, inferior activities are observed for group 8 and group 10. The corresponding ΔG_{max} are 0.93, 1.23, and 1.34 eV for Fe, Ru, and Os atoms, and 0.72 and 0.90 eV for Pd and Pt atoms, respectively. Furthermore, for clarification, the data of the relative overpotentials μ_{ORR} are summarized and collected for the activity comparison, depicted in **Figure 6**. As the atomic number of TM increased from Ni to Fe, the μ_{ORR} reduces and then increases, presenting further evidence to the presence of the classical volcano-shaped activity (Nørskov et al., 2004; Calle-Vallejo et al., 2011; Baran et al., 2014; Zheng et al., 2017). Similar situations are found for the 4*d*/5*d* $TM_3(HITP)_2$ monolayer. Based on the μ_{ORR} data, ORR activity decreases in the order of Ir > Co ≈ Rh > Ni ≈ Pd > Pt ≈ Fe > Ru > Os. Furthermore, compared with the data of the TM supported on graphene and macrocyclic molecules (the minimum μ_{ORR} = 0.4 eV) (Xu et al., 2018), the prominent improvement of the ORR activity on the $Ir_3(HITP)_2$ monolayer is confirmed.

Besides the ORR activity, the ORR selectivity is characterized by the ratio of the corresponding reaction rate k_{2a} (k_{2b}) for step R_{2a} (R_{2b}), via the following equation,

$$\ln(k_{2a}/k_{2b}) = [\Delta G_{2b} - \Delta G_{2a}]/k_BT \quad (12)$$

The data are plotted in **Figure 5B**. As shown, $\ln(k_{2a}/k_{2b})$ shows a linear relationship with E_{ads}(OH). For the weak side, the values of ΔG_{2a} and ΔG_{2b} are 0.48 and 0.41 eV for Ni, 0.57 and 0.37 eV for Pd, and 0.20 and 0.19 eV for Pt, respectively. The corresponding

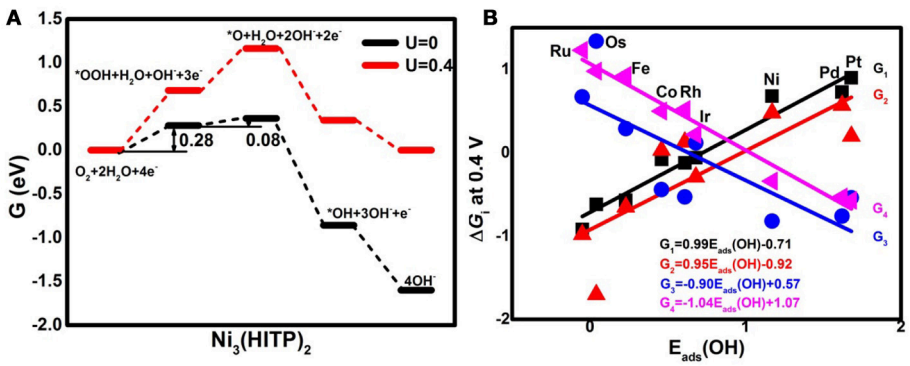

FIGURE 4 | The free energy *G* diagrams of $Ni_3(HITP)_2$ in the alkaline medium **(A)** and the free energy change ΔG_i of the elemental step R_i at the ideal potential of 0.4 eV **(B)**.

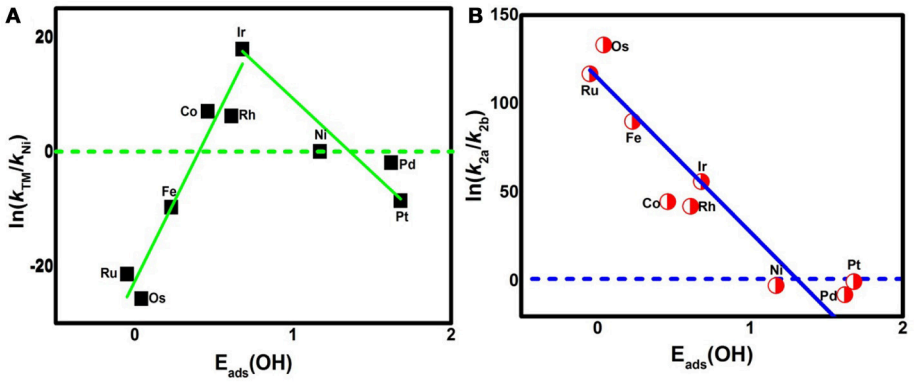

FIGURE 5 | The activity enhancement factor of $TM_3(HITP)_2$ referred to the $Ni_3(HITP)_2$ **(A)** and the selectivity of the $4e^-$ reduction referred to the $2e^-$ pathway **(B)**.

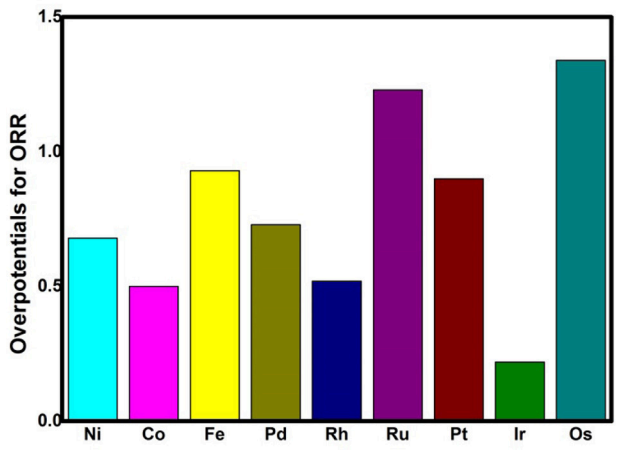

FIGURE 6 | The overpotentials μ_{ORR} of the $TM_3(HITP)_2$ monolayer for the $4e^-$ mechanism.

TABLE 1 | The E_{ads} and ΔG of ORR intermediates at the potential $U = 0.4$V with and without the vdW corrections.

	Without vdW			With vdW		
	Co	Rh	Ir	Co	Rh	Ir
E_{ads} (O_2)	−0.64	−0.41	−0.31	−0.67	−0.50	−0.39
E_{ads} (OOH)	3.42	3.52	3.59	3.20	3.41	3.49
E_{ads} (O)	2.53	2.59	2.16	2.54	2.55	2.11
E_{ads} (OH)	0.46	0.61	0.68	0.28	0.54	0.61
ΔG_1	−0.08	−0.12	−0.06	−0.31	−0.23	−0.16
ΔG_{2a}	0.03	0.13	−0.29	0.26	0.20	−0.23
ΔG_{2b}	1.18	1.21	1.15	1.40	1.32	1.26
ΔG_3	−0.44	−0.53	0.12	−0.64	−0.56	0.09
ΔG_4	0.50	0.52	0.22	0.68	0.59	0.30
ΔG_{max}	0.50	0.52	0.22	0.68	0.59	0.30

$\ln(k_{2a}/k_{2b})$ are −2.72, −7.78, and −0.39, indicating the energy favorability of R_{2b} compared with that of R_{2a} for group 10. Furthermore, considering the $\ln(k_{2a}/k_{2b})$ data, the $2e^-$ reduction of O_2 to H_2O_2 is prevalent at the Ni and Pd centers, while the mixing of $2/4e^-$ ORR is reasonable for the Pt center. By contrast, R_{2a} is preferred for other elements indicated by the positive $\ln(k_{2a}/k_{2b})$. That is, the $4e^-$ mechanism is dominant for group 8 and group 9. Obviously, as the E_{ads}(OH) is strengthened, the catalytic selectivity is changed from the $2e^-$ to $4e^-$ pathway. The two sides of the catalytic activity profile shown in **Figure 5A** essentially distinguish the $2e^-$ catalysts (weak binding side) from the $4e^-$ catalysts (strong binding side) (Viswanathan et al., 2012b; Zagal and Koper, 2016). That is, the former suffering from the insufficient O_2 activation favors the H_2O_2 formation; the latter poisoned by the O–containing intermediates generally prefers the H_2O formation. The formation of H_2O_2 not only decreases the ORR efficiency, but also degrades the proton exchange membrane (Tsuneda et al., 2017). In short, the dramatic enhancements in oxygen-reduction rates and product selectivity are achieved by selecting TM centers in group 9, in line with the previous works (Gao et al., 2017; Wannakao et al., 2017).

To understand the influence of the long-term electrostatic potential on the ORR performance, the vdW correction is further applied for analyzing the optimum Ir/Co/Rh systems, where the corresponding adsorption energy and the free energy changes are listed in **Table 1**. Intuitively, the adsorption abilities of the mentioned systems are enhanced due to the presence of the long-term interaction, in consistence with our calculation data. For the $Ir_3(HITP)_2$ monolayer, the E_{ads} are slightly increased to −0.39, 3.49, 2.11, and 0.61 eV for O_2, OOH, O, and OH, respectively, in comparison with the uncorrected values of −0.31, 3.59, 2.16, and 0.68 eV. The perturbation of the binding strength hinders the OH removal from the Ir active site, leading to the uphill of the ΔG_{max} from 0.22 to 0.30 eV. Despite the activity decrease, the $4e^-$ reduction pathway remains, supported by the values of ΔG_{2a} with −0.23 eV and ΔG_{2b} with 1.26 eV. Herein, the same phenomenon is found for $Co_3(HITP)_2$ and $Rh_3(HITP)_2$ with the ΔG_{max} of 0.68 and 0.59 eV, respectively. The corresponding ORR activity with th $4e^-$ reaction mechanism follows the order of Ir > Rh ≈ Co. Despite the numerical variation, the trend

is roughly consistent with the results without considering vdW interaction.

Despite the presence of the $Ni_3(HITP)_2$ experimentally, other 2D catalysts are only theoretical models, which need the confirmation of their synthesis. It should be noted that changing metal atoms would significantly modify the corresponding structures. Thus, by replacing the Ni central atom, the dimensionality of the $Cr_3(HITP)_2$ could be transferred from 2D to 3D due to the energetic favorable insertion of the spacer linker (Foster et al., 2016). Different structures inevitably lead to distinct catalytic performances (Sun et al., 2014). In this regard, although the theoretical candidates have been rationally predicted, the ORR performance of the optimum $TM_3(HITP)_2$ with the Co/Rh/Ir active sites crucially needs further experimentally verification.

CONCLUSION

Based on the DFT, the ORR mechanisms on $TM_3(HITP)_2$ monolayer have been studied. It is found that the selection of central metals affects the adsorption behaviors, tuning ORR activity and its selectivity. It is realized that the adsorption abilities are monotonously enhanced as the *d* band upshifts from group 10 to group 8. A classical volcano relationship for the predicted ORR activity as a function of calculated OH adsorption energy is observed. From the calculated ΔG data, the ORR activity decreases in the order of Ir > Co ≈ Rh > Ni ≈ Pd > Pt ≈ Fe > Ru > Os. That is, group 9 possesses superior activity compared with other elements. Furthermore, owing to the insufficient O_2 activation, the $2e^-$ mechanism is prevalent in group 10, while the desirable $4e^-$ mechanism is dominant for others. These results would throw insights into the nature of the ORR mechanisms of $TM_3(HITP)_2$. The materials of the $Co_3(HITP)_2$, $Rh_3(HITP)_2$, and $Ir_3(HITP)_2$ have been screened out and served as the potential candidates for the ORR electrocatalysis.

AUTHOR CONTRIBUTIONS

BX carried out the simulation and wrote the paper. QJ revised the paper. HZ, HL, and XJ entered the discussion. All authors commented on the manuscript.

ACKNOWLEDGMENTS

We acknowledge the support from the National Natural Science Foundation of China (No. 21503097, 51631004) and the Natural Science Foundation of Jiangsu (No.BK20140518).

REFERENCES

Baran, J. D., Grönbeck, H., and Hellman, A. (2014). Analysis of porphyrines as catalysts for electrochemical reduction of O_2 and oxidation of H_2O. *J. Am. Chem. Soc.* 136, 1320–1326. doi: 10.1021/ja4060299

Calle-Vallejo, F., Martinez, J. I., and Rossmeisl, J. (2011). Density functional studies of functionalized graphitic materials with later transition metals for oxygen reduction reaction. *Phys. Chem. Chem. Phys.* 13, 15639–15643. doi: 10.1039/c1cp21228a

Chen, D., Xu, Y., Hu, B., Yan, C., and Lu, L. (2018). Investigation of proper external air flow path for tubular fuel cell stacks with an anode support feature. *Energ. Convers. Manage.* 171, 807–814. doi: 10.1016/j.enconman.2018.06.036

Chen, D., Xu, Y., Tade, M. O., and Shao, Z. (2017). General regulation of air flow distribution characteristics within planar solid oxide fuel cell stacks. *ACS Energy Lett.* 2, 319–326. doi: 10.1021/acsenergylett.6b00548

Chen, S., Dai, J., and Zeng, X. C. (2015). Metal–organic kagome lattices M_3(2,3,6,7,10, 11-hexaiminotriphenylene)$_2$ (M= Ni and Cu): from semiconducting to metallic by metal substitution. *Phys. Chem. Chem. Phys.* 17, 5954–5958. doi: 10.1039/C4CP05328A

Choi, C. H., Lim, H. K., Chung, M. W., Park, J. C., Shin, H., Kim, H., et al. (2014). Long-range electron transfer over graphene-based catalyst for high-performing oxygen reduction reactions: importance of size, N-doping, and metallic impurities. *J. Am. Chem. Soc.* 136, 9070–9077. doi: 10.1021/ja5033474

Choi, W. I., Wood, B. C., Schwegler, E., and Ogitsu, T. (2015). Combinatorial search for high-activity hydrogen catalysts based on transition-metal-embedded graphitic carbons. *Adv. Energy. Mater.* 5:1501423. doi: 10.1002/aenm.201501423

Colić, V., and Bandarenka, A. S. (2016). Pt alloy electrocatalysts for oxygen reduction reaction: from model surfaces to nanostructured systems. *ACS Catal.* 6, 5378–5385. doi: 10.1021/acscatal.6b00997

Debe, M. K. (2012). Electrocatalyst approaches and challenges for automotive fuel cells. *Nature* 486, 43–51. doi: 10.1038/nature11115

Delley, B. (1990). An all-electron numerical method for solving the local density functional for polyatomic molecules. *J. Chem. Phys.* 92, 508–517. doi: 10.1063/1.458452

Delley, B. (2000). From molecules to solids with the $DMol^3$ approach. *J. Chem. Phys.* 113, 7756–7764. doi: 10.1063/1.1316015

Delley, B. (2002). Hardness conserving semilocal pseudopotentials. *Phys. Rev. B* 66:155125. doi: 10.1103/PhysRevB.66.155125

Favaro, M., Ferrighi, L., Fazio, G., Colazzo, L., Di Valentin, C., Durante, C., et al. (2015). Single and multiple doping in graphene quantum dots: unraveling the origin of selectivity in the oxygen reduction reaction. *ACS Catal.* 5, 129–144. doi: 10.1021/cs501211h

Foster, M. E., Sohlberg, K., Spataru, C. D., and Allendorf, M. D. (2016). Proposed modification of the graphene analogue $Ni_3(HITP)_2$ to yield a semiconducting material. *J. Phys. Chem. C* 120, 15001–15008. doi: 10.1021/acs.jpcc.6b05746

Gao, G., Bottle, S., and Du, A. (2018). Understanding the activity and selectivity of single atom catalysts for hydrogen and oxygen evolution via ab initial study. *Catal. Sci. Technol.* 8, 996–1001. doi: 10.1039/C7CY02463K

Gao, G., Waclawik, E. R., and Du, A. (2017). Computational screening of two-dimensional coordination polymers as efficient catalysts for oxygen evolution and reduction reaction. *J. Catal.* 352, 579–585. doi: 10.1016/j.jcat.2017.06.032

Greeley, J., Stephens, I. E. L., Bondarenko, A. S., Johansson, T. P., Hansen, H. A., Jaramillo, T. F., et al. (2009). Alloys of platinum and early transition metals as oxygen reduction electrocatalysts. *Nat. Chem.* 1, 552–556. doi: 10.1038/nchem.367

Hammer, B., and Nørskov, J. K. (2000). Theoretical surface science and catalysis-calculations and concepts. *Adv. Catal.* 45, 71–129. doi: 10.1016/S0360-0564(02)45013-4

Hou, X., Zhang, P., Li, S., and Liu, W. (2016). Enhanced electrocatalytic activity of nitrogen-doped olympicene/graphene hybrids for the oxygen reduction reaction. *Phys. Chem. Chem. Phys.* 18, 22799–22804. doi: 10.1039/C6CP03451A

Jasinski, R. (1964). A new fuel cell cathode catalyst. *Nature* 201, 1212–1213. doi: 10.1038/2011212a0

Jia, Y., Zhang, L., Du, A., Gao, G., Chen, J., Yan, X., et al. (2016). Defect graphene as a trifunctional catalyst for electrochemical reactions. *Adv. Mater.* 28, 9532–9538. doi: 10.1002/adma.201602912

Kattel, S., Atanassov, P., and Kiefer, B. (2013). Catalytic activity of Co-Nx/C electrocatalysts for oxygen reduction reaction: a density functional theory study. *Phys. Chem. Chem. Phys.* 15, 148–153. doi: 10.1039/C2CP42609A

Kattel, S., Atanassov, P., and Kiefer, B. (2014). A density functional theory study of oxygen reduction reaction on non-PGM Fe-Nx-C electrocatalysts. *Phys. Chem. Chem. Phys.* 16, 13800–13806. doi: 10.1039/c4cp01634c

Lang, X. Y., Han, G. F., Xiao, B. B., Gu, L., Yang, Z. Z., Wen, Z., et al. (2015). Mesostructured intermetallic compounds of platinum and non-transition metals for enhanced electrocatalysis of oxygen reduction reaction. *Adv. Funct. Mater.* 25, 230–237. doi: 10.1002/adfm.201401868

Li, F., Han, G. F., Noh, H. J., Kim, S.-J., Lu, Y., Jeong, H. Y., et al. (2018). Boosting oxygen reduction catalysis with abundant copper single atom active sites. *Energy Environ. Sci.* 11, 2263–2269. doi: 10.1039/C8EE01169A

Liang, H. W., Wei, W., Wu, Z.-S., Feng, X., and Müllen, K. J. (2013). Mesoporous metal-nitrogen-doped carbon electrocatalysts for highly efficient oxygen reduction reaction. *J. Am. Chem. Soc.* 135, 16002–16005. doi: 10.1021/ja407552k

Lim, D. H., and Wilcox, J. (2012). Mechanisms of the oxygen reduction reaction on defective graphene-supported Pt nanoparticles from first-principles. *J. Phys. Chem. C* 116, 3653–3660. doi: 10.1021/jp210796e

Liu, J., Jiao, M., Lu, L., Barkholtz, H. M., Li, Y., Wang, Y., et al. (2017). High performance platinum single atom electrocatalyst for oxygen reduction reaction. *Nat. Commun.* 8:15938. doi: 10.1038/ncomms15938

Liu, K., Kattel, S., Mao, V., and Wang, G. (2016). Electrochemical and computational study of oxygen reduction reaction on nonprecious transition metal/nitrogen doped carbon nanofibers in acid medium. *J. Phys. Chem. C* 120, 1586–1596. doi: 10.1021/acs.jpcc.5b10334

Miner, E. M., Fukushima, T., Sheberla, D., Sun, L., Surendranath, Y., and Dincă, M. (2016). Electrochemical oxygen reduction catalysed by Ni_3(hexaiminotriphenylene)$_2$. *Nat. Commun.* 7:10942. doi: 10.1038/ncomms10942

Nie, X., Luo, W., Janik, M. J., and Asthagiri, A. (2014). Reaction mechanisms of CO_2 electrochemical reduction on Cu (1 1 1) determined with density functional theory. *J. Catal.* 312, 108–122. doi: 10.1016/j.jcat.2014.01.013

Nørskov, J. K., Rossmeisl, J., Logadottir, A., Lindqvist, L., Kitchin, J. R., Bligaard, T., et al. (2004). Origin of the overpotential for oxygen reduction at a fuel–cell cathode. *J. Phys. Chem. B* 108, 17886–17892. doi: 10.1021/jp047349j

Palaniselvam, T., Kashyap, V., Bhange, S. N., Baek, J. B., and Kurungot, S. (2016). Nanoporous graphene enriched with Fe/Co-N active sites as a promising oxygen reduction electrocatalyst for anion exchange membrane fuel cells. *Adv. Funct. Mater.* 26, 2150–2162. doi: 10.1002/adfm.201504765

Peng, H., Mo, Z., Liao, S., Liang, H., Yang, L., Luo, F., et al. (2013). High performance Fe- and N- doped carbon catalyst with graphene structure for oxygen reduction. *Sci. Rep.* 3:1765. doi: 10.1038/srep01765

Perdew, J. P., Burke, K., and Ernzerhof, M. (1996). Generalized gradient approximation made simple. *Phys. Rev. Lett.* 77, 3865–3868. doi: 10.1103/PhysRevLett.77.3865

Sha, Y., Yu, T. H., Merinov, B. V., Shirvanian, P., and Goddard, W. A. (2011). Oxygen hydration mechanism for the oxygen reduction reaction at Pt and Pd fuel cell catalysts. *J. Phys. Chem. Lett.* 2, 572–576. doi: 10.1021/jz101753e

Sheberla, D., Sun, L., Blood-Forsythe, M. A., Er, S., Wade, C. R., Brozek, C. K., et al. (2014). High electrical conductivity in Ni_3(2,3,6,7,10,11-hexaiminotriphenylene)$_2$, a semiconducting metal-organic graphene analogue. *J. Am. Chem. Soc.* 136, 8859–8862. doi: 10.1021/ja502765n

Stephens, I. E. L., Bondarenko, A. S., Grønbjerg, U., Rossmeisl, J., and Chorkendorff, I. (2012). Understanding the electrocatalysis of oxygen reduction on platinum and its alloys. *Energy Environ. Sci.* 5, 6744–6762. doi: 10.1039/C2EE03590A

Sun, J., Fang, Y., and Liu, Z. (2014). Electrocatalytic oxygen reduction kinetics on Fe-center of nitrogen-doped graphene. *Phys. Chem. Chem. Phys.* 16, 13733–13740. doi: 10.1039/C4CP00037D

Tang, C., Wang, H. F., Chen, X., Li, B. Q., Hou, T. Z., Zhang, B., et al. (2016). Topological defects in metal-free nanocarbon for oxygen electrocatalysis. *Adv. Mater.* 28, 6845–6851. doi: 10.1002/adma.201601406

Todorova, T., and Delley, B. (2008). Wetting of paracetamol surfaces studied by DMol^3-COSMO calculations. *Mol. Simul.* 34, 1013–1017. doi: 10.1080/08927020802235672

Tsuneda, T., Singh, R. K., Iiyama, A., and Miyatake, K. (2017). Theoretical Investigation of the H_2O_2-Induced Degradation Mechanism of Hydrated Nafion Membrane via Ether-Linkage Dissociation. *ACS Omega* 2, 4053–4064. doi: 10.1021/acsomega.7b00594

Viswanathan, V., Hansen, H. A., Rossmeisl, J., and Nørskov, J. K. (2012a). Universality in oxygen reduction electrocatalysis on metal surfaces. *ACS Catal.* 2, 1654–1660. doi: 10.1021/cs300227s

Viswanathan, V., Hansen, H. A., Rossmeisl, J., and Nørskov, J. K. (2012b). Unifying the $2e^-$ and $4e^-$ reduction of oxygen on metal surfaces. *J. Phys. Chem. Lett.* 3, 2948–2951. doi: 10.1021/jz301476w

Wang, N., Feng, L., Shang, Y., Zhao, J., Cai, Q., and Jin, P. (2016a). Two-dimensional iron-tetracyanoquinodimethane(Fe-TCNQ) monolayer: an efficient electrocatalysts for the oxygen reduction reaction. *RSC Adv.* 6, 72952–72958. doi: 10.1039/C6RA14339C

Wang, N., Liu, Y., Zhao, J., and Cai, Q. (2016b). DFT-based study on the mechanisms of the oxygen reduction reaction on Co(acetylacetonate)$_2$ supported by N-doped graphene nanoribbon. *RSC Adv.* 6, 79662–79667. doi: 10.1039/C6RA17651H

Wang, Y., Yuan, H., Li, Y., and Chen, Z. (2015). Two-dimensional iron-phthalocyanine (Fe-Pc) monolayer as a promising single-atom-catalyst for oxygen reduction reaction: a computational study. *Nanoscale* 7, 11633–11641. doi: 10.1039/C5NR00302D

Wannakao, S., Maihom, T., Kongpatpanich, K., Limtrakul, J., and Promarak, V. (2017). Halogen substitutions leading to enhanced oxygen evolution and oxygen reduction reactions in metalloporphyrin frameworks. *Phys. Chem. Chem. Phys.* 19, 29540–29548. doi: 10.1039/C7CP06187K

Xia, W., Mahmood, A., Liang, Z., Zou, R., and Guo, S. (2016). Earth-abundant nanomaterials for oxygen reduction. *Angew. Chem. Int. Ed.* 55, 2650–2676. doi: 10.1002/anie.201504830

Xia, Z., An, L., Chen, P., and Xia, D. (2016). Non-Pt nanostructured catalysts for oxygen reduction reaction: synthesis, catalytic activity and its key factors. *Adv. Energy Mater.* 6:1600458. doi: 10.1002/aenm.201600458

Xiao, B. B., Jiang, X. B., and Jiang, Q. (2016). Density functional theory study of oxygen reduction reaction on Pt/Pd_3Al(111) alloy electrocatalyst. *Phys. Chem. Chem. Phys.* 18, 14234–14243. doi: 10.1039/C6CP01066K

Xiao, B. B., Liu, H. Y., Jiang, X. B., Yu, Z. D., and Jiang, Q. (2017). A bifunctional two dimensional $TM_3(HHTP)_2$ monolayer and its variations for oxygen electrode reactions. *RSC Adv.* 7, 54332–54340. doi: 10.1039/C7RA09974F

Xu, H., Cheng, D., Cao, D., and Zeng, X. C. (2018). A universal principle for a rational design of single-atom electrocatalysts. *Nat. Catal.* 1, 339–348. doi: 10.1038/s41929-018-0063-z

Yang, X., Zheng, Y., Yang, J., Shi, W., Zhong, J. H., Zhang, C., et al. (2017). Modeling Fe/N/C catalysts in monolayer graphene. *ACS Catal.* 7, 139–145. doi: 10.1021/acscatal.6b02702

Yin, P., Yao, T., Wu, Y., Zheng, L., Lin, Y., Liu, W., et al. (2016). Single cobalt atoms with precise N-coordination as superior oxygen reduction reaction catalysts. *Angew. Chem. Int. Ed.* 55, 10800–10805. doi: 10.1002/anie.201604802

Zagal, J. H., and Koper, M. (2016). Reactivity descriptors for the activity of molecular MN_4 catalysts for the oxygen reduction reaction. *Angew. Chem. Int. Ed.* 55, 14510–14521. doi: 10.1002/anie.201604311

Zhang, P., Hou, X., Liu, L., Mi, J., and Dong, M. (2015). Two-dimensional π-conjugated metal bis(dithiolene) complex nanosheets as selective catalysts for oxygen reduction reaction. *J. Phys. Chem. C* 119, 28028–28037. doi: 10.1021/acs.jpcc.5b09148

Zhang, Q., Mamtani, K., Jain, D., Ozkan, U., and Asthagiri, A. (2016). CO poisoning effects on FeNC and CNx ORR catalysts: a combined experimental-computational study. *J. Phys. Chem. C* 120, 15173–15184. doi: 10.1021/acs.jpcc.6b03933

Zheng, Y., Jiao, Y., Zhu, Y., Cai, Q., Vasileff, A., Li, L. H., et al. (2017). Molecule-Level g-C_3N_4 coordinated transition metals as a new class of electrocatalysts for oxygen electrode reactions. *J. Am. Chem. Soc.* 139, 3336–3339. doi: 10.1021/jacs.6b13100

Conflict of Interest Statement: The authors declare that the research was conducted in the absence of any commercial or financial relationships that could be construed as a potential conflict of interest.

Advantages of publishing in Frontiers

OPEN ACCESS
Articles are free to read for greatest visibility and readership

FAST PUBLICATION
Around 90 days from submission to decision

HIGH QUALITY PEER-REVIEW
Rigorous, collaborative, and constructive peer-review

TRANSPARENT PEER-REVIEW
Editors and reviewers acknowledged by name on published articles

Frontiers
Avenue du Tribunal-Fédéral 34
1005 Lausanne | Switzerland

Visit us: www.frontiersin.org
Contact us: info@frontiersin.org | +41 21 510 17 00

REPRODUCIBILITY OF RESEARCH
Support open data and methods to enhance research reproducibility

DIGITAL PUBLISHING
Articles designed for optimal readership across devices

FOLLOW US
@frontiersin

IMPACT METRICS
Advanced article metrics track visibility across digital media

EXTENSIVE PROMOTION
Marketing and promotion of impactful research

LOOP RESEARCH NETWORK
Our network increases your article's readership